Study of quantum annealing by simulating the time evolution of flux qubits

Von der Fakultät für Mathematik, Informatik und Naturwissenschaften der RWTH Aachen University zur Erlangung des akademischen Grades einer Doktorin der Naturwissenschaften genehmigte Dissertation

vorgelegt von

MADITA FRANZISKA WILLSCH GEB. NOCON, M.Sc.

aus

Leverkusen

Berichter: Prof. Dr. Kristel Michielsen

Prof. Dr. David DiVincenzo

Tag der mündlichen Prüfung: 7. Juli 2020

Diese Dissertation ist auf den Internetseiten der Universitätsbibliothek verfügbar.

Abstract

In this thesis, we study the operation of existing quantum annealers by simulating the realtime dynamics of two coupled flux qubits based on SQUIDs (superconducting quantum interference devices) during quantum annealing processes.

We investigate two aspects. First, we study the influence of the higher energy levels which are neglected when deriving the qubit Hamiltonian from the superconducting circuit model including the tunable coupler. Second, we investigate the influence of an environment on the qubit system during quantum annealing. For the latter, we examine two different models for the environment, a generic spin bath and non-interacting two-level systems. For simulating the dynamics, we use the Suzuki-Trotter product-formula algorithm to solve the time-dependent Schrödinger equation numerically.

We find that the higher energy levels as well as the presence of the tunable coupler have little influence on the performance of the quantum annealing process for most of the investigated problem instances, suggesting that the two-level approximation works very well. However, we find that for a particular class of instances, the results of the SQUID model and the qubit model show certain deviations.

Additionally, we perform experiments on the D-Wave 2000Q quantum annealer. Our study of the two models for the environment suggests that the model of non-interacting two-level systems is better suited to describe the data obtained from the real device than the generic spin bath model.

Zusammenfassung

In dieser Dissertation untersuchen wir die Funktionsweise existierender Quanten-Annealer, indem wir Computersimulationen der Echtzeit-Dynamik zweier gekoppelter, auf SQUIDs (supraleitenden Quanteninterferenzeinheiten, engl. superconducting quantum interference devices) basierenden Fluss-Qubits während Quanten-Annealing-Prozessen durchführen.

Dabei gehen wir auf zwei Aspekte ein. Zuerst untersuchen wir den Einfluss der höheren Energiezustände, welche bei der Herleitung des Qubit-Hamiltonoperators ausgehend vom supraleitenden Schaltkreismodell einschließlich eines steuerbaren Kopplers, vernachlässigt werden. Als Zweites untersuchen wir den Einfluss der Umgebung auf das Qubitsystem während des Quanten-Annealing-Prozesses. Dazu studieren wir zwei verschiedene Modelle für die Umgebung: ein generisches Spinreservoir und nicht miteinander wechselwirkende Zwei-Zustands-Systeme. Zur Simulation der Dynamik verwenden wir den Suzuki-Trotter Product-Formula-Algorithmus um die zeitabhängige Schrödingergleichung numerisch zu lösen.

Wir finden, dass sowohl die höheren Energiezustände als auch die Präsenz des steuerbaren Kopplers für die meisten untersuchten Probleminstanzen wenig Einfluss auf die Funktion des Quanten-Annealing-Prozesses haben, was nahe legt, dass die Zwei-Zustands-Approximation sehr gut funktioniert. Wir finden jedoch auch, dass für eine spezielle Klasse von Instanzen die Ergebnisse des SQUID-Modells und des Qubit-Modells gewisse Unterschiede aufweisen.

Zusätzlich führen wir Experimente auf dem D-Wave 2000Q Quanten-Annealer durch. Unsere Untersuchung der beiden Modelle für die Umgebung suggeriert, dass das Modell der nicht miteinander wechselwirkenden Zwei-Zustands-Systeme besser geeignet ist, die auf dem echten Gerät gewonnenen Daten zu beschreiben, als das generische Spinreservoir.

Contents

1	Intr	oducti		1
	1.1	The q	ubit	2
	1.2	Brief o	overview of superconducting qubits	6
	1.3	Outlin	ne	7
2	Adi	abatic	quantum computation and quantum annealing	9
	2.1	The ti	me-dependent Hamiltonian	11
		2.1.1	The qubit Hamiltonian	11
	2.2	Relati	on to optimization problems	13
	2.3	Relati	on to the Landau-Zener theory	16
3	The	Suzul	ki-Trotter product-formula algorithm	19
	3.1	Princi	ple	19
	3.2	Implei	mentation	21
		3.2.1	Pauli updates	22
		3.2.2	Decomposition of a tridiagonal matrix	23
		3.2.3	Decomposition of a matrix with elements on the m -th diagonals	24
		3.2.4	Decompositions in tensor-product spaces	28
		3.2.5	Efficiency and non-Pauli updates	29
	3.3	Error	analysis	30
4	Sup	ercono	lucting flux qubits	37
	4.1	Super	conducting circuits	37
		4.1.1	The Josephson effect	37
		4.1.2	Circuit quantization	38
	4.2	Supere	conducting quantum interference device	41
		4.2.1	Theoretical model of a single SQUID	42
		4.2.2	Tunable coupling between SQUIDs	43
		4.2.3	Mapping SQUIDs to two-level systems for quantum annealing $$	47
5	Sim	ulatio	ns of quantum annealing with SQUIDs	51
	5.1	Discre	tization of the Hamiltonian	51
		5.1.1	Coordinate basis	51
		5.1.2	Basis of number states	56
		5.1.3	Two SQUIDs as qubits	60
		5.1.4	Computational basis and qubit density matrix	65
	5.2	Metho	ods to estimate the annealing scheme	66
			Computing the annealing scheme for a single qubit	66

		5.2.2	Comparing simulation data to approximate analytical results from	
			the qubit model	. 68
	5.3	Analy	sis of the results	
		5.3.1	Effective coupling strength $(s = 1)$	
		5.3.2	Effective annealing scheme $(0 \le s \le 1) \dots \dots \dots$. 75
		5.3.3	Comparison to the ideal qubit model	
		5.3.4	Three different classes of problem instances	. 82
		5.3.5	Influence of the higher energy levels	. 85
		5.3.6	Brief summary of the results	. 94
		5.3.7	Comparison with the experiment on the D-Wave 2000Q quantum	
			annealer	. 95
6	Qua	ntum	annealing in the presence of an environment	97
	6.1		ation: Studying the D-Wave data	. 98
	6.2		ing the environment	
		6.2.1	Model I: Generic spin bath	. 105
		6.2.2	Model II: Non-interacting two-level defects	
	6.3	Simula	ation results	
		6.3.1	Results for the spin bath (model I)	
		6.3.2	Results for the non-interacting defects (model II)	
		6.3.3	Comparison	
7	Sun	nmary	and conclusion	123
٨	Cina	anit an	nantization of the studied systems	127
A	A.1	-	e SQUID	
			ed SQUIDs	
	A.2	Coupi	ed SQUIDs	. 150
В	\mathbf{Adc}	litiona	l calculations and proofs	135
	B.1	Basis	transformation	. 135
	B.2	Monot	tonicity	. 138
	B.3		uting energies from device parameters	
	B.4	Time	evolution of the coupler	. 139
	B.5	Pertur	bation theory during the annealing process	. 140
A	cknov	wledgn	nents	145
Bi	bliog	graphy		147
Li	st of	Public	cations	161
	~ 0 01	- abii		101

Chapter 1

Introduction

Simulating quantum systems on a conventional computer requires exponentially growing memory and run time with increasing system size, and to date, it is believed that there is in general no efficient (i.e. scaling only polynomially) algorithm when using conventional computers. This renders simulations (excluding semi-classical approximations) of large many-body quantum systems infeasible even for the largest supercomputers.

In 1982, Feynman proposed the idea to simulate quantum systems by means of another generic quantum system which he called a *quantum computer* [Fey82]. The reason for this quantum computer to be able to simulate quantum systems more efficiently than a conventional computer is that it naturally follows the same quantum mechanical laws as the quantum system to be simulated, thus circumventing the exponential growth of resources.

Two different kinds of quantum computing have been proposed — the gate model of quantum computing [Fey86; Bar+95; DiV00], and adiabatic quantum computation also called quantum annealing [Fin+94; Bro+99; Far+00; CFP01].

The gate-model quantum computer operates in a way similar to a conventional computer in terms of gates, a combination of which can be used to construct an algorithm. One of the most commonly known algorithms for quantum computers is probably Shor's factoring algorithm [Sho94; Sho97], which can in principle determine the prime factors of (large) numbers in polynomial time. It is not proven that there exists no efficient factoring algorithm for conventional computers but so far, none is known and factoring seems to be a hard problem for conventional computers. The same holds for the problem of finding the discrete logarithm [Sho94]. Currently used public-key cryptosystems, such as RSA [RSA78], rely on the assumption that factoring large numbers into its two (large) prime factors or finding the discrete logarithm are difficult tasks for a conventional computer. However, with a large enough, fault-tolerant quantum computer, these prime factors could in principle be computed efficiently and thus, the cryptosystem would break. But we are still far away from building a large, fault-tolerant quantum computer. Current quantum devices built in various laboratories around the world are at the stage of the so-called noisy intermediate-scale quantum (NISQ) devices [Pre18], meaning that system sizes are rather small and the imperfect gates are not yet error-corrected.

Other applications which may already work on these NISQ devices [Pre18], and have a wider application area, are hybrid variational algorithms such as the quantum approximate optimization algorithm (QAOA) [FGG14] or the variational quantum eigensolver (VQE) [Per+14; McC+16]. Another goal, which does not necessarily have a practical ap-

plication, is to show quantum supremacy [Boi+18; Nei+18], that is, to find a task which can be efficiently performed on a (NISQ) device, but a conventional computer would need an exponentially long run time or an exponential amount of memory to perform the same task. Recently, quantum supremacy has been shown on a 53-qubit chip [Aru+19] (of the gate-model type), by sampling from a probability distribution characterized by a random circuit [Boi+18].

A quantum annealer functions in a way that is fundamentally different from the gate-model quantum computer. The idea is to make use of the natural (adiabatic) evolution of a quantum system prepared initially in its ground state. For a quantum annealer, no gates are used. Instead, problems (usually optimization problems) are defined by specifying the parameters of a problem Hamiltonian. The Hamiltonian of the quantum system changes adiabatically in time from an initial Hamiltonian into this problem Hamiltonian.

Adiabatic quantum computation and the gate model of quantum computing have been found to be computationally equivalent in the sense that one can simulate the other with only polynomial overhead and vice versa [Aha+07]. Although a lot of theoretical work has been done on adiabatic quantum computation [AL18], there are not many groups working experimentally in this direction. However, D-Wave Systems Inc. manufactures and sells quantum annealers, and their current device is much larger (about 2000 qubits [Kin+18]) than current gate-model quantum computers (53 qubits [Aru+19]). In this thesis, we investigate, by numerical simulation on conventional computers, the qubits built and used by D-Wave Systems Inc. for their quantum annealing processors [Har+10a].

In the following section, we summarize definitions, including the one of a *qubit*, and key concepts of quantum computation as described in Refs. [NC10] and [Pre]. Subsequently, we give a short summary on superconducting circuits as this is the technology used for the quantum systems that we investigate in this thesis. Finally, we outline the content of the main part of this thesis.

1.1 The qubit

The basic unit to represent and process information on a quantum computer is called quantum bit or *qubit*. Like the "classical" bit, a qubit can represent a 0 or a 1. However, in contrast to the "classical" bit which is a Boolean variable, a qubit can be described as a unit vector in a two-dimensional complex vector space (Hilbert space) \mathcal{C} . The vectors representing 0 and 1 are usually denoted by

$$|0\rangle = \begin{pmatrix} 1\\0 \end{pmatrix}, \qquad |1\rangle = \begin{pmatrix} 0\\1 \end{pmatrix}, \tag{1.1}$$

where we introduced the braket notation $|0\rangle$ and $|1\rangle$ of the two vectors, and these two vectors form a basis of $\mathcal{C} \simeq \mathbb{C}^2$. This basis is often called the *computational basis*. A general qubit state $|\psi\rangle$ can be expressed as a linear combination of the basis vectors, which is called *superposition*,

$$|\psi\rangle = a|0\rangle + b|1\rangle = \begin{pmatrix} a \\ b \end{pmatrix},$$
 (1.2)

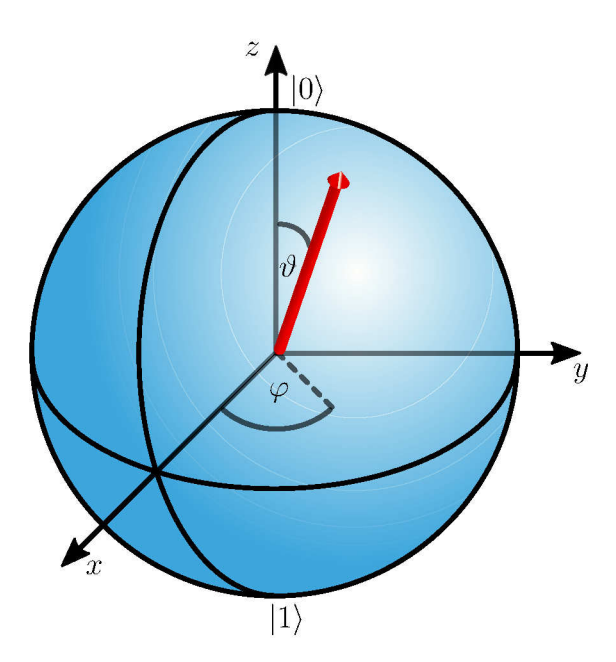


Figure 1.1: The Bloch sphere representation of a qubit. The red arrow shows the qubit state defined by the angles ϑ and φ according to Eq. (1.3).

where $a, b \in \mathbb{C}$ and $|a|^2 + |b|^2 = 1$. Enforcing the latter constraint and omitting the global phase, we can write the qubit state as

$$|\psi\rangle = \cos\left(\frac{\vartheta}{2}\right)|0\rangle + e^{i\varphi}\sin\left(\frac{\vartheta}{2}\right)|1\rangle,$$
 (1.3)

where $\vartheta \in [0, \pi]$ and $\varphi \in [0, 2\pi]$. Since the Hilbert space \mathcal{C} describes a quantum-mechanical two-level system such as the spin degree-of-freedom of a spin-1/2 particle, we can equivalently denote the two basis vectors by spin-up $|\uparrow\rangle \equiv |0\rangle$ and spin-down $|\downarrow\rangle \equiv |1\rangle$. It is also possible to use any orthonormal basis of \mathbb{C}^2 to represent the qubit state such as, for instance,

$$|+\rangle = \frac{|0\rangle + |1\rangle}{\sqrt{2}} = \frac{1}{\sqrt{2}} \begin{pmatrix} 1\\1 \end{pmatrix}, \quad |-\rangle = \frac{|0\rangle - |1\rangle}{\sqrt{2}} = \frac{1}{\sqrt{2}} \begin{pmatrix} 1\\-1 \end{pmatrix}.$$
 (1.4)

A qubit state $|\psi\rangle$ can be represented as a vector of unit length in a three-dimensional unit sphere, called *Bloch sphere*, where $|0\rangle$ and $|1\rangle$ correspond to the points at the poles and the angles ϑ and φ define the vector uniquely, see Fig. 1.1.

According to the axioms of quantum theory, the amplitudes a and b cannot be measured directly. A measurement of the state yields one of two possible outcomes with probabilities p_0 and p_1 , and destroys the superposition leaving the state in the measured one. If the state $|\psi\rangle$ is given by Eq. (1.3) and the measurement is performed in the basis $\{|0\rangle, |1\rangle\}$, i.e., with respect to the z axis, then the probabilities are given by

$$p_0 = |\langle 0|\psi\rangle|^2 = \cos^2(\theta/2), \quad p_1 = |\langle 1|\psi\rangle|^2 = \sin^2(\theta/2),$$
 (1.5)

where $\langle i|\psi\rangle$ denotes the scalar product of the states $|i\rangle$ $(i \in \{0,1\})$ and $|\psi\rangle$. However, if the measurement is performed in the basis $\{|+\rangle, |-\rangle\}$, i.e, with respect to the x axis, the

probabilities are given by

$$p_0 = |\langle +|\psi\rangle|^2 = \frac{1+\sin\theta\cos\varphi}{2}, \quad p_1 = |\langle -|\psi\rangle|^2 = \frac{1-\sin\theta\cos\varphi}{2}. \tag{1.6}$$

A more general way of writing down the qubit state is in terms of a *density matrix*, usually denoted by ρ . If the qubit state is given by the vector $|\psi\rangle$, the corresponding density matrix is

$$\rho = |\psi\rangle\langle\psi|. \tag{1.7}$$

A density matrix which can be expressed in this way describes a *pure state*. A density matrix such as

$$\rho = \frac{1}{2}(|0\rangle\langle 0| + |1\rangle\langle 1|),\tag{1.8}$$

which cannot be written in the form of Eq. (1.7), describes a mixed state. As mentioned previously, a pure state can be represented by a vector of unit length on the Bloch sphere. A mixed state, however, is represented by a vector within the Bloch sphere, that is, the norm of the vector is less than one. In fact, the state given in Eq. (1.8) corresponds to a point at the origin. For this particular state, the probabilities for the two possible measurement outcomes are $p_0 = p_1 = 1/2$, independent of the basis.

The time-evolution of a qubit is governed by the (time-dependent) Schrödinger equation (TDSE)

$$i\frac{\partial}{\partial t}|\psi(t)\rangle = H(t)|\psi(t)\rangle,$$
 (1.9)

where we used $\hbar=1$, as we do throughout this thesis, and the Hamiltonian H(t) is a Hermitian 2×2 -matrix. The formal solution of Eq. (1.9) is given by $|\psi(t+\tau)\rangle=U(t+\tau,t)|\psi(t)\rangle$ where the operator $U(t+\tau,t)$ is the unitary time-evolution operator which evolves the state $|\psi(t)\rangle$ from time t to $t+\tau$.

The Pauli-matrices

$$\sigma^x = \begin{pmatrix} 0 & 1 \\ 1 & 0 \end{pmatrix}, \quad \sigma^y = \begin{pmatrix} 0 & -i \\ i & 0 \end{pmatrix}, \quad \sigma^z = \begin{pmatrix} 1 & 0 \\ 0 & -1 \end{pmatrix}, \tag{1.10}$$

and the 2×2 -identity matrix \mathbb{I}_2 are unitary matrices which form a basis of the matrices in $\mathbb{C}^{2\times 2}$. Thus, for a single qubit, the Hamiltonian can be written as a linear combination of the Pauli-matrices. Terms proportional to the identity matrix can be neglected as these only add a global phase factor in the time evolution.

Systems consisting of N qubits are described by unit vectors in a 2^N -dimensional complex vector space. This vector space is a tensor-product space of the two-dimensional complex vector spaces of the single qubits. This means that the states

$$\{|i_1\rangle \otimes |i_2\rangle \otimes \cdots \otimes |i_N\rangle | i_1, i_2, \dots, i_N \in \{0, 1\}\}, \tag{1.11}$$

where \otimes denotes the tensor product, form a basis of the N-qubit vector space \mathbb{C}^{2^N} . A state vector $|\Psi\rangle \in \mathbb{C}^{2^N}$ is called a *product state* if there exist $|\psi_i\rangle \in \mathbb{C}^2$, $i=1,2,\ldots,N$ such that

$$|\Psi\rangle = |\psi_1\rangle \otimes |\psi_2\rangle \otimes \cdots \otimes |\psi_N\rangle.$$
 (1.12)

If $|\Psi\rangle \in \mathbb{C}^{2^N}$ cannot be expressed as a product state, $|\Psi\rangle$ is called an *entangled state*.

Omitting the \otimes and writing all single-qubit states in a single ket, a general multi-qubit state can be written as

$$|\Psi\rangle = a_0|0...000\rangle + a_1|0...001\rangle + a_2|0...010\rangle + \cdots + a_{2^N-1}|1...1\rangle,$$
 (1.13)

where the 2^N amplitudes a_i are complex numbers and satisfy $\sum_{i=0}^{2^N-1} |a_i|^2 = 1$. Using the tensor-product structure of the vector space, the previously discussed concepts such as density matrices and the time evolution, can be straightforwardly extended to the multi-qubit case.

For the gate-based quantum computer, quantum gates need to be defined. A universal gate set is a set of gates which can be used to construct any other (multi-qubit) gate with a finite sequence of gates from this set. A possibility to construct a universal gate set would be to use two single-qubit gates, which perform rotations around independent axes and at least one of them includes a free parameter, and an entangling two-qubit gate. An example for such a set would be $\{R_X(\theta), R_Z(\phi), \text{CNOT}\}\$, where $R_X(\theta)$ rotates a single-qubit state (see Fig. 1.1) around the x axis by an angle θ (changing the projection onto the z axis) and $R_Z(\phi)$ performs a rotation around the z axis by an angle ϕ (effectively adding a phase factor to the state $|1\rangle$), and CNOT is the controlled-NOT gate, performing a bit flip (application of σ^x) on the target qubit if the control qubit is in the state $|1\rangle$. There are of course other possibilities for universal gate sets [Bar+95], which we will not discuss here. The Hamiltonian determining the time evolution of the qubit system has to be chosen in such a way that all gates of a given universal gate set can be performed by changing external parameters only. For this, the qubit system may need to be coupled to another auxiliary quantum system.

Like the composition of multi-qubit spaces, composite vector spaces of qubits and these auxiliary quantum systems, which may be for instance modeled as harmonic oscillators, are also described by tensor-product spaces. To state something about the qubit system after the time evolution of the composite system, we have to perform the partial trace over the auxiliary system (e.g. the harmonic oscillators) to obtain the reduced density matrix describing the qubit system. If the composite system can be described by a pure but entangled state, the reduced density matrix of the qubit system describes a mixed state. This is not desirable, so entanglement with the auxiliary system at the time of the measurement is to be avoided. While this can be in principle controlled for the auxiliary system, unwanted but inevitable coupling of the qubit system to the environment leads to decoherence. Not only can the qubit relax from the excited state to the ground state by exchanging energy with the environment, but also the unitary time evolution of the entire system can lead to entanglement of the qubit system and the environment, which yields a non-unitary evolution of the reduced qubit density matrix. The interaction with the environment yields then a mixed state for the qubit system, which loses phase coherence, i.e., superpositions of the qubit states are destroyed.

Now that we have introduced the main concepts of qubit systems, in the next section, we briefly outline experimental challenges and advances in building qubits from superconducting circuits.

1.2 Brief overview of superconducting qubits

One of the currently popular devices used to build artificial two-level systems to be utilized in a quantum computer are superconducting circuits. Although these systems are not genuine two-level systems, i.e. qubits, they are commonly referred to as *superconducting qubits*. Here, we briefly give an overview of some historically and currently important designs and implementations, and mention some advantages and disadvantages of these designs. A more detailed discussion including the circuit geometry of the system that we study in this thesis is presented in Chapter 4 and Appendix A.

There are three basic types of superconducting qubits – the charge qubit [SSH97; NPT99], the phase qubit [Mar+02; Ste+06] and the flux qubit [Chi00; MSS01].

The first realization of a charge qubit – the Cooper-pair box [SSH97; Bou+98] – suffered from charge noise [Nak+02]. For the transmon [Koc+07], an extended version of the Cooper-pair box, a reduced sensitivity to charge noise could be shown successfully [Sch+08]. However, like the phase qubit, the transmon qubit has a weak anharmonicity leading to excitations to higher energy levels outside the computational subspace (leakage), which is a limiting factor for gate operations [Mot+09; Luc+10; Gam+11; WBE16; Wil+17; WG18]. To overcome this issue, many pulse-shaping techniques have been suggested [Mot+09; Gam+11; McK+17] and implemented [Cho+10; Luc+10; Kel+14; Che+16; McK+17]. Variations of the transmon qubit have been proposed, and studies of and with transmon qubits are currently performed by various groups in academia [Bar+13; Lar+15; Bra+16; Bur+19; Gon+19; Rol+19] as well as in industry [Cal+18; Kli+18; McK+19].

The simplest design of a flux qubit is a superconducting quantum interference device (SQUID) [Chi00; MSS01]. However, this device was found to be sensitive to flux noise, which limits the coherence time of this type of flux qubit [Ben+09; Wen17]. Long coherence times (a large multiple of the time needed to perform a single gate operation so that error correction can be applied) are crucial for the gate-based model of quantum computation to work [DiV00]. More sophisticated designs such as the three-junction qubit [Moo+99; Orl+99; Wal+00; Gra+04], the fluxonium qubit [Man+09; Pop+14; Ngu+19] or the capacitively shunted (C-shunt) flux qubit [You+07; Ste+10; Yan+16] have been studied to be used for a gate-based quantum computer. For the three-junction qubit, however, the coherence time did not improve significantly. The fluxonium qubit and the C-shunt flux qubit seem to be more promising designs, attaining longer coherence times [Wen17].

There are various coupling schemes for superconducting qubits. Couplings can be realized by using inductances (inductive coupling) or by using capacitances (capacitive coupling). The coupling may need to be controllable, either for application of two-qubit gates or to control the annealing process. This can be achieved by tunable couplers [Plo+04; BBY05; Har+07; Che+14] or by tuning frequency-tunable (transmon) qubits close to resonance [Maj+07; DiC+09]. Alternatively, two-qubit gates can be performed by driving the qubits [Lee+09; Cho+11] or resonators which couple to the qubits [Pai+16].

The qubits used in the D-Wave quantum annealer are of the SQUID type [Har+09b; Har+10a] and controllable inductive coupling is realized through tunable couplers [Har+09a]. This type of qubit turned out to be unsuited for the gate model of quantum computation due to the short coherence time. The role of decoherence and temperature effects during

quantum annealing is a controversial topic and has been discussed theoretically [CFP01; SL05; AJN06; ATA09; Arc+17] and investigated experimentally [Boi+13; Dic+13]. Flux qubits usually have a large anharmonicity, hence they are considered less prone to leakage [Yos+14; Kra+19]. In this thesis, we investigate to what extent this is true for the flux qubits used for quantum annealing by D-Wave Systems Inc.

1.3 Outline

The structure of this thesis is as follows. In Chapter 2, we recapitulate the concepts of adiabatic quantum computation and quantum annealing. We also introduce the (time-dependent) Hamiltonian which we use in subsequent chapters. We briefly comment on complexity theory when we discuss the relation between the Ising spin Hamiltonian and optimization problems in Section 2.2. In Section 2.3, we outline the Landau-Zener theory and discuss its relation to adiabatic quantum computation and quantum annealing.

In Chapter 3, we present the Suzuki-Trotter product-formula algorithm which is the method we use to solve the TDSE numerically. First, we discuss the working principle before we illustrate in more detail the implementation. We conclude Chapter 3 by discussing the numerical errors of the method.

We begin in Chapter 4 by recapitulating the Josephson effect which arises in superconducting point contacts. Then we summarize the circuit quantization rules. Subsequently, we discuss the Hamiltonian of the SQUIDs used by D-Wave Systems Inc. to model their qubits as well as the Hamiltonian of two SQUIDs coupled via a third SQUID which mediates the coupling. We go through the steps needed to arrive at the qubit Hamiltonian.

In Chapter 5, we first discuss the discretization of the one-, two- and three-SQUID Hamiltonians studied in Chapter 4. We consider some analytical calculations and methods which we apply in the simulations. Then, we present and discuss our results.

Chapter 6 deals with the ideal qubit model in contact with an environment and we study the effects on the quantum annealing process in comparison with the data obtained from the D-Wave 2000Q quantum annealer. We consider two different models for the environment based on two-level systems.

We conclude in Chapter 7 by summarizing and discussing our results.

Parts of Chapters 4, 5 and 6 have been published in Ref. [Wil+20] (publication [1]).

Chapter 2

Adiabatic quantum computation and quantum annealing

In this chapter, we first summarize the ideas of adiabatic quantum computation and quantum annealing and present the mathematical framework in some detail. Subsequently, we discuss the relation to optimization problems and to the Landau-Zener theory.

The idea of quantum annealing stems from a variation of the (classical) simulated-annealing algorithm [KGV83] where thermal fluctuations of the state vector are replaced by quantum fluctuations [ACF89; Fin+94; KN98]. The motivation was that a quantum system can tunnel through high but narrow energy barriers, while a classical system only performing thermal jumps would be trapped in local minima separated by narrow but high barriers [ACF89; DS15]. Although intended as an optimization algorithm for conventional computers, quantum annealing was soon investigated experimentally [Bro+99]. In this experiment, annealing of a disordered magnet from the paramagnetic phase to the glassy phase was performed in two different ways: first cooling, then turning on an external transverse magnetic field, or first turning on a large transverse magnetic field, then cooling and finally turning down the magnetic field, representing the classical and quantum annealing protocols, respectively. The results indicated that the quantum annealing protocol might have an advantage over thermal annealing in finding low energy states, and the idea of quantum computers using thermal cooling and a transverse magnetic field to solve spin problems was proposed [Bro+99].

Shortly afterwards, adiabatic quantum computation [Far+00; Far+01] has been proposed, the idea being that a quantum system evolves adiabatically (according to the adiabatic theorem [BF28]) with a time-dependent Hamiltonian whose ground state at the end of the evolution encodes the solution to an optimization problem. Although initially formulated as an algorithm for a gate-model quantum computer [Far+00], an adiabatic quantum computer has been proposed as a physical device performing the quantum computation by its natural adiabatic evolution [CFP01].

Despite the different motivations of quantum annealing and adiabatic quantum computation, the operating principles of these types of quantum computation are basically the same [MN08] and the names are often used interchangeably [ST06]. However, sometimes people distinguish between the two. Adiabatic quantum computation may denote the closed-system, adiabatic version while quantum annealing may denote the case when the evolution is not necessarily adiabatic, i.e., non-adiabatic transitions or thermal excitations (i.e., considering an open system) may occur [Dic+13; Boi+14; KM14; CT15]. Sometimes,

one wants to distinguish between the more general adiabatic quantum computation proven to be polynomially equivalent to the gate model of quantum computation [Aha+07] and thus universal, and the more restricted version closer to the initial proposal which is then referred to as quantum annealing [VAL16; Pre18]. We will mainly use the former distinction. However, when referring to differences in the initial proposals of quantum annealing and adiabatic quantum computation, we will also distinguish between those two names. We may also refer explicitly to universal, open-system or closed-system adiabatic quantum computation.

Now, we give the formal description of quantum annealing and adiabatic quantum computation including the definitions which we need in the following chapters. Here, we give a brief overview and go into detail only where necessary. A detailed review on (closed-system) adiabatic quantum computation is given in Ref. [AL18].

A (closed) quantum system is prepared in the ground state of a time-dependent Hamiltonian $\mathcal{H}(t)$ at time t=0 which we call the initial Hamiltonian H_{init} . The time evolution of the quantum system is governed by the time-dependent Hamiltonian through the TDSE

$$i\frac{\partial}{\partial t}|\psi(t)\rangle = \mathcal{H}(t)|\psi(t)\rangle,$$
 (2.1)

where $|\psi(t)\rangle$ denotes the wave function of the quantum system. If the time-dependent Hamiltonian changes sufficiently slowly, according to the adiabatic theorem [BF28; Kat50], the quantum system stays in the instantaneous ground state such that at the end of the process at $t = t_a$, the system is in the ground state of the final Hamiltonian $\mathcal{H}(t_a) = H_P$. More generally, the adiabatic theorem of quantum mechanics states that if the time-dependent Hamiltonian $\mathcal{H}(t)$ describing the quantum system under consideration changes sufficiently slowly, the quantum system stays in the *i*-th eigenstate of the instantaneous Hamiltonian during the evolution if it was initially in the *i*-th eigenstate of $\mathcal{H}(0)$ [BF28; Kat50].

There are various proofs quantifying under which conditions the change of the Hamiltonian is "slow enough", see for instance the review in [AL18]. We give the (non-degenerate) version presented in Ref. [Ami09], which relates the time t_a to the inverse energy gap squared

$$\max_{s \in [0,1]} \frac{|\langle \psi_m(s)|H'(s)|\psi_n(s)\rangle|}{(E_m(s) - E_n(s))^2} \ll t_a, \qquad \forall \, m \neq n, \tag{2.2}$$

where $s = t/t_a \in [0,1]$ is the rescaled, dimensionless time, $|\psi_n(s)\rangle$ denotes the *n*-th eigenstate of H(s) with eigenenergy $E_n(s)$ and H'(s) is the derivative of H(s) with respect to s. When the system starts in the ground state, it is usually sufficient to consider the condition for the ground state and the first excited state:

$$\max_{s \in [0,1]} \frac{|\langle \psi_1(s) | H'(s) | \psi_0(s) \rangle|}{(E_1(s) - E_0(s))^2} \ll t_a. \tag{2.3}$$

For practical applications, the time needed to perform an adiabatic evolution may be prohibitive or not a priori determinable such that for a chosen time t_a the Hamiltonian may not change slowly enough and non-adiabatic transitions occur. Then, the system does not necessarily end in the ground state of H(s=1) but may end up with considerable probability in an excited state. We will refer to the probability to find the system at s=1 in the ground state of H_P as success probability.

2.1 The time-dependent Hamiltonian

In this section, we discuss commonly used models of the time-dependent Hamiltonian used for quantum annealing and adiabatic quantum computation. Usually, the time dependence of the Hamiltonian

$$H(s) = A(s)H_{\text{init}} + B(s)H_P, \tag{2.4}$$

is denoted by the dimensionless anneal fraction $s = t/t_a \in [0,1]$ and the functions A(s) and B(s) define the annealing schedule. The symbol H_{init} denotes the initial Hamiltonian and H_P denotes the final or problem Hamiltonian. Initially, the functions A(s) and B(s) were often chosen to be linear functions A(s) = (1-s), B(s) = s [Far+00; Far+01; CFP01; Chi+02] in the context of adiabatic quantum computation, and A(s) changing from very large (compared to the energy scale of H_P) at s = 0 to A(1) = 0, and B(s) = 1 in the context of quantum annealing [KN98; San+02]. However, different annealing functions satisfying $A(0) \gg B(0)$ and $B(1) \gg A(1)$ have been studied theoretically [RC02; MN08] and implemented experimentally [Har+10b; Joh+11; Lan+14].

Other possibilities of annealing paths including an intermediate catalyst or driver Hamiltonian H_C to improve the success probability have been investigated [FGG02; HS14; Cro+14; ZZS16; Hor+17]. The time-dependent Hamiltonian is then, for instance, given by [AL18]

$$\widetilde{H}(s) = (1-s)H_{\text{init}} + s(1-s)H_C + sH_P,$$
(2.5)

such that H_C does not contribute for s = 0 and for s = 1.

Methods to improve the success probability such as non-adiabatic evolution due to fast annealing [Cro+14], special annealing schedules [Can+11; SNK12] or thermal excitation and relaxation [ALT08; Dic+13; Arc+17; Mar+19] are also studied. If the system has a considerable probability to be in a (low-energy) excited state before an avoided crossing of the energy levels, the probability might be transferred back to the ground state at the avoided crossing [Cro+14; SNK12] or the system can relax to the ground state [Dic+13; Mar+19] due to energy exchange with the environment.

2.1.1 The qubit Hamiltonian

One of the simplest Hamiltonians for an N-qubit system with known ground state, which is a product state and easy to prepare, is given by

$$H_{\text{init}} = -\Gamma \sum_{i=1}^{N} \sigma_i^x, \tag{2.6}$$

where Γ defines the energy scale, and the ground state is the uniform superposition of all computational basis states. The choice of the initial Hamiltonian for adiabatic quantum computation is not completely arbitrary. For instance, taking the one-dimensional projector onto the uniform superposition state as H_{init} , the ground state would be the same but the required time to reach a constant success probability for an adiabatic evolution would scale exponentially in the number of qubits, even for easy problem instances [Far+08].

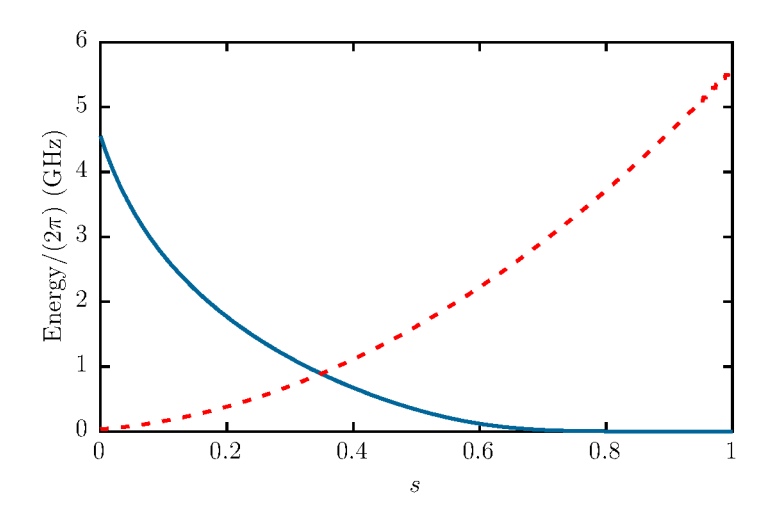


Figure 2.1: The annealing functions A(s) (blue, solid line) and B(s) (red, dashed line) of the time-dependent Hamiltonian H(s) (Eq. (2.8)) of one of the D-Wave 2000Q chips.

The initial Hamiltonian proposed in Ref. [Far+00] is similar to Eq. (2.6) but reflects even more the structure of the final Hamiltonian.

The motivation to use the Hamiltonian given in Eq. (2.6) in the context of quantum annealing was that it introduces quantum fluctuations since it does not commute with the Ising spin Hamiltonian

$$H_P = -\zeta \left(\sum_{i=1}^N h_i \sigma_i^z + \sum_{j < i} J_{ji} \sigma_j^z \sigma_i^z \right), \tag{2.7}$$

which is often considered as the problem Hamiltonian for quantum annealing [KN98; Bro+99; San+02; Har+10b], and where ζ defines the energy scale so that the parameters h_i and J_{ji} are dimensionless. In the context of adiabatic quantum computation, the problem Hamiltonian is usually diagonal in the computational basis but less restrictive, also allowing for multi-qubit terms with more than two qubits [Far+00; Far+01; HY11]. The time-dependent annealing Hamiltonian which we use in this thesis, because it is also implemented in the D-Wave quantum annealer [Har+10b; Boi+13], is given by

$$H(s) = -A(s) \sum_{i=1}^{N} \sigma_i^x - B(s) \left(\sum_{i=1}^{N} h_i \sigma_i^z + \sum_{j < i} J_{ji} \sigma_j^z \sigma_i^z \right), \qquad (2.8)$$

where A(s) and B(s) have units of energy and the parameters h_i and J_{ji} are dimensionless real numbers in the interval [-1, 1].

An exemplary annealing schedule used on the D-Wave 2000Q quantum annealer is shown in Fig. 2.1. The choice of the annealing schedule is partially given by the restrictions due to the qubit design which does not allow for an independent control of the functions A(s) and B(s) [Har+10b]. Usually, the control flux is chosen so that B(s) is quadratic in s which then also determines A(s) [DWa]. Moreover, the qubit connectivity of the D-Wave 2000Q quantum annealer is given by the Chimera graph [Bun+14]. As a consequence, some of the J_{ji} in Eq. (2.8) are fixed to zero.

Equation (2.8) describes a stoquastic Hamiltonian, that is, the off-diagonal elements of the Hamiltonian matrix (in a given basis, e.g. the computational basis) are all real and non-positive [Bra+08]. It is not clear whether adiabatic quantum computation with a stoquastic Hamiltonian can show quantum speedup [PT13; Røn+14]. However, there is evidence that adiabatic quantum computation with stoquastic Hamiltonians is not universal if the system has to stay in its instantaneous ground state, but it becomes universal if a non-adiabatic evolution is allowed [AL18].

Stoquastic and non-stoquastic catalyst Hamiltonians have been studied in [Cro+14] and [Hor+17], showing that stoquastic catalyst Hamiltonians lead to small improvement of the performance for many of the investigated instances while non-stoquastic catalyst Hamiltonians improve the performance only for a few instances but if they do, this improvement is then typically larger. The improvement of the performance when including the stoquastic catalyst Hamiltonian is due to an enlarged minimal energy gap and/or a reduced number of avoided crossings. On the other hand, improvement due to a non-stoquastic catalyst Hamiltonian is often caused by an increased number of avoided crossings. Thus, for the hard instances it seems to be sometimes more beneficial to introduce more avoided crossings than to enlarge the (very small) minimal energy gap [Hor+17] indicating that non-adiabatic evolutions can improve the success probability for hard instances. Unfortunately, in [Hor+17], data is not shown for all instances with all catalyst Hamiltonians but only for the catalyst Hamiltonian with the largest improvement.

D-Wave Systems Inc. have started experiments including non-stoquastic qubit Hamiltonians [Ozf+20].

2.2 Relation to optimization problems

Optimization problems which can be directly mapped onto the Ising spin Hamiltonian Eq. (2.7) are quadratic unconstrained binary optimization (QUBO) problems. These problems can be formulated as [PJ92]

$$\min_{z \in \{0,1\}^N} z^T \mathbf{M} z = \min_{z \in \{0,1\}^N} \left(\sum_{i=1}^N \mathbf{M}_{ii} z_i + 2 \sum_{i < j} \mathbf{M}_{ij} z_i z_j \right),$$
(2.9)

where **M** is a symmetric $N \times N$ -matrix, $z = (z_1, z_2, \dots, z_N)^T$, $z_i \in \{0, 1\}$ and $z_i^2 = z_i$. The string (or strings) of binary variables z which minimize(s) Eq. (2.9), is the solution of the QUBO. The binary variables z_i can be replaced by the σ_i^z matrices with eigenvalues ± 1 by mapping $z_i \mapsto (1 - \sigma_i^z)/2$. The additional constant term can be neglected as it is neither relevant for the minimization nor for the Hamiltonian. Thus, QUBOs are problems which map naturally to quantum annealing with the Hamiltonian given in Eq. (2.8). Solving a general QUBO is an NP-hard problem [PJ92; Koc+14]. We summarize informally and very briefly some concepts and definitions of complexity theory from the book [AB09]:

The class P contains decision problems ("yes"/"no" answer) which can be solved in polynomial time by a deterministic Turing machine. A (deterministic) Turing machine is a device which performs computations by reading a character from an infinite tape, writing a new character and moving left or right depending on the input at the current position and the current internal state according to a transition rule. The transition rule may also change the internal state. It is a simplification of a computing device which can,

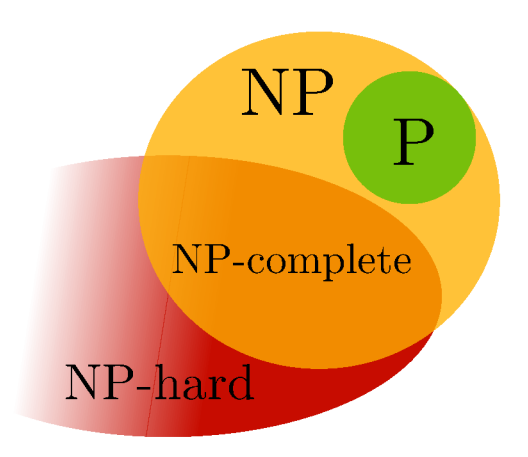


Figure 2.2: Sketch of the inclusions of the complexity classes P, NP, NP-complete and NP-hard if $P \neq NP$.

according to the (strong) Church-Turing thesis, simulate every realizable computation device (with polynomial overhead). Problems in P are also said to be efficiently solvable.

In contrast, NP denotes the complexity class non-deterministic polynomial time, i.e., a non-deterministic Turing machine finds the answer to a decision problem in polynomial time and, in the "yes" case, provides a solution (also called witness or certificate) which can be verified in polynomial time by a deterministic Turing machine. A non-deterministic Turing machine has two transition rules but only one of them is picked at each step. If there is a sequence of choices for the transition rules which leads to a solution in a polynomial number of steps, the non-deterministic Turing machine, which is only a theoretical device, can solve the problem in polynomial time.

NP-hard problems are at least as hard as any other problem in the class NP, and any problem in the class NP can be transformed to an NP-hard problem in polynomial time. NP-hard problems are not necessarily contained in the class NP, but those that are, are called NP-complete. NP-hard problems which are not NP-complete are for instance optimization problems such as the traveling salesman problem. Optimization problems do not belong to the class NP because they are not decision problems which return a "yes"/"no" answer. Rather, their solutions are answers to the question "Which configuration is best?" It is easy to see that optimization problems are harder than decision problems: If we know the solution of an optimization problem, it is easy to answer the question of the corresponding decision problem "Is there a solution with cost smaller than cost?" for a given constant cost. We only have to check if the optimal configuration yields a cost which is larger or smaller than cost. On the other hand, if we only know the answer to the decision problem, we do not have the solution of the optimization problem. Figure 2.2 shows a sketch of the inclusions if $P \neq NP$.

There are many problems in NP for which a polynomial-time algorithm to find the solution is not known, suggesting that $P \neq NP$. However, up to date, no proof exists. Not all instances of a given problem are equally difficult and some instances can be solved easily. The most difficult instances are often referred to as the worst-case instances. Finding a polynomial-time algorithm to solve a general NP-complete problem including the worst-case instances would imply P = NP.

We will not dive deeper into complexity theory but mention only that since QUBO is NP-hard, any problem in NP can be transformed in polynomial time to a QUBO or Ising model. Some examples are reviewed in Refs. [Luc14; Koc+14]. QUBO also includes other NP-hard problems such as maximum cut or maximum clique [PJ92], and constrained

quadratic binary optimization problems can be transformed to QUBOs if the constraints satisfy certain conditions [Koc+14]. For the D-Wave quantum annealer, some of the J_{ji} in Eq. (2.8) are fixed to zero due to the structure of the connectivity graph. Consequently, not all QUBO instances can be directly mapped onto the D-Wave quantum annealer, but embedding methods [Bun+14] need to be applied which may lead to additional constraints on the problem to be embedded [Luc14].

The possibility to map NP(-hard) problems onto the Hamiltonian for quantum annealing or adiabatic quantum computation and the hope of using quantum effects to solve NP-hard problems has pushed research in this field and many NP(-hard) problems have been studied in the context of quantum annealing and adiabatic quantum computation. Studies include theoretical and numerical work, for instance, examinations of the scaling properties by solving the time-dependent Schrödinger equation numerically for small instances of the exact cover problem [Far+01], the set partition problem [STT01], the problem of finding cliques of size k in random graphs [Chi+02], by using quantum Monte Carlo for satisfiability problems [HY11], random spin glass instances [Kar+10], 3-regular 3-XORSAT and 3-regular maximum cut problems including a semi-analytical approach [Far+12], by using discretized and heuristic methods for satisfiability problems [Hog03] or numerical [Cho10] and perturbative [DA11] investigations of the change of the minimum energy gap when modifying the problem or driving Hamiltonian for maximum independent set problems. Later, when the D-Wave quantum annealer became available, also comparisons to experiments performed on D-Wave's quantum annealing processors have been made [Boi+14; Røn+14; Hen+15]. Earlier studies reported polynomial scaling of the complexity with problem size (the dependence of the minimal energy gap on the problem size), although only for small problem sizes [Far+01; Chi+02; Hog03]. Later work, however, indicated that the scaling with the problem size may rather be exponential [HY11; Far+12]. Nevertheless, these studies still consider small system sizes only and conclusions on the asymptotic scaling behavior cannot be drawn. Additionally, only adiabatic evolutions are taken into account. Non-adiabatic evolutions, among other modifications also mentioned previously, may show different scaling behavior [SNK12; AL18]. Up to date, there is no analytical proof stating whether scaling improvement is possible or not for the model given by the Hamiltonian in Eq. (2.8). Due to the (polynomial) equivalence to the gate model of quantum computation, universal adiabatic quantum computation should show the same speedup as gate-model quantum computation. A quadratic speedup was shown theoretically [RC02] for searching in an unordered database (similar to Grover's algorithm in the case of the gate-model quantum computer). There are still many open questions regarding the complexity and potential quantum speedup through adiabatic quantum computation [AL18] which we will not discuss any further here.

Of course, not only search and optimization problems can be studied on a quantum annealing device, but also for instance quantum simulations. This is another promising field for applications of quantum annealing. Experimental quantum simulations of condensed-matter physics on the D-Wave 2000Q quantum annealer (using modified annealing schemes) have been reported [Kin+18; Har+18].

2.3 Relation to the Landau-Zener theory

In this section, we discuss the relation between adiabatic quantum computation and the Landau-Zener theory [Lan32; Zen32]. First, we summarize the basic concepts of the Landau-Zener theory. Subsequently, we discuss in more detail under which circumstances adiabatic quantum computation with a single spin-1/2 particle can be mapped onto the Landau-Zener Hamiltonian.

The Landau-Zener theory describes a spin-1/2 particle in a linearly increasing magnetic field vt, where t denotes the time which goes from $-\infty$ to ∞ and v can be regarded as the "sweep velocity" of the magnetic field. In addition, a constant transverse field h'_x is applied. Thus, the Landau-Zener Hamiltonian can be written as

$$H_{\rm LZ}(t) = -h_x' \sigma^x - vt\sigma^z. \tag{2.10}$$

Without the transverse field h'_x , the eigenenergies become degenerate at t=0 and the energy levels cross at this point. For non-zero transverse field, however, the eigenenergies do not become degenerate and at t=0, there is an avoided crossing of the energy levels (see Fig. 2.3(a)). The Landau-Zener theory provides a formula for the probability that the particle changes its spin direction while evolving through the avoided crossing. This means if the particle starts in its ground state ($|\downarrow\rangle$ for v>0 and $t\to-\infty$), the probability to find the particle in the excited state $|\downarrow\rangle$ at $t\to\infty$, i.e., that the particle undergoes a non-adiabatic transition, is given by [Zen32]

$$P_1 = e^{-\pi h_x'^2/v}. (2.11)$$

For large sweep velocities v (a fast change of the magnetic field) and small transverse fields $h_x'^2/v \to 0$, $P_1 \to 1$. Accordingly, the probability to find the particle in the ground state $|\uparrow\rangle$ at $t \to \infty$ is given by

$$P_0 = 1 - P_1 = 1 - e^{-\pi h_x^{\prime 2}/v}, (2.12)$$

and plotted for an example in Fig. 2.3(b).

For a single spin-1/2 particle, the Landau-Zener theory provides a formula for the probabilities P_0 and P_1 in the case of a non-adiabatic evolution, and an estimate for which parameters the evolution stays (very close to) adiabatic. The exact mapping to the Hamiltonian for adiabatic quantum computation, however, is only possible under certain conditions which we study in the following.

In the simple case of only a single spin-1/2 particle which undergoes linear adiabatic quantum computation, the time-dependent Hamiltonian is given by

$$H_{\text{lin}}(s) = -(1-s)h_x\sigma^x - sh_z\sigma^z, \qquad (2.13)$$

where $s \in [0, 1]$. It is straightforward to compute the energy gap $\Delta E(s)$ and the minimal energy gap $\Delta E_{\min} = \min_{s \in [0, 1]} \Delta E(s)$ of this Hamiltonian:

$$\Delta E(s) = 2\sqrt{(1-s)^2 h_x^2 + s^2 h_z^2},\tag{2.14a}$$

$$\Delta E_{\min} = \Delta E(s^*) = \frac{2|h_x h_z|}{\sqrt{h_x^2 + h_z^2}}, \quad s^* = \frac{h_x^2}{h_x^2 + h_z^2}.$$
 (2.14b)

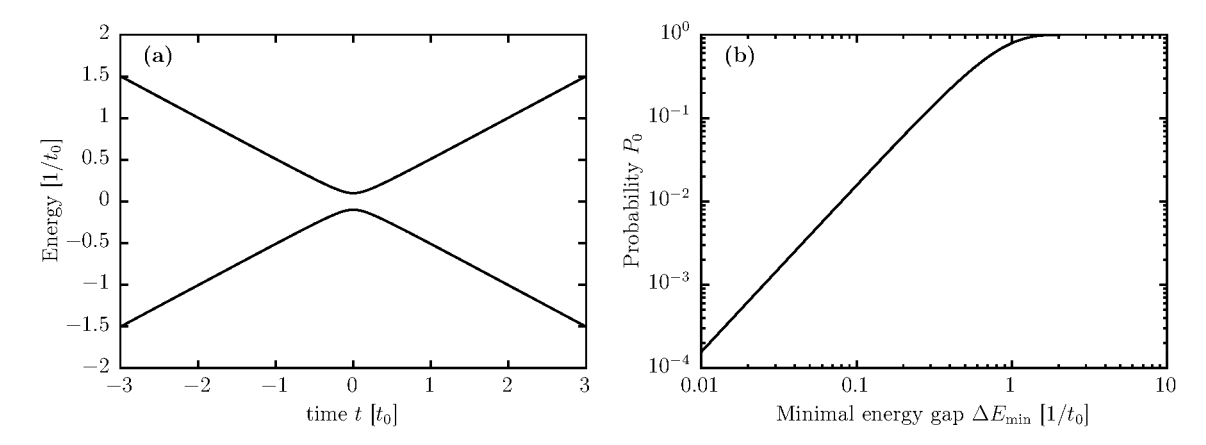


Figure 2.3: (a) The eigenenergies of the Hamiltonian $H_{\rm LZ}$ (Eq. (2.10)) for $v = 0.5/t_0^2$, $h'_x = 0.1/t_0$ as a function of time t in units of an arbitrary time scale t_0 . (b) The probability P_0 to find the system in the ground state at the end of the sweep as a function of the minimal energy gap $\Delta E_{\rm min} = 2|h'_x|$ for $v = 0.5/t_0^2$.

In order to find a relation between the Landau-Zener Hamiltonian H_{LZ} given in Eq. (2.10) and the Hamiltonian H_{lin} given in Eq. (2.13), we write the Landau-Zener Hamiltonian in terms of the dimensionless time $s = (1+t/t_s)/2$ for a finite sweeping time (i.e. $t \in [-t_s, t_s]$ and with $s \in [0, 1]$)

$$H_{LZ}(s) = -h'_x \sigma^x - h'_z (2s - 1)\sigma^z,$$
 (2.15)

where we defined $h'_z = vt_s$. The energy gap $\Delta E'(s)$ and the minimal energy gap $\Delta E'_{\min}$ of this Hamiltonian are given by

$$\Delta E'(s) = 2\sqrt{h_x'^2 + h_z'^2(2s - 1)^2},\tag{2.16a}$$

$$\Delta E'_{\min} = \Delta E'(s^*) = 2|h'_x|, \quad s^* = \frac{1}{2}.$$
 (2.16b)

We are interested in the region where the Hamiltonian H_{lin} given in Eq. (2.13) can be mapped onto the Landau-Zener Hamiltonian H_{LZ} Eq. (2.15). For this purpose, we try to find a transformation that maps the Hamiltonian

$$H_{\text{lin}}(s) = -h_x \sigma^x + s \left(h_x \sigma^x - h_z \sigma^z \right) \tag{2.17}$$

to the Landau-Zener Hamiltonian

$$H_{\rm LZ}(s) = h_z' \sigma^z - h_x' \sigma^x - 2s h_z' \sigma^z. \tag{2.18}$$

Since the s-dependent part of H_{LZ} is diagonal, we diagonalize the s-dependent part of H_{lin} . There are two unitary transformations which diagonalize the 2×2 -matrix, corresponding to the two possible orderings of the eigenvalues. For the first unitary transformation

$$U = \begin{pmatrix} \frac{h_z - \sqrt{h_x^2 + h_z^2}}{\sqrt{2}h_x} \sqrt{\frac{h_x^2}{h_x^2 + h_z^2 - h_z \sqrt{h_x^2 + h_z^2}}} & \frac{h_z + \sqrt{h_x^2 + h_z^2}}{\sqrt{2}h_x} \sqrt{\frac{h_x^2}{h_x^2 + h_z^2 + h_z \sqrt{h_x^2 + h_z^2}}} \\ - \sqrt{\frac{h_x^2}{2(h_x^2 + h_z^2 - h_z \sqrt{h_x^2 + h_z^2})}} & - \sqrt{\frac{h_x^2}{2(h_x^2 + h_z^2 + h_z \sqrt{h_x^2 + h_z^2})}} \end{pmatrix},$$
(2.19)

we obtain

$$U^{\dagger} \left(h_x \sigma^x - h_z \sigma^z \right) U = \sqrt{h_x^2 + h_z^2} \tilde{\sigma}^z, \tag{2.20a}$$

$$U^{\dagger} \sigma^x U = \frac{h_x}{\sqrt{h_x^2 + h_z^2}} \tilde{\sigma}^z - \operatorname{sign}(h_x) \frac{h_z}{\sqrt{h_x^2 + h_z^2}} \tilde{\sigma}^x, \qquad (2.20b)$$

and thus

$$U^{\dagger}H_{\text{lin}}(s)U = -\frac{h_x^2}{\sqrt{h_x^2 + h_z^2}}\tilde{\sigma}^z + \frac{|h_x|h_z}{\sqrt{h_x^2 + h_z^2}}\tilde{\sigma}^x + s\sqrt{h_x^2 + h_z^2}\tilde{\sigma}^z.$$
 (2.21)

In order to write this Hamiltonian in the form of Eq. (2.18), the following conditions must be satisfied:

$$h_z' = -\frac{h_x^2}{\sqrt{h_x^2 + h_z^2}} \qquad |h_z| = |h_x| \qquad (2.22a)$$

$$-2h'_z = \sqrt{h_x^2 + h_z^2} \qquad \Leftrightarrow \qquad h'_z = -\frac{|h_z|}{\sqrt{2}} \tag{2.22b}$$

$$-h'_{x} = \frac{|h_{x}|h_{z}}{\sqrt{h_{x}^{2} + h_{z}^{2}}} \qquad h'_{x} = -\frac{h_{z}}{\sqrt{2}}.$$
 (2.22c)

The second unitary transformation is given by

$$U' = \begin{pmatrix} \frac{h_z + \sqrt{h_x^2 + h_z^2}}{\sqrt{2}h_x} \sqrt{\frac{h_x^2}{h_x^2 + h_z^2 + h_z} \sqrt{\frac{h_x^2 + h_z^2}{\sqrt{2}h_x}}} & \frac{h_z - \sqrt{h_x^2 + h_z^2}}{\sqrt{2}h_x} \sqrt{\frac{h_x^2}{h_x^2 + h_z^2 - h_z} \sqrt{\frac{h_x^2}{h_x^2 + h_z^2 - h_z} \sqrt{\frac{h_x^2 + h_z^2}{h_x^2 + h_z^2}}} \\ - \sqrt{\frac{h_x^2}{2\left(h_x^2 + h_z^2 + h_z\sqrt{h_x^2 + h_z^2}\right)}} & -\sqrt{\frac{h_x^2}{2\left(h_x^2 + h_z^2 - h_z\sqrt{h_x^2 + h_z^2}\right)}} \end{pmatrix},$$
 (2.23)

and yields for the transformed Hamiltonian for adiabatic quantum computation

$$U'^{\dagger}H_{\text{lin}}(s)U' = \frac{h_x^2}{\sqrt{h_x^2 + h_z^2}}\tilde{\sigma}^z + \frac{|h_x|h_z}{\sqrt{h_x^2 + h_z^2}}\tilde{\sigma}^x - s\sqrt{h_x^2 + h_z^2}\tilde{\sigma}^z, \tag{2.24}$$

and for the conditions

$$h'_z = \frac{h_x^2}{\sqrt{h_x^2 + h_z^2}} \qquad |h_z| = |h_x| \qquad (2.25a)$$

$$2h'_z = \sqrt{h_x^2 + h_z^2} \qquad \Leftrightarrow \qquad h'_z = \frac{|h_z|}{\sqrt{2}} \tag{2.25b}$$

$$-h'_{x} = \frac{|h_{x}|h_{z}}{\sqrt{h_{x}^{2} + h_{z}^{2}}} \qquad h'_{x} = -\frac{h_{z}}{\sqrt{2}}.$$
 (2.25c)

Thus, we could show that a transformation which maps the Hamiltonian $H_{\text{lin}}(s)$ onto the Landau-Zener Hamiltonian exists if and only if $|h_z| = |h_x|$.

Although the direct mapping can only be performed in special cases and the Landau-Zener theory has other additional prerequisites (such as $t_s \to \infty$ and $\Delta E'(s=1) \gg \Delta E'(s^*)$), the Landau-Zener theory provides a qualitative description whether or not the evolution of adiabatic quantum computation and quantum annealing of a single particle is adiabatic. Nevertheless, a quantum system composed of more than a single spin-1/2 particle may show similar behavior when evolving through an avoided level crossing [DeR+97; AAN09; Hob15].

Chapter 3

The Suzuki-Trotter product-formula algorithm

A major issue when numerically solving the time-dependent Schrödinger equation (TDSE)

$$i\frac{\partial}{\partial t}|\psi\rangle = H(t)|\psi\rangle,$$
 (3.1)

where the Hamiltonian H(t) explicitly depends on time, is that for numerical diagonalization, the Hamiltonian would need to be diagonalized at each time step, which has to be small compared to the time scale on which the Hamiltonian changes. Since diagonalization of a $D \times D$ -matrix scales with $\mathcal{O}(D^3)$, this becomes infeasible for large matrices or a large amount of necessary time steps. Additionally, if the size of the matrix representing the Hamiltonian (i.e. the dimension D of the Hilbert space of the system) becomes very large, the problem of storing the complete matrix arises. For large but time-independent Hamiltonians there are different algorithms which can cope with this issue as for instance the Chebyshev algorithm [TK84]. To compute only a few eigenvalues and eigenstates, for example only the ground state energy, for instance the Lanczos algorithm can be used [Pai72]. However, to solve the Schrödinger equation in high-dimensional Hilbert spaces and for a time-dependent Hamiltonian, the state-of-the-art algorithm is the Suzuki-Trotter product-formula algorithm [DeR87]. We discuss this algorithm in the following sections.

3.1 Principle

For a time-independent Hamiltonian H(t) = H, the formal solution of the Schrödinger equation is given by

$$|\psi(t)\rangle = e^{-i(t-t_0)H}|\psi(t_0)\rangle = U(t-t_0)|\psi(t_0)\rangle, \tag{3.2}$$

where the time-evolution operator $U(t-t_0)$ evolves the state $|\psi(t_0)\rangle$ from time t_0 to time t. Usually, the Hamiltonian is not given in diagonal form and a diagonalization is not possible due to the dimension of the Hilbert space, i.e., the size of the matrix H. Thus, an (unconditionally) stable algorithm which approximates $\exp(-i\tau H)$ so that the multiplication by $|\psi(t_0)\rangle$ becomes feasible, is needed. For instance, the Cranck-Nicholson

method approximating $\exp(-i\tau H)$ by

$$e^{-i\tau H} \approx U_{CN}(\tau) = \left(\mathbb{I} - \frac{i\tau H}{2}\right) \left(\mathbb{I} + \frac{i\tau H}{2}\right)^{-1}$$
 (3.3)

is unconditionally stable, but due to the matrix inversion, it is an implicit method which is costly and becomes useless for large systems [DeR87].

However, in most cases the Hamiltonian is not a dense matrix but a sparse matrix such that there exists a decomposition into K matrices

$$H = \sum_{k=1}^{K} A_k, \tag{3.4}$$

where the A_k are diagonal or block-diagonal. A more detailed discussion on how to choose the A_k is given in Section 3.2. Here, we consider for clarity the case where $H = A_1 + A_2$. The generalization to a sum of more operators as in Eq. (3.4) is discussed in Refs. [Suz76], [Suz85] and [DeR87] and works analogously. The basic idea of the Suzuki-Trotter product-formula algorithm is to use this decomposition and the Trotter formula for bounded operators A and B [Tro59]

$$\lim_{n \to \infty} \left(e^{A/n} e^{B/n} \right)^n = e^{A+B}, \tag{3.5}$$

to obtain an approximation of the time-evolution operator which is easy to handle. In order to do so, we have to set n in Eq. (3.5) to a constant, large but finite integer. The error made by fixing n is given by [Suz85]

$$\left| \left| e^{A+B} - \left(e^{A/n} e^{B/n} \right)^n \right| \right| \le \frac{\left| \left| [A, B] \right| \right|}{2n} e^{\left| |A| + \left| |B| \right|},$$
 (3.6)

and vanishes with 1/n. Thus, we can approximate the time-evolution operator by

$$U(t - t_0) = e^{-i(t - t_0)(A_1 + A_2)} \approx \left(e^{-i(t - t_0)A_1/n}e^{-i(t - t_0)A_2/n}\right)^n = \left(e^{-i\tau A_1}e^{-i\tau A_2}\right)^n = U_1^n(\tau),$$
(3.7)

where we introduced $\tau = (t - t_0)/n$ and $U_1(\tau) = \exp(-i\tau A_1) \exp(-i\tau A_2)$, the (first-order) approximation of the time-evolution operator for the small time step τ .

In Ref. [Suz76], Suzuki derives higher-order approximations of $\exp(A+B)$ which converge faster than $(\exp(A/n)\exp(B/n))^n$. For example, Suzuki's second-order approximation is given by

$$e^{A+B} \approx \left(e^{A/n}e^{B/n}e^{-[A,B]/(2n^2)}\right)^n$$
 (3.8)

Applying this approximation to the time-evolution operator for a small time-step τ , we get

$$e^{-i\tau(A_1+A_2)} \approx e^{-i\tau A_1} e^{-i\tau A_2} e^{[A_1,A_2]\tau^2/2}.$$
 (3.9)

However, symmetrized versions of these approximants turned out to be simpler and at least as accurate. For Monte Carlo simulations, they are even necessary to avoid a non-Hermitian approximation of the Hermitian operator $\exp(-\beta H)$ [DD83]. The symmetrized second-order and fourth-order approximations are [DD83; DeR87]

$$e^{-i\tau(A_1+A_2)} \approx e^{-i\tau A_1/2} e^{-i\tau A_2} e^{-i\tau A_1/2} = U_2(\tau),$$
 (3.10a)

$$e^{-i\tau(A_1+A_2)} \approx e^{-i\tau A_1/2} e^{-i\tau A_2/2} e^{i\tau^3 C_3/4} e^{-i\tau A_2/2} e^{-i\tau A_1/2} = U_4(\tau),$$
 (3.10b)

respectively, with $C_3 = [A_1 + 2A_2, [A_1, A_2]]/6$. Moreover, independent of K, higher-order approximations can be computed from the lower-order approximations [Suz91; DM06]:

$$U_2(\tau) = U_1^{\dagger}(-\tau/2)U_1(\tau/2), \tag{3.11a}$$

$$U_4(\tau) = U_2(c\tau)U_2(c\tau)U_2((1-4c)\tau)U_2(c\tau)U_2(c\tau),$$
(3.11b)

where $c = 1/(4 - 4^{1/3})$.

For the right choice of the A_k , we can update the state vector $|\psi\rangle$ by applying ℓ -component updates only, for a small integer ℓ (usually $\ell = 2$). Since U_1 , U_2 and U_4 are unitary approximations if the A_k are Hermitian, an algorithm based on these approximations preserves the norm of the state vector and is unconditionally stable [DM06].

In the case of a time-dependent Hamiltonian H(t), the time-evolution operator $U(t, t_0)$ which evolves the state $|\psi(t_0)\rangle$ from time t_0 to time t is given by

$$U(t, t_0) = \mathcal{T} \exp\left(-i \int_{t_0}^t H(t')dt'\right), \qquad (3.12)$$

where the symbol \mathcal{T} denotes the time-ordering operator which has to be applied if H(t) does not commute with H(t') for any $t' \neq t$. In order to compute $|\psi(t)\rangle = U(t, t_0)|\psi(t_0)\rangle$, we can use

$$U(t, t_0) = U(t = t_0 + n\tau, t_0 + (n - 1)\tau) \cdots U(t_0 + 2\tau, t_0 + \tau)U(t_0 + \tau, t_0). \tag{3.13}$$

There are special cases where H(t) commutes with H(t') for all $t' \neq t$ and $U(t_0 + (m+1)\tau, t_0 + m\tau)$ can be calculated analytically. In general, however, we have to use that if the time step $\tau = (t - t_0)/n$ is small enough, we can discretize the Hamiltonian in time and the Hamiltonian is approximately constant during the time step τ . Then, we can write

$$U(t_{0} + (m+1)\tau, t_{0} + m\tau) \approx \exp\left(-i\int_{t_{0} + m\tau}^{t_{0} + (m+1)\tau} H(t_{0} + (m+1/2)\tau)dt'\right)$$

$$\approx \exp(-i\tau H(t_{0} + (m+1/2)\tau))$$

$$=: \widetilde{U}(t_{0} + (m+1)\tau, t_{0} + m\tau), \tag{3.14}$$

where $0 \le m \le n-1$ and $H(t_0 + (m+1/2)\tau)$ denotes the Hamiltonian at time $t_0 + (m+1/2)\tau$ which we use instead of the time-dependent Hamiltonian during the short time from $t_0 + m\tau$ to $t_0 + (m+1)\tau$. For the approximated time-evolution operator $\widetilde{U}(t_0 + (m+1)\tau, t_0 + m\tau)$, we can apply the same first-, second- or fourth-order approximations as for the time-independent Hamiltonian discussed previously.

3.2 Implementation

After the discussion of the main idea, in this section, we elaborate on the details of the implementation of the algorithm presented in Ref. [DeR87]. As mentioned in Section 3.1,

the aim is to partition the Hamiltonian into a sum of K diagonal and block-diagonal matrices A_k so that $\exp(-i\tau A_k)|\psi\rangle$ can be computed without constructing the full matrix and using ℓ -component updates only, for a small integer ℓ .

When decomposing the Hamiltonian H into a sum of non-commuting operators A_k and approximating the time evolution operator by

$$U_1(t+\tau,t) = e^{-i\tau A_1} e^{-i\tau A_2} \cdots e^{-i\tau A_K}, \tag{3.15}$$

in the implementation, we have to take care of the order of the product in $U_1^{\dagger}(t+\tau,t)$ so that

$$U_1^{\dagger}(t+\tau,t) = e^{i\tau A_K} e^{i\tau A_{K-1}} \cdots e^{i\tau A_1}, \tag{3.16}$$

and $U_1(t+\tau,t)U_1^{\dagger}(t+\tau,t)=U_1^{\dagger}(t+\tau,t)U_1(t+\tau,t)=\mathbb{I}$ to keep the algorithm unconditionally stable.

For a diagonal matrix A_k with eigenvalues $a_k^{(j)}$, $j = 0, 1, \ldots, D - 1$, it is clear that we have

$$e^{-i\tau A_k} = \exp\left(-i\tau \begin{pmatrix} a_k^{(0)} & & \\ & \ddots & \\ & & a_k^{(D-1)} \end{pmatrix}\right) = \begin{pmatrix} e^{-i\tau a_k^{(0)}} & & \\ & \ddots & \\ & & e^{-i\tau a_k^{(D-1)}} \end{pmatrix}, \quad (3.17)$$

which means for the product $\exp(-i\tau A_k)|\psi\rangle$ that each element ψ_j of the state vector $|\psi\rangle$ is multiplied by a factor $\exp(-i\tau a_k^{(j)})$. This takes $\mathcal{O}(D)$ operations.

For a block-diagonal matrix $A_{k'}$ with L blocks $A_{k'}^{(l)}$,

$$e^{-i\tau A_{k'}} = \exp\left(-i\tau \begin{pmatrix} A_{k'}^{(0)} & & \\ & \ddots & \\ & & A_{k'}^{(L-1)} \end{pmatrix}\right) = \begin{pmatrix} e^{-i\tau A_{k'}^{(0)}} & & \\ & \ddots & \\ & & e^{-i\tau A_{k'}^{(L-1)}} \end{pmatrix}$$
(3.18)

is again a block-diagonal matrix with blocks $\exp(-i\tau A_{k'}^{(l)})$. We will use this relation extensively in this chapter.

3.2.1 Pauli updates

The decomposition of the Hamiltonian is usually chosen in such a way that the blocks $A_{k'}^{(l)}$ of the block-diagonal matrix $A_{k'}$ are 2×2 -matrices and can be written as a sum of Pauli-matrices

$$A_{k'}^{(l)} = \alpha_x \sigma^x + \alpha_y \sigma^y + \alpha_z \sigma^z = \alpha \cdot \sigma, \qquad \alpha = \begin{pmatrix} \alpha_x \\ \alpha_y \\ \alpha_z \end{pmatrix} \in \mathbb{R}^3, \quad \sigma = \begin{pmatrix} \sigma^x \\ \sigma^y \\ \sigma^z \end{pmatrix}. \tag{3.19}$$

Then, the analogue of Euler's formula for Pauli matrices can be applied to compute the exponential analytically

$$e^{-i\tau A_{k'}^{(l)}} = e^{-i\tau\alpha\cdot\sigma} = \cos(\tau||\alpha||)\mathbb{I} - i\sin(\tau||\alpha||)\frac{\alpha\cdot\sigma}{||\alpha||},$$
(3.20)

where $|\alpha|$ denotes the norm of α . The update rule for the coefficients ψ_j and ψ_{j+1} of the state vector, which are affected by the block $\exp(-i\tau A_{k'}^{(l)})$, is given by

$$\psi_{j} \leftarrow \left(\cos(\tau||\alpha||) - i\sin(\tau||\alpha||)\frac{\alpha_{z}}{||\alpha||}\right)\psi_{j} - i\sin(\tau||\alpha||)\frac{\alpha_{x} - i\alpha_{y}}{||\alpha||}\psi_{j+1}$$

$$\psi_{j+1} \leftarrow -i\sin(\tau||\alpha||)\frac{\alpha_{x} + i\alpha_{y}}{||\alpha||}\psi_{j} + \left(\cos(\tau||\alpha||) + i\sin(\tau||\alpha||)\frac{\alpha_{z}}{||\alpha||}\right)\psi_{j+1}. \tag{3.21}$$

If the contribution of the σ^z matrix is included in the diagonal matrix A_k , i.e., $\alpha_z = 0$, the update rule simplifies to

$$\psi_{j} \leftarrow \cos(\tau ||\alpha||) \psi_{j} - \sin(\tau ||\alpha||) \frac{i\alpha_{x} + \alpha_{y}}{||\alpha||} \psi_{j+1}$$

$$\psi_{j+1} \leftarrow -\sin(\tau ||\alpha||) \frac{i\alpha_{x} - \alpha_{y}}{||\alpha||} \psi_{j} + \cos(\tau ||\alpha||) \psi_{j+1}. \tag{3.22}$$

Updating the full state vector $|\psi\rangle$ by $\exp(-i\tau A_{k'})$ takes $\mathcal{O}(D)$ operations.

3.2.2 Decomposition of a tridiagonal matrix

We consider a $D \times D$ tridiagonal matrix A of the form

$$A = \begin{pmatrix} a_0 & x - iy \\ x + iy & a_1 & x - iy \\ & x + iy & a_2 & \ddots \\ & & \ddots & \ddots & x - iy \\ & & & x + iy & a_{D-1} \end{pmatrix}.$$
 (3.23)

For simplicity, we have chosen the entries $x \pm iy$ on the subdiagonal to be all equal. However, the following decomposition can be straightforwardly extended to the general case. To decompose A, we can choose a diagonal matrix A_0

$$A_0 = \begin{pmatrix} a_0 & & & \\ & a_1 & & \\ & & \ddots & \\ & & a_{D-1} \end{pmatrix}, \tag{3.24}$$

and 2 block-diagonal matrices A_1 and A_2 with blocks of size 2×2 where

and

if D is even, or

and

if D is odd. In this way, we obtain block-diagonal matrices with blocks of Pauli-matrices whose exponentiation we just discussed, leading to the update rule Eq. (3.22), where even j (with odd j + 1) and odd j (with even j + 1) are processed separately. The additional zeros yield a factor of one when exponentiated. Thus, a tridiagonal matrix can be decomposed into three matrices: a diagonal matrix and two block-diagonal matrices.

3.2.3 Decomposition of a matrix with elements on the m-th diagonals

Another type of matrix which occurs often is given by (Hermitian) matrices with elements only on the m-th diagonals. For $m \ge 1$, the elements of such a matrix A are given by

$$a_{lj} = \begin{cases} x + iy & \text{if } l = j + m \\ x - iy & \text{if } l = j - m \\ 0 & \text{else.} \end{cases}$$
 (3.27)

The j-th submatrix containing only the elements a_{jj} , $a_{j,m+j}$, $a_{m+j,j}$ and $a_{m+j,m+j}$

$$\begin{pmatrix}
0 & \dots & 0 \\
\vdots & a_{jj} & a_{j,m+j} \\
\vdots & a_{m+j,j} & a_{m+j,m+j} \\
0 & \dots & 0
\end{pmatrix} = \begin{pmatrix}
0 & \dots & 0 \\
\vdots & \ddots & \vdots \\
0 & x+iy & 0 \\
\vdots & x+iy & 0
\end{bmatrix},$$

$$\begin{pmatrix}
0 & \dots & 0 \\
\vdots & \ddots & \vdots \\
0 & \dots & 0
\end{pmatrix},$$

$$(3.28)$$

has the same properties as σ^x and σ^y when being exponentiated and thus, we can apply Euler's formula to obtain the exponential of this submatrix:

$$\exp\left(-i\begin{pmatrix}0 & \dots & 0\\ \ddots & & & \\ a_{jj} & a_{j,m+j} & & \\ \vdots & \ddots & & \vdots\\ a_{m+j,j} & a_{m+j,m+j} & & \\ 0 & \dots & & 0\end{pmatrix}\right)$$

$$=\begin{pmatrix}0 & \dots & & 0\\ \ddots & & & \\ \cos(\sqrt{x^2+y^2}) & -\sin(\sqrt{x^2+y^2})\frac{ix+y}{\sqrt{x^2+y^2}} & & \\ \vdots & & \ddots & & \\ -\sin(\sqrt{x^2+y^2})\frac{ix-y}{\sqrt{x^2+y^2}} & \cos(\sqrt{x^2+y^2}) & & \\ 0 & \dots & & 0\end{pmatrix}$$
(3.29)

Since the j-th and the (j+i)-th (for $i=1,\ldots,m-1$) submatrices commute, we decompose the matrix A with non-zero elements only on the m-th diagonals into the two block-diagonal matrices A_1 and A_2 with maximal block size $2m \times 2m$. The matrices A_1 and A_2 are chosen to be

$$A_{1} = \begin{pmatrix} B_{0} & & & \\ & B_{2m} & & \\ & & \ddots & \\ & & & \widetilde{B}_{2lm} \end{pmatrix}$$

$$(3.30a)$$

and

if $\lceil D/m \rceil$ is even and $l \in \mathbb{N}_0$ and $k \in \{0, 1, \dots m-1\}$ such that D = 2lm + m + k + 1, or, if $\lceil D/m \rceil$ is odd and $l \in \mathbb{N}_0$ and $k \in \{0, 1, \dots m-1\}$ such that D = 2lm + k + 1,

and

$$A_{2} = \begin{pmatrix} 0 & & & & & \\ & \ddots & & & & \\ & & 0 & & & \\ & & & B_{m} & & \\ & & & \ddots & & \\ & & & \widetilde{B}_{(2l-1)m} \end{pmatrix}, \tag{3.31b}$$

with blocks B_i of size $2m \times 2m$

and blocks \widetilde{B}_j of size $(m+k+1) \times (m+k+1)$, with $0 \le k = D-m-j-1 < m$ as above,

Exponentiating the matrices $-iA_1$ and $-iA_2$ then basically means we have to exponentiate the matrices $-iB_j$ and $-i\widetilde{B}_j$ and we use Eq. (3.29) with $c = \cos(\sqrt{x^2 + y^2})$ and $s = -\sin(\sqrt{x^2 + y^2})(ix + y)/\sqrt{x^2 + y^2}$:

$$e^{-iB_{j}} = \begin{pmatrix} c & & & s & & \\ & c & & & s & & \\ & & \ddots & & \ddots & & \\ & & c & & s & & \\ & & c & & s & & \\ & & -s^{*} & & c & & \\ & & \ddots & & \ddots & & \\ & & -s^{*} & & c & & c \end{pmatrix}, \tag{3.34a}$$

Updating the state vector is then done by applying the modified update rule

$$\psi_{j} \leftarrow \cos(\sqrt{x^{2} + y^{2}})\psi_{j} - \sin(\sqrt{x^{2} + y^{2}}) \frac{ix + y}{\sqrt{x^{2} + y^{2}}} \psi_{j+m}$$

$$\psi_{j+m} \leftarrow -\sin(\sqrt{x^{2} + y^{2}}) \frac{ix - y}{\sqrt{x^{2} + y^{2}}} \psi_{j} + \cos(\sqrt{x^{2} + y^{2}}) \psi_{j+m}, \tag{3.35}$$

for the blocks of A_1 and A_2 separately since they do not commute.

3.2.4 Decompositions in tensor-product spaces

In the case of tensor-product spaces, the relations

$$e^{A\otimes \mathbb{I}} = e^A \otimes \mathbb{I} \tag{3.36}$$

and

$$e^{A \otimes \mathbb{I} + \mathbb{I} \otimes B} = \left(e^A \otimes \mathbb{I} \right) \left(\mathbb{I} \otimes e^B \right) \tag{3.37}$$

may be useful to find a suitable decomposition into block matrices. Moreover, if A has the property $A^{2n} = \mathbb{I}$ and $A^{2n+1} = A$, as for instance block matrices of Pauli matrices do, then

$$e^{-iA\otimes B} = \sum_{n=0}^{\infty} (-i)^n \frac{A^n \otimes B^n}{n!} = \mathbb{I} \otimes \sum_{n=0}^{\infty} (-1)^n \frac{B^{2n}}{(2n)!} - iA \otimes \sum_{n=0}^{\infty} (-1)^n \frac{B^{2n+1}}{(2n+1)!}$$
$$= \mathbb{I} \otimes \cos(B) - iA \otimes \sin(B). \tag{3.38}$$

If B is diagonal, $\cos(B)$ and $\sin(B)$ can be easily evaluated by replacing the eigenvalues b_i of B by $\cos(b_i)$ and $\sin(b_i)$ respectively. Choosing for example $A = \sigma^x$, the update rule for the state vector ψ (stored in a two-dimensional array) is

$$\psi_{0,j} \leftarrow \cos(b_j)\psi_{0,j} - i\sin(b_j)\psi_{1,j} \psi_{1,j} \leftarrow \cos(b_j)\psi_{1,j} - i\sin(b_j)\psi_{0,j}.$$
(3.39)

In the case that ψ is stored as a one-dimensional array and the dimension of B is $M \times M$, the update rule can be written as

$$\psi_j \leftarrow \cos(b_j)\psi_j - i\sin(b_j)\psi_{M+j}$$

$$\psi_{M+j} \leftarrow \cos(b_j)\psi_{M+j} - i\sin(b_j)\psi_j,\tag{3.40}$$

which is very similar to Eq. (3.35) for y = 0 and m = M. For a block-diagonal matrix of σ^x matrices

$$A = \begin{pmatrix} \sigma^x & & \\ & \ddots & \\ & & \sigma^x \end{pmatrix}, \tag{3.41}$$

the update rule is extended accordingly (for even i):

$$\psi_{iM+j} \leftarrow \cos(b_j)\psi_{iM+j} - i\sin(b_j)\psi_{(i+1)M+j} \psi_{(i+1)M+j} \leftarrow \cos(b_j)\psi_{(i+1)M+j} - i\sin(b_j)\psi_{iM+j}.$$
(3.42)

In this way, we can find decompositions of Hamiltonians in tensor-product spaces by identifying terms like $A \otimes \mathbb{I}$ or $A \otimes B$ as used in Eqs. (3.37) and (3.38).

3.2.5 Efficiency and non-Pauli updates

Using any of the update rules discussed here, the update $\exp(-iA_k)|\psi\rangle$ of a state vector $|\psi\rangle$ of dimension D can be performed in $\mathcal{O}(D)$ operations. For a Hamiltonian of dimension $D \times D$ decomposed into K matrices, the update

$$\prod_{k=1}^{K} e^{-i\tau A_k} |\psi\rangle \tag{3.43}$$

can be performed in $\mathcal{O}(KD)$ operations. Thus, the algorithm is more efficient if the number K of matrices, into which the Hamiltonian is decomposed, is small.

The update of two coefficients ψ_j and ψ_l of the state vector requires read access only to these two coefficients when applying any of the rules discussed in the previous sections. Thus, pairs of coefficients can be updated in parallel and the implementation using OpenMP is straightforward. Therefore, we use OpenMP for the parallelization of the algorithm.

If a partition into 2×2 -matrices such that Pauli-updates can be performed is not efficiently possible, it may be useful to consider block-diagonal matrices with (time-independent) blocks $A_{k'}^{(l)}$ of dimension $\ell \times \ell$, $\ell > 2$. These blocks are then diagonalized (either analytically or numerically) such that

$$A_{k'}^{(l)} = V^{(l)} \mathcal{D}^{(l)} V^{(l)\dagger}$$
(3.44)

with $\mathcal{D}^{(l)}$ diagonal. The update of the state vector is then computed by

$$\begin{pmatrix} \psi_{j} \\ \psi_{j+1} \\ \vdots \\ \psi_{j+\ell-1} \end{pmatrix} \leftarrow V^{(l)} e^{-i\tau \mathcal{D}^{(l)}} V^{(l)\dagger} \begin{pmatrix} \psi_{j} \\ \psi_{j+1} \\ \vdots \\ \psi_{j+\ell-1} \end{pmatrix}. \tag{3.45}$$

This means (assuming all blocks $A_{k'}^{(l)}$ of $A_{k'}$ have the same dimension $\ell \times \ell$ and $D/\ell = L$) that the update $\exp(-i\tau A_{k'})|\psi\rangle$ takes $\mathcal{O}(L\ell^2 = D\ell)$ operations. Thus, to keep the algorithm efficient, ℓ should not be too big.

3.3 Error analysis

In this section, we discuss how the error due to the approximation made in the product-formula algorithm behaves. Error bounds for the local error, that is the error introduced in a single step of time τ , can be derived for the k-th order approach [DeR87]:

$$|||\psi_{\text{exact}}(\tau)\rangle - |\psi_k(\tau)\rangle|| = ||(U(\tau) - U_k(\tau))|\psi(0)\rangle|| \le ||U(\tau) - U_k(\tau)|| \le c_k \tau^{k+1}, \quad (3.46)$$

where $|\psi_{\text{exact}}(\tau)\rangle$ is obtained by exact diagonalization, $|\psi_k(\tau)\rangle$ is obtained by the k-th order product-formula algorithm, and c_k is a constant depending on the order of the approach and the specific decomposition of the Hamiltonian as well as the (time-independent) Hamiltonian itself. The operator norm is the norm induced by the vector norm $||A|| = \sup_{|||\psi\rangle||=1}(||A|\psi\rangle||)$ for some operator A, and since we use the L^2 -norm (Euclidean norm) for vectors, the induced norm equals the spectral norm (largest singular value). For this metric, the global error, that is the accumulated error at time $t = n\tau$, is bounded by [DeR87]

$$|||\psi_{\text{exact}}(t)\rangle - |\psi_k(t)\rangle|| \le nc_k \tau^{k+1}. \tag{3.47}$$

Similar error bounds can be derived for the time-dependent Hamiltonian, in particular, the local error vanishes as τ^{k+1} for the k-th order method [HD90].

We can use Eq. (3.46) to test the implementation of the product-formula algorithm. Reducing the size of the system so that exact diagonalization becomes feasible, we can compute the left-hand side of Eq. (3.46) for different values of τ and look at the scaling with increasing τ . If we do not observe the scaling with τ^{k+1} for the k-th order method, there is an error in the implementation. If we observe the expected behavior, we cannot rule out for sure that there is still a mistake in the implementation, but it is very unlikely that a mistake does not affect the scaling behavior, and thus an error in the implementation becomes unlikely.

However, the metric $|||\psi_{\rm exact}(\tau)\rangle - |\psi_k(\tau)\rangle||$ is rather pessimistic because an error in the global phase increases this bound, although due to the free choice of the global phase, we would not consider a difference in the global phase as an error. Consider the following case. The state vectors $|\psi\rangle$ and $|\phi\rangle$ differ only by a global phase $0 < \vartheta < 2\pi$, that is $|\psi\rangle = e^{i\vartheta}|\phi\rangle$, in which case we would still consider these state vectors to describe the same physical state and evaluating any observable would yield the same result. However, we find

$$|||\psi\rangle - |\phi\rangle|| = ||(e^{i\vartheta} - 1)|\phi\rangle|| = \sqrt{2(1 - \cos(\vartheta))} \neq 0.$$
(3.48)

Other metrics which yield zero if the states $|\psi\rangle$ and $|\phi\rangle$ only differ by a global phase are $1 - |\langle \psi | \phi \rangle|$ and $1 - |\langle \psi | \phi \rangle|^2$, and we can show for $1 - |\langle \psi_{\text{exact}}(\tau) | \psi_k(\tau) \rangle|^2$ and $1 - |\langle \psi_{\text{exact}}(\tau) | \psi_k(\tau) \rangle|^2$:

$$|||\psi_{\text{exact}}(\tau)\rangle - |\psi_{k}(\tau)\rangle||^{2} = \langle \psi_{\text{exact}}(\tau)|\psi_{\text{exact}}(\tau)\rangle + \langle \psi_{k}(\tau)|\psi_{k}(\tau)\rangle - \langle \psi_{\text{exact}}(\tau)|\psi_{k}(\tau)\rangle - \langle \psi_{k}(\tau)|\psi_{\text{exact}}(\tau)\rangle = 2(1 - \Re(\langle \psi_{\text{exact}}(\tau)|\psi_{k}(\tau)\rangle)) \le c_{k}^{2}\tau^{2k+2}$$

$$1 - |\langle \psi_{\text{exact}}(\tau)|\psi_{k}(\tau)\rangle| = 1 - \sqrt{\Re(\langle \psi_{\text{exact}}(\tau)|\psi_{k}(\tau)\rangle)^{2} + \underbrace{\Im(\langle \psi_{\text{exact}}(\tau)|\psi_{k}(\tau)\rangle)^{2}}_{>0}}$$
(3.49)

$$\leq 1 - |\Re(\langle \psi_{\text{exact}}(\tau) | \psi_{k}(\tau) \rangle)| \leq 1 - \Re(\langle \psi_{\text{exact}}(\tau) | \psi_{k}(\tau) \rangle)
= \frac{1}{2} |||\psi_{\text{exact}}(\tau) \rangle - |\psi_{k}(\tau) \rangle||^{2},$$

$$(3.50)$$

$$1 - |\langle \psi_{\text{exact}}(\tau) | \psi_{k}(\tau) \rangle|^{2} = 1 - \Re(\langle \psi_{\text{exact}}(\tau) | \psi_{k}(\tau) \rangle)^{2} - \Im(\langle \psi_{\text{exact}}(\tau) | \psi_{k}(\tau) \rangle)^{2}
\leq 1 - \Re(\langle \psi_{\text{exact}}(\tau) | \psi_{k}(\tau) \rangle)^{2}
= (1 - \Re(\langle \psi_{\text{exact}}(\tau) | \psi_{k}(\tau) \rangle)) (1 + \Re(\langle \psi_{\text{exact}}(\tau) | \psi_{k}(\tau) \rangle))
\leq 1
\leq 2 (1 - \Re(\langle \psi_{\text{exact}}(\tau) | \psi_{k}(\tau) \rangle)) = |||\psi_{\text{exact}}(\tau) \rangle - |\psi_{k}(\tau) \rangle||^{2}.$$
(3.51)

However, we are often interested in expectation values of Hermitian operators A instead of the state vector itself. Thus, the quantity to look at is the difference between the expectation values in the exact state $|\psi_{\text{exact}}\rangle$ and in the state $|\psi_k\rangle$ obtained from the k-th order product-formula algorithm. We can derive the following bound:

$$\begin{aligned} & |\langle \psi_{\text{exact}} | A | \psi_{\text{exact}} \rangle - \langle \psi_k | A | \psi_k \rangle| \\ & \leq 2 \sqrt{\text{Var}_{|\psi_k\rangle}(A)} |\langle \psi_k | \psi_{\text{exact}} \rangle| \sqrt{1 - |\langle \psi_k | \psi_{\text{exact}} \rangle|^2} + 2||A|| \left(1 - |\langle \psi_k | \psi_{\text{exact}} \rangle|^2\right) \\ & \leq 2 \sqrt{\text{Var}_{|\psi_k\rangle}(A)} c_k \tau^{k+1} + 2||A|| c_k^2 \tau^{2k+2} = 2c_k \tau^{k+1} \left(\sqrt{\text{Var}_{|\psi_k\rangle}(A)} + ||A|| c_k \tau^{k+1}\right), \quad (3.53) \end{aligned}$$

where ||A|| denotes (in the case of an Hermitian operator A) the absolute value of the eigenvalue with the largest magnitude, and we could in principle also compute the variance $\operatorname{Var}_{|\psi_k\rangle}(A) = \langle \psi_k | A^2 | \psi_k \rangle - \langle \psi_k | A | \psi_k \rangle^2$ with respect to the state $|\psi_{\text{exact}}\rangle$ instead of $|\psi_k\rangle$. However, except for a few cases where we can obtain the state $|\psi_{\text{exact}}\rangle$ analytically or by exact diagonalization, we do not know the exact state and thus, computing the variance with respect to $|\psi_k\rangle$ is more practical.

Proof of Eq. (3.52): First note that we can write

$$|\psi_{\text{exact}}\rangle = \alpha |\psi_k\rangle + \beta |\chi\rangle \tag{3.54}$$

with $|\alpha|^2 + |\beta|^2 = 1$, $\langle \psi_k | \psi_{\text{exact}} \rangle = \alpha$, $\langle \psi_k | \chi \rangle = 0$ and $\langle \psi_k | \psi_k \rangle = \langle \psi_{\text{exact}} | \psi_{\text{exact}} \rangle = \langle \chi | \chi \rangle = 1$. For states $|x_1\rangle$ and $|x_2\rangle$ with $\langle x_1 | x_2 \rangle = 0$ and $\langle x_1 | x_1 \rangle = \langle x_2 | x_2 \rangle = 1$, we can use the Gram-Schmidt process to complete $|x_1\rangle$ and $|x_2\rangle$ to an orthonormal basis. We denote this basis by $\{|x_j\rangle\}_j$. Since $\langle x_1 | A | x_j \rangle \langle x_j | A | x_1 \rangle = |\langle x_1 | A | x_j \rangle|^2 \geq 0$ for an Hermitian operator A, we obtain

$$|\langle x_2|A|x_1\rangle|^2 = \langle x_1|A|x_2\rangle\langle x_2|A|x_1\rangle + \langle x_1|A|x_1\rangle\langle x_1|A|x_1\rangle - \langle x_1|A|x_1\rangle\langle x_1|A|x_1\rangle$$

$$\leq \langle x_1|A\sum_j |x_j\rangle\langle x_j|A|x_1\rangle - \langle x_1|A|x_1\rangle\langle x_1|A|x_1\rangle$$

$$= \langle x_1|A^2|x_1\rangle - \langle x_1|A|x_1\rangle^2 = \operatorname{Var}_{|x_1\rangle}(A). \tag{3.55}$$

For two normalized states $|x_1\rangle$ and $|x_2\rangle$, the bound given by

$$|\langle x_1|A|x_1\rangle - \langle x_2|A|x_2\rangle| \le 2||A|| \tag{3.56}$$

is tight. First, we show that 2||A|| is indeed an upper bound:

$$|\langle x_1|A|x_1\rangle - \langle x_2|A|x_2\rangle| \le |\langle x_1|A|x_1\rangle| + |\langle x_2|A|x_2\rangle| \le ||A|x_1\rangle|| + ||A|x_2\rangle|| \le 2||A||.$$
(3.57)

Now we show that the bound is tight by showing that the bound is attained for a special choice of A, $|x_1\rangle$ and $|x_2\rangle$. Let A be a bounded Hermitian operator with largest positive eigenvalue $\lambda > 0$ and largest negative eigenvalue $-\lambda < 0$, i.e., $||A|| = \lambda$. Let $|x_1\rangle$ be an eigenstate with eigenvalue λ and $|x_2\rangle$ an eigenstate with eigenvalue $-\lambda$. In this case, the states $|x_1\rangle$ and $|x_2\rangle$ are orthonormal. Then

$$|\langle x_1|A|x_1\rangle - \langle x_2|A|x_2\rangle| = |\langle x_1|\lambda|x_1\rangle + \langle x_2|\lambda|x_2\rangle| = |2\lambda| = 2||A||. \tag{3.58}$$

Thus, the bound Eq. (3.56) is tight and we cannot find a better one if $|x_1\rangle$ and $|x_2\rangle$ are orthogonal. Note that inserting $\langle \psi_k | \psi_{\text{exact}} \rangle = 0$ in Eq. (3.52) gives again 2||A|| as an upper bound. However, for the states $|\psi_{\text{exact}}\rangle$ and $|\psi_k\rangle$, we expect that they are not orthogonal, but almost equal with $|\langle \psi_k | \psi_{\text{exact}} \rangle| \approx 1$.

For the difference between the expectation values with respect to the states $|\psi_k\rangle$ and $|\psi_{\text{exact}}\rangle$, we then have

$$\begin{aligned} &|\langle \psi_{\text{exact}}|A|\psi_{\text{exact}}\rangle - \langle \psi_{k}|A|\psi_{k}\rangle| \\ &\stackrel{(3.54)}{=}||\alpha|^{2}\langle \psi_{k}|A|\psi_{k}\rangle + \alpha\beta^{*}\langle \chi|A|\psi_{k}\rangle + \alpha^{*}\beta\langle \psi_{k}|A|\chi\rangle + |\beta|^{2}\langle \chi|A|\chi\rangle - \langle \psi_{k}|A|\psi_{k}\rangle| \\ &= |(1-|\alpha|^{2})\left(\langle \chi|A|\chi\rangle - \langle \psi_{k}|A|\psi_{k}\rangle\right) + 2\Re\left(\alpha\beta^{*}\langle \chi|A|\psi_{k}\rangle\right)| \\ &\leq (1-|\alpha|^{2})\left|\langle \chi|A|\chi\rangle - \langle \psi_{k}|A|\psi_{k}\rangle\right| + 2|\Re\left(\alpha\beta^{*}\langle \chi|A|\psi_{k}\rangle\right)| \\ &\stackrel{(3.56)}{\leq} 2(1-|\alpha|^{2})||A|| + 2|\alpha\beta^{*}\langle \chi|A|\psi_{k}\rangle| \\ &\leq 2(1-|\alpha|^{2})||A|| + 2|\alpha||\beta|\sqrt{\langle \psi_{k}|A|\chi\rangle\langle \chi|A|\psi_{k}\rangle} \\ &\stackrel{(3.55)}{\leq} 2(1-|\alpha|^{2})||A|| + 2|\alpha|\sqrt{1-|\alpha|^{2}}\sqrt{\mathrm{Var}_{|\psi_{k}\rangle}(A)} \\ &= 2\sqrt{\mathrm{Var}_{|\psi_{k}\rangle}(A)}|\langle \psi_{k}|\psi_{\text{exact}}\rangle|\sqrt{1-|\langle \psi_{k}|\psi_{\text{exact}}\rangle|^{2}} + 2||A||\left(1-|\langle \psi_{k}|\psi_{\text{exact}}\rangle|^{2}\right). \quad \Box \end{aligned}$$

When decomposing $|\psi_k\rangle$ instead of $|\psi_{\text{exact}}\rangle$ (see Eq. (3.54)), we obtain the same bound except that the variance is then computed with respect to the state $|\psi_{\text{exact}}\rangle$, but as mentioned previously, in most cases it is more useful to compute the variance with respect to $|\psi_k\rangle$.

Example: The harmonic oscillator We investigate the error bounds by the simple example of the harmonic oscillator. That is, the Hamiltonian is given by

$$H_{\rm osc} = -E_C \frac{\partial^2}{\partial \varphi^2} + E_L \frac{\varphi^2}{2},\tag{3.59}$$

where φ is the coordinate variable and E_C and E_L are energies. The expectation value of the operator φ is to be computed and the bound Eq. (3.52) is to be investigated. We may expect some difficulties because the operator φ is unbounded. However, on the computer, we have to discretize the operator φ and represent it by an $N \times N$ -matrix covering a finite range $[\varphi_{\min}, \varphi_{\max}]$ which is bounded. We use N = 47, $E_C = 4.68\,\text{GHz}$,

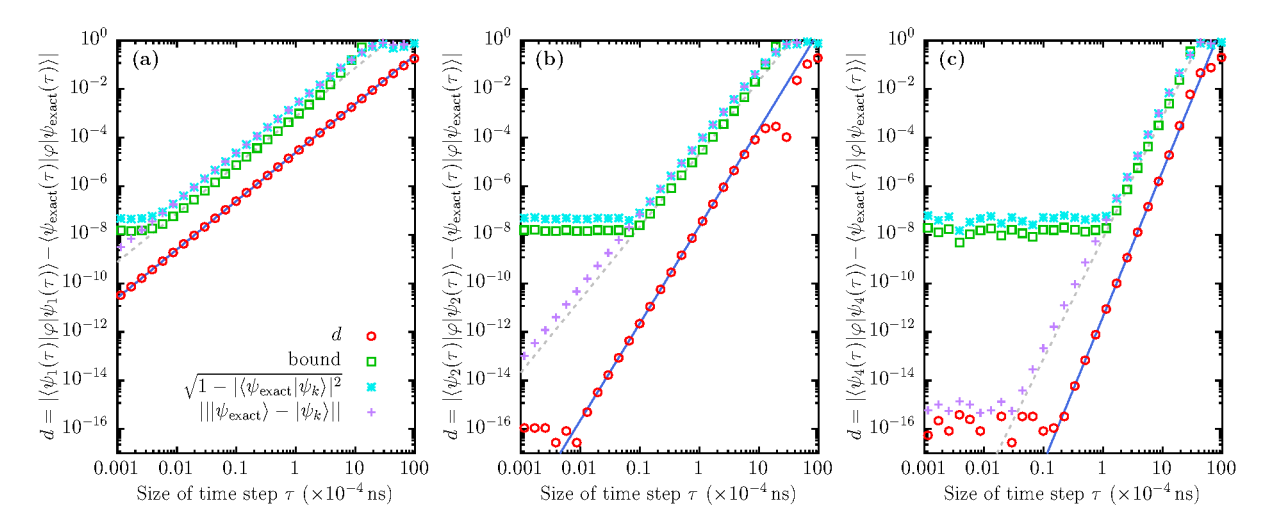


Figure 3.1: The difference of expectation values $d = |\langle \psi_k | \varphi | \psi_k \rangle - \langle \psi_{\text{exact}} | \varphi | \psi_{\text{exact}} \rangle|$ (red circles), the bound Eq. (3.52) (green squares), and the quantities $\sqrt{1 - |\langle \psi_{\text{exact}} | \psi_k \rangle|^2}$ (cyan asterisks) and $|||\psi_{\text{exact}}\rangle - |\psi_k\rangle||$ (purple pluses) as a function of the time-step τ for the (a) first-order, (b) second-order, and (c) fourth-order product-formula algorithm. The fitted exponents to d and the bound Eq. (3.52) are, respectively, given by (a) 2.00 and 2.00, (b) 4.00 and 3.00, (c) 5.99 and 4.97.

 $E_L = 3480.88 \,\mathrm{GHz}, \ \varphi_{\min} = -2 \ \mathrm{and} \ \varphi_{\max} = 2, \ \mathrm{and} \ \mathrm{thus} \ ||\varphi|| = 2.$ The initial state is set to the uniform superposition of the ground state $|\psi^0\rangle$ and the first excited state $|\psi^1\rangle$: $|\psi(0)\rangle = (|\psi^0\rangle + |\psi^1\rangle)/\sqrt{2}$. We evolve this state for a time step τ , firstly by using exact diagonalization, and secondly by applying the k-th order product-formula algorithm (see Eqs. (3.7), (3.11a) and (3.11b)). These we use to compute the quantities $d = |\langle \psi_k | \varphi | \psi_k \rangle - \langle \psi_{\mathrm{exact}} | \varphi | \psi_{\mathrm{exact}} \rangle|, \sqrt{1 - |\langle \psi_{\mathrm{exact}} | \psi_k \rangle|^2}, |||\psi_{\mathrm{exact}}\rangle - |\psi_k\rangle||$, and the bound given in Eq. (3.52). The results are presented in Fig. 3.1.

First of all, we note that the quantity $|||\psi_{\text{exact}}\rangle - |\psi_k\rangle||$ (purple pluses) scales with τ^{k+1} as expected, indicating that there is no mistake in the implementation. We find that for the second- and fourth-order algorithms, d (red circles), and for the fourth-order also $|||\psi_{\text{exact}}\rangle - |\psi_4\rangle||$, reach the numerical precision limit of the computer for small τ and therefore, the scaling with τ is no longer observable.

Although analytically $\sqrt{1-|\langle\psi_{\rm exact}|\psi_k\rangle|^2} \leq |||\psi_{\rm exact}\rangle - |\psi_k\rangle||$ (see Eq. (3.51)), we find that, in Fig. 3.1, $|||\psi_{\rm exact}\rangle - |\psi_k\rangle|| < \sqrt{1-|\langle\psi_{\rm exact}|\psi_k\rangle|^2}$ for small enough τ . One might think that either the inequality is not correct or there is a mistake in the program. The answer, however, is that we get earlier into numerical precision limitations when computing $\sqrt{1-|\langle\psi_{\rm exact}|\psi_k\rangle|^2}$ than when computing $|||\psi_{\rm exact}(\tau)\rangle - |\psi_k(\tau)\rangle||$. The reason is that even if $|\psi_{\rm exact}\rangle$ equals $|\psi_k\rangle$ up to numerical precision, the difference $1-|\langle\psi_{\rm exact}|\psi_k\rangle|^2$ equals its relative error with $(1-|\langle\psi_{\rm exact}|\psi_k\rangle|^2) \gtrsim 2.22 \times 10^{-16}$ (machine epsilon¹). Taking the square root then yields about $\sqrt{1-|\langle\psi_{\rm exact}|\psi_k\rangle|^2} \approx 10^{-7}-10^{-8}$. On the other hand, when considering $|||\psi_{\rm exact}\rangle - |\psi_k\rangle||$, we expect the difference vector $|\psi_{\rm exact}\rangle - |\psi_k\rangle = |\xi\rangle$ to be close to the zero vector. Because the elements of the vectors $|\psi_{\rm exact}\rangle$ and $|\psi_k\rangle$ cannot be larger than one, the differences of these elements are of the order of machine epsilon or smaller if we expect $|\psi_{\rm exact}\rangle$ and $|\psi_k\rangle$ to be al-

¹As defined in in C++.

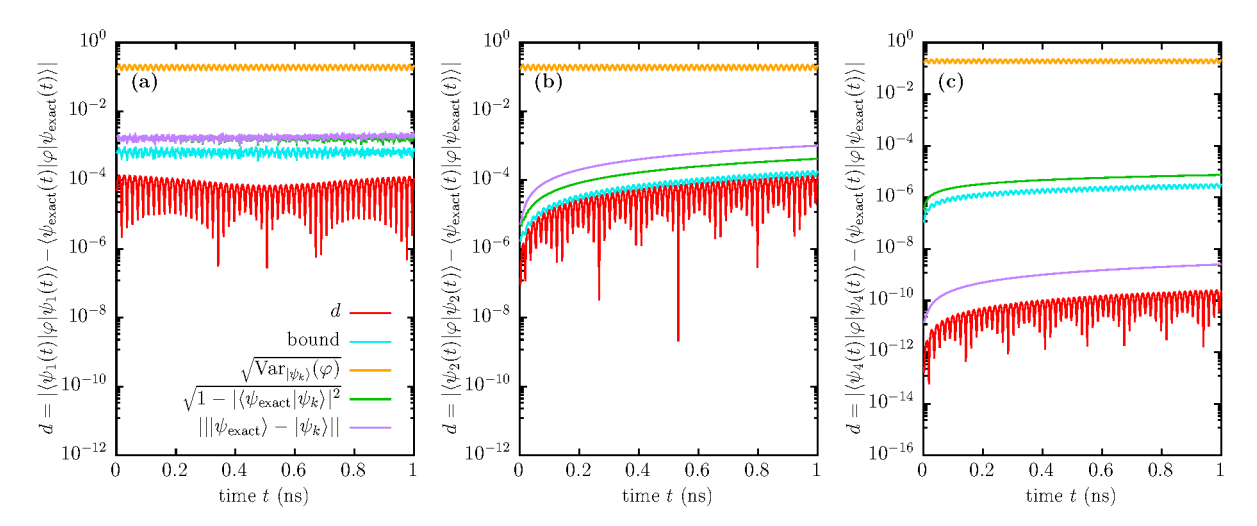


Figure 3.2: The difference of expectation values $d = |\langle \psi_k | \varphi | \psi_k \rangle - \langle \psi_{\text{exact}} | \varphi | \psi_{\text{exact}} \rangle|$ (red), the bound Eq. (3.52) (cyan), the variance of φ with respect to $|\psi_k\rangle$ (orange), and the quantities $\sqrt{1 - |\langle \psi_{\text{exact}} | \psi_k \rangle|^2}$ (green) and $|||\psi_{\text{exact}}\rangle - |\psi_k\rangle||$ (purple) as a function of time t for the (a) first-order, (b) second-order, and (c) fourth-order product-formula algorithm.

most equal. Thus, the elements ξ_i of the vector $|\xi\rangle$ are expected to be of the order of machine epsilon: $\xi_i = \xi_{(i)} \times 10^{-16}$, where $\xi_{(i)}$ is of the order of one. This yields for the norm $|||\xi\rangle|| = \sqrt{\langle \xi|\xi\rangle} = \sqrt{\sum_i \xi_{(i)}^* \xi_{(i)}} \times 10^{-32} = \sqrt{\sum_i \xi_{(i)}^* \xi_{(i)}} \times 10^{-16}$. Therefore, numerically, $|||\psi_{\rm exact}\rangle - |\psi_k\rangle||$ can become smaller than $\sqrt{1 - |\langle \psi_{\rm exact}|\psi_k\rangle|^2}$, and we see that $\sqrt{1 - |\langle \psi_{\rm exact}|\psi_k\rangle|^2}$ saturates at around 10^{-7} to 10^{-8} whereas $|||\psi_{\rm exact}\rangle - |\psi_k\rangle||$ saturates at around 10^{-15} .

We also find that d is always smaller than the bound (Eq. (3.52)). However, the bound is not tight. Thus, we examine the behavior of the same quantities as a function of time t for a fixed value of $\tau = 10^{-5}$ ns (see Fig. 3.2). We see that the quantities as a function of time exhibit different features for the first-, second- and fourth-order algorithms. For the first-order algorithm (Fig. 3.2(a)), the quantities $\sqrt{1 - |\langle \psi_{\text{exact}}|\psi_k\rangle|^2}$ and $|||\psi_{\text{exact}}\rangle - |\psi_k\rangle||$ are almost equal and d is smaller than the bound Eq. (3.52) by about an order of magnitude. In the case of the second-order algorithm, Fig. 3.2(b), $\sqrt{1 - |\langle \psi_{\text{exact}}|\psi_k\rangle|^2}$ is visibly smaller than $|||\psi_{\text{exact}}\rangle - |\psi_k\rangle||$, and the bound is very close to the difference d, although not perfectly tight. The fourth-order algorithm is in the region where $\sqrt{1 - |\langle \psi_{\text{exact}}|\psi_k\rangle|^2}$ has limited numerical accuracy compared to $|||\psi_{\text{exact}}(\tau)\rangle - |\psi_k(\tau)\rangle||$ and d (see also Fig. 3.1(c)), and thus, the bound is much too high, see Fig. 3.2(c). In this case, it seems more useful to approximate $\sqrt{1 - |\langle \psi_{\text{exact}}|\psi_k\rangle|^2}$ by $|||\psi_{\text{exact}}\rangle - |\psi_k\rangle||$ in Eq. (3.52). In all cases, the variance oscillates and thus, the bound shows the same oscillations. The difference d exhibits oscillations with the same frequency but deeper dips, yielding periodically much smaller errors than estimated by the bound Eq. (3.52).

Nevertheless, by considering the projector $P = |\psi(0)\rangle\langle\psi(0)|$ we can show that the bound is tight. In Fig. 3.3, we show the difference of the expectation values $d = |\langle\psi_{\rm exact}|P|\psi_{\rm exact}\rangle - \langle\psi_2|P|\psi_2\rangle|$ and the corresponding bound for the second-order product-formula algorithm. We find that the quantity d and the bound are almost perfectly on top of each other; they differ only a little in the beginning. The bound is also found to be tight for transmon qubits, see Ref. [Wil20]. All in all, we could improve the error estimate

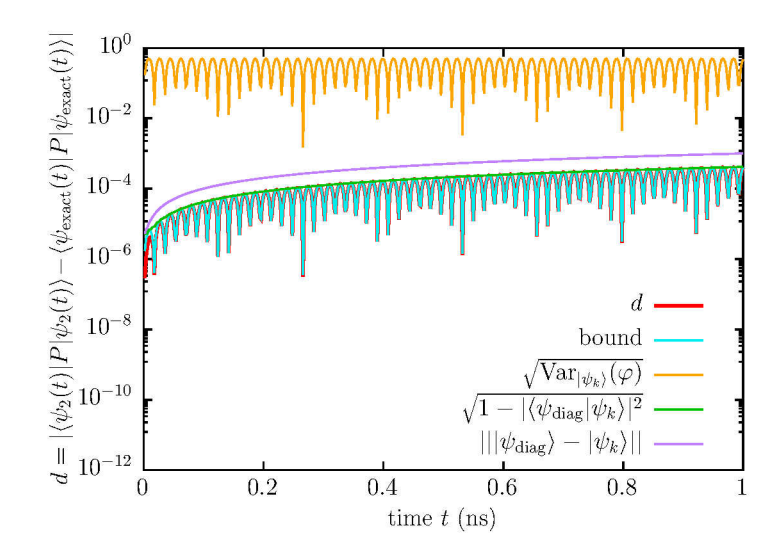


Figure 3.3: The difference of expectation values $d = |\langle \psi_2 | P | \psi_2 \rangle - \langle \psi_{\text{exact}} | P | \psi_{\text{exact}} \rangle|$ (red), the bound Eq. (3.52) (cyan), the square root of the variance of P with respect to $|\psi_2\rangle$ (orange), and the quantities $\sqrt{1 - |\langle \psi_{\text{exact}} | \psi_k \rangle|^2}$ (green) and $|||\psi_{\text{exact}}\rangle - |\psi_k\rangle||$ (purple) as a function of time t for the second-order product-formula algorithm.

which uses $|||\psi_{\text{exact}}\rangle - |\psi_k\rangle||$ only, and show that a general bound better than Eq. (3.52) cannot be found.

Chapter 4

Superconducting flux qubits

As discussed in the introduction, a qubit is a quantum system with two energy eigenstates only, i.e., a two-level system. Such a system could be, for instance, the spin of an electron. But already in this case, we have to neglect all the other energy eigenstates of the particle such as energy eigenstates induced by an external potential in position space. All two-level systems we can think of are actually simplifications of systems with more energy levels for which a two-dimensional subspace is well separated from the rest of the space [WL02]. Superconducting qubits which are multi-level systems based on superconducting circuits are thus also not genuine qubits in the sense that they are not perfect two-level systems. Rather, a well-separated subspace of the larger system is used to model the qubit. Nevertheless, these multi-level systems are commonly called superconducting qubits.

In this chapter, we will use the terms SQUID (superconducting quantum interference device) model or $flux\ model$ when referring to the multi-level system and use qubit only when we refer to the model comprising (the approximate) two-level systems. Before we discuss the SQUID Hamiltonian and the mapping of the flux model to the qubit model, we give a brief introduction to superconducting circuits.

4.1 Superconducting circuits

Superconducting circuits are built from circuit elements known from classical electrodynamics such as capacitances and inductances. In principle, dissipative elements can also be considered [Dev97; BKD04]. However, in this thesis we do not study circuits comprising dissipative elements. An element which does not occur in classical circuits but is important in superconducting circuits used to build qubits, is the Josephson junction [Jos62; Jos64]. A Josephson junction is basically a nonlinear inductance which introduces anharmonicities in the Hamiltonian, separating the two qubit energy levels from the other energy levels. Before we summarize the circuit quantization technique in general and in particular for two example circuits, we briefly describe the Josephson effect. As before, we use units with $\hbar=1$ throughout this chapter.

4.1.1 The Josephson effect

In the BCS theory of superconductors [BCS57], below the critical temperature, the charge carriers are described as Cooper pairs. These Cooper pairs are bound pairs of electrons

near the Fermi surface which experience an effectively attractive potential induced by the electron-phonon coupling. In their ground state, the two electrons in a Cooper pair have momenta \vec{k} and $-\vec{k}$ and opposite spins, effectively forming boson-like particles which can condense to a macroscopic, coherent ground state, similar to Bose-Einstein condensation. A Josephson (tunnel) junction consists of two superconductors separated by an insulating barrier. Cooper pairs can tunnel through this barrier coherently, leading to a nonzero supercurrent at zero voltage and an oscillating supercurrent at constant voltage [Jos62; Jos64].

A Josephson junction can be regarded as a capacitance C_J in parallel with a nonlinear inductance characterized by the current-flux relation

$$I(t) = I_c \sin(2e\phi(t)), \tag{4.1}$$

where I_c denotes the junction-specific critical current and e denotes the electron charge. The dimensionless flux $2e\phi = \varphi$ equals the gauge invariant phase difference of two coupled superconductors [Dev97].

The term for the potential energy of the Josephson junction is given by

$$W = -E_J \cos(2e\phi), \tag{4.2}$$

where $E_J = I_c/(2e)$. This can be verified by deriving the Euler-Lagrange equation from the Lagrangian

$$\mathcal{L} = T - W = \frac{C_J}{2}\dot{\phi}^2 + E_J\cos(2e\phi). \tag{4.3}$$

Under consideration that the conjugate variable of the flux is given by the charge $Q = \frac{\partial \mathcal{L}}{\partial \dot{\phi}}$, we obtain

$$\frac{\partial \mathcal{L}}{\partial \phi} = -\frac{\partial W}{\partial \phi} = -I_c \sin(2e\phi) = \frac{\mathrm{d}}{\mathrm{d}t} \frac{\partial \mathcal{L}}{\partial \dot{\phi}} = \frac{\mathrm{d}}{\mathrm{d}t} Q = -I. \tag{4.4}$$

which yields the characteristic relation Eq. (4.1).

4.1.2 Circuit quantization

An important step for the description, and thus for the simulation, of a superconducting circuit is to go from the circuit diagram to the quantum-mechanical Hamiltonian. This step is usually called circuit quantization and is discussed in detail in Ref. [Dev97]. A concise summary is given in Ref. [Bis10], providing a recipe to construct the Hamiltonian from a circuit diagram which we outline briefly:

- Simplify the circuit using the rules for series and parallel connections (optional).
- Choose a node which serves as ground. This freedom of choice is analogous to the gauge freedom in classical electrodynamics [Dev97].
- Choose a spanning tree S connecting all nodes to ground without closing any loops. The branches of the spanning tree are called tree branches b. The other branches closing the loops are called closure branches b'.

- Define node fluxes as $\Phi_n(t) = \sum_{b \in \mathcal{S}} S_{nb} \int_{-\infty}^t v_b(t') dt'$, where the node flux of the ground node is $\Phi_{\text{ground}} = 0$, $v_b(t)$ is the voltage across the circuit element of branch b, and $S_{nb} = \pm 1$ if b is on the path from ground to the node n (with the sign depending on the orientation) and $S_{nb} = 0$ otherwise.
- A branch flux of a tree branch b is defined as the difference $\phi_b = \Phi_{n_2} \Phi_{n_1}$ between the node fluxes Φ_{n_1} and Φ_{n_2} of the two nodes n_1 and n_2 that are connected by the branch b. The branch flux of a closure branch b' is defined as the difference between the node fluxes of the two nodes n'_1 and n'_2 minus the external flux ϕ^x piercing the loop: $\phi_{b'} = \Phi_{n'_2} \Phi_{n'_1} \phi^x$. Alternatively, the flux of a closure branch b' can be written as the sum (taking into account the orientation) of the fluxes ϕ_{b_i} of the tree branches b_i of the loop ℓ minus the external flux ϕ^x_ℓ threading the loop: $\phi_{b'} = \sum_{b_i \in \ell} \phi_{b_i} \phi^x_\ell$.
- Formulate the kinetic and potential energy terms as functions of the branch fluxes and their time derivatives (the branch voltages $v_b = \dot{\phi}_b$). Either express all branch fluxes in terms of node fluxes or express the branch fluxes of closure branches in terms of the branch fluxes of tree branches. If time-dependent external fluxes are present, terms proportional to the time derivative of such an external flux may arise which cannot be neglected in general [YSK19].
- Form the Lagrangian \mathcal{L} . If possible, eliminate superfluous variables by using, e.g., the method described in [Ric18]. In the case of time-dependent external fluxes (especially if one is interested in multi-time observables), one may want to perform a variable transformation to the irrotational degrees of freedom as discussed in Ref. [YSK19].
- Perform the Legendre transformation $H = \sum_{b=1}^{N} \dot{\phi}_b Q_b \mathcal{L}$ with $Q_b = \frac{\partial \mathcal{L}}{\partial \dot{\phi}_b}$ (or $H = \sum_{n=1}^{N} \dot{\Phi}_n \widetilde{Q}_n \mathcal{L}$ with $\widetilde{Q}_n = \frac{\partial \mathcal{L}}{\partial \dot{\Phi}_n}$), assuming that the system of equations for Q_b (\widetilde{Q}_n) is invertible, to arrive at the Hamiltonian.
- Finally, replace the variables by their corresponding operators satisfying the commutation relations $[\phi_b, Q_b] = i$ (or $[\Phi_n, \widetilde{Q}_n] = i$).

As an example, we apply the circuit quantization rules to derive the Hamiltonian of the circuits shown in Fig. 4.1 and Fig. 4.2. The first circuit is a simple LC-circuit with capacitance C and inductance L. We apply the circuit quantization rules:

- We choose the lower of the two nodes to be ground with node flux $\Phi_{ground} = 0$ and label the upper node flux by Φ .
- We choose the branch over the capacitance to be the tree branch and the branch over the inductance to be the closure branch.
- The branch flux of the tree branch with label ϕ_1 is expressed in node fluxes by $\phi_1 = \Phi \Phi_{\text{ground}} = \Phi$ and the branch flux of the closure branch is $\phi_2 = \Phi \Phi_{\text{ground}} = \Phi$.
- The capacitance contributes to the kinetic energy with $T = C\dot{\phi}_1^2/2 = C\dot{\Phi}^2/2$ and the inductance contributes to the potential energy with $W = \phi_2^2/(2L) = \Phi^2/(2L)$, where we expressed all branch fluxes in terms of the node fluxes.

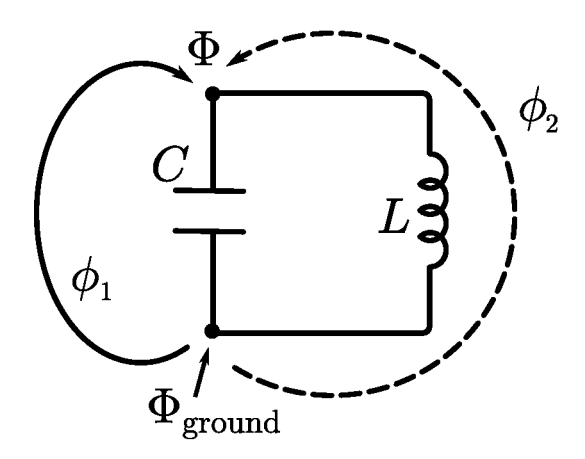


Figure 4.1: The LC-circuit used as an example for the circuit quantization showing the branch fluxes ϕ_1 , and ϕ_2 , the node fluxes Φ and Φ_{ground} , a capacitance C and an inductance L. The flux of the chosen tree branch is indicated by a solid line and the flux of the closure branch by a dashed line.

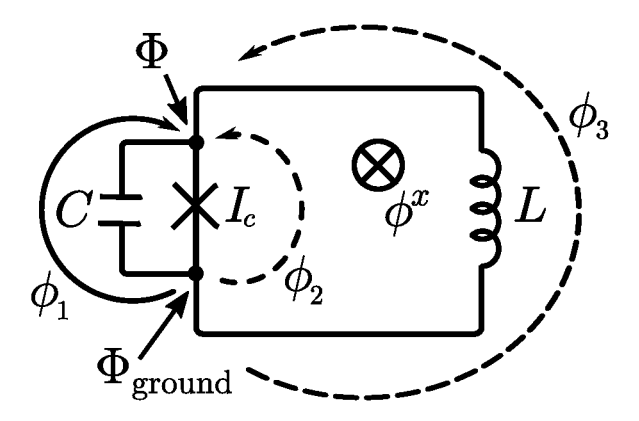


Figure 4.2: Example circuit for the circuit quantization showing the branch fluxes ϕ_1 , ϕ_2 and ϕ_3 , the node fluxes Φ and Φ_{ground} , the external flux ϕ^x , a capacitance C, an inductance L and a Josephson junction with critical current I_c . The flux of the chosen tree branch is indicated by a solid line and the fluxes of the closure branches by dashed lines.

- The Lagrangian is given by $\mathcal{L} = T W = C\dot{\Phi}^2/2 \Phi^2/(2L)$.
- Performing the Legendre transformation, we obtain the Hamiltonian

$$H = \dot{\Phi}\widetilde{Q} - \mathcal{L} = \frac{\widetilde{Q}^2}{2C} + \frac{\Phi^2}{2L},$$

which is the classical Hamiltonian of a harmonic oscillator.

• Replacing the variables \widetilde{Q} and Φ by their corresponding operators, we obtain the quantum mechanical Hamiltonian of the harmonic oscillator.

The circuit shown in Fig. 4.2 is a bit more complex as it contains, in addition to the capacitance C and the inductance L, a Josephson junction with critical current I_c and an external flux $\phi^x = \varphi^x/(2e)$. The circuit has two nodes and three branches. We choose the lower node as ground and the branch over the capacitance C as spanning tree, connecting the upper node with ground. The branches over the inductance L and the Josephson junction with critical current I_c are thus closure branches in this choice. Labeling the node flux of the upper node by Φ , we obtain for the branch fluxes

$$\phi_1 = \Phi - \Phi_{\text{ground}} = \Phi, \tag{4.5a}$$

$$\phi_2 = \Phi - \Phi_{\text{ground}} = \Phi = \phi_1, \tag{4.5b}$$

$$\phi_3 = \Phi - \Phi_{\text{ground}} - \phi^x = \Phi - \phi^x = \phi_1 - \phi^x,$$
(4.5c)

where we have to account for the orientations of the fluxes. The energies of the circuit elements are $T = C\dot{\phi}_1^2/2$ originating from the capacitance, $W_J = -E_J\cos(2e\phi_2)$ from the

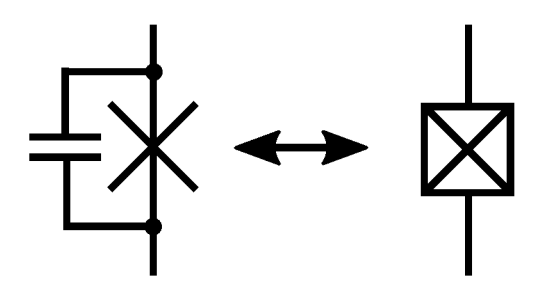


Figure 4.3: The circuit diagram of a Josephson junction with a capacitance connected in parallel (left) and the circuit diagram showing a Josephson junction with a square (right) are equivalent.

Josephson junction, and $W_L = \phi_3^2/(2L)$ from the inductance. Using Eqs. (4.5a) - (4.5c) we can express the Lagrangian in terms of ϕ_1

$$\mathcal{L} = \frac{C}{2}\dot{\phi}_1^2 + E_J \cos(2e\phi_1) - \frac{1}{L}\frac{(\phi_1 - \phi^x)^2}{2}.$$
 (4.6)

The conjugate variable Q_1 is given by $Q_1 = C\dot{\phi}_1$ and we obtain the Hamiltonian

$$H = \frac{Q_1^2}{2C} - E_J \cos(2e\phi_1) + \frac{1}{L} \frac{(\phi_1 - \phi^x)^2}{2}$$

$$= \frac{4e^2}{2C} n_1^2 - E_J \cos(\varphi_1) + \frac{1}{4e^2L} \frac{(\varphi_1 - \varphi^x)^2}{2},$$
(4.7)

where we have for the operators $[\phi_1, Q_1] = i$ (and accordingly $[\varphi_1, n_1] = i$, where $n_1 = Q_1/(2e)$ is the number operator of the Cooper pairs). Indeed, we find that the Josephson junction adds an anharmonic term to the Hamiltonian of the harmonic oscillator. This anharmonicity removes the equidistant level spacing of the harmonic oscillator. As a result, the subspace corresponding to the two lowest energy levels can in principle be regarded as an effective two-level system – the qubit.

The Hamiltonian given in Eq. (4.7) describes a SQUID which can be used to construct a simple flux qubit if $E_J \gg 4e^2/(2C)$ [WS07]. As mentioned in Section 1.2, there are also different types of qubits [SSH97; Mar+02; Koc+07; Wen17], but we will only focus on qubits of the flux type such as the compound Josephson-junction SQUID [Har+09b]. Thus, we investigate this type of qubit more thoroughly.

In the course of this example, we found that a Josephson junction element in parallel with a capacitance can effectively be described as a single element contributing to the kinetic energy and the potential energy if the loop is not threaded by an external flux. Thus, we will also use the boxed Josephson junction shown in Fig. 4.3 and used in the literature, as a symbol for a Josephson junction and its net capacitance.

4.2 Superconducting quantum interference device

A superconducting quantum interference device (SQUID) consists of a superconducting loop interrupted by a Josephson junction, see Fig. 4.2. SQUIDs have already been studied since 1967 [SZ67] and used as magnetometers [ZTH70; GLB76], before they were used to study tunneling and superpositions of macroscopically distinct quantum states [Pra+81;

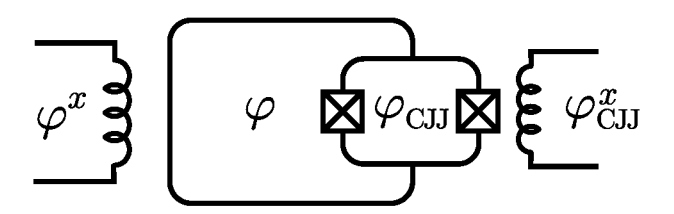


Figure 4.4: Sketch of the circuit of a SQUID with CJJ loop.

RHL95; Fri+00], and introduced to the field of quantum computation as possible qubits [MSS00] and coupler elements [Plo+04].

In this section, we first discuss the theoretical model of a single compound Josephson junction SQUID and then how to use a SQUID as a tunable coupler element between two SQUIDs. Subsequently, we study the mapping of the SQUID model onto a two-level model to obtain the description of the quantum annealing Hamiltonian in terms of qubits (see Eq. (2.8)).

Some of the results presented in this section have been published in [Wil+20].

4.2.1 Theoretical model of a single SQUID

The simple rf-SQUID, consisting of a superconducting loop and a Josephson junction, was already examined in Section 4.1.2 as an example for the application of circuit quantization. The compound Josephson junction (CJJ) SQUID (also called double SQUID) on which we focus in this section, and which is used by D-Wave Systems Inc. as a building block for qubits [Har+08] and couplers [Har+09a], was already studied by Han, Lapointe and Lukens in 1989 [HLL89]. The circuit of the SQUID with CJJ loop is shown in Fig. 4.4. It consists of a superconducting loop interrupted by a dc-SQUID (a loop which contains two Josephson junctions, also called the compound Josephson junction loop). The external fluxes φ^x and φ^x_{CJJ} are applied to the (main) loop and the CJJ loop, respectively. The advantage of the additional CJJ loop is that it functions as a Josephson junction with an energy tunable by changing the applied external flux φ^x_{CJJ} [LHL90].

The derivation of the Hamiltonian description using the circuit quantization rules, discussed in Section 4.1.2, is summarized in Appendix A.1, yielding the Hamiltonian given in Ref. [Har+10a]

$$H_{\text{SQUID}} = -E_C \partial_{\varphi}^2 - E_{C_{\text{CJJ}}} \partial_{\varphi_{\text{CJJ}}}^2 - E_J \cos(\varphi) \cos\left(\frac{\varphi_{\text{CJJ}}}{2}\right) + E_L \frac{(\varphi - \varphi^x)^2}{2} + E_{L_{\text{CJJ}}} \frac{(\varphi_{\text{CJJ}} - \varphi_{\text{CJJ}}^x)^2}{2}, \tag{4.8}$$

where $\varphi = 2\pi\phi/\phi_0 = 2e\phi$ is the dimensionless magnetic flux of the main loop, φ_{CJJ} denotes the flux of the CJJ loop, and φ^x and φ^x_{CJJ} are the dimensionless external fields that can be controlled. The symbol ϕ_0 denotes the magnetic flux quantum and e is the electron charge. The parameters E_C and $E_{C_{\text{CJJ}}}$ are capacitive energies, E_L and $E_{L_{\text{CJJ}}}$ are inductive energies, and E_J is the Josephson energy. The energies relate to the inductances L, capacitances C and critical current I_c as follows:

$$E_C = \frac{2e^2}{C},$$
 $E_L = \frac{1}{4e^2} \frac{1}{L + L_{\text{CJJ}}/4},$ $E_J = \frac{I_c}{2e},$ (4.9a)

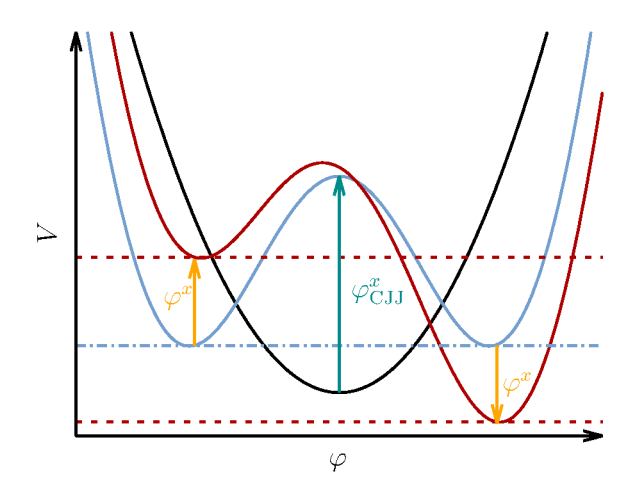


Figure 4.5: Visualization of the influence of the external fluxes φ^x and φ^x_{CJJ} on the potential energy $V(\varphi)$ (not to scale).

$$E_{C_{\text{CJJ}}} = \frac{2e^2}{C_{\text{CJJ}}}, \qquad E_{L_{\text{CJJ}}} = \frac{1}{4e^2} \frac{1}{L_{\text{CJJ}}}.$$
 (4.9b)

We find that the Josephson term in Eq. (4.8) can indeed be interpreted as providing a tunable energy $E_J \cos(\varphi_{\text{CJJ}}/2)$ via φ_{CJJ}^x if $\varphi_{\text{CJJ}} \approx \varphi_{\text{CJJ}}^x$, which holds if $L \gg L_{\text{CJJ}}$. This means, the effective potential for φ can be changed from a monostable potential to a double-well potential with tunable barrier height by changing φ_{CJJ}^x . The external flux φ^x can be used to bias one of the potential wells [Fri+00]. The influence of the external fluxes on the potential energy is visualized in Fig. 4.5. The dependence of the form of the potential on the external flux φ_{CJJ}^x is used by D-Wave Systems Inc. to control the annealing process for the SQUIDs representing the qubits [Har+10b]. For SQUIDs functioning as a coupler, this dependence is used to tune the coupling strength between two SQUIDs [Har+09a]. More specifically, for the SQUIDs functioning as qubits, the two Josephson junctions are replaced by dc SQUIDs themselves to compensate for fabrication asymmetries between the Josephson junctions [Har+10a]. However, since in the simulation, we can set the junctions to be equal, we use the Hamiltonian given in Eq. (4.8).

4.2.2 Tunable coupling between SQUIDs

For the mapping of different optimization problems onto the Hamiltonian Eq. (2.7), the coupling constants J_{jk} need to be tunable. Thus, for the implementation of qubits using SQUIDs, the coupling strength between the two SQUIDs needs to be tunable. This can be achieved by using a SQUID as tunable coupler [BBY05; Har+07; Har+09a]. We study a system of two SQUIDs (labeled by "1" and "2") resembling the qubits coupled through a SQUID which mediates the coupling. We label the variables and parameters of the SQUIDs 1 and 2 by an index "1" and "2", respectively, and accordingly the variables and parameters of the coupling SQUID by an index "0". Parameters without index are the same for SQUID 1 and 2, hence we drop the index in these cases. The circuit of the system is shown in Fig. 4.6.

The construction of the Hamiltonian of the system of three coupled SQUIDs is pre-

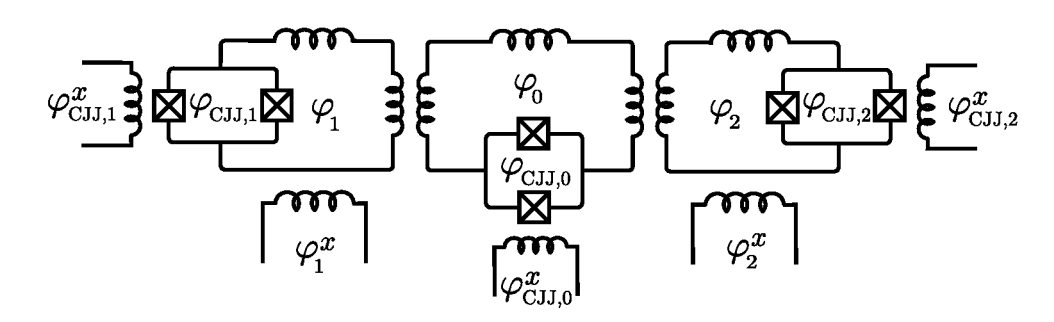


Figure 4.6: Circuit of the three SQUIDs being studied. The fluxes φ_i and $\varphi_{\text{CJJ},i}$ are the dynamical variables of the system. The external fluxes φ_i^x and $\varphi_{\text{CJJ},i}^x$ are used to control the operation of the device.

sented in Appendix A.2 and results in the total system Hamiltonian [BBY05]

$$H_{\text{total}} = \sum_{i=0}^{2} \left(E_{L_{\text{CJJ},i}} \frac{\left(\varphi_{\text{CJJ},i} - \varphi_{\text{CJJ},i}^{x}\right)^{2}}{2} - E_{C_{i}} \partial_{\varphi_{i}}^{2} - E_{C_{\text{CJJ},i}} \partial_{\varphi_{\text{CJJ},i}}^{2} - E_{J_{i}} \cos(\varphi_{i}) \cos\left(\frac{\varphi_{\text{CJJ},i}}{2}\right) \right) + E_{L} \left(1 + \frac{M^{2}}{(L + L_{\text{CJJ}}/4)L_{\text{eff}}} \right) \left(\frac{(\varphi_{1} - \varphi_{1}^{x})^{2}}{2} + \frac{(\varphi_{2} - \varphi_{2}^{x})^{2}}{2} \right) + E_{L_{\text{eff}}} \frac{(\varphi_{0} - \varphi_{0}^{x})^{2}}{2} + \frac{M^{2}E_{L}}{(L + L_{\text{CJJ}}/4)L_{\text{eff}}} (\varphi_{1} - \varphi_{1}^{x})(\varphi_{2} - \varphi_{2}^{x}) + \frac{ME_{L}}{L_{\text{eff}}} (\varphi_{1} - \varphi_{1}^{x} + \varphi_{2} - \varphi_{2}^{x})(\varphi_{0} - \varphi_{0}^{x}),$$

$$(4.10)$$

where the energies of the SQUIDs 1 and 2 representing the qubits are still given by Eqs. (4.9a) and (4.9b), and the energies of the coupling SQUID 0 are given accordingly. In addition, we defined

$$E_{L_{\text{eff}}} = \frac{1}{4e^2 L_{\text{eff}}}, \quad L_{\text{eff}} = L_0 + \frac{L_{\text{CJJ},0}}{4} - \frac{2M^2}{L + L_{\text{CJJ}}},$$
 (4.11)

where $L_{\text{CJJ},0}$ denotes the inductance of the coupler CJJ loop, L_0 denotes the inductance of the coupler main loop and M denotes the mutual inductance between the coupling SQUID and the other two SQUIDs. To function as a tunable coupler, the coupling SQUID can be operated without an external flux φ_0^x piercing the main loop [Har+09a]. Thus, we set $\varphi_0^x = 0$.

The aim of including the SQUID mediating the coupling between the two SQUIDs functioning as qubits is to introduce an effective direct coupling term between φ_1 and φ_2 that can be tuned by changing the flux $\varphi_{\text{CJJ},0}^x$ through the coupler's CJJ loop. That is, the desired term is of the form $C(\varphi_{\text{CJJ},0}^x)\varphi_1\varphi_2$. In order to derive an effective Hamiltonian containing this coupling term and decoupling SQUIDs 1 and 2 from the coupler, we first apply a Born-Oppenheimer approximation similar to the one presented in Ref. [DBK06]. Thereby, we can eliminate the variable $\varphi_{\text{CJJ},0}$ by substituting it with its (approximate) ground state expectation value. We use Eq. (4.8) for the coupling SQUID, i.e., the external flux $\varphi_0^x = 0$, and we set $\varphi_0 = 0$ for this derivation and expand the Hamiltonian to second order in $\varphi_{\text{CJJ},0} - \varphi_{\text{CJJ},0}^x$, yielding

$$H_{\text{SQUID}}^{\varphi_0=0} \approx -E_{C_{\text{CJJ},0}} \partial_{\varphi_{\text{CJJ},0}}^2 + E_{L_{\text{CJJ},0}} \frac{\left(\varphi_{\text{CJJ},0} - \varphi_{\text{CJJ},0}^x\right)^2}{2}$$

$$+E_{J_0} \left(\frac{\left(\varphi_{\text{CJJ},0} - \varphi_{\text{CJJ},0}^x\right)^2}{8} \cos\left(\frac{\varphi_{\text{CJJ},0}^x}{2}\right) + \frac{\left(\varphi_{\text{CJJ},0} - \varphi_{\text{CJJ},0}^x\right)}{2} \sin\left(\frac{\varphi_{\text{CJJ},0}^x}{2}\right) \right)$$

$$= -E_{C_{\text{CJJ},0}} \partial_{\varphi_{\text{CJJ},0}}^2 + \frac{E'_{L_{\text{CJJ},0}}}{2} \left(\varphi_{\text{CJJ},0} - \varphi_{\text{CJJ},0}^x + \frac{E_{J_0} \sin(\varphi_{\text{CJJ},0}^x/2)}{2E'_{L_{\text{CJJ},0}}}\right)^2, \quad (4.12)$$

where $E'_{L_{\text{CJJ},0}} = E_{L_{\text{CJJ},0}} + E_{J_0} \cos(\varphi^x_{\text{CJJ},0}/2)$ /4. Since the resulting Hamiltonian describes a shifted harmonic oscillator, we can immediately recognize the expectation value of $\varphi_{\text{CJJ},0}$ in its ground state

$$\langle \varphi_{\text{CJJ},0} \rangle = \varphi_{\text{CJJ},0}^x - \frac{E_{J_0} \sin(\varphi_{\text{CJJ},0}^x/2)}{2E_{L_{\text{CJJ},0}} + E_{J_0} \cos(\varphi_{\text{CJJ},0}^x/2)/2}.$$
 (4.13)

We can use the result of this Born-Oppenheimer analysis to replace $\varphi_{\text{CJJ},0}$ by $\langle \varphi_{\text{CJJ},0} \rangle$ in H_{total} (Eq. (4.10)). We now want to effectively decouple the degree of freedom φ_0 of the coupler from the other two SQUIDs by means of a basis transformation similar to a Schrieffer-Wolff transformation [SW66]. To this end, we perform the basis transformation

$$e^{iT(t)}H_{\text{total}}^{\langle\varphi_{\text{CJJ},0}\rangle}e^{-iT(t)} - ie^{iT(t)}\left(\frac{\partial}{\partial t}e^{-iT(t)}\right)$$

$$= H_{\text{total}}^{\langle\varphi_{\text{CJJ},0}\rangle} + [iT(t), H_{\text{total}}^{\langle\varphi_{\text{CJJ},0}\rangle}] + \frac{1}{2!}[iT(t), [iT(t), H_{\text{total}}^{\langle\varphi_{\text{CJJ},0}\rangle}]]$$

$$+ \frac{1}{3!}[iT(t), [iT(t), [iT(t), H_{\text{total}}^{\langle\varphi_{\text{CJJ},0}\rangle}]]] + \dots - ie^{iT(t)}\left(\frac{\partial}{\partial t}e^{-iT(t)}\right) = H_{\text{eff}}, \qquad (4.14)$$

with

$$T = T(t) = i\alpha(\varphi_1 - \varphi_1^x + \varphi_2 - \varphi_2^x)\partial_{\varphi_0}, \tag{4.15}$$

where α is a parameter to be determined accordingly. Note that we have to take into account the explicit time dependence of the basis transformation. Thus, for the time evolution of the state vector $\exp(iT(t))|\psi\rangle$ to satisfy the Schrödinger equation, the Hamiltonian has to be transformed according to (see also [Mes61]):

$$i\frac{\partial}{\partial t}|\psi\rangle = H|\psi\rangle$$
 (4.16a)

$$\Leftrightarrow i\frac{\partial}{\partial t}e^{-iT(t)}e^{iT(t)}|\psi\rangle = He^{-iT(t)}e^{iT(t)}|\psi\rangle \tag{4.16b}$$

$$\Leftrightarrow i\frac{\partial}{\partial t}e^{iT(t)}|\psi\rangle = \left(e^{iT(t)}He^{-iT(t)} - ie^{iT(t)}\left(\frac{\partial}{\partial t}e^{-iT(t)}\right)\right)e^{iT(t)}|\psi\rangle, \qquad (4.16c)$$

resulting in the additional term $-i \exp(iT(t))$ ($\partial_t \exp(-iT(t))$). The calculation of the basis transformation Eq. (4.14) is given in Appendix B.1, yielding the effective Hamiltonian in the new basis

$$H_{\text{eff}} = \sum_{i=1}^{2} \left(-E_C \partial_{\varphi_i}^2 - E_{C_{\text{CJJ}}} \partial_{\varphi_{\text{CJJ},i}}^2 - E_J \cos(\varphi_i) \cos\left(\frac{\varphi_{\text{CJJ},i}}{2}\right) + E_{L_{\text{CJJ}}} \frac{(\varphi_{\text{CJJ},i} - \varphi_{\text{CJJ}}^x)^2}{2} \right)$$

$$+E_{L}\left(1+\frac{M^{2}}{(L+L_{\text{CJJ}}/4)L_{\text{eff}}}+\alpha^{2}\frac{L+L_{\text{CJJ}}/4}{L_{\text{eff}}}-2\frac{\alpha M}{L_{\text{eff}}}\right)\left(\frac{(\varphi_{1}-\varphi_{1}^{x})^{2}}{2}+\frac{(\varphi_{2}-\varphi_{2}^{x})^{2}}{2}\right)$$

$$+E_{L_{\text{eff}}}\frac{\varphi_{0}^{2}}{2}-\left(E_{C_{0}}+2E_{C}\alpha^{2}\right)\partial_{\varphi_{0}}^{2}+\left(\frac{ME_{L}}{L_{\text{eff}}}-\alpha E_{L_{\text{eff}}}\right)(\varphi_{1}-\varphi_{1}^{x}+\varphi_{2}-\varphi_{2}^{x})\varphi_{0}$$

$$+\left(\frac{M^{2}E_{L}}{(L+L_{\text{CJJ}}/4)L_{\text{eff}}}+\alpha^{2}E_{L_{\text{eff}}}-2\frac{\alpha ME_{L}}{L_{\text{eff}}}\right)(\varphi_{1}-\varphi_{1}^{x})(\varphi_{2}-\varphi_{2}^{x})$$

$$+\left(i\alpha\frac{\partial}{\partial t}\left(\varphi_{1}^{x}+\varphi_{2}^{x}\right)-2E_{C}\alpha\left(\partial_{\varphi_{1}}+\partial_{\varphi_{2}}\right)\right)\partial_{\varphi_{0}}$$

$$-E_{J_{0}}\cos\left(\frac{\langle\varphi_{\text{CJJ},0}\rangle}{2}\right)\cos(\varphi_{0}-\alpha(\varphi_{1}-\varphi_{1}^{x}+\varphi_{2}-\varphi_{2}^{x})). \tag{4.17}$$

Defining

$$\beta_{\text{eff}} = \frac{E_{J_0}}{E_{L_{\text{eff}}}} \cos\left(\frac{\langle \varphi_{\text{CJJ},0} \rangle}{2}\right), \tag{4.18}$$

and approximating $\cos(\varphi_0 - \alpha(\varphi_1 - \varphi_1^x + \varphi_2 - \varphi_2^x))$ to second order in (the products of) φ_0 , $\varphi_1 - \varphi_1^x$ and $\varphi_2 - \varphi_2^x$ yields

$$H_{\text{eff}} \approx \sum_{i=1}^{2} \left(-E_{C} \partial_{\varphi_{i}}^{2} - E_{C_{\text{CJJ}}} \partial_{\varphi_{\text{CJJ},i}}^{2} - E_{J} \cos(\varphi_{i}) \cos\left(\frac{\varphi_{\text{CJJ},i}}{2}\right) + E_{L_{\text{CJJ}}} \frac{(\varphi_{\text{CJJ},i} - \varphi_{\text{CJJ}}^{x})^{2}}{2} \right)$$

$$+ E_{L} \left(1 + \frac{M^{2}}{(L + L_{\text{CJJ}}/4)L_{\text{eff}}} - \frac{2\alpha M}{L_{\text{eff}}} + \frac{\alpha^{2}(L + L_{\text{CJJ}}/4)(1 + \beta_{\text{eff}})}{L_{\text{eff}}} \right) \left(\frac{(\varphi_{1} - \varphi_{1}^{x})^{2}}{2} + \frac{(\varphi_{2} - \varphi_{2}^{x})^{2}}{2} \right)$$

$$+ E_{L_{\text{eff}}} \left(1 + \beta_{\text{eff}} \right) \frac{\varphi_{0}^{2}}{2} - \left(E_{C_{0}} + 2E_{C}\alpha^{2} \right) \partial_{\varphi_{0}}^{2} + \left(i\alpha \frac{\partial}{\partial t} \left(\varphi_{1}^{x} + \varphi_{2}^{x} \right) - 2E_{C}\alpha(\partial_{\varphi_{1}} + \partial_{\varphi_{2}}) \right) \partial_{\varphi_{0}}$$

$$+ \frac{E_{L}}{L_{\text{eff}}} \left(M - \alpha(L + L_{\text{CJJ}}/4)(1 + \beta_{\text{eff}}) \right) (\varphi_{1} - \varphi_{1}^{x} + \varphi_{2} - \varphi_{2}^{x}) \varphi_{0}$$

$$+ \frac{E_{L}}{L_{\text{eff}}} \left(\frac{M^{2}}{(L + L_{\text{CJJ}}/4)} - 2\alpha M + \alpha^{2}(L + L_{\text{CJJ}}/4)(1 + \beta_{\text{eff}}) \right) (\varphi_{1} - \varphi_{1}^{x}) (\varphi_{2} - \varphi_{2}^{x}).$$
 (4.19)

Choosing $\alpha = M/((L + L_{\text{CJJ}}/4)(1 + \beta_{\text{eff}}))$, the term proportional to $(\varphi_1 - \varphi_1^x + \varphi_2 - \varphi_2^x)\varphi_0$ vanishes and we obtain

$$H_{\text{eff}} \approx \sum_{i=1}^{2} \left(-E_{C} \partial_{\varphi_{i}}^{2} - E_{C_{\text{CJJ}}} \partial_{\varphi_{\text{CJJ},i}}^{2} - E_{J} \cos(\varphi_{i}) \cos\left(\frac{\varphi_{\text{CJJ},i}}{2}\right) + E_{L_{\text{CJJ}}} \frac{(\varphi_{\text{CJJ},i} - \varphi_{\text{CJJ}}^{x})^{2}}{2} \right)$$

$$+ E_{L} \left(1 + \frac{M^{2}}{(L + L_{\text{CJJ}}/4) L_{\text{eff}}} \frac{\beta_{\text{eff}}}{(1 + \beta_{\text{eff}})} \right) \left(\frac{(\varphi_{1} - \varphi_{1}^{x})^{2}}{2} + \frac{(\varphi_{2} - \varphi_{2}^{x})^{2}}{2} \right)$$

$$+ E_{L_{\text{eff}}} \left(1 + \beta_{\text{eff}} \right) \frac{\varphi_{0}^{2}}{2} - \left(E_{C_{0}} + \frac{2E_{C}M^{2}}{(L + L_{\text{CJJ}}/4)^{2} (1 + \beta_{\text{eff}})^{2}} \right) \partial_{\varphi_{0}}^{2}$$

$$+ \frac{M}{(L + L_{\text{CJJ}}/4) (1 + \beta_{\text{eff}})} \left(i \frac{\partial}{\partial t} \left(\varphi_{1}^{x} + \varphi_{2}^{x} \right) - 2E_{C} \left(\partial_{\varphi_{1}} + \partial_{\varphi_{2}} \right) \right) \partial_{\varphi_{0}}$$

$$+ \frac{E_{L}M^{2}}{(L + L_{\text{CJJ}}/4) L_{\text{eff}}} \frac{\beta_{\text{eff}}}{(1 + \beta_{\text{eff}})} \left(\varphi_{1} - \varphi_{1}^{x} \right) \left(\varphi_{2} - \varphi_{2}^{x} \right).$$

$$(4.20)$$

The effective Hamiltonian Eq. (4.20) exhibits a coupling term between φ_1 and φ_2 which is tunable by changing β_{eff} which is a function of $\varphi_{\text{CJJ},0}^x$ (cf. Eqs. (4.18) and (4.13)).

This transformation to obtain the effective Hamiltonian is also outlined in [Wil+20].

4.2.3 Mapping SQUIDs to two-level systems for quantum annealing

Since $E_C \ll E_L$ and the prefactor $E_L M/L_{\rm eff}$ is roughly 300 times larger than $2E_C M/(L+L_{\rm CJJ}/4)$, we can neglect the term proportional to $(\partial_{\varphi_1} + \partial_{\varphi_2})\partial_{\varphi_0}$ in Eq. (4.20), and we find that the Hamiltonian part of the coupler is decoupled from the rest of the Hamiltonian. The Hamiltonian for φ_0 is the harmonic oscillator with displacement in momentum. In this section, we write explicitly the dependence of the external fluxes on the dimensionless time s. We obtain for the effective Hamiltonian of the two SQUIDs 1 and 2 corresponding to the qubits (omitting some global constants)

$$H_{\text{eff}} \approx \sum_{i=1}^{2} \left[-E_{C} \partial_{\varphi_{i}}^{2} - E_{C_{\text{CJJ}}} \partial_{\varphi_{\text{CJJ},i}}^{2} - E_{J} \cos(\varphi_{i}) \cos\left(\frac{\varphi_{\text{CJJ},i}}{2}\right) + E_{L_{\text{CJJ}}} \frac{(\varphi_{\text{CJJ},i} - \varphi_{\text{CJJ}}^{x}(s))^{2}}{2} + \widetilde{E}_{L} \frac{\varphi_{i}^{2}}{2} \right] - \widetilde{E}_{L} (\varphi_{1}^{x}(s)\varphi_{1} + \varphi_{2}^{x}(s)\varphi_{2}) + \frac{E_{L} M^{2}}{(L + L_{\text{CJJ}}/4)L_{\text{eff}}} \frac{\beta_{\text{eff}}}{(1 + \beta_{\text{eff}})} (\varphi_{1}\varphi_{2} - \varphi_{1}^{x}(s)\varphi_{2} - \varphi_{2}^{x}(s)\varphi_{1}),$$

$$(4.21)$$

where

$$\widetilde{E}_L = E_L \left(1 + \frac{M^2}{(L + L_{\text{CJJ}}/4)L_{\text{eff}}} \frac{\beta_{\text{eff}}}{1 + \beta_{\text{eff}}} \right). \tag{4.22}$$

In the following, we outline the mapping onto the qubit subspace as explained in Refs. [Har+09b; Har+10a] and in the supplementary material of Ref. [Boi+16]. In addition, we derive an expression for the external fluxes φ_i^x , i=1,2, which we will use in the simulation, and a relation between the coupling J in the Ising model and the external flux $\varphi_{\text{CJJ},0}^x$. This relation has to be solved numerically to determine the value for $\varphi_{\text{CJJ},0}^x$ for a given value of J.

The part in square brackets in Eq. (4.21) is used to define the computational subspace of qubit i=1,2. The instantaneous ground state $|g(s)\rangle_i$ and first excited state $|e(s)\rangle_i$ of this part of the Hamiltonian with energies $E_g(s)$ and $E_e(s)$, respectively, span the computational subspace of qubit i=1,2. However these states are not used as the computational basis states. Diagonalization of the operator φ_i in the subspace spanned by $|g(s)\rangle_i$ and $|e(s)\rangle_i$ yields the computational basis states $|\uparrow(s)\rangle_i$ and $|\downarrow(s)\rangle_i$ given by the eigenvectors of φ_i in the subspace. These eigenvectors are given by

$$\frac{|g(s)\rangle_i + |e(s)\rangle_i}{\sqrt{2}}, \qquad \frac{|g(s)\rangle_i - |e(s)\rangle_i}{\sqrt{2}}, \tag{4.23}$$

where the state with the lower energy is defined as $|\downarrow(s)\rangle_i$ and the state with the higher energy is defined as $|\uparrow(s)\rangle_i$. In particular, the eigenvalues are given by $\pm I_p(s)/(2e\widetilde{E}_L)$, where e denotes the electron charge and $I_p(s)$ the persistent current. Thus, the projection

of the operator $\widetilde{E}_L \varphi_i$ onto the subspace is, in the $\{|\uparrow(s)\rangle_i, |\downarrow(s)\rangle_i\}$ -basis, represented by the Pauli-z operator $\sigma_i^z I_p(s)/(2e)$. The matrix which is diagonal in the $\{|g(s)\rangle_i, |e(s)\rangle_i\}$ -basis, is represented in the $\{|\uparrow(s)\rangle_i, |\downarrow(s)\rangle_i\}$ -basis by $-\Delta(s)\sigma_i^x/2$, where σ_i^x is the Pauli-x operator, and $\Delta(s) = E_e(s) - E_g(s)$ the energy difference between the ground state $|g(s)\rangle_i$ and the first excited state $|e(s)\rangle_i$. Thus, writing the Hamiltonian (corresponding to the qubits) in the computational basis yields

$$H_{\text{eff,sub}} \approx -\frac{\Delta(s)}{2} (\sigma_1^x + \sigma_2^x) - \frac{I_p(s)}{2e} (\varphi_1^x(s)\sigma_1^z + \varphi_2^x(s)\sigma_2^z) + \frac{E_L^2}{\widetilde{E}_L^2} \frac{M^2 I_p^2(s)}{L_{\text{eff}}} \frac{\beta_{\text{eff}}}{(1 + \beta_{\text{eff}})} \sigma_1^z \sigma_2^z - \frac{E_L}{\widetilde{E}_L} \frac{I_p(s)M^2}{2e(L + L_{\text{CJJ}}/4)L_{\text{eff}}} \frac{\beta_{\text{eff}}}{(1 + \beta_{\text{eff}})} (\varphi_1^x(s)\sigma_2^z + \varphi_2^x(s)\sigma_1^z).$$
(4.24)

The term $E_L^2 \beta_{\text{eff}} / (\widetilde{E}_L^2 (1 + \beta_{\text{eff}}))$ is a strictly monotonically decreasing function in $\varphi_{\text{CJJ},0}^x$ for $\varphi_{\text{CJJ},0}^x \in [0, 3\pi/2]$ (see Appendix B.2). Thus, for $\varphi_{\text{CJJ},0}^x = 0$, it reaches its maximum

$$\gamma = \max_{\varphi_{\text{CJJ},0}^x} \frac{E_L^2}{\widetilde{E}_L^2} \frac{\beta_{\text{eff}}}{(1+\beta_{\text{eff}})} = \frac{\beta}{1+\beta} \frac{1}{\left(1 + \frac{M^2}{(L+L_{\text{CJJ}}/4)L_{\text{eff}}} \frac{\beta}{1+\beta}\right)^2}.$$
 (4.25)

Obviously, its infimum is smaller than $-\gamma$. Thus, we can find for each $\varphi_{\text{CLL},0}^x$ with

$$-\gamma \le \frac{E_L^2}{\widetilde{E}_L^2} \frac{\beta_{\text{eff}}}{(1+\beta_{\text{eff}})} \le \gamma \tag{4.26}$$

a unique $J \in [-1, 1]$ such that

$$\frac{E_L^2}{\widetilde{E}_L^2} \frac{\beta_{\text{eff}}}{(1+\beta_{\text{eff}})} = -J\gamma. \tag{4.27}$$

Inserting Eq. (4.27) into Eq. (4.24) yields

$$H_{\text{eff,sub}} \approx -\frac{\Delta(s)}{2} (\sigma_1^x + \sigma_2^x) - \frac{I_p(s)}{2e} (\varphi_1^x(s)\sigma_1^z + \varphi_2^x(s)\sigma_2^z) - \frac{J\gamma M^2 I_p^2(s)}{L_{\text{eff}}} \sigma_1^z \sigma_2^z + \frac{\widetilde{E}_L}{E_L} \frac{J\gamma I_p(s)M^2}{2e(L + L_{\text{CJJ}}/4)L_{\text{eff}}} (\varphi_1^x(s)\sigma_2^z + \varphi_2^x(s)\sigma_1^z).$$
(4.28)

By choosing

$$\varphi_i^x(s) = h_i \frac{2eI_p(s)M^2\gamma}{L_{\text{eff}}},\tag{4.29}$$

we can achieve that the terms proportional to $h_i \sigma_i^z$ and $J \sigma_1^z \sigma_2^z$ have the same prefactor:

$$H_{\text{eff,sub}} \approx -\frac{\Delta(s)}{2} (\sigma_1^x + \sigma_2^x) - \frac{I_p^2(s) M^2 \gamma}{L_{\text{eff}}} (h_1 \sigma_1^z + h_2 \sigma_2^z + J \sigma_1^z \sigma_2^z)$$

$$+ \frac{\tilde{E}_L}{E_L} \frac{J \gamma^2 I_p^2(s) M^4}{(L + L_{\text{CJJ}}/4) L_{\text{eff}}^2} (h_1 \sigma_2^z + h_2 \sigma_1^z).$$
(4.30)

Identifying

$$A(s) = \frac{\Delta(s)}{2},\tag{4.31a}$$

$$B(s) = \frac{\gamma M^2 I_p^2(s)}{L_{\text{eff}}},$$
 (4.31b)

the effective Hamiltonian in the subspace can be written in the form

$$H_{\text{eff,sub}} \approx -A(s)(\sigma_1^x + \sigma_2^x) - B(s)(h_1\sigma_1^z + h_2\sigma_2^z + J\sigma_1^z\sigma_2^z) + B(s)\frac{\tilde{E}_L}{E_L} \frac{\gamma M^2}{(L + L_{\text{CJJ}}/4)L_{\text{eff}}} J(h_1\sigma_2^z + h_2\sigma_1^z),$$
(4.32)

which is, up to the last term, the annealing Hamiltonian Eq. (2.8) discussed in Chapter 2. The last term has only a small contribution since $L, L_{\text{eff}} \gg M$. It represents a certain kind of crosstalk between the qubits and the external fluxes controlling the other qubit [Alb+15b; DWa19], i.e., qubit 1 is affected by the external flux φ_2^x (h_2) which controls qubit 2 and vice versa.

The mapping to the qubit model including the derivation of the function for the external flux φ_i^x (Eq. (4.29)) and the conditional equation for the external flux $\varphi_{\text{CJJ},0}^x$ (Eq. (4.27)) is also discussed in [Wil+20].

Chapter 5

Simulations of quantum annealing with SQUIDs

This chapter deals with the implementation and the results of the simulation of the system discussed in Section 4.2. We start with the description of the discretization of the Hamiltonian in two different bases for a single SQUID before we discuss the system of two coupled SQUIDs with and without the tunable coupler. Apart from the decompositions of the Hamiltonians, we also look at the verification of the product-formula implementation and the determination of the values for the discretization parameters in space and time. In addition, we outline a few procedures which we use to obtain and analyze the results which are discussed subsequently. Finally, we compare our simulation results to results obtained with the D-Wave 2000Q quantum annealer.

5.1 Discretization of the Hamiltonian

5.1.1 Coordinate basis

First, we start with the discussion of a single SQUID corresponding to a single qubit. For this purpose, we look at Eq. (4.8). A majority of the terms in the Hamiltonian are diagonal in the variables φ and φ_{CJJ} . The only non-diagonal terms are the derivatives. Thus, the coordinate basis $\{|\varphi_{\text{CJJ}},\varphi\rangle \mid \varphi_{\text{CJJ}},\varphi \in \mathbb{R}\}$ is a reasonable choice of basis. For the simulation, we have to discretize the variables. Hence, the basis states are given by

$$\{|\varphi_{\mathrm{CJJ}}\,\varphi\rangle\,|\,\varphi_{\mathrm{CJJ}}\in\{\varphi_{\mathrm{CJJ}}^{(0)},\ldots,\varphi_{\mathrm{CJJ}}^{(\mathcal{M}-1)}\},\varphi\in\{\varphi^{(0)},\ldots,\varphi^{(\mathcal{N}-1)}\}\},$$

where $\varphi_{\text{CJJ}}^{(m)} = \varphi_{\text{CJJ}}^{\text{min}} + m\Delta\varphi_{\text{CJJ}}$ and $\varphi^{(n)} = \varphi^{\text{min}} + n\Delta\varphi$ with φ^{min} , $\varphi_{\text{CJJ}}^{\text{min}}$, $\Delta\varphi$, $\Delta\varphi_{\text{CJJ}}$, \mathcal{N} and \mathcal{M} parameters that need to be determined in such a way that the discretization effects are minimized while keeping memory requirements and computation time within reasonable bounds. In this basis, three of the five terms of the Hamiltonian given in Eq. (4.8) are diagonal. The only non-diagonal terms are the derivatives $-E_C\partial_{\varphi}^2$ and $-E_{C_{\text{CJJ}}}\partial_{\varphi_{\text{CJJ}}}^2$. We have to discretize the derivatives, which we do by applying (central) finite differences to the wave function $\Psi(\varphi)$

$$\frac{\partial}{\partial \varphi} \Psi(\varphi) \approx \frac{\Psi(\varphi + \Delta \varphi/2) - \Psi(\varphi - \Delta \varphi/2)}{\Delta \varphi},\tag{5.1}$$

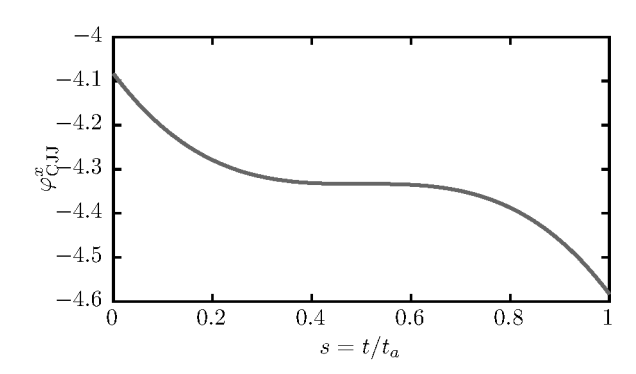


Figure 5.1: The external flux φ_{CJJ}^x as a function of the annealing fraction $s = t/t_a$ as it is used for the first series of simulation runs.

$$\frac{\partial^2}{\partial \varphi^2} \Psi(\varphi) \approx \frac{\Psi(\varphi + \Delta \varphi) - 2\Psi(\varphi) + \Psi(\varphi - \Delta \varphi)}{\Delta \varphi^2}.$$
 (5.2)

Then, in the discretized basis, the matrix elements of the derivative can be written as

$$\langle \varphi | \frac{\partial^2}{\partial \varphi^2} | \varphi' \rangle = -\frac{1}{\Delta \varphi^2} \left(2\delta_{\varphi, \varphi'} - \delta_{\varphi, \varphi' + \Delta \varphi} - \delta_{\varphi, \varphi' - \Delta \varphi} \right), \tag{5.3}$$

and accordingly for φ_{CJJ} , yielding the matrix elements of the Hamiltonian in the coordinate basis

$$\langle \varphi'_{\text{CJJ}} \varphi' | H_{\text{SQUID}} | \varphi_{\text{CJJ}} \varphi \rangle = \frac{E_C}{\Delta \varphi^2} \left(2\delta_{\varphi,\varphi'} - \delta_{\varphi,\varphi'+\Delta\varphi} - \delta_{\varphi,\varphi'-\Delta\varphi} \right) \delta_{\varphi_{\text{CJJ}},\varphi'_{\text{CJJ}}}$$

$$+ \left(E_L \frac{(\varphi - \varphi^x(s))^2}{2} + E_{L_{\text{CJJ}}} \frac{(\varphi_{\text{CJJ}} - \varphi^x_{\text{CJJ}}(s))^2}{2} - E_J \cos(\varphi) \cos\left(\frac{\varphi_{\text{CJJ}}}{2}\right) \right) \delta_{\varphi,\varphi'} \delta_{\varphi_{\text{CJJ}},\varphi'_{\text{CJJ}}}$$

$$+ \frac{E_{C_{\text{CJJ}}}}{\Delta \varphi^2_{\text{CJJ}}} \left(2\delta_{\varphi_{\text{CJJ}},\varphi'_{\text{CJJ}}} - \delta_{\varphi_{\text{CJJ}},\varphi'_{\text{CJJ}}} - \delta_{\varphi_{\text{CJJ}},\varphi'_{\text{CJJ}}} - \delta_{\varphi_{\text{CJJ}},\varphi'_{\text{CJJ}}} \right) \delta_{\varphi,\varphi'}.$$

$$(5.4)$$

First, we use the SQUID parameters listed in the supplementary material of Ref. [Boi+16]:

$$E_C = 2\pi \times 0.67 \,\text{GHz}, \qquad E_{C_{CH}} = 2\pi \times 1.35 \,\text{GHz}, \qquad (5.5a)$$

$$E_L = 2\pi \times 537 \,\text{GHz}, \qquad E_{L_{\text{CII}}} = 2\pi \times 11680 \,\text{GHz}, \qquad (5.5b)$$

$$E_C = 2\pi \times 0.67 \,\text{GHz},$$
 $E_{C_{\text{CJJ}}} = 2\pi \times 1.35 \,\text{GHz},$ (5.5a)
 $E_L = 2\pi \times 537 \,\text{GHz},$ $E_{L_{\text{CJJ}}} = 2\pi \times 11680 \,\text{GHz},$ (5.5b)
 $E_J = 2\pi \times 1071 \,\text{GHz},$ $\varphi^x(s) = (4.11s + 1.21) \times h \times 10^{-3},$ (5.5c)

and the function for $\varphi_{\text{CJJ}}^{x}(s)$ shown in Fig. 5.1. See Appendix B.3 for the conversion between energy in GHz and other quantities such as capacitance, inductance and current in SI units. The time evolution of the state vector is then computed by using the Suzuki-Trotter product-formula algorithm (see Chapter 3). The decomposition of H_{SQUID} in the coordinate basis used for the algorithm is given by

$$H_{\text{SQUID}} = \mathbf{D} + \mathbb{I}_{\mathcal{M}} \otimes \mathbf{A} + \mathbf{B} \otimes \mathbb{I}_{\mathcal{N}}, \tag{5.6}$$

where $\mathbb{I}_{\mathcal{N}}$ ($\mathbb{I}_{\mathcal{M}}$) is the \mathcal{N} - (\mathcal{M} -) dimensional identity matrix and

$$\mathbf{D} = \begin{pmatrix} d(\varphi_{\text{CJJ}}^{(0)}, \varphi^{(0)}) & 0 & \cdots & 0 \\ 0 & d(\varphi_{\text{CJJ}}^{(0)}, \varphi^{(1)}) & & & \\ \vdots & & \ddots & & \\ 0 & & d(\varphi_{\text{CJI}}^{(\mathcal{M}-1)}, \varphi^{(\mathcal{N}-1)}) \end{pmatrix},$$
(5.7a)

$$d(\varphi_{\text{CJJ}}^{(m)}, \varphi^{(n)}) = \frac{2E_C}{\Delta \varphi^2} + \frac{2E_{C_{\text{CJJ}}}}{\Delta \varphi_{\text{CJJ}}^2} - E_J \cos(\varphi^{(n)}) \cos\left(\frac{\varphi_{\text{CJJ}}^{(m)}}{2}\right) + E_L \frac{\left(\varphi^{(n)} - \varphi^x(s)\right)^2}{2} + E_{L_{\text{CJJ}}} \frac{\left(\varphi_{\text{CJJ}}^{(m)} - \varphi^x_{\text{CJJ}}(s)\right)^2}{2},$$
(5.7b)

$$\mathbf{A} = \frac{E_C}{\Delta \varphi^2} \begin{pmatrix} 0 & 1 & & & \\ 1 & 0 & 1 & & & \\ & 1 & \ddots & \ddots & & \\ & & \ddots & 0 & 1 \\ & & & 1 & 0 \end{pmatrix}, \tag{5.7c}$$

$$\mathbf{B} = \frac{E_{C_{\text{CJJ}}}}{\Delta \varphi_{\text{CJJ}}^2} \begin{pmatrix} 0 & 1 & & & \\ 1 & 0 & 1 & & & \\ & 1 & \ddots & \ddots & & \\ & & \ddots & 0 & 1 \\ & & & 1 & 0 \end{pmatrix}.$$
 (5.7d)

With the decomposition Eqs. (5.7a)-(5.7d), the product-formula algorithm is implemented according to the method outlined in Section 3.2.

The state vector

$$|\psi\rangle = \int_{-\infty}^{\infty} d\varphi_{\text{CJJ}} \int_{-\infty}^{\infty} d\varphi \, \psi(\varphi_{\text{CJJ}}, \varphi) |\varphi_{\text{CJJ}} \, \varphi\rangle$$
 (5.8)

is given in its discretized form by

$$|\psi\rangle = \sum_{m=0}^{\mathcal{M}-1} \sum_{n=0}^{\mathcal{N}-1} \psi_{\varphi_{\text{CJJ}}^{(m)}, \varphi^{(n)}} |\varphi_{\text{CJJ}}^{(m)} \varphi^{(n)}\rangle, \tag{5.9}$$

where the coefficients $\psi_{\varphi_{\text{CJJ}}^{(m)}, \varphi^{(n)}}$ are stored as an array of complex double precision numbers.

For the verification of the algorithm, the scaling of the local error as a function of the size of the time step, as discussed in Section 3.3, is investigated. Fig. 5.2 shows the norm of the difference between the state vector obtained with the product-formula algorithm $(\psi_{\text{PF}}(\tau))$ and the state vector obtained by (numerical) exact diagonalization $(\psi_{\text{exact}}(\tau))$ by using the Linear Algebra PACKage LAPACK. The norm is expected to scale with τ^{k+1} where k denotes the order of the product-formula algorithm (see Section 3.3). The fitted exponents agree very well with the expected exponents. Thus, we infer that the likelihood for mistakes in the implementation is very low.

While for the verification of the implementation the parameters φ^{\min} , φ^{\min}_{CJJ} , $\Delta\varphi$, $\Delta\varphi_{CJJ}$ can be chosen more or less arbitrarily but reasonably (\mathcal{N} and \mathcal{M} should be rather small to allow for the comparison with the exact diagonalization), we now have to choose these parameters in such a way that they do not introduce discretization errors (i.e., the result

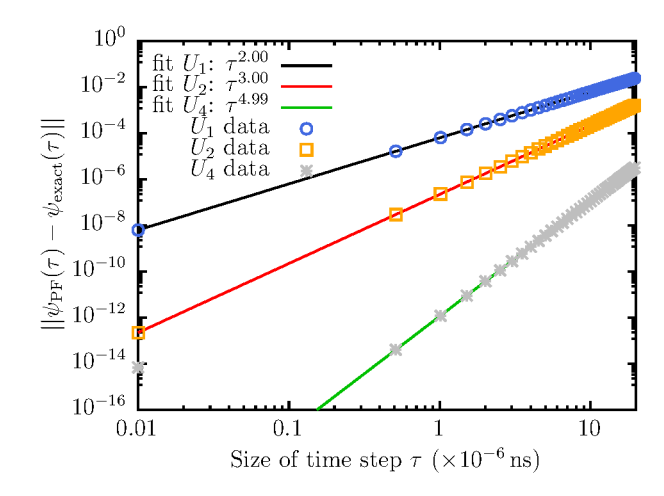


Figure 5.2: Scaling of the error due to the time step discretization in the product-formula algorithm for U_1 (circles), U_2 (squares) and U_4 (asterisks). U_k is expected to scale with τ^{k+1} (see Section 3.3). The fitted functions $x\tau^y$ (solid lines) with fitting parameters x and y show very good agreement with the expectation.

should not depend on the choice of the parameters). In order to find good values, we try different combinations of values for the parameters and check if the results stabilize, i.e., after passing a threshold, changing the parameters does not change the result. The results for various parameter values are shown in Fig. 5.3 and for different values of the time step τ in Fig. 5.4.

For the parameters φ^{\min} , $\Delta\varphi_{\text{CJJ}}$ and $\varphi^{\min}_{\text{CJJ}}$ it is quite clear how to choose the values as visible deviations vanish when the values are small enough and for smaller values the curves are perfectly on top of each other. For $\Delta\varphi$, all tested curves are very close, but they do not match as perfectly as for the other parameters. To avoid that the state vector becomes too large and that too small values of $\Delta\varphi$ lead to the need of smaller and smaller time steps τ , we choose $\Delta\varphi = 0.080$ since the green and blue curves are sufficiently close. When fixing the values for φ^{\min} , $\varphi^{\min}_{\text{CJJ}}$, $\Delta\varphi$ and $\Delta\varphi_{\text{CJJ}}$, the values for $\mathcal N$ and $\mathcal M$ are also fixed as we chose symmetric intervals around 0 (for φ) and around -4.33 (for φ_{CJJ}). As the yellow, green and blue curves in Fig. 5.4 are on top of each other, the time step is chosen to be $\tau = 10^{-4}$ ns.

Looking at the marginal distributions

$$||\psi(\varphi^{(n)})||^2 = \int_{-\infty}^{\infty} ||\psi(\varphi_{\text{CJJ}}, \varphi^{(n)})||^2 \, \mathrm{d}\varphi_{\text{CJJ}} \approx \sum_{m=0}^{\mathcal{M}-1} ||\psi_{\varphi_{\text{CJJ}}^{(m)}, \varphi^{(n)}}||^2$$
 (5.10a)

$$||\psi(\varphi_{\text{CJJ}}^{(m)})||^2 = \int_{-\infty}^{\infty} ||\psi(\varphi_{\text{CJJ}}^{(m)}, \varphi)||^2 \, \mathrm{d}\varphi \approx \sum_{n=0}^{N-1} ||\psi_{\varphi_{\text{CJJ}}^{(m)}, \varphi^{(n)}}||^2, \tag{5.10b}$$

plotted in Fig. 5.5 for s=0 (begin of the annealing process) and s=1 (end of the annealing process) for two different sets of parameter values, we find that the marginal distribution $||\psi(\varphi^{(n)})||^2$ is the same for both sets of parameter values, but the marginal distribution $||\psi(\varphi^{(n)}_{\text{CJJ}})||^2$ shows some small deviations. This is reasonable as we only used the expectation value $\langle \psi | \varphi | \psi \rangle$ as an indicator for the convergence (since it is the degree of freedom defining the qubit). To be sure that these differences do not introduce some unwanted effects in further simulations, we would need to reduce $\varphi^{\min}_{\text{CJJ}}$ and $\Delta \varphi_{\text{CJJ}}$ even further. This basis however, leads to quite large state vectors for a single qubit already with $\mathcal{M}=11$. Therefore, we investigate the discretization in an alternative basis, given

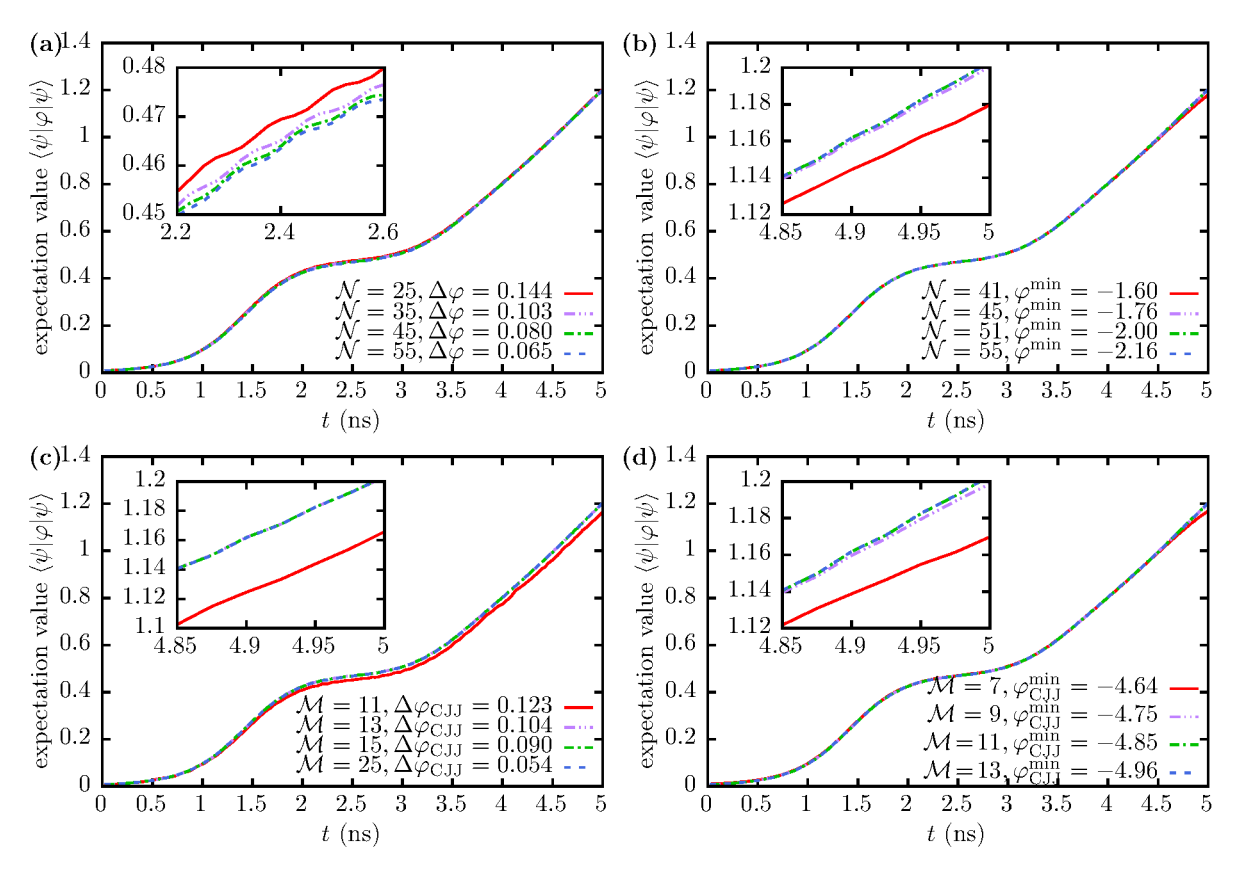


Figure 5.3: The expectation value $\langle \psi | \varphi | \psi \rangle$ used to test the dependency of the simulation results on the parameter values is plotted for (a) different values of $\Delta \varphi$ and \mathcal{N} , and fixed $\varphi^{\min} = -1.76$, $\mathcal{M} = 11$, $\Delta \varphi_{\text{CJJ}} = 0.104$ and $\varphi^{\min}_{\text{CJJ}} = -4.85$ (b) different values of φ^{\min} and \mathcal{N} , and fixed $\Delta \varphi = 0.080$, $\mathcal{M} = 11$, $\Delta \varphi_{\text{CJJ}} = 0.104$ and $\varphi^{\min}_{\text{CJJ}} = -4.85$ (c) different values of $\Delta \varphi_{\text{CJJ}}$ and \mathcal{M} , and fixed $\varphi^{\min}_{\text{CJJ}} = -4.96$, $\mathcal{N} = 51$, $\Delta \varphi = 0.080$ and $\varphi^{\min} = -2.00$ (d) different values of $\varphi^{\min}_{\text{CJJ}}$ and \mathcal{M} , and fixed $\Delta \varphi_{\text{CJJ}} = 0.104$, $\mathcal{N} = 51$, $\Delta \varphi = 0.080$ and $\varphi^{\min} = -2.00$. In all panels $\tau = 10^{-5}\,\text{ns}$. The insets show a zoom into the indicated region. We find that $\Delta \varphi = 0.080$, $\mathcal{N} = 51$, $\varphi^{\min} = -2.0$, $\Delta \varphi_{\text{CJJ}} = 0.104$, $\mathcal{M} = 11$ and $\varphi^{\min}_{\text{CJJ}} = -4.85$ is a suitable choice for the parameters.

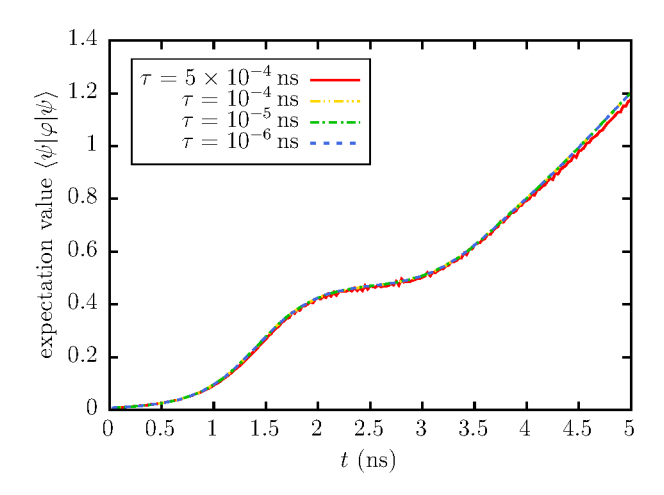


Figure 5.4: Expectation value $\langle \psi | \varphi | \psi \rangle$ used to check the dependency of the simulation results on the size of the time step τ . Shown are results for different values of τ with fixed $\Delta \varphi = 0.08$, $\mathcal{N} = 51$, $\varphi^{\min} = -2.00$, $\Delta \varphi_{\text{CJJ}} = 0.104$, $\mathcal{M} = 11$ and $\varphi_{\text{CJJ}}^{\min} = -4.85$. The curve for $\tau = 5 \times 10^{-4}\,\text{ns}$ (red) slightly deviates from the others. The other three curves are perfectly on top of each other.

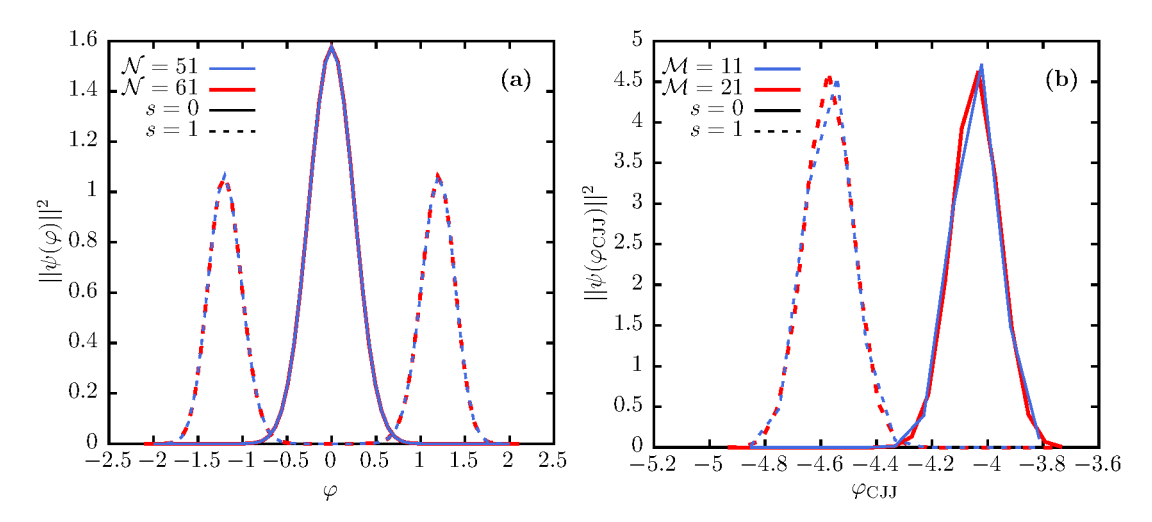


Figure 5.5: The marginal distributions (a) $||\psi(\varphi)||^2$ and (b) $||\psi(\varphi_{\text{CJJ}})||^2$ in coordinate space for the parameter values picked previously (blue) and additionally for (a) $\varphi^{\text{min}} = -2.1$, $\Delta \varphi = 0.070$ (red) and (b) $\varphi_{\text{CJJ}}^{\text{min}} = -4.93$, $\Delta \varphi_{\text{CJJ}} = 0.060$ (red). While for $||\psi(\varphi)||^2$ there is no visible difference, $||\psi(\varphi_{\text{CJJ}})||^2$ still shows some deviations.

by the eigenstates of the harmonic oscillator (number states) in which the Hamiltonian is diagonal up to the coupling term $-E_J \cos(\varphi) \cos(\varphi_{\text{CJJ}}/2)$.

5.1.2 Basis of number states

The Hamiltonian H_{SQUID} given by Eq. (4.8) can also be seen as two harmonic oscillators in the variables φ and φ_{CJJ} , respectively, with a coupling term $-E_J \cos(\varphi) \cos(\varphi_{\text{CJJ}}/2)$. Thus, using the number states $\{|m\,n\rangle\,|\,m\in\{0,\ldots,\mathcal{M}-1\},n\in\{0,\ldots,\mathcal{N}-1\}\}$ for the discretization also seems to be a reasonable choice. The matrix elements of the Hamiltonian are then given by

$$\langle m' n' | H_{\text{SQUID}} | m n \rangle = \left(\sqrt{2E_C E_L} \left(n + \frac{1}{2} \right) + \sqrt{2E_{C_{\text{CJJ}}} E_{L_{\text{CJJ}}}} \left(m + \frac{1}{2} \right) \right) \delta_{m,m'} \delta_{n,n'} - E_J \langle n' | \cos(\varphi) | n \rangle \langle m' | \cos\left(\frac{\varphi_{\text{CJJ}}}{2}\right) | m \rangle.$$
 (5.11)

The matrix elements of the basis transformation

$$\langle \varphi | n \rangle = \langle n | \varphi \rangle = \frac{1}{\sqrt{2^n n!}} \left(\frac{\xi}{\pi} \right)^{\frac{1}{4}} e^{-\frac{\xi}{2} (\varphi - \varphi^x(s))^2} \mathcal{H}_n \left(\sqrt{\xi} \left(\varphi - \varphi^x(s) \right) \right), \tag{5.12a}$$

$$\xi = \sqrt{\frac{E_L}{2E_C}},\tag{5.12b}$$

and

$$\langle \varphi_{\text{CJJ}} | m \rangle = \langle m | \varphi_{\text{CJJ}} \rangle = \frac{1}{\sqrt{2^m m!}} \left(\frac{\eta}{\pi} \right)^{\frac{1}{4}} e^{-\frac{\eta}{2} \left(\varphi_{\text{CJJ}} - \varphi_{\text{CJJ}}^x(s) \right)^2} \mathcal{H}_m(\sqrt{\eta} \left(\varphi_{\text{CJJ}} - \varphi_{\text{CJJ}}^x(s) \right)),$$
(5.12c)

$$\eta = \sqrt{\frac{E_{L_{\rm CJJ}}}{2E_{C_{\rm CJJ}}}},\tag{5.12d}$$

where $\mathcal{H}_n(x)$ denote the Hermite polynomials, explicitly depend on time (annealing fraction s) in such a way that the number states are always centered at the value of the external flux $\varphi^x(s)$ or $\varphi^x_{\text{CJJ}}(s)$. We denote this time-dependent basis transformation by $\Upsilon(t)$. Since $\Upsilon(t)$ is time-dependent, we have to add an additional term to the Hamiltonian (cf. Eq. (4.16c))

$$H_{\text{SQUID}} \to \Upsilon(t) H_{\text{SQUID}} \Upsilon^{\dagger}(t) - i \Upsilon(t) \left(\frac{\partial}{\partial t} \Upsilon^{\dagger}(t) \right).$$
 (5.13)

Since the transformations are basically the same for both the φ - and φ_{CJJ} -space, we present the calculation for φ only. For a single matrix element, we have

$$-i\left(\Upsilon_{\varphi}(t)\frac{\partial}{\partial t}\Upsilon_{\varphi}^{\dagger}(t)\right)_{nn'}$$

$$=-i\sqrt{\frac{\xi}{\pi}}\int d\varphi \frac{e^{-\frac{\xi}{2}(\varphi-\varphi^{x}(s))^{2}}}{\sqrt{2^{n+n'}n!n'!}}\mathcal{H}_{n}(\sqrt{\xi}(\varphi-\varphi^{x}(s)))\frac{\partial}{\partial t}\left(e^{-\frac{\xi}{2}(\varphi-\varphi^{x}(s))^{2}}\mathcal{H}_{n'}(\sqrt{\xi}(\varphi-\varphi^{x}(s)))\right)$$

$$=-i\sqrt{\frac{\xi}{2}}\frac{\partial\varphi^{x}(s)}{\partial s}\frac{\partial s(t)}{\partial t}\left(\sqrt{n}\,\delta_{n,n'+1}-\sqrt{n+1}\,\delta_{n,n'-1}\right),\tag{5.14}$$

which yields the matrices

$$-i\Upsilon_{\varphi}(t)\frac{\partial}{\partial t}\Upsilon_{\varphi}^{\dagger}(t) = -i\sqrt{\frac{\xi}{2}}\frac{\partial \varphi^{x}(s)}{\partial s}\frac{\partial s(t)}{\partial t}\left(a^{\dagger} - a\right)$$
 (5.15a)

$$-i\Upsilon_{\varphi_{\text{CJJ}}}(t)\frac{\partial}{\partial t}\Upsilon_{\varphi_{\text{CJJ}}}^{\dagger}(t) = -i\sqrt{\frac{\eta}{2}}\frac{\partial \varphi_{\text{CJJ}}^{x}(s)}{\partial s}\frac{\partial s(t)}{\partial t}\left(b^{\dagger} - b\right),\tag{5.15b}$$

where a^{\dagger} (a) and b^{\dagger} (b) denote the creation (annihilation) operators for the harmonic oscillator in φ - and φ_{CJJ} -space, respectively. Due to the time dependence, the matrix elements $\langle n'|\cos(\varphi)|n\rangle$ and $\langle m'|\cos(\varphi_{\text{CJJ}}/2)|m\rangle$ need to be re-computed at least every few time steps, rendering the use of large bases infeasible (in fact Eqs. (5.15a) and (5.15b) also depend on time, but they represent sparse matrices, and thus, they do not cause a problem). For the parameters listed in Eqs. (5.5a) - (5.5c), $E_{L_{\text{CJJ}}} \gg E_J$. Therefore, the coupling term can be seen as a perturbation to the harmonic potential in the variable φ_{CJJ} . However, $E_L < E_J$ which leads to the presumption that the number states are not very well suited to represent the state vector in the variable φ . This is also confirmed by the results shown in Fig. 5.6. The plot shows the marginal distributions $||\psi(n)||^2$ and $||\psi(m)||^2$ at the beginning of the annealing process (s=0, red) and at the end (s=1,blue). While $||\psi(m)||^2$ is peaked at small $m \leq 2$, i.e., the higher states (almost) do not contribute and can thus be safely neglected, the distribution $||\psi(n)||^2$, which is also centered at small n < 10 in the beginning, dissolves during the annealing process. As a consequence, at the end of the annealing process, all simulated number states have a considerable contribution. Possibly, even more states are necessary. However, the simulation with 21 number states already takes longer than the one with 51 states in the coordinate basis. Therefore, there is no advantage in using the number states to represent φ , and we only use the number states to represent φ_{CJJ} and keep the coordinate basis to represent φ . Then, the discretized Hamiltonian is a mixture of Eq. (5.4), Eq. (5.11) and Eq. (5.15b):

$$\langle m' \varphi^{(n')} | \widetilde{H}_{\text{SQUID}} | m \varphi^{(n)} \rangle = \langle m' \varphi^{(n')} | H_{\text{SQUID}} - i \Upsilon_{\varphi_{\text{CJJ}}}(t) \left(\frac{\partial}{\partial t} \Upsilon_{\varphi_{\text{CJJ}}}^{\dagger}(t) \right) | m \varphi^{(n)} \rangle$$

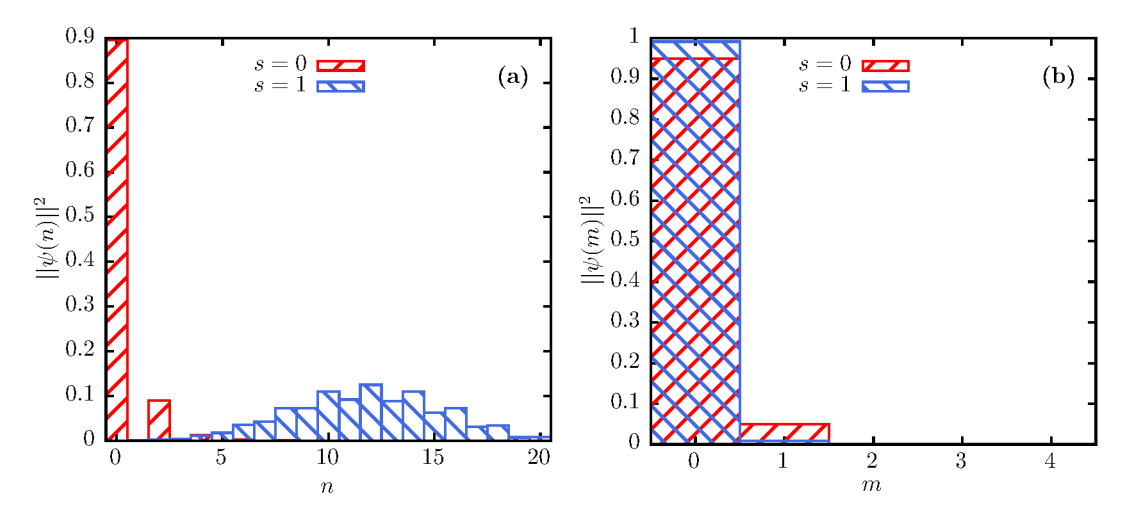


Figure 5.6: The marginal distributions (a) $||\psi(n)||^2$ and (b) $||\psi(m)||^2$ using the number states as basis. Boxes with stripes from lower left to upper right (red) show the distribution at s=0 and boxes with stripes from upper left to lower right (blue) show the distributions at s=1. For $||\psi(m)||^2$ only the first two states have substantial contributions, the contribution of the third state is already very small and the other contributions are not visible anymore. For $||\psi(n)||^2$, less than 10 number states are needed to represent the initial state, however, at s=1 even the 20th number state has a considerable contribution.

$$= -\underbrace{E_{J}\cos(\varphi^{(n)})\langle m'|\cos\left(\frac{\varphi_{\text{CJJ}}}{2}\right)|m\rangle}_{=:b(m',m,\varphi^{(n)})} \delta_{\varphi^{(n)},\varphi^{(n')}}$$

$$-\frac{i}{t_{a}}\sqrt{\frac{\eta}{2}}\frac{\partial\varphi_{\text{CJJ}}^{x}(s)}{\partial s}\left(\sqrt{m+1}\delta_{m'-1,m}-\sqrt{m}\delta_{m'+1,m}\right)\delta_{\varphi^{(n)},\varphi^{(n')}}$$

$$+\underbrace{\left(\frac{2E_{C}}{\Delta\varphi^{2}}+E_{L}\frac{\left(\varphi^{(n)}-\varphi^{x}(s)\right)^{2}}{2}+\sqrt{2E_{C_{\text{CJJ}}}E_{L_{\text{CJJ}}}}\left(m+\frac{1}{2}\right)\right)}_{=:a(\varphi^{(n)},m)}\delta_{\varphi^{(n)},\varphi^{(n')}}\delta_{m,m'}$$

$$-\frac{E_{C}}{\Delta\varphi^{2}}\left(\delta_{\varphi^{(n)},\varphi^{(n'+1)}}+\delta_{\varphi^{(n)},\varphi^{(n'-1)}}\right)\delta_{m,m'}. \tag{5.16}$$

The matrix for $\mathcal{M} = 3$ is given by

$$\widetilde{H}_{\text{SQUID}} = \begin{pmatrix} \mathbf{A}_0 & \mathbf{B}_{0,1} - i\mathbf{G}_{0,1} & \mathbf{B}_{0,2} \\ \hline \\ \mathbf{B}_{1,0} + i\mathbf{G}_{1,0} & \mathbf{A}_1 & \mathbf{B}_{1,2} - i\mathbf{G}_{1,2} \\ \hline \\ \mathbf{B}_{2,0} & \mathbf{B}_{2,1} + i\mathbf{G}_{2,1} & \mathbf{A}_2 \end{pmatrix}, (5.17)$$

where

$$\mathbf{A}_{m} = \begin{pmatrix} a'(\varphi^{(0)}, m) & -\frac{E_{C}}{\Delta \varphi^{2}} \\ -\frac{E_{C}}{\Delta \varphi^{2}} & a'(\varphi^{(1)}, m) & \ddots \\ & \ddots & \ddots & -\frac{E_{C}}{\Delta \varphi^{2}} \\ & -\frac{E_{C}}{\Delta \varphi^{2}} & a'(\varphi^{(N-1)}, m) \end{pmatrix}$$

$$= \begin{pmatrix} a'(\varphi^{(0)}, m) & & & \\ & \ddots & & \\ & & a'(\varphi^{(N-1)}, m) \end{pmatrix} - \underbrace{\frac{E_{C}}{\Delta \varphi^{2}} \begin{pmatrix} 0 & 1 & & \\ 1 & 0 & \ddots & & \\ & \ddots & \ddots & 1 & \\ & & 1 & 0 \end{pmatrix}}_{\mathbf{D}_{m}}, \qquad (5.18a)$$

$$a'(\varphi^{(n)}, m) = a(\varphi^{(n)}, m) - b(m, m, \varphi^{(n)}),$$
 (5.18b)

$$\mathbf{B}_{m',m} = \begin{pmatrix} b(m', m, \varphi^{(0)}) & & & & \\ & b(m', m, \varphi^{(1)}) & & & \\ & & \ddots & & \\ & & b(m', m, \varphi^{(N-1)}) \end{pmatrix},$$
(5.18c)

$$\mathbf{G}_{m',m} = \mathbf{G}_{m,m'} = -\frac{1}{t_a} \frac{\partial \varphi_{\mathrm{CJJ}}^x(s)}{\partial s} \sqrt{\frac{\eta \max(m',m)}{2}} \, \mathbb{I}_{\mathcal{N}}. \tag{5.18d}$$

Since

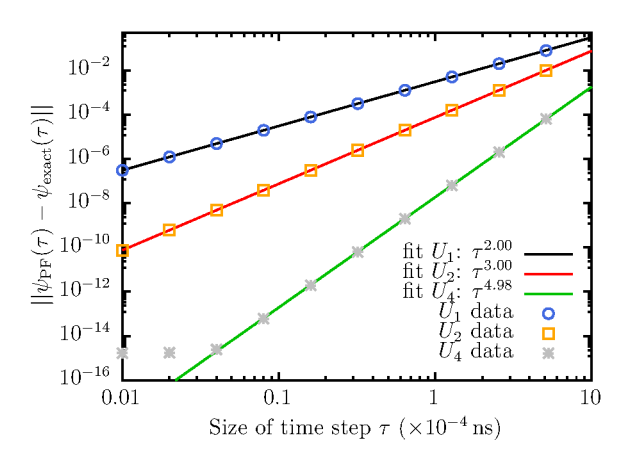
$$b(m', m, \varphi^{(n)}) = b(m, m', \varphi^{(n)})$$

$$= E_{J} \cos \left(\varphi^{(n)}\right) \int_{-\infty}^{\infty} \frac{e^{-\eta \left(\varphi_{\text{CJJ}} - \varphi_{\text{CJJ}}^{x}(s)\right)^{2}}}{2^{m+m'} m! m'!} \sqrt{\frac{\eta}{\pi}} \mathcal{H}_{m}\left(\sqrt{\eta} \left(\varphi_{\text{CJJ}} - \varphi_{\text{CJJ}}^{x}(s)\right)\right)$$

$$\times \mathcal{H}_{m'}\left(\sqrt{\eta} \left(\varphi_{\text{CJJ}} - \varphi_{\text{CJJ}}^{x}(s)\right)\right) \cos \left(\frac{\varphi_{\text{CJJ}}}{2}\right) d\varphi_{\text{CJJ}}, \quad (5.19)$$

we have $\mathbf{B}_{m',m} = \mathbf{B}_{m,m'}$ and we can choose the decomposition

$$\widetilde{H}_{\text{SQUID}} = \mathbf{D} - \mathbb{I}_{\mathcal{M}} \otimes \boldsymbol{\mu} + \begin{pmatrix} \begin{pmatrix} 0 & -i & 0 \\ i & 0 & 0 \\ 0 & 0 & 0 \end{pmatrix} \otimes \mathbf{G}_{0,1} + \begin{pmatrix} 0 & 1 & 0 \\ 1 & 0 & 0 \\ 0 & 0 & 0 \end{pmatrix} \otimes \mathbf{B}_{0,1} \end{pmatrix} \\
+ \begin{pmatrix} \begin{pmatrix} 0 & 0 & 0 \\ 0 & 0 & -i \\ 0 & i & 0 \end{pmatrix} \otimes \mathbf{G}_{1,2} + \begin{pmatrix} 0 & 0 & 0 \\ 0 & 0 & 1 \\ 0 & 1 & 0 \end{pmatrix} \otimes \mathbf{B}_{1,2} \end{pmatrix} + \begin{pmatrix} 0 & 0 & 1 \\ 0 & 0 & 0 \\ 1 & 0 & 0 \end{pmatrix} \otimes \mathbf{B}_{0,2} \quad (5.20)$$



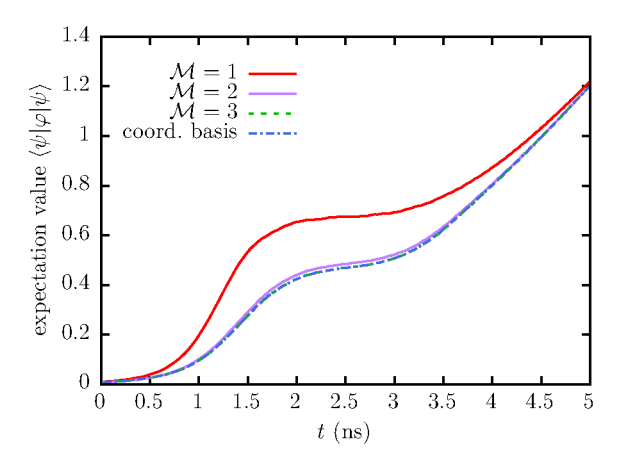


Figure 5.7: Local error caused by the approximation made in the product-formula algorithm as a function of the size of the time step τ for U_1 (circles), U_2 (squares) and U_4 (asterisks). As in Fig. 5.2, the data agree perfectly with the expectation ($U_k \propto \tau^{k+1}$, see Section 3.3). The solid lines are functions $x \cdot \tau^y$ fitted to the data with fitting parameters x and y.

Figure 5.8: The expectation value $\langle \psi | \varphi | \psi \rangle$ as a function of time t used to test the dependency of the simulation data on the dimension \mathcal{M} of the space corresponding to φ_{CJJ} . Parameters for the discretization in φ are $\Delta \varphi = 0.080$ and $\varphi^{\min} = -2.00$, the time step is $\tau = 10^{-5}$ ns. Data using $\mathcal{M} = 1, 2, 3$, and for comparison, using the coordinate basis in φ_{CJJ} with parameters $\varphi_{\text{CJJ}} = 0.054$ and $\varphi_{\text{CJJ}}^{\min} = -4.98$, is shown.

with

$$\mathbf{D} = \begin{pmatrix} 1 & & \\ & 0 & \\ & & 0 \end{pmatrix} \otimes \mathbf{D}_0 + \begin{pmatrix} 0 & & \\ & 1 & \\ & & 0 \end{pmatrix} \otimes \mathbf{D}_1 + \begin{pmatrix} 0 & & \\ & 0 & \\ & & 1 \end{pmatrix} \otimes \mathbf{D}_2$$
 (5.21)

for the product-formula algorithm. As discussed in the previous section and in Section 3.3, we look at the local error caused by the approximation made in the product-formula algorithm. The results are shown in Fig. 5.7 and indicate that the implementation is correct because the scaling with τ is as expected.

The next step is to verify that $\mathcal{M}=3$ is indeed sufficient to achieve the same results as with the simulation using the coordinate basis. To do this, we plot the data generated with $\mathcal{M}=3$ (additionally for $\mathcal{M}=1$ and $\mathcal{M}=2$) and compare them to the results obtained from the simulation using the coordinate basis. The plot is shown in Fig. 5.8. We find that for $\mathcal{M}=1$ and $\mathcal{M}=2$ there are indeed visible differences to the reference results obtained by using the coordinate basis. The curve for $\mathcal{M}=3$ is perfectly on top of the reference curve. Thus, we conclude that we only need three number states to represent the φ_{CJJ} -degree of freedom.

5.1.3 Two SQUIDs as qubits

As long as the coupling SQUID is not taken into account, the extension from a single SQUID to two (or in principle even more) SQUIDs is straightforward. The coupling term $E_M(\varphi_1 - \varphi_1^x)(\varphi_2 - \varphi_2^x)$ between the SQUIDs with the coupling energy E_M is diagonal in

the coordinate basis. Therefore, the matrix of the Hamiltonian for two SQUIDs is given by

$$H_2 = \widetilde{H}_{\text{SQUID},2} \otimes \mathbb{I}_{\mathcal{N} \cdot \mathcal{M}} + \mathbb{I}_{\mathcal{N} \cdot \mathcal{M}} \otimes \widetilde{H}_{\text{SQUID},1} + \mathbf{C}, \tag{5.22}$$

where

$$\mathbf{C} = E_M \begin{pmatrix} \left(\varphi_1^{(0)} - \varphi_1^x\right) \left(\varphi_2^{(0)} - \varphi_2^x\right) & \\ \left(\varphi_1^{(1)} - \varphi_1^x\right) \left(\varphi_2^{(0)} - \varphi_2^x\right) & \\ & & \ddots & \\ \left(\varphi_1^{(\mathcal{N}-1)} - \varphi_1^x\right) \left(\varphi_2^{(\mathcal{N}-1)} - \varphi_2^x\right) \end{pmatrix}$$

$$= E_{M} \cdot \mathbb{I}_{\mathcal{M}} \otimes \begin{pmatrix} \varphi_{2}^{(0)} - \varphi_{2}^{x} & & \\ & \ddots & \\ & & \varphi_{2}^{(\mathcal{N}-1)} - \varphi_{2}^{x} \end{pmatrix} \otimes \mathbb{I}_{\mathcal{M}} \otimes \begin{pmatrix} \varphi_{1}^{(0)} - \varphi_{1}^{x} & & \\ & & \ddots & \\ & & & \varphi_{1}^{(\mathcal{N}-1)} - \varphi_{1}^{x} \end{pmatrix}$$

$$(5.23)$$

is diagonal and can thus be included in the diagonal update. This leaves non-diagonal terms only in $H_{\text{SQUID},i}$ which were discussed in the previous section.

Two SQUIDs with an additional coupler

The extension to include an additional SQUID as coupler is not very different from the extension to more SQUIDs functioning as qubits. However, we have to take into account that the dependencies on the external fields for the coupler as well as the energies $E_{L_{\text{eff}}}$, E_{C_0} , E_{J_0} , $E_{L_{\text{CJJ},0}}$, and $E_{C_{\text{CJJ},0}}$ and the parameters for the discretization are different. Thus, we denote the coupler's discretization parameters by an index "0". Keeping this in mind, we can decompose the Hamiltonian

$$H_{\text{total}} = \mathbb{I}_{\mathcal{N}_0 \cdot \mathcal{M}_0} \otimes \left(\widetilde{H}_{\text{SQUID},2} \otimes \mathbb{I}_{\mathcal{N} \cdot \mathcal{M}} + \mathbb{I}_{\mathcal{N} \cdot \mathcal{M}} \otimes \widetilde{H}_{\text{SQUID},1} + \mathbf{C} \right)$$
$$+ \widetilde{H}_{\text{SQUID},0} \otimes \mathbb{I}_{(\mathcal{N} \cdot \mathcal{M})^2} + \mathbf{C}_{01} + \mathbf{C}_{02}, \tag{5.24}$$

where E_M in C is here replaced by $E_M = E_L M^2/((L + L_{CJJ}/4)L_{eff})$ and

Since the matrices C, C_{01} and C_{02} are diagonal, we can add them to the diagonal parts D of $H_{SOUID,i}$ and perform the update of all the diagonal matrices at once.

 •					
Parameter	Value (GHz)	Parameter	Value (GHz)	Parameter	Value (pH)
E_C	$0.931 \times 2\pi$	E_{C_0}	$1.435 \times 2\pi$	M	13.7
$E_{C_{\mathrm{CJJ}}}$	$21.17 \times 2\pi$	$E_{C_{\mathrm{CJJ,0}}}$	$33.98 \times 2\pi$		
E_L	$554 \times 2\pi$	E_{L_0}	$2494 \times 2\pi$		
$E_{L_{\mathrm{CJJ}}}$	$11680 \times 2\pi$	$E_{L_{\mathrm{CJJ,0}}}$	$56370 \times 2\pi$		
E_J	$1242 \times 2\pi$	E_{J_0}	$2980 \times 2\pi$		

Table 5.1: Parameter values of the D-Wave 2000Q processor provided by D-Wave Systems Inc.

-4					0.01
-4.05					0.009
-4.1				معمد	0.008
-4.15				. e e e e e	0.007
\bigcirc -4.2	****	-			0.006
$\begin{array}{c c} & -4.2 \\ \hline & -4.25 \\ \hline & -4.3 \\ \end{array}$					0.005
$\stackrel{\text{sO}}{\Rightarrow}$ -4.3			-		0.004
-4.35	معمد	••			0.003
-4.4					0.002
-4.45					0.001
−4.5 L		ı			<u></u> 0
0	0.2	0.4	0.6	0.8	1
			3		

Figure 5.9: The external fluxes $\varphi_{\text{CJJ}}^x(s)$ (blue) and $\varphi^x(s)$ (red) as a function of the dimensionless time $s = t/t_a$. The bright dash-dotted curve for $\varphi_{\text{CJJ}}^x(s)$ indicates a fitted polynomial of degree seven which is used to compute the values in the simulation.

For the implementation including the SQUID which functions as tunable coupler, D-Wave Systems Inc. provided the functions of the external fluxes $\varphi(s)^x$ and $\varphi_{\text{CJJ}}^x(s)$, and parameters of the D-Wave 2000Q processor [DWa19]. The parameters are listed in Table 5.1 and the functions of $\varphi^x(s)$ and $\varphi_{\text{CJJ}}^x(s)$ are plotted in Fig. 5.9. For use in the simulation, we fit a polynomial of degree seven to the data for $\varphi_{\text{CJJ}}^x(s)$. The fitted polynomial is shown by the dash-dotted, light-blue curve on top of the dark-blue data curve. To obtain a value for the external flux $\varphi_{\text{CJJ},0}^x$, which determines the effective coupling strength between the two SQUIDs 1 and 2, according to a given value of J, Eq. (4.27) has to be solved numerically for $\varphi_{\text{CJJ},0}^x$.

We can compute the annealing scheme for a single qubit using the method discussed in Section 5.2.1. Figure 5.10(a) shows the computed annealing scheme in comparison to the annealing scheme provided by D-Wave Systems Inc. We find that the annealing schemes do not match very well. The main reason seems to be a mismatch between the measured and the computed persistent currents which lead to mismatches in the annealing schemes and the external fluxes $\varphi^x(s)$ computed according to Eq. (4.29) and provided by D-Wave Systems Inc. (see also Fig. 5.10(b)). Since the expression for $\varphi^x(s)$ given by Eq. (4.29), which we use in the simulation, depends on the SQUID parameters through $I_p(s)$ and on the mutual inductance M, potential changes in these parameters also affect $\varphi^x(s)$. Adjusting a few of the parameters

$$E_C: 0.931 \times 2\pi \,\text{GHz} \to 0.745 \times 2\pi \,\text{GHz}$$
 (5.26a)

$$E_{L_{\text{CJJ}}}: 11680 \times 2\pi \,\text{GHz} \to 8680 \times 2\pi \,\text{GHz}$$
 (5.26b)

$$M: 13.7 \, \text{pH} \rightarrow 15.97 \, \text{pH}$$
 (5.26c)

produces an annealing scheme and external flux which match the data provided by D-

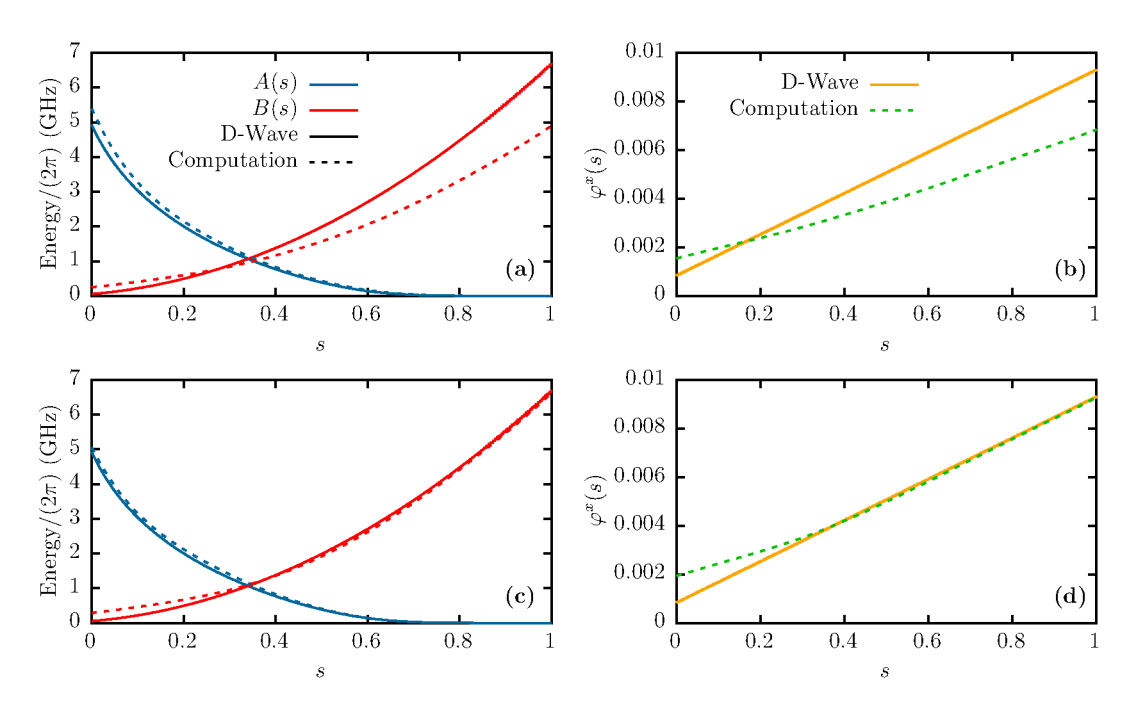


Figure 5.10: (a) Annealing scheme provided by D-Wave Systems Inc. (solid lines) and obtained from the simulation (dashed lines) for a single qubit by the procedure discussed in Section 5.1.2 with the parameters provided by D-Wave Systems Inc. and listed in Table 5.1. The external flux $\varphi^x(s)$ is computed according to Eq. (4.29). (b) The external flux $\varphi^x(s)$ provided by D-Wave Systems Inc. (solid line) and from the computation according to Eq. (4.29) (dashed line). The difference between the functions for $\varphi^x(s)$ and the difference in the functions B(s) in the annealing scheme are related. (c) Same as (a) but using the adjusted parameters Eqs. (5.26a) - (5.26c) in the simulation. (d) Same as (b) but using the adjusted parameters.

Wave Systems Inc. much better (see Fig. 5.10(c) and (d)). Although simulation data and data from D-Wave Systems Inc. match better now, the agreement is still not perfect as there is a difference for $s \lesssim 0.3$ in B(s) and $\varphi^x(s)$. At this point, we have two options. The first one is to keep the annealing scheme as it is, even though the match with the annealing scheme provided by D-Wave Systems Inc. is not perfect. The second option is to use the function for the external flux provided by D-Wave Systems Inc. which also improves the function B(s). However, in this case we would violate Eq. (4.29) which means that the prefactors for the single-qubit σ^z terms and the $\sigma_1^z \sigma_2^z$ coupling term would not be the same. Since we want to avoid this, we choose option one and keep the annealing scheme as shown in Fig. 5.10(c). We remark that the deviation from the original D-Wave annealing scheme is irrelevant for a comparison of the results of the simulation based on Eq. (4.10) to the results of the qubit-model simulation.

The next step is to check the implementation including the SQUID functioning as tunable coupler by investigating the scaling of the local error as discussed in Section 3.3. We find very good agreement with the theoretical expectation (see Fig. 5.11) which suggests that the implementation is correct.

Since the parameters for the SQUIDs corresponding to the qubits changed from the ones given in Eqs. (5.5a) - (5.5c) to the ones listed in Table 5.1 and Eqs. (5.26a) and (5.26b),

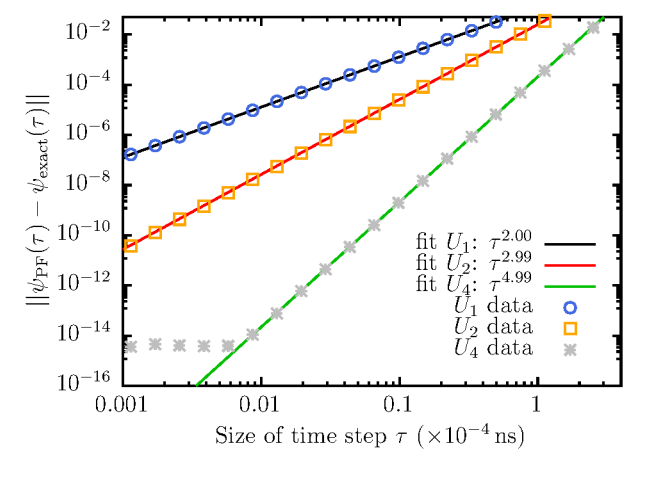
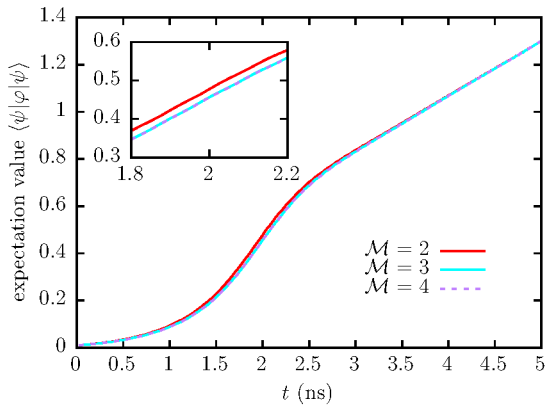


Figure 5.11: Local error induced by the approximation in the product-formula algorithm as a function of the size of the time step τ for U_1 (circles), U_2 (squares) and U_4 (asterisks) for the system of three SQUIDs (two representing the qubits and one the tunable coupler). The data agree nicely with the expectation ($U_k \propto \tau^{k+1}$, see Section 3.3). The solid lines are functions $x \cdot \tau^y$ fitted to the data with fitting parameters x and y.



0.97 0.8 0.96 probability of $|\uparrow\uparrow\rangle$ 0.95 0.94 0.60.93 0.4 $0.090 \\ 0.080$ 0.2 $0.064 \\ 0.080$ 0.080 0 0.2 0.6 0.8

Figure 5.12: Expectation value $\langle \psi | \varphi | \psi \rangle$ of a single qubit used to test the dependence on the number of states representing the space of φ_{CJJ} for the parameters provided by D-Wave Systems Inc.

Figure 5.13: Probability that the system is in the state $|\uparrow\uparrow\rangle$ used to test the dependence on the discretization of the coordinate basis for φ .

we have to check that the discretization parameters are still appropriate. The results are shown in Figs. 5.12 and 5.13. We find that three number states are still sufficient to represent the variable φ_{CJJ} as the cyan and purple curves for $\mathcal{M}=3$ and $\mathcal{M}=4$, shown in Fig. 5.12, are perfectly on top of each other. We also find that $\mathcal{M}=2$ states are not sufficient. Data with varying values for the parameters φ^{\min} and $\Delta \varphi$ are shown in Fig. 5.13 and indicate that the previously chosen parameters are still sufficient for the updated SQUID parameters. Since there are no visible differences when increasing $\Delta \varphi$ a bit, we use $\Delta \varphi = 0.087$, $\mathcal{N} = 47$ and $\varphi^{\min} = -2.00$. We now focus on the parameters φ_0^{\min} , $\Delta \varphi_0$ and \mathcal{M}_0 of the coupling SQUID. Results of simulation runs with varying $\Delta \varphi_0$, φ_0^{\min} and \mathcal{M}_0 are shown in Figs. 5.14(a), (b) and (c), respectively. We find that the results are sufficiently accurate for values $\Delta \varphi_0 = 0.067$, $\mathcal{N}_0 = 31$, $\varphi_0^{\text{min}} = -1.00$ and $\mathcal{M}_0 = 3$. The last step is to determine the time step τ which is needed to achieve sufficiently accurate results. Data for different sizes of the time step are shown in Fig. 5.14(d). We find that a time step of $\tau = 10^{-4}$ ns which was sufficient for the single qubit simulation is not sufficient anymore as the corresponding curve shows significant deviations from the others. The other curves stabilize for $\tau \approx 1-2 \times 10^{-5}$ ns. Thus, we conclude that we have to decrease

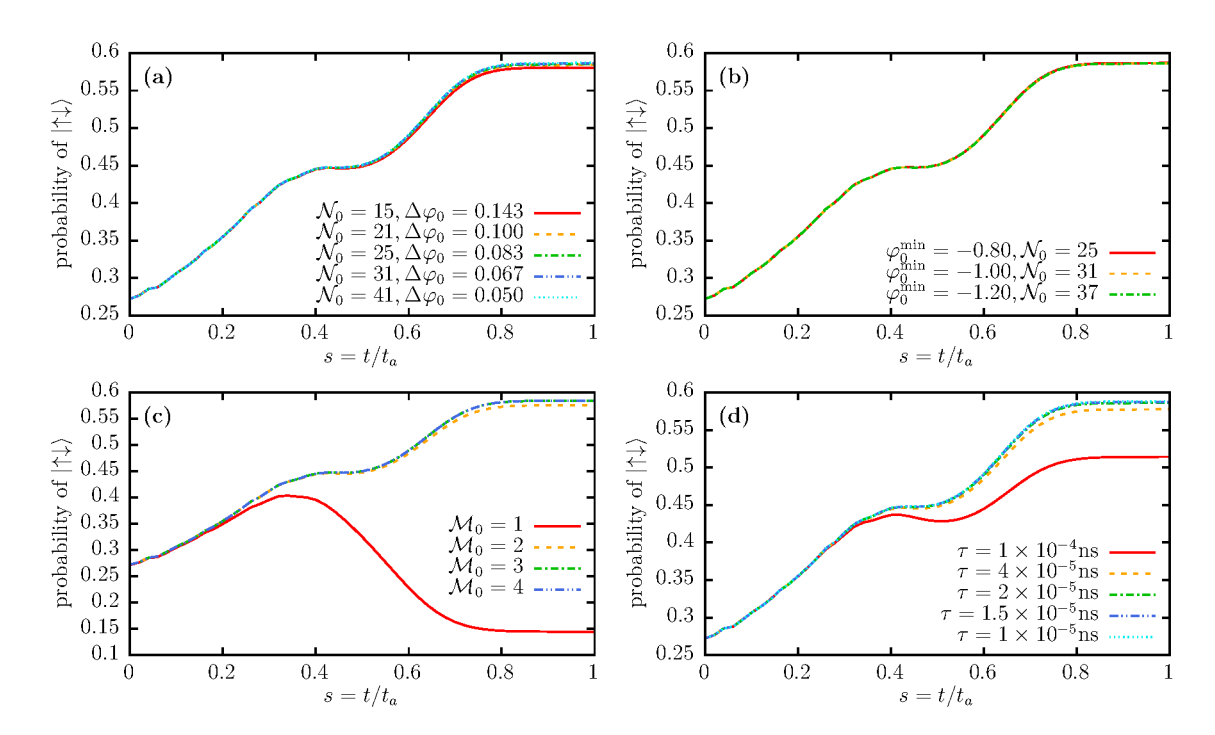


Figure 5.14: Probability that the state vector $|\psi\rangle$ is measured in the basis state $|\uparrow\downarrow\rangle$ during the annealing process as a test of the dependence of the results on the discretization parameters. (a) The parameters $\Delta\varphi_0$ and \mathcal{N}_0 are changed in such a way that $\varphi_0^{\min} = -1.0$ is constant. (b) The parameters φ_0^{\min} and \mathcal{N}_0 are changed in such a way that $\Delta\varphi_0 = 0.067$ is constant. (c) The parameter \mathcal{M}_0 of the $\varphi_{\text{CJJ},0}$ space is changed. (d) The time step τ is changed. The parameters are $\Delta\varphi_0 = 0.067$, $\varphi_0^{\min} = -1.00$ and $\mathcal{M}_0 = 3$. In panels (a), (b) and (c), the time step is $\tau = 2 \times 10^{-5}$ ns.

the time step to about $\tau = 1.5 \times 10^{-5} \,\mathrm{ns}$.

5.1.4 Computational basis and qubit density matrix

In the case without the coupler, the projections of the state vector

$$|\psi\rangle = \sum_{i_1, i_2, m_1, m_2} \psi_{m_2 i_2 m_1 i_1} |m_2 \varphi_2^{(i_2)} m_1 \varphi_1^{(i_1)}\rangle$$
 (5.27)

onto the basis states $|\uparrow\uparrow\rangle$, $|\uparrow\downarrow\rangle$, $|\downarrow\uparrow\rangle$ and $|\downarrow\downarrow\rangle$ can be computed in the following way. The states $|\uparrow\rangle = \sum_{i,m} a^{\uparrow}_{im} |\varphi^{(i)}m\rangle$ and $|\downarrow\rangle = \sum_{i,m} a^{\downarrow}_{im} |\varphi^{(i)}m\rangle$ are computed by diagonalizing the SQUID Hamiltonian with $\varphi^x = 0$ as discussed in Section 4.2.3 and, in the subspace spanned by the ground and first exited states, by diagonalizing the operator $E_L\varphi$. The basis states $|x_2 x_1\rangle$ $(x_i \in \{\uparrow,\downarrow\})$ which are product states are computed as the tensor product

$$|x_2 x_1\rangle = \sum_{i_1, i_2, m_1, m_2} a_{i_1 m_1}^{x_1} a_{i_2 m_2}^{x_2} |m_2 \varphi_2^{(i_2)} m_1 \varphi_1^{(i_1)}\rangle.$$
 (5.28)

The computation of the projections $\langle x_1 x_2 | \psi \rangle$ is straightforward:

$$\langle x_2 \, x_1 | \psi \rangle = \sum_{i_1, i_2, m_1, m_2} (a_{i_1 m_1}^{x_1})^* (a_{i_2 m_2}^{x_2})^* \psi_{m_2 i_2 m_1 i_1}. \tag{5.29}$$

These can be used to compute the probabilities $|\langle x_2 x_1 | \psi \rangle|^2$ to find the system described by the state vector $|\psi\rangle$ in the basis state $|x_2 x_1\rangle$.

In the case that the coupler is present, we can only obtain the density matrix in the computational subspace ρ^{qubits} . The state vector is given as before but with two additional degrees of freedom labeled by an index "0"

$$|\psi\rangle = \sum_{\substack{i_0, i_1, i_2 \\ m_0, m_1, m_2}} \psi_{m_0 i_0 m_2 i_2 m_1 i_1} |m_0 \varphi_0^{(i_0)} m_2 \varphi_2^{(i_2)} m_1 \varphi_1^{(i_1)} \rangle.$$
 (5.30)

The density matrix ρ^{SQUIDs} of the system consisting of the two SQUIDs corresponding to the qubits is obtained by performing the partial trace over the space of the coupler

$$\rho^{\text{SQUIDs}} = \text{Tr}_{\text{coupler}} (|\psi\rangle\langle\psi|) = \sum_{i_0,m_0} \langle m_0 \,\varphi_0^{(i_0)} |\psi\rangle\langle\psi| m_0 \,\varphi_0^{(i_0)} \rangle
= \sum_{\substack{i_1,i_2 \\ m_1,m_2}} \sum_{\substack{i'_1,i'_2 \\ m'_1,m'_2}} \sum_{i_0,m_0} \psi_{m_0 i_0 m_2 i_2 m_1 i_1} \psi^*_{m_0 i_0 m'_2 i'_2 m'_1 i'_1} |m_2 \,\varphi_2^{(i_2)} m_1 \,\varphi_1^{(i_1)} \rangle \langle m'_2 \,\varphi_2^{(i'_2)} m'_1 \,\varphi_1^{(i'_1)} |. \tag{5.31}$$

The 4×4 - matrix of the qubit space is computed by projecting the density matrix ρ^{SQUIDs} onto the subspace spanned by the basis vectors $|x_2 x_1\rangle$ (Eq. (5.28))

$$\rho^{\text{qubits}} = \sum_{\substack{x_1, x_2 \\ x'_1, x'_2'}} |x_2 x_1\rangle \langle x_2 x_1 | \rho^{\text{SQUIDs}} | x'_2 x'_1\rangle \langle x'_2 x'_1 | \\
= \sum_{\substack{x_1, x_2 \\ x'_1, x'_2}} \sum_{i_0, m_0} \sum_{\substack{i_1, i_2 \\ m_1, m_2}} (a_{i_1 m_1}^{x_1})^* (a_{i_2 m_2}^{x_2})^* \psi_{m_0 i_0 m_2 i_2 m_1 i_1} \sum_{\substack{i'_1, i'_2 \\ m'_1, m'_2}} a_{i'_1 m'_1}^{x'_1} a_{i'_2 m'_2}^{x'_2} \psi^*_{m_0 i_0 m'_2 i'_2 m'_1 i'_1} |x_2 x_1\rangle \langle x'_2 x'_1 | \\
= \sum_{i_0, m_0} \sum_{\substack{x_1, x_2 \\ x'_1, x'_2}} V_{i_0 m_0}^{x_1, x_2} \left(V_{i_0 m_0}^{x'_1 x'_2}\right)^* |x_2 x_1\rangle \langle x'_2 x'_1|. \tag{5.32}$$

An efficient way to compute this sum is outlined in pseudo code in algorithm 1. The four diagonal elements of ρ^{qubits} contain the probabilities to measure the state of the two SQUIDs in the four computational basis states, respectively. The probability of the ground state of a particular problem Hamiltonian is later used as a measure of success. The trace of ρ^{qubits} is used to compute the amount of leakage, which is given by $1 - \text{Tr}(\rho^{\text{qubits}})$. The trace of $(\rho^{\text{qubits}})^2$ yields the purity of the state $(\text{Tr}((\rho^{\text{qubits}})^2) = 1$ for a pure state). We also use $\text{Tr}(\rho^{\text{qubits}}O)$ to compute expectation values of the operator O in the computational subspace.

5.2 Methods to estimate the annealing scheme

5.2.1 Computing the annealing scheme for a single qubit

In Section 5.1.2, we found that the Hamiltonian of the SQUID, using the time-dependent basis of number states for the variable φ_{CJJ} , is given by

$$\widetilde{H}_{\text{SQUID}} = H_{\text{SQUID}} - i \Upsilon_{\varphi_{\text{CJJ}}} \frac{\partial}{\partial t} \Upsilon_{\varphi_{\text{CJJ}}}^{\dagger}.$$
 (5.33)

Algorithm 1: Computing the qubit density matrix ρ

```
Data: \mathcal{N}, \mathcal{M}, \mathcal{N}_0, \mathcal{M}_0 (the dimensions of \varphi- and \varphi_{\text{CJJ}}-spaces), \mathcal{N} \cdot \mathcal{M} - dimensional vectors a^{\uparrow} and a^{\downarrow} (the states |\uparrow\rangle and |\downarrow\rangle), \mathcal{N}^2 \cdot \mathcal{M}^2 \cdot \mathcal{N}_0 \cdot \mathcal{M}_0 - dimensional vector \psi (the state vector |\psi\rangle)

Result: 4 \times 4 - matrix \rho (qubit density matrix)

initialization: V_0, V_1, V_2, V_3 = 0, \rho = 0

for i_0 = 0, 1, \dots, \mathcal{N}_0 - 1; m_0 = 0, 1, \dots, \mathcal{M}_0 - 1 do

for i_1 = 0, 1, \dots, \mathcal{N} - 1; m_1 = 0, 1, \dots, \mathcal{M} - 1 do

for i_2 = 0, 1, \dots, \mathcal{N} - 1; m_2 = 0, 1, \dots, \mathcal{M} - 1 do

\begin{vmatrix} V_0 \leftarrow V_0 + \cos(a^{\downarrow}_{i_1 m_1} a^{\downarrow}_{i_2 m_2}) \psi_{m_0 i_0 m_2 i_2 m_1 i_1} \\ V_1 \leftarrow V_1 + \cos(a^{\downarrow}_{i_1 m_1} a^{\downarrow}_{i_2 m_2}) \psi_{m_0 i_0 m_2 i_2 m_1 i_1} \\ V_2 \leftarrow V_2 + \cos(a^{\uparrow}_{i_1 m_1} a^{\downarrow}_{i_2 m_2}) \psi_{m_0 i_0 m_2 i_2 m_1 i_1} \\ V_3 \leftarrow V_3 + \cos(a^{\uparrow}_{i_1 m_1} a^{\downarrow}_{i_2 m_2}) \psi_{m_0 i_0 m_2 i_2 m_1 i_1} \\ \text{end} \\ \text{end} \\ \text{for } j_1 = 0 \dots 3; \ j_2 = 0 \dots 3 \ \text{do} \\ |\rho_{j_1 j_2} \leftarrow \rho_{j_1 j_2} + V_{j_1} \cdot \cos(V_{j_2}) \\ \text{end} \\ \text
```

Under the assumption that leakage is negligible, we have for the state $|\psi\rangle$ and projectors $P = |\uparrow(s)\rangle\langle\uparrow(s)| + |\downarrow(s)\rangle\langle\downarrow(s)|$ and $Q = \mathbb{I} - P$ the relations $P|\psi\rangle \approx |\psi\rangle$ and $Q|\psi\rangle \approx 0$. Then, we can compute the effective Hamiltonian for a single qubit by projecting the SQUID Hamiltonian onto the subspace and including a correction term due to the time dependence of the projector P

$$i\frac{\partial}{\partial t}P|\psi\rangle = i\frac{\partial P}{\partial t}|\psi\rangle + iP\frac{\partial}{\partial t}|\psi\rangle = i\frac{\partial P}{\partial t}|\psi\rangle + P\widetilde{H}_{\text{SQUID}}|\psi\rangle$$

$$\approx \left(i\frac{\partial P}{\partial t} + P\widetilde{H}_{\text{SQUID}}P\right)P|\psi\rangle. \tag{5.34}$$

We can use this effective Hamiltonian to compute the functions A(s) and B(s) of the annealing scheme for a single qubit: We diagonalize the single SQUID Hamiltonian with $\varphi^x = 0$ at a time s to obtain the states $|\uparrow(s)\rangle$ and $|\downarrow(s)\rangle$ as discussed in Section 5.1.4. The matrix elements of $P\widetilde{H}_{SQUID}P$ are then used to compute the annealing functions

$$A(s) = \frac{1}{2} \left(\langle \uparrow(s) | \widetilde{H}_{\text{SQUID}} | \downarrow(s) \rangle + \langle \downarrow(s) | \widetilde{H}_{\text{SQUID}} | \uparrow(s) \rangle \right)$$
 (5.35a)

$$B(s) = \frac{1}{2} \left(\langle \uparrow(s) | \widetilde{H}_{\text{SQUID}} | \uparrow(s) \rangle - \langle \downarrow(s) | \widetilde{H}_{\text{SQUID}} | \downarrow(s) \rangle \right). \tag{5.35b}$$

The remaining term $\partial P/\partial t$ vanishes for large annealing times $t_a \to \infty$ as

$$\frac{\partial P}{\partial t} = \frac{\partial P}{\partial s} \frac{\partial s}{\partial t} = \frac{1}{t_a} \frac{\partial P}{\partial s} \to 0, \tag{5.36}$$

and our numerical results reveal that $\partial P/\partial s$ is already quite small compared to the other elements.

This procedure can also be used for the two directly coupled SQUIDs, but unfortunately, it cannot be applied when the coupling SQUID is present. Thus, we need different methods to obtain an estimate of the annealing scheme in this case.

5.2.2 Comparing simulation data to approximate analytical results from the qubit model

For $s \approx 1$, the Hamiltonian of the ideal qubit system Eq. (2.8) is approximately given by the problem Hamiltonian Eq. (2.7) since then $A(s) \approx 0$. Considering the Hamiltonian at a fixed time s_0 close to one, the Hamiltonian, and thus the time-evolution operator, are diagonal in the computational basis and the time-evolution operator for a time step τ is given by

$$U(\tau) = e^{-i\tau(-B(s_0))\left(h_1\sigma_1^z + h_2\sigma_2^z + J\sigma_1^z\sigma_2^z\right)}$$

$$= e^{i\tau B(s_0)(h_1 + h_2 + J)}|\uparrow\uparrow\rangle\langle\uparrow\uparrow| + e^{i\tau B(s_0)(h_1 - h_2 - J)}|\uparrow\downarrow\rangle\langle\uparrow\downarrow|$$

$$+ e^{i\tau B(s_0)(h_2 - h_1 - J)}|\downarrow\uparrow\rangle\langle\downarrow\uparrow| + e^{i\tau B(s_0)(J - h_1 - h_2)}|\downarrow\downarrow\rangle\langle\downarrow\downarrow|.$$
(5.37)

The time evolution of the state $|++\rangle = (|\uparrow\uparrow\rangle + |\uparrow\downarrow\rangle + |\downarrow\downarrow\rangle) /2$ under the Hamiltonian at fixed s_0 is given by

$$U(\tau)|++\rangle = \frac{1}{2} \left(e^{i\tau B(s_0)(h_1+h_2+J)} |\uparrow\uparrow\rangle + e^{i\tau B(s_0)(h_1-h_2-J)} |\uparrow\downarrow\rangle + e^{i\tau B(s_0)(h_2-h_1-J)} |\downarrow\uparrow\rangle + e^{i\tau B(s_0)(J-h_1-h_2)} |\downarrow\downarrow\rangle \right).$$
 (5.38)

The expectation values $\langle \sigma_1^{\alpha_1} \sigma_2^{\alpha_2} \rangle = \langle ++ | U^{\dagger}(\tau) \sigma_1^{\alpha_1} \sigma_2^{\alpha_2} U(\tau) | ++ \rangle$ $(\alpha_1, \alpha_2 \in \{x, y, z, 0\}, \sigma^0 = \mathbb{I})$ at time τ can be calculated straightforwardly:

$$\langle \sigma_1^x \rangle = \cos(2\tau J B(s_0)) \cos(2\tau h_1 B(s_0)), \qquad \langle \sigma_2^x \rangle = \cos(2\tau J B(s_0)) \cos(2\tau h_2 B(s_0)),$$

$$\langle \sigma_1^y \rangle = -\cos(2\tau J B(s_0)) \sin(2\tau h_1 B(s_0)), \qquad \langle \sigma_2^y \rangle = -\cos(2\tau J B(s_0)) \sin(2\tau h_2 B(s_0)),$$

$$\langle \sigma_1^z \rangle = 0, \qquad \langle \sigma_2^z \rangle = 0,$$

$$\langle \sigma_1^x \sigma_2^x \rangle = \cos(2\tau h_1 B(s_0)) \cos(2\tau h_2 B(s_0)), \qquad \langle \sigma_1^y \sigma_2^y \rangle = \sin(2\tau h_1 B(s_0)) \sin(2\tau h_2 B(s_0)),$$

$$\langle \sigma_1^x \sigma_2^y \rangle = -\cos(2\tau h_1 B(s_0)) \sin(2\tau h_2 B(s_0)), \qquad \langle \sigma_1^y \sigma_2^x \rangle = -\sin(2\tau h_1 B(s_0)) \cos(2\tau h_2 B(s_0)),$$

$$\langle \sigma_1^x \sigma_2^z \rangle = -\sin(2\tau h_1 B(s_0)) \sin(2\tau J B(s_0)), \qquad \langle \sigma_1^z \sigma_2^z \rangle = -\sin(2\tau h_2 B(s_0)) \sin(2\tau J B(s_0)),$$

$$\langle \sigma_1^y \sigma_2^z \rangle = -\cos(2\tau h_1 B(s_0)) \sin(2\tau J B(s_0)), \qquad \langle \sigma_1^z \sigma_2^z \rangle = -\cos(2\tau h_2 B(s_0)) \sin(2\tau J B(s_0)),$$
and
$$\langle \sigma_1^z \sigma_2^z \rangle = 0. \qquad (5.39)$$

We will focus only on the coupling strength, i.e., we set $h_1 = h_2 = 0$, and the only non-zero expectation values are

$$\langle \sigma_1^x \rangle = \langle \sigma_2^x \rangle = \cos(2\tau J B(s_0)),$$
 (5.40a)

$$\langle \sigma_1^y \sigma_2^z \rangle = \langle \sigma_1^z \sigma_2^y \rangle = -\sin(2\tau J B(s_0)), \tag{5.40b}$$

$$\langle \sigma_1^x \sigma_2^x \rangle = 1. \tag{5.40c}$$

These are the analytical results for the expectation values of the ideal two-qubit system. To compare with the results obtained by the simulation of the full flux model (Eq. (4.10)) at fixed s=1 and for various values of J, we initialize the SQUIDs corresponding to the qubits in the state $|++\rangle$ in the computational subspace and the coupling SQUID in the ground state of the (uncoupled) SQUID Hamiltonian. Using the model Eq. (4.10), we simulate the time evolution and use ρ^{qubits} derived in Section 5.1.4 to compute the expectation values $\langle \sigma_1^{\alpha_1} \sigma_2^{\alpha_2} \rangle = \text{Tr}(\rho^{\text{qubits}} \sigma_1^{\alpha_1} \sigma_2^{\alpha_2})$ for various time intervals to visualize the time dependence. We can then plot the expectation values as a function of time and fit the oscillation frequencies $\Omega_J = 2JB(s=1)$ for different values of J. This procedure can be used to verify the linear dependence on J (see Eq. (4.32)), and thus the validity of Eq. (4.27) to transform a given value for J to a value for the external flux φ_{CLLO}^x .

When investigating the case with s < 1 and thus A(s) > 0, we directly consider the case with $h_1 = h_2 = 0$. For fixed s_0 , the qubit Hamiltonian is given by

$$H_{\text{qubit}}(s_0) = -\frac{\Delta(s_0)}{2} \left(\sigma_1^x + \sigma_2^x\right) - JB(s_0)\sigma_1^z \sigma_2^z.$$
 (5.41)

Diagonalizing this Hamiltonian yields (writing $\Delta = \Delta(s_0)$, $B = B(s_0)$)

$$H_{\text{qubit}}(s_0) = \begin{pmatrix} -\sqrt{\Delta^2 + J^2 B^2} & & & \\ & -JB & & \\ & & JB & \\ & & & \sqrt{\Delta^2 + J^2 B^2} \end{pmatrix}, \tag{5.42}$$

with eigenvectors given by

$$|\xi_1\rangle = \frac{\Delta}{2\sqrt{\Delta^2 + J^2B^2 - JB\varpi}} \left(|\uparrow\uparrow\rangle + |\downarrow\downarrow\rangle + \frac{\varpi - JB}{\Delta} \left(|\uparrow\downarrow\rangle + |\downarrow\uparrow\rangle \right) \right), \tag{5.43a}$$

$$|\xi_2\rangle = \frac{1}{\sqrt{2}} \left(|\uparrow\uparrow\rangle - |\downarrow\downarrow\rangle\right),$$
 (5.43b)

$$|\xi_3\rangle = \frac{1}{\sqrt{2}} (|\uparrow\downarrow\rangle - |\downarrow\uparrow\rangle),$$
 (5.43c)

$$|\xi_4\rangle = \frac{\Delta}{2\sqrt{\Delta^2 + J^2B^2 + JB\varpi}} \left(|\uparrow\uparrow\rangle + |\downarrow\downarrow\rangle - \frac{\varpi + JB}{\Delta} \left(|\uparrow\downarrow\rangle + |\downarrow\uparrow\rangle \right) \right), \tag{5.43d}$$

where we defined $\varpi = \sqrt{\Delta^2 + J^2 B^2}$.

The time evolution of the state $|++\rangle$ can be calculated by writing it in the new basis

$$|++\rangle = \frac{\varpi + JB + \Delta}{2\sqrt{\Delta^2 + J^2B^2 + JB\varpi}} |\xi_1\rangle + \frac{\varpi - JB - \Delta}{2\sqrt{\Delta^2 + J^2B^2 - JB\varpi}} |\xi_4\rangle, \tag{5.44}$$

and applying the time-evolution operator $U_{s_0}(\tau) = e^{-i\tau H_{\text{qubit}}(s_0)}$ which results in the state

$$U_{s_0}(\tau)|++\rangle = e^{i\tau\varpi} \frac{\varpi + JB + \Delta}{2\sqrt{\Delta^2 + J^2B^2 + JB\varpi}} |\xi_1\rangle + e^{-i\tau\varpi} \frac{\varpi - JB - \Delta}{2\sqrt{\Delta^2 + J^2B^2 - JB\varpi}} |\xi_4\rangle$$

$$= \frac{1}{2} \left(\cos(\varpi\tau) + \frac{\Delta + JB}{\varpi} i \sin(\varpi\tau) \right) (|\uparrow\uparrow\rangle + |\downarrow\downarrow\rangle)$$

$$+ \frac{1}{2} \left(\cos(\varpi\tau) + \frac{\Delta - JB}{\varpi} i \sin(\varpi\tau) \right) (|\uparrow\downarrow\rangle + |\downarrow\uparrow\rangle). \tag{5.45}$$

In the same way as for $A(s) \approx 0$, we can calculate the expectation values $\langle \sigma_1^{\alpha_1} \sigma_2^{\alpha_2} \rangle$ analytically, yielding

$$\langle \sigma_1^x \rangle = \langle \sigma_2^x \rangle = \cos^2(\varpi \tau) + \frac{\Delta^2 - J^2 B^2}{\Delta^2 + J^2 B^2} \sin^2(\varpi \tau)$$
 (5.46a)

$$\langle \sigma_1^y \rangle = \langle \sigma_2^y \rangle = 0 \tag{5.46b}$$

$$\langle \sigma_1^z \rangle = \langle \sigma_2^z \rangle = 0 \tag{5.46c}$$

$$\langle \sigma_1^x \sigma_2^x \rangle = 1 \tag{5.46d}$$

$$\langle \sigma_1^y \sigma_2^y \rangle = -\frac{2JB\Delta}{\Delta^2 + J^2 B^2} \sin^2(\varpi \tau)$$
 (5.46e)

$$\langle \sigma_1^z \sigma_2^z \rangle = \frac{2JB\Delta}{\Delta^2 + J^2 B^2} \sin^2(\varpi \tau)$$
 (5.46f)

$$\langle \sigma_1^x \sigma_2^y \rangle = \langle \sigma_1^y \sigma_2^x \rangle = 0 \tag{5.46g}$$

$$\langle \sigma_1^x \sigma_2^z \rangle = \langle \sigma_1^z \sigma_2^x \rangle = 0 \tag{5.46h}$$

$$\langle \sigma_1^y \sigma_2^z \rangle = \langle \sigma_1^z \sigma_2^y \rangle = -\frac{2JB}{\varpi} \sin(\varpi \tau) \cos(\varpi \tau).$$
 (5.46i)

The numerical evaluation of the expectation values for the full flux model Eq. (4.10) is performed by using $\text{Tr}(\rho^{\text{qubits}}\sigma_1^{\alpha_1}\sigma_2^{\alpha_2})$ as discussed in Section 5.1.4. As mentioned previously, we can fit the analytical functions to the simulation data to obtain values for the variables $JB(s_0)$ and $\Delta(s_0)$. These can then be compared to the annealing scheme and the validity of the effective Hamiltonian description can be assessed.

5.3 Analysis of the results

In this section, we present and analyze the simulation results obtained by using the methods discussed in the previous sections of this chapter. We also discuss the results in comparison to the results obtained from the ideal qubit model to address the question whether an effective qubit description is appropriate.

Parts of the results presented in this section have been published in [Wil+20].

5.3.1 Effective coupling strength (s = 1)

As mentioned in Section 5.2.2, we can fit the analytical expressions for the expectation values to the simulation data. From the fitting procedure, we can obtain values for the products $JB(s_0)$, $h_1B(s_0)$ and $h_2B(s_0)$. To determine the coupling strength, we set $h_1 = h_2 = 0$. In this way, the expectation values have a simpler time dependence and we expect to obtain the best fitting results for $\Omega_J = JB(s_0)$. We need Ω_J for different values of J to verify that Eq. (4.27) yields a good value for $\varphi_{\text{CJJ},0}$ for a given J.

We use Eq. (5.40b) for fitting $JB(s_0)$ as the sine gives a signed value in contrast to the cosine (Eq. (5.40a)). Two example plots are shown in Figs. 5.15 and 5.16. We find that the cosine and sine (and the expectation values $\langle \sigma_1^x \sigma_2^x \rangle$ and $\langle \sigma_1^y \sigma_2^y \rangle$ which are supposed to be constant) are modulated by the oscillations of the purity (see Section 5.1.4). We conclude that the system of the SQUIDs corresponding to the qubits becomes entangled with the coupler SQUID. The amplitude of the modulating oscillations is stronger for $J \to$

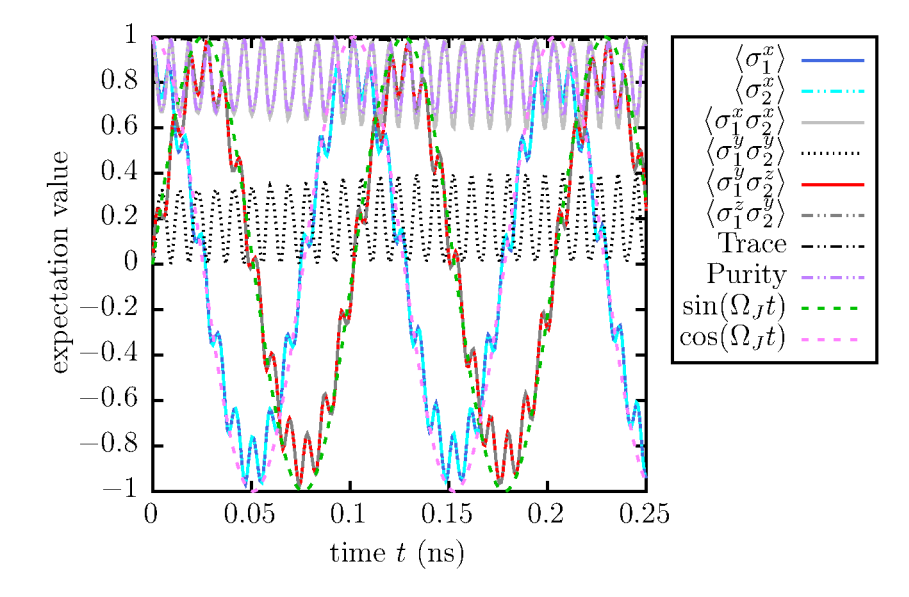


Figure 5.15: Non-zero expectation values, trace and purity (see legend) as a function of time for the state $|++\rangle$ evolving with the Hamiltonian H(s = 1) where J = -0.75. The green dashed and red dashed curves show $\sin(\Omega t)$ and $\cos(\Omega t)$, respectively, where $\Omega = \Omega_J$ is obtained from fitting the sine.

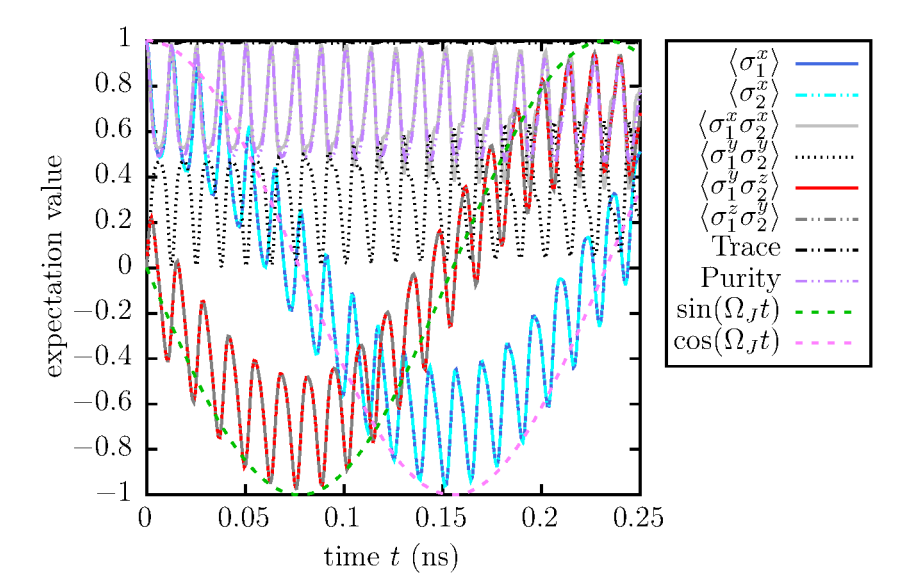


Figure 5.16: Same as Fig. 5.15 but with J = 0.25.

1 and less strong for $J \to -1$ which makes sense as the direct SQUID-SQUID coupling corresponds to negative J (which represents an anti-ferromagnetic coupling because of the additional minus sign in Eq. (2.8)). Thus, to achieve ferromagnetic coupling, the system has to interact more strongly with the SQUID mediating the coupling. We examine this in more detail for a simplified model.

Assuming that the Hamiltonian

$$H_{\text{model}} = \omega a^{\dagger} a + c \sigma_1^z \sigma_2^z + g \left(\sigma_1^z + \sigma_2^z\right) \left(a^{\dagger} + a\right), \tag{5.47}$$

where $a^{\dagger}a$ describes a harmonic oscillator representing the coupler and σ_1^z and σ_2^z model the qubits, is a good simplification of the Hamiltonian Eq. (4.10) at time $t=t_a$ with appropriate parameters ω , c and g, we can infer an analytical approximation of the dynamics of the coupled system. First, we investigate the time-evolution of the four basis states $|\downarrow\uparrow\rangle\otimes|0\rangle$, $|\uparrow\downarrow\rangle\otimes|0\rangle$, $|\uparrow\uparrow\rangle\otimes|0\rangle$, and $|\downarrow\downarrow\rangle\otimes|0\rangle$, where $|0\rangle$ denotes the ground state

of the harmonic approximation of the coupler:

$$U(\tau)|\downarrow\uparrow\rangle\otimes|0\rangle = e^{-i\tau\left(\omega a^{\dagger}a + c\sigma_1^z\sigma_2^z + g\left(\sigma_1^z + \sigma_2^z\right)\left(a^{\dagger} + a\right)\right)}|\downarrow\uparrow\rangle\otimes|0\rangle = e^{i\tau c}|\downarrow\uparrow\rangle\otimes|0\rangle, \tag{5.48a}$$

$$U(\tau)|\uparrow\downarrow\rangle\otimes|0\rangle = e^{i\tau c}|\uparrow\downarrow\rangle\otimes|0\rangle, \tag{5.48b}$$

$$U(\tau)|\uparrow\uparrow\rangle\otimes|0\rangle = e^{-i\tau\left(c+\omega a^{\dagger}a+2g\left(a^{\dagger}+a\right)\right)}|\uparrow\uparrow\rangle\otimes|0\rangle = e^{-i\tau\left(c-\frac{4g^2}{\omega}\right)}|\uparrow\uparrow\rangle\otimes|-\frac{2g}{\omega}\left(1-e^{-i\omega\tau}\right)\rangle,$$
(5.48c)

$$U(\tau)|\downarrow\downarrow\rangle\otimes|0\rangle = e^{-i\tau\left(c+\omega a^{\dagger}a-2g\left(a^{\dagger}+a\right)\right)}|\downarrow\downarrow\rangle\otimes|0\rangle = e^{-i\tau\left(c-\frac{4g^{2}}{\omega}\right)}|\downarrow\downarrow\rangle\otimes|\frac{2g}{\omega}\left(1-e^{-i\omega\tau}\right)\rangle,$$
(5.48d)

where $|\pm \frac{2g}{\omega} (1 - e^{-i\omega\tau})\rangle$ denote coherent states with $|\alpha\rangle = e^{-|\alpha|^2/2} \sum_{n=0}^{\infty} \alpha^n / \sqrt{n!} |n\rangle$. The proof showing that the time evolution of $|\uparrow\uparrow\rangle \otimes |0\rangle$ and $|\downarrow\downarrow\rangle \otimes |0\rangle$ is indeed given by Eq. (5.48c) and Eq. (5.48d), respectively, is presented in Appendix B.4. The time evolution of the state $|++\rangle \otimes |0\rangle$ is then given by

$$|\psi(\tau)\rangle = U(\tau)|++\rangle \otimes |0\rangle = \frac{e^{i\tau c}}{2} \left(\left(|\uparrow\downarrow\rangle + |\downarrow\uparrow\rangle \right) \otimes |0\rangle + e^{-2i\tau \left(c - \frac{2g^2}{\omega}\right)} \left(|\uparrow\uparrow\rangle \otimes |-\frac{2g}{\omega} \left(1 - e^{-i\omega\tau}\right)\rangle + |\downarrow\downarrow\rangle \otimes |\frac{2g}{\omega} \left(1 - e^{-i\omega\tau}\right)\rangle \right) \right). \tag{5.49}$$

From this, we can obtain the density matrix in the qubit subspace by performing the partial trace over the harmonic degrees of freedom

$$\rho_{q}(\tau) = \operatorname{Tr}\left(|\psi(\tau)\rangle\langle\psi(\tau)|\right) = \sum_{n=0}^{\infty} \langle n|\psi(\tau)\rangle\langle\psi(\tau)|n\rangle$$

$$= \frac{1}{4} \left((|\uparrow\downarrow\rangle + |\downarrow\uparrow\rangle) \left(\langle\uparrow\downarrow| + \langle\downarrow\uparrow| \right) + e^{2i\tau\left(c - \frac{2g^{2}}{\omega}\right)} e^{-\frac{1}{2}\left|\frac{2g}{\omega}(1 - e^{-i\omega\tau})\right|^{2}} \left(|\uparrow\uparrow\rangle + |\downarrow\uparrow\rangle \right) \left(\langle\uparrow\uparrow| + \langle\downarrow\downarrow| \right) \right)$$

$$+ e^{-2i\tau\left(c - \frac{2g^{2}}{\omega}\right)} e^{-\frac{1}{2}\left|\frac{2g}{\omega}(1 - e^{-i\omega\tau})\right|^{2}} \left(|\uparrow\uparrow\rangle + |\downarrow\downarrow\rangle \right) \left(\langle\uparrow\downarrow| + \langle\downarrow\uparrow| \right)$$

$$+ e^{-\left|\frac{2g}{\omega}\left(1 - e^{-i\omega\tau}\right)\right|^{2}} \sum_{n=0}^{\infty} \left(\frac{\left|\frac{2g}{\omega}\left(1 - e^{-i\omega\tau}\right)\right|^{2n}}{n!} \left(|\uparrow\uparrow\rangle\langle\downarrow\downarrow| + |\downarrow\downarrow\rangle\langle\downarrow\downarrow| \right) \right)$$

$$+ \frac{(-1)^{n}\left|\frac{2g}{\omega}\left(1 - e^{-i\omega\tau}\right)\right|^{2n}}{n!} \left(|\uparrow\uparrow\rangle\langle\downarrow\downarrow| + |\downarrow\downarrow\rangle\langle\uparrow\uparrow| \right) \right)$$

$$= \frac{1}{4} \left(\left(|\uparrow\downarrow\rangle + |\downarrow\uparrow\rangle \right) \left(\langle\uparrow\downarrow| + \langle\downarrow\uparrow| \right) + |\uparrow\uparrow\rangle\langle\uparrow\uparrow| + |\downarrow\downarrow\rangle\langle\downarrow\downarrow| + e^{-\frac{16g^{2}}{\omega^{2}}(1 - \cos\omega\tau)} \left(|\uparrow\uparrow\rangle\langle\downarrow\downarrow| + |\downarrow\downarrow\rangle\langle\uparrow\uparrow| \right) \right)$$

$$+ e^{-\frac{4g^{2}}{\omega^{2}}(1 - \cos\omega\tau)} \left(e^{2i\tau\left(c - \frac{2g^{2}}{\omega}\right)} \left(|\uparrow\uparrow\rangle + |\downarrow\downarrow\uparrow\rangle \right) \left(\langle\uparrow\uparrow| + \langle\downarrow\downarrow| \right) + e^{-2i\tau\left(c - \frac{2g^{2}}{\omega}\right)} \left(|\uparrow\uparrow\rangle + |\downarrow\downarrow\rangle \right) \left(\langle\uparrow\downarrow| + \langle\downarrow\uparrow| \right) \right). \tag{5.50}$$

As discussed previously, we can use $\text{Tr}(\rho_q(\tau)\sigma_1^{\alpha_1}\sigma_2^{\alpha_2})$ to compute the expectation values. Now, we can also include effects caused by the coupling of the qubit system to the coupler,

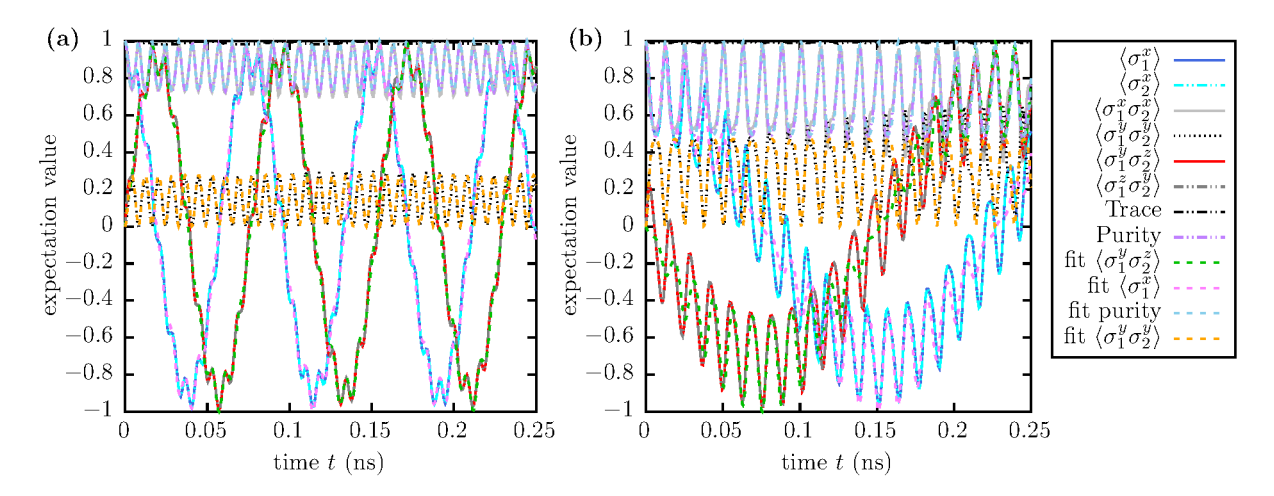


Figure 5.17: Non-zero expectation values, trace and purity (simulation results and fitted analytical results, see legend) as a function of time for the state $|++\rangle$ evolving with the full flux model Hamiltonian H(s=1) (a) with J=-1, (b) with J=0.25.

and an approximate analytical result for the purity $\text{Tr}(\rho_q^2(\tau))$.

$$\operatorname{Tr}(\sigma_1^x \rho_q(\tau)) = \operatorname{Tr}(\sigma_2^x \rho_q(\tau)) = \cos\left(2\tau \left(c - \frac{2g^2}{\omega}\right)\right) e^{-\frac{4g^2}{\omega^2}(1 - \cos(\omega \tau))}$$
(5.51a)

$$\operatorname{Tr}(\sigma_1^y \rho_q(\tau)) = \operatorname{Tr}(\sigma_2^y \rho_q(\tau)) = \operatorname{Tr}(\sigma_1^z \rho_q(\tau)) = \operatorname{Tr}(\sigma_2^z \rho_q(\tau)) = 0$$
 (5.51b)

$$Tr(\sigma_1^x \sigma_2^x \rho_q(\tau)) = \frac{1}{2} \left(1 + e^{-\frac{16g^2}{\omega^2} (1 - \cos(\omega \tau))} \right)$$
 (5.51c)

$$Tr(\sigma_1^y \sigma_2^y \rho_q(\tau)) = \frac{1}{2} \left(1 - e^{-\frac{16g^2}{\omega^2} (1 - \cos(\omega \tau))} \right)$$
 (5.51d)

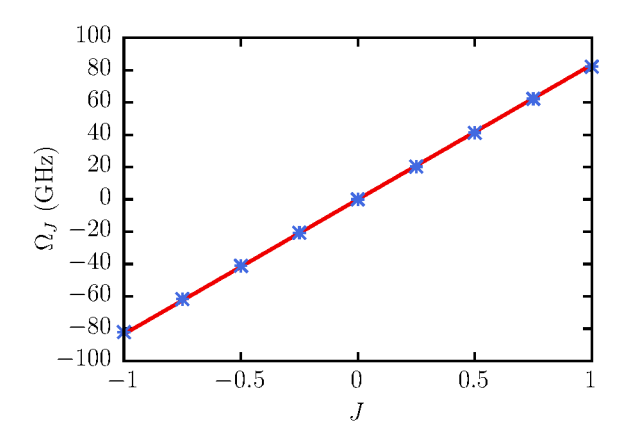
$$\operatorname{Tr}(\sigma_1^z \sigma_2^z \rho_q(\tau)) = \operatorname{Tr}(\sigma_1^x \sigma_2^y \rho_q(\tau)) = \operatorname{Tr}(\sigma_1^y \sigma_2^x \rho_q(\tau)) = 0$$
(5.51e)

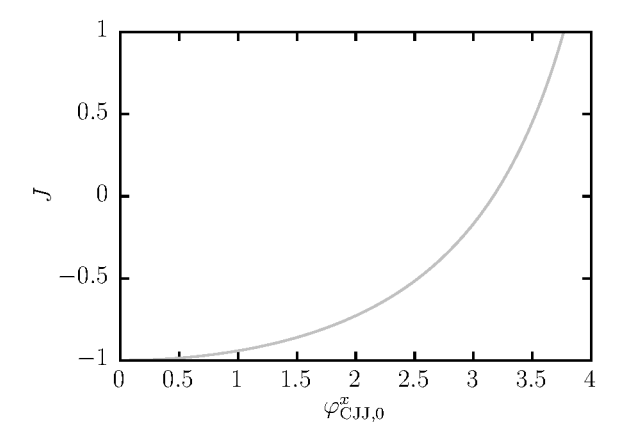
$$\operatorname{Tr}(\sigma_1^x \sigma_2^z \rho_q(\tau)) = \operatorname{Tr}(\sigma_1^z \sigma_2^x \rho_q(\tau)) = 0 \tag{5.51f}$$

$$\operatorname{Tr}(\sigma_1^y \sigma_2^z \rho_q(\tau)) = \operatorname{Tr}(\sigma_1^z \sigma_2^y \rho_q(\tau)) = -\sin\left(2\tau \left(c - \frac{2g^2}{\omega}\right)\right) e^{-\frac{4g^2}{\omega^2}(1 - \cos(\omega \tau))}$$
 (5.51g)

$$\operatorname{Tr}(\rho_q^2(\tau)) = \frac{1}{8} \left(3 + 4e^{-\frac{8g^2}{\omega^2}(1 - \cos(\omega\tau))} + e^{-\frac{32g^2}{\omega^2}(1 - \cos(\omega\tau))} \right). \tag{5.51h}$$

Indeed, the expectation values $\langle \sigma_1^x \sigma_2^x \rangle$ and $\langle \sigma_1^y \sigma_2^y \rangle$ show oscillatory behavior and the expectation values $\langle \sigma_1^x \rangle = \langle \sigma_2^x \rangle$ and $\langle \sigma_1^y \sigma_2^z \rangle = \langle \sigma_1^z \sigma_2^y \rangle$ are modulated by oscillations with the coupler's frequency. Figures 5.17(a) and (b) show example plots for the evolution using the full flux model, in comparison with the analytical results in Eqs. (5.51a), (5.51d), (5.51g), and (5.51h). The parameters of the analytical results have been fitted to the data of the flux model. We find that for J=-1 the agreement between the fitted analytical results and the simulation results is very good (see Fig. 5.17(a)). That is, in this case, we can explain the small oscillations in the expectation values by the entanglement between the SQUIDs representing the qubits and the coupler. However, if J is not close to -1, we find that the modulating oscillations do not match equally well when the expectation values $\langle \sigma_1^x \rangle = \langle \sigma_2^x \rangle$ and $\langle \sigma_1^y \sigma_2^z \rangle = \langle \sigma_1^z \sigma_2^y \rangle$ are close to 0 (see Fig. 5.17(b)). Also, after a short time, $\langle \sigma_1^x \sigma_2^x \rangle$ and $\langle \sigma_1^y \sigma_2^z \rangle$ exhibit oscillations that do not match the analytical results Eq. (5.51c) and Eq. (5.51d). From these observations, we conclude that the model Eq. (5.47) does





as a function of the parameter J in com- of the external flux $\varphi_{\text{CJJ},0}^x$ (see Eq. (4.27)). parison to the theoretical value according to Eq. (4.27) (solid line).

Figure 5.18: The fitted frequency (asterisks) Figure 5.19: The parameter J as a function

not capture all effects of the Hamiltonian Eq. (4.10), especially for $J \neq -1$. This is not surprising, as we neglected the higher energy levels of the SQUIDs representing the qubits and the anharmonicities of the coupler when using Eq. (5.47). Nevertheless, the effective description in terms of H_{model} provides valuable insights into the dynamics of the coupler depending on the value of the external flux $\varphi^x_{\text{CJJ},0}$ and its influence on the dynamics of the SQUIDs modeling the qubits.

To examine the extracted coupling strength as a function of the input coupling strength, we plot the fitted frequencies Ω_J as a function of J together with the theoretical curve $JB(s_0)$ as a reference. The plot is shown in Fig. 5.18. Since E_L instead of E_L occur in the Hamiltonian of the coupled SQUIDs (Eq. (4.21)), and \widetilde{E}_L slightly depends on J, the persistent current which is computed from E_L , also depends slightly on J. Thus, $B(s) \propto I_p^2(s)$ also has a slight dependence on J. However, this is not included in the theoretical curve plotted in Fig. 5.18. For the theoretical curve, $I_p(s=1,J=0)$ is used to compute $B(s_0 = 1)$.

Plotting J as a function of the external flux $\varphi_{\text{CJJ},0}^x$ (see Fig. 5.19), we find that the region of negative J is much more stable with respect to fluctuations in the external flux $\varphi_{\text{CJJ},0}^x$ than in the region of positive J. Therefore, we assume that for values of $J \gtrsim 0$, small inaccuracies in the determined value for the external flux $\varphi_{\text{CJI},0}^x$, for instance caused by the replacement of $\varphi_{\text{CJJ},0}$ by $\langle \varphi_{\text{CJJ},0} \rangle$, have much greater effects than for values of J close to -1. Nevertheless, and although we obtained the mapping between J and $\varphi_{\text{CJJ},0}^x$ (Eq. 4.27) from the approximate qubit description, the linearity in Ω_J as a function of J is excellent.

In principle, the same investigations can be made for $h_i \neq 0$ using Eqs. (5.39). However, the plots for the fitting become much more complex without yielding any new insights. Thus, we stop here and continue with investigating the behavior during the annealing process, i.e., for times s < 1.

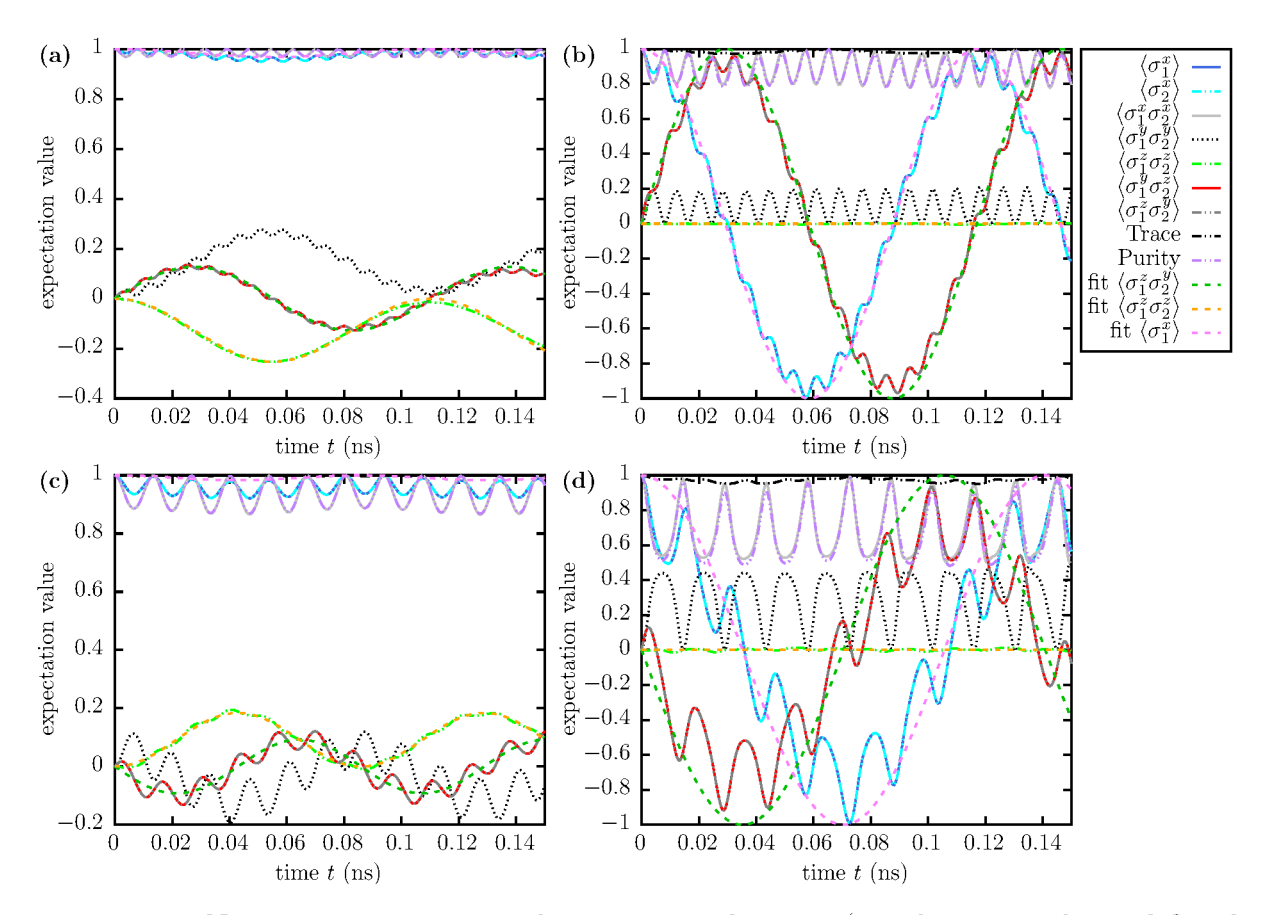


Figure 5.20: Non-zero expectation values, trace and purity (simulation results and fitted analytical results, see legend) as a function of time for the state $|++\rangle$ evolving with the Hamiltonian (a) H(s=0.2) with J=-1, (b) H(s=0.8) with J=-1, (c) H(s=0.1) with J=1, and (d) H(s=0.7) with J=1.

5.3.2 Effective annealing scheme $(0 \le s \le 1)$

To estimate the coupling strength during the annealing process, we apply the procedure explained in Section 5.2.2, for $0 \le s \le 1$ in steps of 0.1 and with $J = \pm 1$. Based on the results from Section 5.3.1 shown in Fig. 5.18, we assume that J attains the desired value sufficiently accurately. Hence, we only consider Δ and B as parameters to be fitted.

For most of the cases, we can use Eq. (5.46f) to fit the parameters Δ and B. Examples are shown in Figs. 5.20(a) and (c). For $s \geq 0.7$, we find that the fitting of Eq. (5.46f) becomes difficult and we assume that we reached the region where the approximation $\Delta \approx 0$ can be applied. Thus, for these cases we fix $\Delta = 0$ and fit B by using Eq. (5.46i) which is then equivalent to Eq. (5.40b). Example plots are shown in Figs. 5.20(b) and (d).

In this way, we obtain for discrete values of s, the effective values for the parameters Δ and B (under the assumption that the qubit model describes the effective Hamiltonian sufficiently well so that the procedure from Section 5.2.2 can be applied). We plot the obtained values together with the annealing scheme obtained for a single SQUID as described in Section 5.2.1 (see Figs. 5.21(a) and 5.21(b)). Using the Hamiltonian given in Eq. (4.8) for the calculation of the annealing scheme, we find that the data points deviate

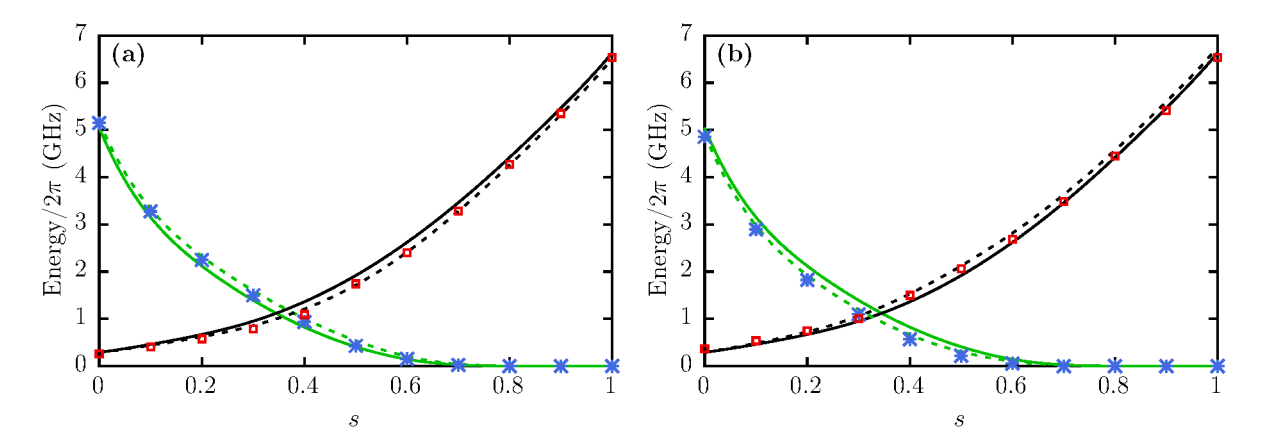
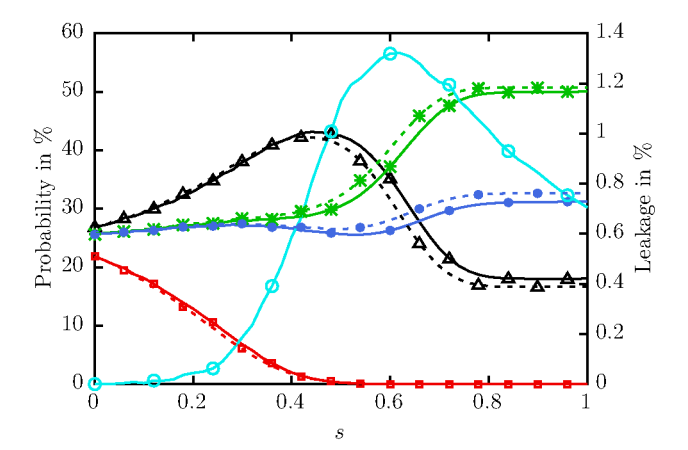


Figure 5.21: The annealing scheme functions $A(s) = \Delta(s)/2$ (green lines) and B(s) (black lines) obtained with the calculation described in Section 5.2.1 for a single SQUID. Solid lines are obtained using Eq. (4.8) and dashed lines are obtained using Eq. (4.8) with E_L replaced by \widetilde{E}_L (defined below Eq. (4.21)). Asterisks and squares denote the values for $\Delta(s)/2$ and B(s), respectively, obtained from the fitting for (a) J = -1, (b) J = 1.

systematically from the calculated annealing scheme. Since the coupling of the SQUIDs effectively changes the inductive energy (cf. Section 4.2.2), the effective annealing scheme of the coupled SQUIDs is slightly different from the effective annealing scheme of a single SQUID. This change in the inductive energy was also found in experiments [Har+09a; Har+10a]. To see if the modified annealing scheme using \tilde{E}_L instead of E_L in Eq. (4.8) describes the simulation data better, we also plot this annealing scheme (dashed lines in Fig. 5.21). Indeed, the modified annealing scheme shows the same trends as the simulation data. However, from the modified annealing scheme, we find systematic deviations to smaller values for J=-1 as well as for J=+1, especially for A(s). Possible reasons could be (i) the modulating oscillations in the expectation values due to the entanglement of the system causing a systematic error in the fitting, (ii) an offset in the mapping from J to $\varphi_{\text{CJJ},0}^x$ causing the effective J to be different from the intended one and affecting the fitting of $\Delta(s)$, or (iii) some other effects due to the coupler or the higher energy levels that cause frequency shifts that are not captured by the simplified model and thus, cannot be explained on the basis of this model.

5.3.3 Comparison to the ideal qubit model

In this section, we compare the results obtained from the simulation of the full flux model Eq. (4.10) to the results of the ideal qubit model Eq. (2.8) in order to examine similarities and differences. In contrast to the previous sections where we examined effective descriptions, we now study the dynamics during the quantum annealing process for the flux model and the qubit model. For this, the system is prepared in the ground state of the initial Hamiltonian. We use the Lanczos method [Pai72] to compute this ground state. As a primary measure, we investigate the probability for the system to be in the ground state at the end of the annealing process (i.e., the success probability to find the correct solution in a measurement). We also study the probabilities for the system to be in the computational states $|\uparrow\uparrow\rangle$, $|\uparrow\downarrow\rangle$, $|\downarrow\uparrow\rangle$, and $|\downarrow\downarrow\rangle$ during the evolution in comparison



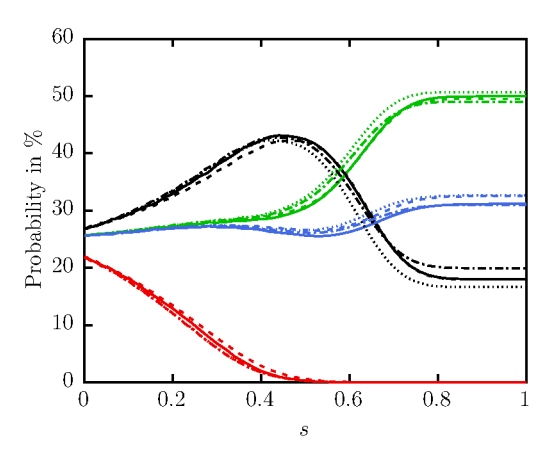


Figure 5.22: Probabilities of the computational states $|\uparrow\uparrow\rangle$ (black triangles), $|\uparrow\downarrow\rangle$ (green asterisks), $|\downarrow\uparrow\rangle$ (blue bullets), and $|\downarrow\downarrow\rangle$ (red squares) during the annealing process for the flux model Eq. (4.10) (solid lines) and the qubit model (dashed lines). Markers are used to indicate the different states. Every 120th data point of the simulation of the qubit model is plotted with a marker and every 6th point of the simulation of the flux model is plotted with a marker. In addition, for the flux model, the probability of leakage (cyan circles) is plotted, see the right y axis. The annealing time was set to $t_a = 5$ ns. The parameters of the problem instance are J = -1, $h_1 = 0.96$ and $h_2 = 0.94$.

Figure 5.23: Probabilities of the computational states $|\uparrow\uparrow\rangle$ (black), $|\uparrow\downarrow\rangle$ (green), $|\downarrow\uparrow\rangle$ (blue), and $|\downarrow\downarrow\rangle$ (red) during the annealing process for the flux model Eq. (4.10) (solid lines) and the qubit system using the usual annealing scheme (dotted lines), the modified annealing scheme (dashed lines, see text), and by taking into account the additional σ^z -terms in Eq. (4.32) (dashdotted lines). The annealing time was set to $t_a = 5$ ns. The parameters of the problem instance are J = -1, $h_1 = 0.96$ and $h_2 = 0.94$.

to the evolution of the qubit system, as well as leakage out of the computational subspace, i.e., the probability that higher energy levels are occupied. Of course, for the ideal qubit system, there is no leakage. Results of the full flux model discussed in this section are obtained using the supercomputer JURECA [Jül18].

Figure 5.22 shows the probabilities of the computational basis states during the annealing process for the problem instance with parameters J=-1, $h_1=0.96$, and $h_2=0.94$. We find that the overall agreement is very good. For times approaching $s\approx 0.64$ where the minimal energy gap is reached, the maximal amount of leakage (cyan circles, right y axis) can be observed but the amount is rather small and drops again for s>0.64. Also, when the leakage increases, small differences in the probabilities between the data of the flux model and the qubit model appear. The deviations can be such that the probabilities for the flux model are higher or lower (depending on the state) than for the qubit model. Hence, leakage alone cannot be the explanation for this. In Fig. 5.23, we show the same results from the simulation of the flux model (solid lines) and the qubit model (dotted lines), but also compare to the results for different modifications of the qubit model. For the first modification (dashed lines), we use the annealing scheme given by the dashed lines in Fig. 5.21(a). For the second modification (dash-dotted lines), we include the additional σ^z -terms from Eq. (4.32) by using the correspondingly adjusted values for the h_i .

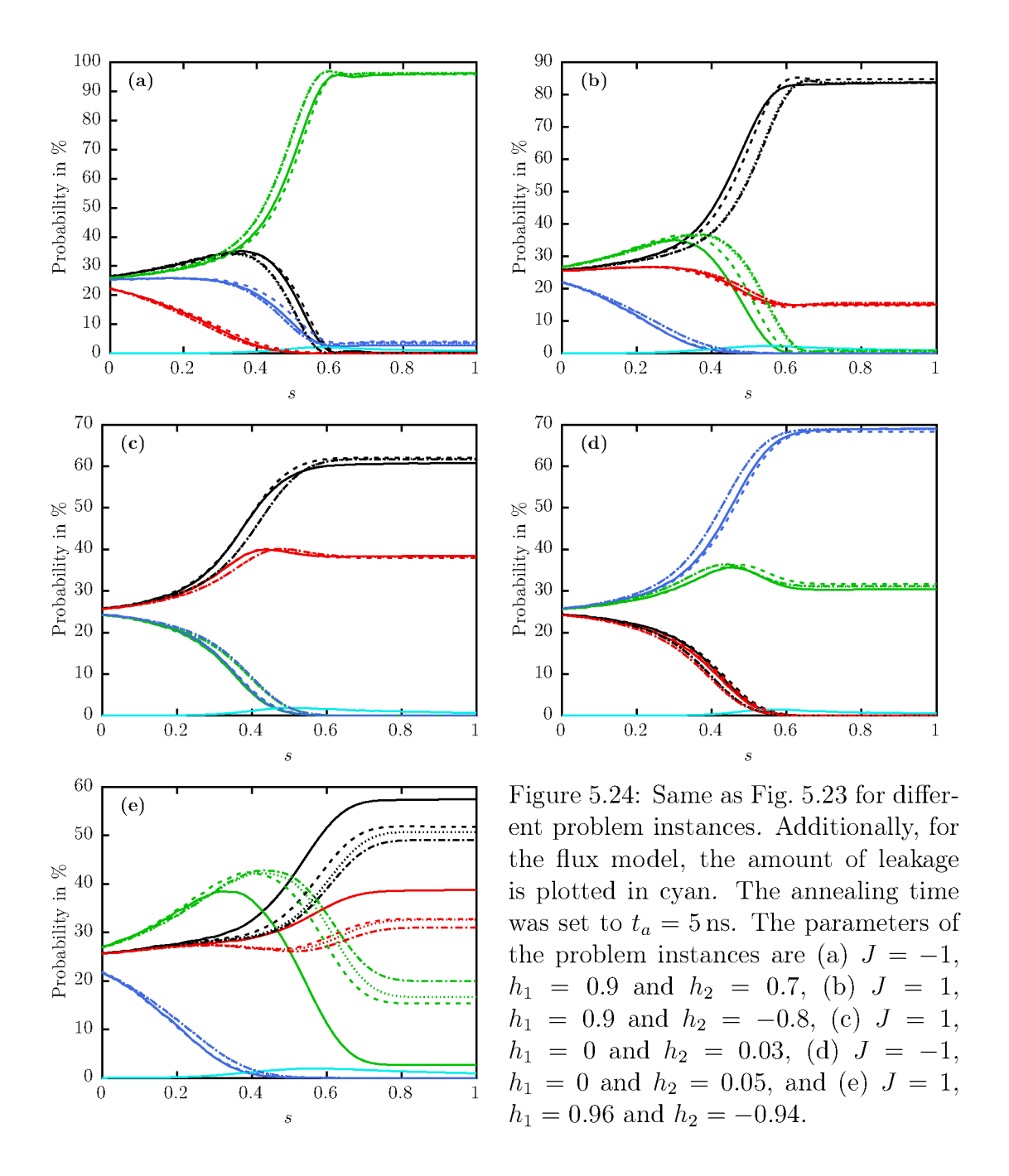
We find that the first modification (the modified annealing scheme) improves the agreement between the results for the states $|\uparrow\downarrow\rangle$ and $|\uparrow\uparrow\rangle$ (green and black lines). Especially at the end of the annealing process, the agreement is excellent. However, there is no improvement for the state $|\downarrow\uparrow\rangle$ (blue line). On the other hand, the second modification (adjusted h_i) leads to very good agreement for this state. For the states $|\uparrow\downarrow\rangle$ and $|\uparrow\uparrow\rangle$, the changes are also in the right direction, but too strong, leading to a similar amount of disagreement as in the non-modified case but in the opposite direction. A combination of both modifications is thus also too strong. A conclusion that can be made based on these observations is that for $J \approx -1$, there are additional effects in the flux model which are not included in the qubit model and which weaken the influence of the modified annealing scheme and the additional σ^z -terms, leading effectively to a result closer to the one of the original qubit problem.

Fig. 5.24 shows the probabilities of the computational states during the annealing process for five additional problem instances. We find that for problem instances with a larger energy gap (see Fig. 5.24(a) and (b)) or small values of the h_i (Fig. 5.24(c)), including the additional σ^z -terms (dash-dotted lines) has almost no effect, as the dotted lines (original problem instances) are almost on top of the dash-dotted lines. This is not surprising as for large energy gaps, the small changes in the h_i do not change the spectrum significantly, and for small h_i or small J, the effective changes in the h_i become negligibly small.

For a large energy gap and J = -1 (case (a)), the agreement with the qubit model using the modified annealing scheme (dashed lines) is very good. The small deviations that can be observed, are as in the case previously discussed, approaching the results from the original qubit problem. In the case of a large energy gap but J = 1 (case (b)), we find similar behavior but with an obvious difference: We still find that the overall agreement is improved when using the qubit model with the modified annealing scheme. However, in this case, the modification does not seem to be strong enough. Only at the end of the annealing process, the success probability matches with the result of the original qubit problem (dotted lines), but this might be a coincidence as there is also a small amount ($\approx 2\%$) of leakage. Taking also the observations from case (b) into account, we can conclude that independent of the sign of J, the effects of the full flux model, which come in addition to the modification of the annealing scheme, change the results in the same direction.

In the case of small h_i (case (c)), we find almost perfect agreement between the data from the flux model (solid lines) and the data from the modified qubit model (dashed lines). The only deviation may be due to the small amount ($\approx 2\%$) of leakage. This observation would lead to the conclusion that the deviations in the other cases are correlated with the rather large values of the parameters h_i . However, in some cases with small h_i , we find very good agreement between the simulation data using Eq. (4.10) and the modified qubit model only in the first part of the annealing process. In the vicinity of the minimal energy gap, the simulation data start to deviate from the modified qubit model and approach the data of the original qubit problem (see Fig. 5.24(d)).

In the case of a small minimal energy gap, J=1 and large $h_1 \approx -h_2$ (case (e)), we find rather large deviations. Using the modified annealing scheme for the qubit model does not lead to a big improvement. Including the additional σ^z terms even worsens the mismatch. We can conclude that the effects due to the non-computational states in the



full flux model are strongest for this class of problem instances.

In most cases, during the annealing process, the full flux model can be very well described as two coupled two-level systems with the modified annealing scheme, the effects on the final success probability being very small. This is also an indication that the effective Hamiltonian on the subspace given by the qubit annealing Hamiltonian Eq. (2.8) is a good approximation except when the minimum gap does become very small, J close to one and $h_1 \approx -h_2$. In this particular case, larger deviations become visible and the modified annealing scheme only yields a small improvement. We conclude that the probabilities of the computational states during the evolution match the data of the modified qubit system very well if the minimal energy gap does not become too small. For small energy gaps, deviations become visible but the evolution still matches the data

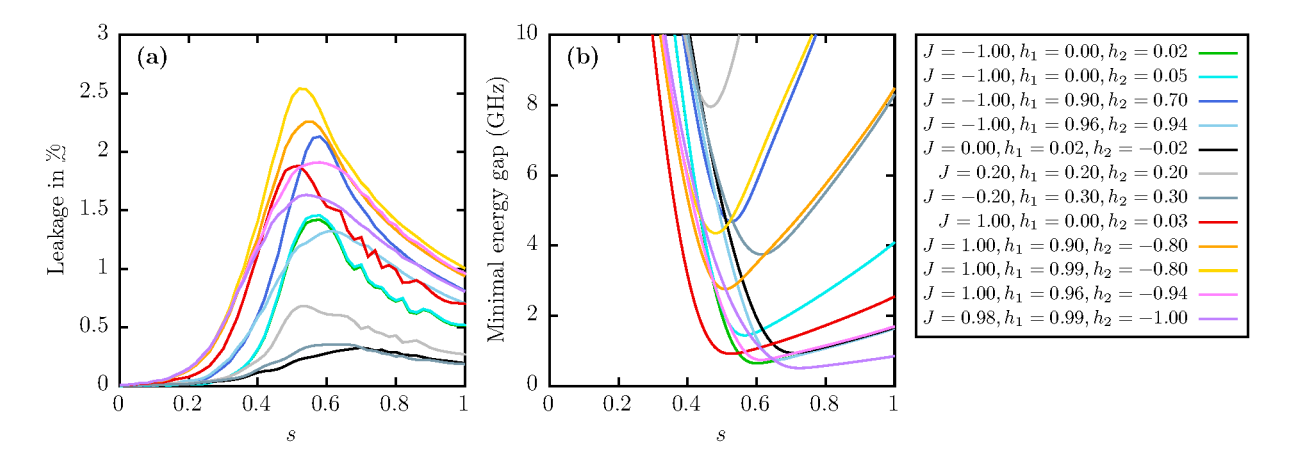


Figure 5.25: (a) Probability of leakage during the annealing process with annealing time $t_a = 5$ ns obtained from the simulation of the flux model Eq. (4.10) for various cases, indicated in the legend. (b) The energy gap during the annealing process for the same cases, computed from the ideal qubit system Eq. (2.8) with the modified annealing scheme (see dashed lines in Fig. 5.21).

of the qubit system nicely if we are not close to the case $J \approx 1$, $h_1 \approx 1 \approx -h_2$ with a small energy gap. Only for these cases, we observed larger deviations that cannot be explained by using the two-level approximation.

We compare the amount of leakage during the annealing process with annealing time $t_a = 5$ ns for various cases. Figure 5.25(a) shows the amount of leakage and Fig. 5.25(b) depicts the energy gap during the annealing process for the qubit model with the modified annealing scheme. We find that maximum leakage is approximately reached when the energy gap becomes minimal. However, the maximal amount of leakage does not seem to be correlated with the value of the minimal energy gap. Rather, the amount of leakage seems to be largest for $J \approx 1$. For $J \approx -1$, the amount of leakage is on average less than for $J \approx 1$ but still significantly larger than for small |J|. That leakage is higher when $J \approx 1$ seems to be caused by the presence of the coupler. It is reasonable that large values for |J| and $|h_i|$ cause more leakage than small values, as the terms proportional to h_i and J are the ones that cause leakage. Nevertheless, despite its simplicity, the two-level model can describe the dynamics of the flux model quite well.

Having analyzed the evolution during the annealing process, we now concentrate on the final probabilities to find the ground state (success probabilities). Figure 5.26 shows the success probabilities as a function of the minimal energy gap ΔE for the qubit model (red, blue and green bullets) and the full flux model Eq. (4.10) (black open circles). The difference between the red, blue and green cases is discussed in Section 5.3.4.

For most of the investigated cases, the data points generated from the full flux model match the data points generated from the qubit model very well. Only for a few exceptions, larger deviations are observable. These few cases belong to the class represented by the green data points. We conclude that the effects, regarding the final success probability, introduced by approximating the flux model by the qubit model are rather small and affect only a special class of problems. In those few cases where deviations are apparent, the success probability is sometimes enhanced and sometimes reduced compared to the qubit model.

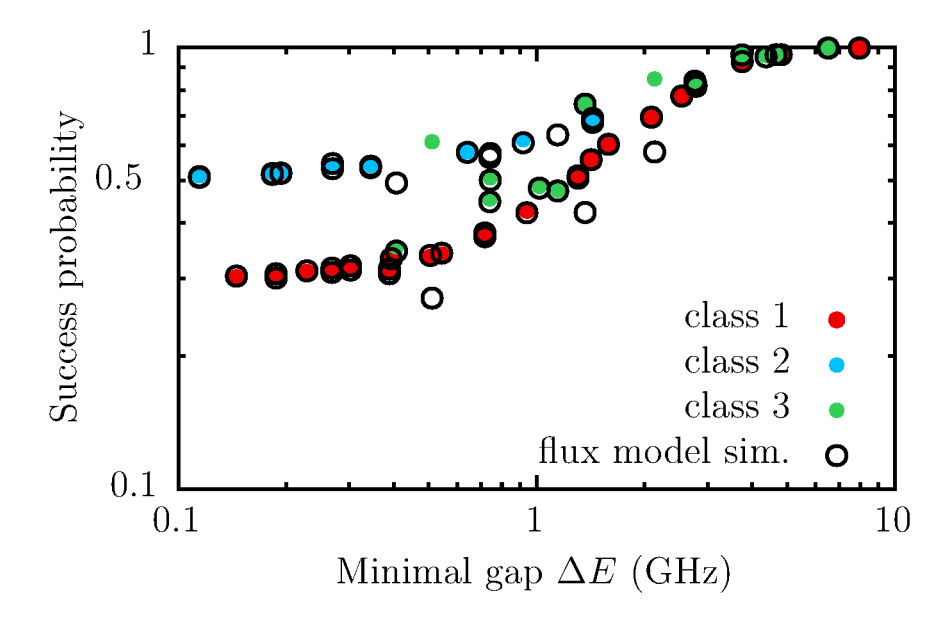


Figure 5.26: Success probabilities at the end of the annealing process with annealing time $t_a = 5$ ns as a function of the minimal energy gap ΔE obtained from the ideal qubit model (red, blue and green bullets) and from the simulation of the full flux model Eq. (4.10) (black open circles). The minimal energy gap ΔE during the annealing process is computed from the ideal qubit system Eq. (2.8). Different colors of the qubit data indicate the different types of energy spectra. Red data points (class 1) correspond to spectra of the type shown in Fig. 5.28(a), blue (class 2) to Fig. 5.28(b) and green (class 3) to Fig. 5.28(c).

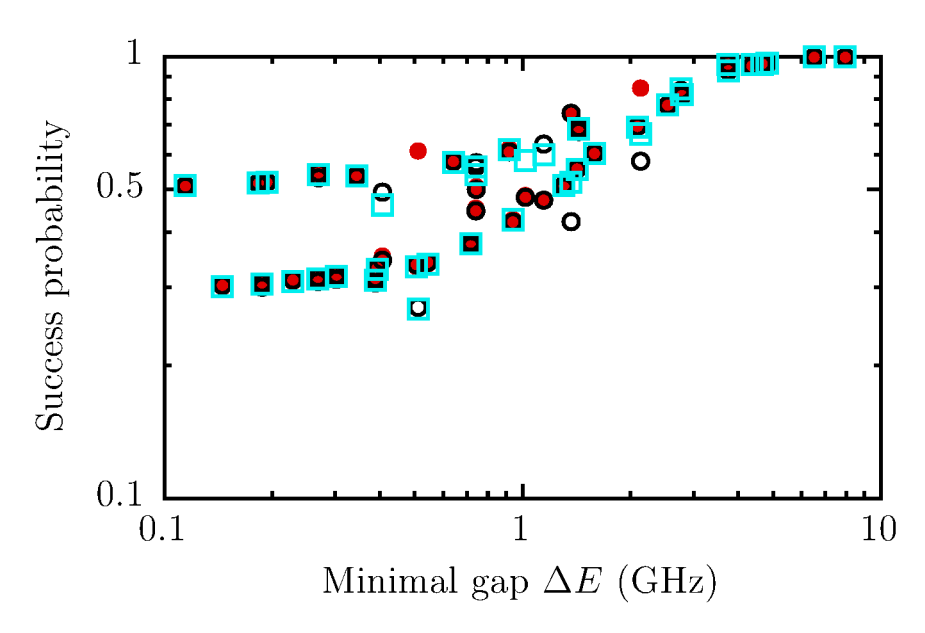


Figure 5.27: Success probabilities at the end of the annealing process with annealing time $t_a = 5$ ns as a function of the minimal energy gap ΔE obtained from the simulation of the full flux model Eq. (4.10) (black circles), from the ideal qubit model (red bullets) and from the simulation of two SQUIDs directly coupled as mentioned in the beginning of section 5.1.3 (cyan squares).

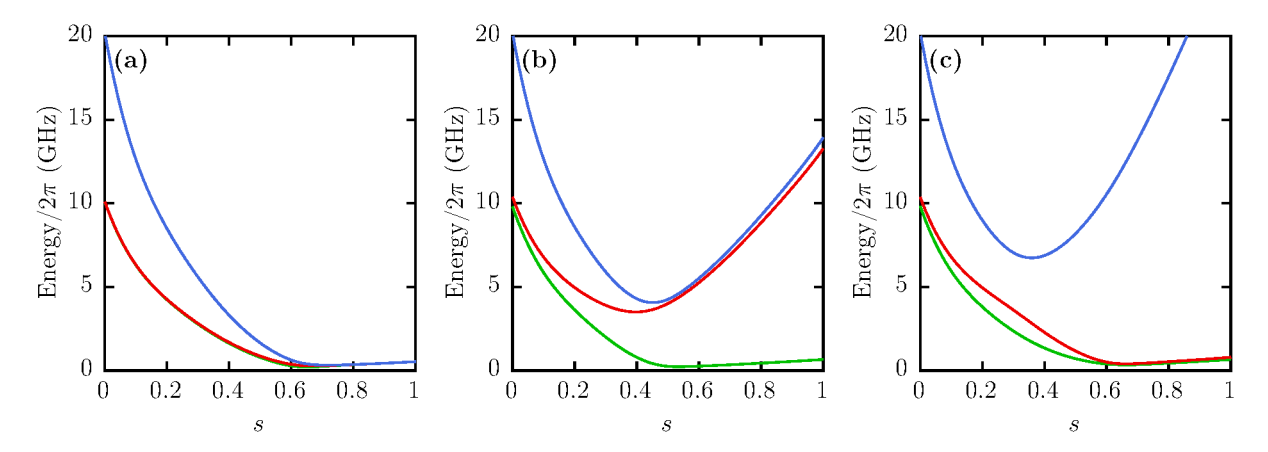


Figure 5.28: Three energy spectra obtained from the ideal qubit representation exhibiting different features corresponding to the classes 1, 2, and 3 in Fig. 5.26. Shown are the energy differences $E_1 - E_0$ (green), $E_2 - E_0$ (red) and $E_3 - E_0$ (blue).

In order to assess the size of the impact of the coupler, we compare the simulation results of the full flux model including the coupler with the results of the simulation of the SQUIDs corresponding to the qubits only, that is, the SQUIDs are directly coupled as described by the effective Hamiltonian given in Eq. (4.21). The results are shown in Fig. 5.27. We find that in most cases, the results fit perfectly with the results of the ideal qubit model and the full flux model simulations. There are a few data points that fit better with the results of the full flux model simulation than with the ideal qubit model results and a few for which it is the other way around. Also, some data points differ from both the full flux-model simulation and the qubit simulation results. Before we investigate this effect in more detail in Section 5.3.5, we study the three different classes of problem instances whose success probabilities for small energy gaps ΔE form clusters around approximately 0.3 (red data points in Fig. 5.26) or around approximately 0.5 (blue data points) or do not form clusters (green data points).

5.3.4 Three different classes of problem instances

In this section, we analyze in more detail the differences between the three classes of problem instances indicated by the three different colors of the data points from the ideal qubit model simulation in Fig. 5.26. These classes distinguish problem instances by characteristic features in the energy spectra. The first class of problems is characterized by energy spectra for which all three excited states come close in energy (see Fig. 5.28(a)), and the size of the minimal energy gap characterizes the separation of the ground state from the excited states. Corresponding problem instances are colored in red.

For the second class of problems (blue), only the first excited state comes close in energy to the ground state during the annealing process while the second and third excited states are separated from the lowest energy state by a large energy gap. An example is shown in Fig. 5.28(b). To the third class (green) belong those problems for which the energies of the first and the second excited states come close to the ground state energy during the annealing process and the third excited state is separated by a large energy gap (see Fig. 5.28(c)).

Considering the energy spectra, we can explain the splitting of the red and blue data points in Fig. 5.26. For the first class of problems (red) and minimal energy gaps $\Delta E \gtrsim 1\,\mathrm{GHz}$, we observe Landau-Zener behavior (see Fig. 2.3(b) in Section 2.3). For small minimal energy gaps, we find that the data points show deviations from the Landau-Zener theory. However, in these cases, we still observe non-adiabatic transitions. As long as the initial Hamiltonian Eq. (2.6) separates the energy levels, the ground state is approximately given by the uniform superposition state of all four computational basis states with small corrections due to the problem Hamiltonian Eq. (2.7) which, in this region, can be regarded as a perturbation. The energy gap is approximately given by $\Delta(s) = 2A(s)$. At the end of the annealing process, when the contribution of the initial Hamiltonian is reduced, that is $A(s) = \Delta(s)/2 \to 0$, the energy splitting is determined by the energy levels of the problem Hamiltonian Eq. (2.7). If the minimal energy gap is small, the system experiences a non-adiabatic transition and stays close to the ground state determined by the Hamiltonian at the time of this transition and which is close to the uniform superposition state. Thus, the success probability does not drop below 1/4.

A similar reasoning applies to the second class of problems (blue). We discuss this case with an example. Consider the case where J is positive and close to one, $h_2 = 0$, and $h_1 = \varepsilon$ with ε small. In the beginning of the annealing process, the energy splitting is again determined by the initial Hamiltonian where basically only the part proportional to J of the problem Hamiltonian acts as a perturbation, yielding the uniform superposition state as the ground state. For decreasing A(s) and increasing B(s), i.e, when JB(s) $A(s) > \varepsilon B(s)$, the problem Hamiltonian effectively splits the Hilbert space into the two subspaces $\{|\uparrow\uparrow\rangle, |\downarrow\downarrow\rangle\}$ and $\{|\uparrow\downarrow\rangle, |\downarrow\uparrow\rangle\}$ with eigenvalues -JB(s) and JB(s), respectively. The initial Hamiltonian can be regarded as a perturbation, causing a level splitting of $\Delta^2(s)/(2JB(s))$ within these subspaces. The ground state is then approximately given by $(|\uparrow\uparrow\rangle + |\downarrow\downarrow\rangle)/\sqrt{2}$. For further decreasing A(s) and increasing B(s), the level splitting within the subspaces due to the initial Hamiltonian is further reduced and it is dominated by the term proportional to ε of the problem Hamiltonian. For small ε , however, nonadiabatic transitions dominate during the annealing process. The system stays then approximately in the state $(|\uparrow\uparrow\rangle + |\downarrow\downarrow\rangle)/\sqrt{2}$. Thus, even for small minimal energy gaps ΔE , the success probability does not drop below 1/2 for this class of problems.

Those cases that show larger deviations belong to the third class represented by the green data points in Fig. 5.26, in particular to problems with parameters $J \approx 1$, $h_1 \approx -h_2 \approx \pm 1$. The green data points show a larger spread than the red and blue ones and explaining this only in terms of the energy spectrum seems difficult as the spectra for points with higher as well as lower success probabilities look almost identical.

Therefore, we have to take into account the results presented in Ref. [MNK09], namely that for quantum annealing with degenerate ground states, not all states are equally likely to be sampled. The green data points, especially for smaller gap sizes, are close to the three-fold degenerate cases with parameters $h_1 = -h_2 = \pm 1$, J = 1 or $h_1 = h_2 = \pm 1$, J = -1. For larger gaps, the problem instances are not that close to these cases and the spread in success probability is smaller (see Fig. 5.26). Let us consider the case $J \lesssim 1$, $h_1 = J + \varepsilon_1$, $h_2 = -(J + \varepsilon_2)$ as an example. The other cases work analogously. As mentioned previously, in the beginning of the annealing process, the ground state is determined by the initial Hamiltonian where the problem Hamiltonian acts as a perturbation. In the region where $JB(s) > A(s) > \varepsilon_i B(s)$, the ground state is basically determined by the

part $H_J = -JB(s)(\sigma_1^z - \sigma_2^z + \sigma_1^z\sigma_2^z)$ of the problem Hamiltonian which has a three-fold degenerate ground state. The basis states with the same energy -JB(s) are $|\uparrow\downarrow\rangle$, $|\uparrow\uparrow\rangle$ and $|\downarrow\downarrow\rangle$. Since in this vicinity $(A(s) > \varepsilon_i B(s))$, the initial Hamiltonian Eq. (2.6) rather than the correction in ε_i of the problem Hamiltonian acts as a perturbation, the first order corrections are in $\Delta(s)$ and we consider the initial Hamiltonian in the degenerate eigenspace spanned by $\{|\uparrow\downarrow\rangle, |\uparrow\uparrow\rangle, |\downarrow\downarrow\rangle\}$:

$$H' = -\frac{\Delta}{2} \begin{pmatrix} 0 & 1 & 1 \\ 1 & 0 & 0 \\ 1 & 0 & 0 \end{pmatrix}. \tag{5.52}$$

Diagonalizing this matrix gives the eigenvalue-eigenvector pairs

$$\left\{-\frac{\Delta}{\sqrt{2}}, \frac{\sqrt{2}|\uparrow\downarrow\rangle + |\uparrow\uparrow\rangle + |\downarrow\downarrow\rangle}{2}\right\}, \left\{0, \frac{|\uparrow\uparrow\rangle - |\downarrow\downarrow\rangle}{\sqrt{2}}\right\}, \left\{\frac{\Delta}{\sqrt{2}}, \frac{\sqrt{2}|\uparrow\downarrow\rangle - |\uparrow\uparrow\rangle - |\downarrow\downarrow\rangle}{2}\right\}. \tag{5.53}$$

The lowest energy state has a higher contribution in the direction of $|\uparrow\downarrow\rangle$, with a probability of 50% while $|\uparrow\uparrow\rangle$ and $|\downarrow\downarrow\rangle$ each only have a probability of 25% for being measured. This means that if the system follows an adiabatic evolution, the probability to measure the basis state $|\uparrow\downarrow\rangle$ is higher than for the other two basis states at this point. At the end of the annealing process, the spectrum is determined by the problem Hamiltonian including the corrections in ε_i . However, the energy splittings caused by the corrections in ε_i are again rather small such that when $\Delta(s) \to 0$, the system undergoes non-adiabatic transitions, staying close to the state $|\psi_G\rangle = (\sqrt{2}|\uparrow\downarrow\rangle + |\uparrow\uparrow\rangle + |\downarrow\downarrow\rangle)/2$ with different probabilities for the three computational states. This leads then to higher or lower success probability in $|\psi_G\rangle$. For example if $\varepsilon_i > 0$, the ground state is given by $|\uparrow\downarrow\rangle$ and the success probability is approximately 1/2. If $\varepsilon_1 > 0 > \varepsilon_2$, the ground state is $|\uparrow\uparrow\rangle$ with a success probability of about 1/4.

Figure 5.29 shows the spectrum of the case J=0.94, $h_1=0.99$ and $h_2=-1$ (solid lines) including the energies obtained by perturbation theory up to third order (see Appendix B.5) in the three regions: $-A(s)H_{\rm init}$ determines the spectrum and H_J is the perturbation (dashed lines with crosses in the left region shaded in yellow), H_J determines the spectrum and $-A(s)H_{\rm init}$ and the corrections in ε_i are the perturbations (dash-dotted lines with squares in the middle region shaded in pink), H_P determines the spectrum and $-A(s)H_{\rm init}$ is the perturbation (dotted lines with bullet points in the right region shaded in blue). Overlapping regions denote regions where neither of the applicable two versions of perturbation theory works perfectly well as the magnitude of the perturbation term is approximately of the same size as the Hamiltonian. Nevertheless, we find that the separation into the three regions allows us to describe the energy spectrum by perturbation theory very well and we can conclude that the reasoning with these three regions is a good approximate description. We also see that the region of the minimal gap is located where the transition between the second and third descriptions takes place.

Table 5.2 shows the numerical values for all cases plotted in Figs. 5.26 and 5.27. Looking deeper into which cases show the discrepancies between the flux model with direct coupling and the other two models (flux model with coupler and qubit model), we make two

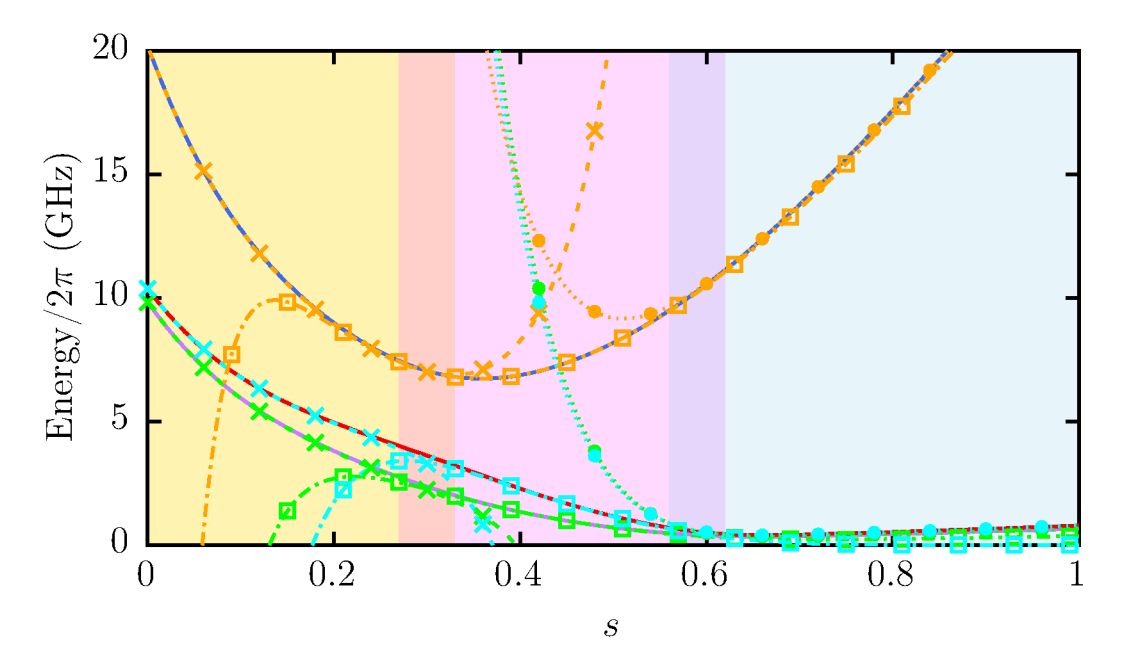


Figure 5.29: Instantaneous energy spectrum (solid lines) of the problem instance with parameters J=0.94, $h_1=0.99$ and $h_2=-1$ during the annealing process as a function of dimensionless time s, including the spectrum obtained from the three different versions of perturbation theory mentioned in the text (dashed lines with crosses in yellow region, dash-dotted lines with squares in pink region, and dotted lines with bullet points in blue region). Overlapping regions are regions where the perturbation and the unperturbed Hamiltonian are approximately of the same size and neither of the two versions of perturbation theory applies perfectly well. The energy difference $E_1 - E_0$ is colored purple/green, $E_2 - E_0$ is colored red/cyan and $E_3 - E_0$ is colored blue/orange.

observations: (i) Cases, for which the results of the flux model without coupler match better with the results of the flux model with coupler than with the results of the qubit model, are the ones where $J \approx 1$, $h_1 \approx -h_2 \approx \pm 1$. (ii) Cases, in which the simulation results of the flux model with direct coupling differ from the other two models, are the ones where $J \approx -1$ and $h_1 \approx h_2 \approx \pm 1$. All these cases belong to the class represented by the green data points (class 3) in Fig. 5.26.

5.3.5 Influence of the higher energy levels

The observed deviations cannot be caused by the coupler alone since the cyan squares in Fig. 5.27 of the flux model without coupler also show deviations. Thus, in this section, we study whether the presence of the higher energy levels can explain these observed deviations and the asymmetry between problem instances with negative and positive coupling constant J when including the coupler.

We investigate the spectra of two representative cases for the model of the directly coupled SQUIDs (with a reduced number of states to make the use of exact diagonalization feasible) to see how the higher energy levels behave. First, we look at a case ($h_1 = 0.02$, $h_2 = 0.08$, and J = 0.05) which yields a success probability that matches with the qubit model result to get an estimate of the accuracy of the reduced flux model (see

Table 5.2: Parameter values of the cases shown in Fig. 5.26, Fig. 5.27 and Fig. 5.34. a) Success probability for the qubit system ($t_a = 5 \text{ns}$) b) success probability for the full flux model with coupler ($t_a = 5 \text{ns}$) c) success probability for the flux model with directly coupled SQUIDs ($t_a = 5 \text{ns}$) d) percentage of successful runs on D-Wave's DW_2000Q_2 and DW_2000Q_2_1 chips ($t_a = 20 \mu \text{s}$, at least 10 reads).

$-\frac{2}{1}$	cmps ($t_a - 20$	μ s, at least				
h_1	h_2	J	minimal gap		ess prob		
	102		ΔE in GHz	a)	b)	c)	d)
0.2	0.2	0.2	7.958914	99.9	99.5	99.8	99.7
0.2	-0.2	0	6.524809	99.8	99.6	99.7	95.8
0.3	-0.3	0.1	6.509859	99.9	99.6	99.9	96.2
0.1	-0.1	-0.1	4.817172	96.5	96.3	96.4	94.0
0.9	0.7	-1	4.660374	96.3	96.2	96.0	93.9
0.99	-0.8	1	4.367788	95.8	95.2	95.9	94.1
0.1	0.1	0	3.750846	93.0	92.8	92.9	80.5
0.3	0.3	-0.2	3.740396	96.2	96.2	95.9	81.4
0.07	-0.07	0	2.786031	82.1	81.6	82.0	66.8
0.07	0.07	0	2.786031	82.1	82.1	82.0	66.9
0.9	-0.8	1	2.766581	83.8	83.9	84.6	80.0
0.02	0.08	0.05	2.542547	77.7	77.6	77.6	71.2
0.99	-1	0.94	2.134413	84.8	57.9	66.8	48.3
0.05	0.05	0	2.092326	69.3	69.4	69.2	56.8
0	-0.05	0.05	1.585987	60.3	60.3	60.3	55.6
0	0.05	1	1.433807	69.0	67.6	68.6	64.4
0	0.05	-1	1.433807	69.0	69.1	68.6	65.3
0.01	0.04	0.025	1.419405	55.6	55.7	55.5	50.4
0.99	-1	0.96	1.366784	74.7	42.3	51.9	38.1
0.99	1	-0.96	1.366784	74.7	74.4	51.9	46.9
0.02	-0.02	-0.02	1.305954	51.1	50.6	51.1	43.8
0.02	0.02	0.02	1.305954	51.1	51.2	51.1	43.9
0.95	-0.99	$0.98 \\ -0.98$	$1.145772 \\ 1.145772$	$47.5 \\ 47.5$	63.4	59.9	55.7
$0.95 \\ 0.99$	$0.99 \\ 0.96$	-0.98 -1	1.145772	48.4	47.3 48.0	$59.9 \\ 58.1$	$52.3 \\ 54.8$
0.99	-0.02	-1	0.939407	42.7	42.2	42.7	36.2
0.02	0.02	1	0.917871	61.8	60.8	61.5	59.0
0.96	-0.94	1	0.742309	50.7	57.5	56.2	55.1
0.96	0.94	-1	0.742309	50.7	50.0	56.2	54.0
0.98	-0.96	1	0.740480	45.4	56.3	54.0	53.4
0.98	0.96	-1	0.740480	45.4	44.7	54.0	51.0
0.01	-0.01	-0.01	0.716800	37.8	37.3	37.7	33.2
0.01	0.01	0.01	0.716800	37.8	38.0	37.7	33.9
0	0.02	-1	0.640932	57.9	57.8	57.7	57.0
0.01	0.009	0.002	0.543047	33.9	34.2	33.9	31.4
0.99	-1	0.98	0.510495	61.1	27.0	26.8	27.5
0.01	0.01	0	0.505201	33.5	33.8	33.5	31.7
0.99	-0.98	1	0.406202	35.3	49.3	46.1	47.2
0.99	0.98	-1	0.406202	35.3	34.6	46.1	45.6
0	-0.01	0.01	0.392828	33.0	33.2	33.0	31.6
0.005	0.005	0.005	0.388173	31.2	31.5	31.2	29.8
0.005	-0.005	-0.005	0.388173	31.2	30.7	31.2	29.1
0	0.01	1	0.343987	54.0	53.4	53.7	52.7
0	0.01	-1	0.343987	54.0	53.8	53.7	53.1
0.007	0	-0.01	0.302380	31.8	31.3	31.8	30.4
0.007	0	0.01	0.302380	31.8	32.0	31.8	30.5
1	0	-0.005	0.269309	54.0	53.1	54.0	52.8
1	0	0.005	0.269309	54.0	54.6	54.0	52.8
0.005	0.001	0.01	0.268263	31.4	31.6	31.4	30.2
0.005	-0.001	-0.01	0.268263	31.4	30.9	31.4	30.0
0.005	$0 \\ 0.005$	0.01	0.228548	30.9	31.2	30.9	29.6
0		0.5	0.193353	52.0	51.8	52.0	51.3
$0 \\ 0.005$	$0.005 \\ -0.001$	$-0.5 \\ 0.01$	0.193353 0.187420	$52.0 \\ 30.5$	51.9	52.0	52.3 29.3
0.005	-0.001	-0.01	0.187420 0.187420	$30.5 \\ 30.5$	$30.7 \\ 30.0$	$30.5 \\ 30.5$	$\frac{29.3}{28.4}$
0.005	0.001 0.005	-0.01	0.187420	50.5 52.0	50.0 51.5	50.5 51.8	$\frac{28.4}{50.7}$
0.005	0.003	-1	0.183074 0.183074	52.0 52.0	51.8	51.8	50.7
0.003	0	0.01	0.145233	30.1	30.3	30.1	29.2
0.003	0.003	-1	0.1145235 0.114519	51.2	50.5	50.1 51.0	51.0
0	0.003	1	0.114519	51.2	50.8	51.0	50.1
		-	5.211510	~ + - 4	50.0		~ ~ . 1

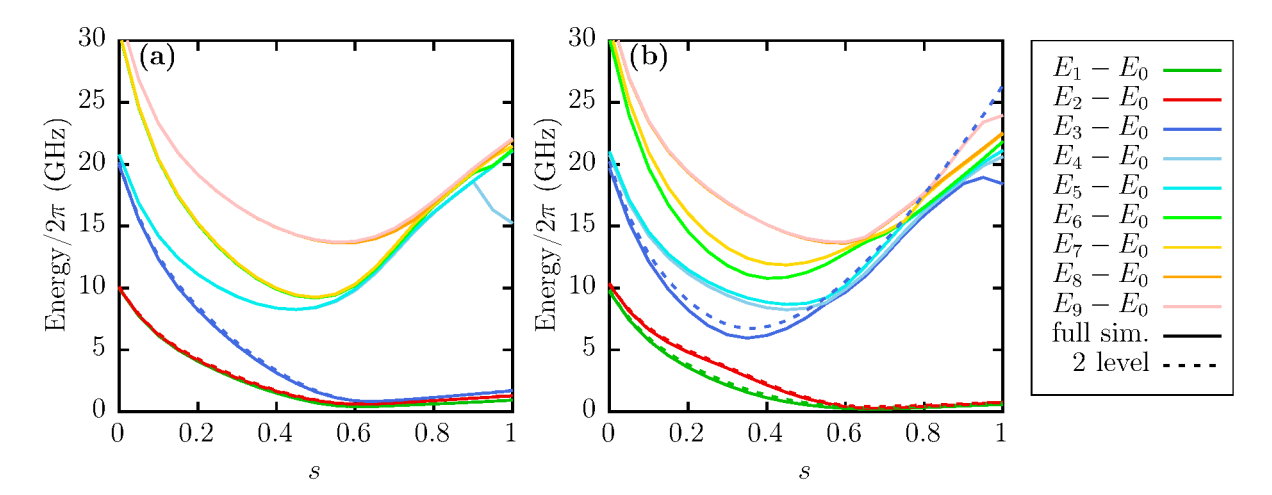


Figure 5.30: The ten lowest energies (relative to the ground state energy) of the flux model with reduced number of states during the annealing process for the case with parameters (a) $h_1 = 0.02$, $h_2 = 0.08$, and J = 0.05, (b) $h_1 = 0.99$, $h_2 = -1$, and J = 0.94. In panel (a), the curves for the first (green) and second (red) excited states are almost on top of each other.

Fig. 5.30(a)). We find that the spectrum for the four lowest energies obtained from the SQUID simulation (solid lines) fits nicely with the spectrum obtained from the qubit representation (dashed lines) meaning that the simulation with a reduced number of states yields results which are sufficiently accurate for this purpose. The results for the case with $h_1 = 0.99$, $h_2 = -1$ and J = 0.94 are shown in Fig. 5.30(b) and we can see some deviations between the spectra obtained from the flux model and the qubit model. For the two lowest energy differences we find only small deviations but the third excited state crosses the higher energy levels. Nevertheless, since the third excited state is already quite well separated from the three lower energy levels, this should not have an effect on the final success probability. This is also supported by the findings that at the end of the annealing process, the probability for the third excited state ($\approx 10^{-6}$ %) is very low, even much lower than the probability for leakage (0.2%).

These observations suggest that states which do not belong to the computational subspace have some small contributions to the lowest energy states and their presence has some effect on the distribution of the basis states for the three-fold degenerate and close-to-degenerate cases discussed previously; for example, by lifting or changing the (near) degeneracy in the pink region in Fig. (5.29). This is the region where the higher energy levels are closest to the three lowest energy levels and also the leakage is largest (see Fig. (5.25)). Thus, it is reasonable to assume that the lowest energy states have some small contributions outside of the computational subspace, which lead effectively to a different ground state in the critical region shortly before the non-adiabatic transition happens. This would support the hypothesis that in these cases the ground state of the flux model does not lie in the computational subspace during the whole annealing process. The nice agreement of the energies for the lowest energy states can then be explained with the variational ansatz: Assume that during the complete annealing process the ground state of the flux model can be described by a state of the form

$$|\psi_{VA}\rangle = \varrho|\uparrow\uparrow\rangle + \zeta|\uparrow\downarrow\rangle + \xi|\downarrow\uparrow\rangle + \nu|\downarrow\downarrow\rangle, \tag{5.54}$$

where ϱ , ζ , ξ and $\nu \in \mathbb{C}$ have to be determined by minimizing $\langle \psi_{\text{VA}} | H_{\text{total}} | \psi_{\text{VA}} \rangle$ under the constraint $|\varrho|^2 + |\zeta|^2 + |\xi|^2 + |\nu|^2 = 1$. This minimization corresponds to diagonalization of the Hamiltonian H_{total} projected onto the computational subspace and taking the smallest energy eigenvalue, which corresponds to the consideration of the qubit model Hamiltonian. According to the variational theorem, the minimal energy E_{VA} found by this procedure, is greater or equal to the true ground state energy E_0 . From the variational theorem, we also know that if the ground state found with the variational ansatz $|\psi_{VA}\rangle$ is close to the true ground state of the system $|\psi_0\rangle$, then the energy E_{VA} is close to E_0 . However, if we only know that the energy E_{VA} is close to the energy E_0 , then the state $|\psi_{\text{VA}}\rangle$ is not necessarily close to the state $|\psi_0\rangle$. Thus, our results suggest that the ground state of the flux model does have some small contributions outside of the computational subspace, whose magnitudes depend on the particular problem instance. Interestingly, the presence of the coupler seems to compensate for these effects for the cases with $J \approx -1$, since the simulation results of the full flux model including the coupler nicely match with the results of the qubit model, also for these close-to-degenerate cases. However, for the problem instances with $J \approx 1$, the effect seems to be enhanced (see Fig. 5.27 and Table 5.2). In the following, we investigate the cause of the deviations in more detail.

Let us consider the Hamiltonian $H_{\rm CS}$ of the computational subspace and the Hamiltonian $H_{\rm HL}$ of the higher energy levels. At this moment, the coupler is not yet taken into account. Then we can write the Hamiltonian of the flux model as

$$H_{\text{total}} = \begin{pmatrix} H_{\text{CS}} & \lambda V \\ \lambda V^{\dagger} & H_{\text{HL}} \end{pmatrix}, \tag{5.55}$$

where the matrix V describes the coupling between the two subspaces and λ is considered to be the small perturbation parameter. We can use the Schrieffer-Wolff transformation [SW66] to eliminate the coupling between the subspaces and obtain an effective Hamiltonian for the computational subspace (since this is the part that we are interested in). In order to do so, we need to find a transformation matrix $\exp(-i\widetilde{S})$ such that $\exp(i\widetilde{S})H\exp(-i\widetilde{S})$ yields a block-diagonal matrix where the two subspaces are effectively decoupled. We apply the procedure described in Ref. [Gam13]. To remove the coupling to first order in λ , we have the condition for

$$\widetilde{S} = \begin{pmatrix} 0 & S \\ S^{\dagger} & 0 \end{pmatrix}, \tag{5.56}$$

that

$$i\left[\widetilde{S}, \begin{pmatrix} H_{\rm CS} & 0\\ 0 & H_{\rm HL} \end{pmatrix}\right] = -\begin{pmatrix} 0 & \lambda V\\ \lambda V^{\dagger} & 0 \end{pmatrix}. \tag{5.57}$$

Which yields the equation (and its Hermitian conjugate)

$$H_{\rm CS}S - SH_{\rm HL} = -i\lambda V. \tag{5.58}$$

Equation (5.58) is the Sylvester equation which has a unique solution if and only if $H_{\rm CS}$ and $H_{\rm HL}$ do not have common eigenvalues. Mostly, this is true in our case; however, we found in Fig. 5.30(b) that during the annealing process the highest energy state of the computational subspace attains an energy similar to the ones of some of the low energy

states outside the computational subspace. Thus, we expect that at the crossing points (and when the energies grow very close), if a solution of Eq. (5.58) exists, it is not unique.

This means that if a computational state has an energy close to the energy of one or more states outside the computational subspace, these states cannot be (uniquely) separated into two distinct subspaces with effectively no coupling. Therefore, in such a case the method breaks down and we cannot use the Schrieffer-Wolff transformation to obtain the block-diagonal effective Hamiltonian in this region.

Since \widetilde{S} is block off-diagonal (and linear in λ), terms quadratic in λ are only contained in the block-diagonal parts and the effective Hamiltonian up to second order in λ is given by

$$H^{\text{eff}} = \begin{pmatrix} H_{\text{CS}} & 0 \\ 0 & H_{\text{HL}} \end{pmatrix} - \frac{1}{2} \begin{bmatrix} \widetilde{S}, \begin{bmatrix} \widetilde{S}, \begin{pmatrix} H_{\text{CS}} & 0 \\ 0 & H_{\text{HL}} \end{pmatrix} \end{bmatrix} \end{bmatrix} + i \begin{bmatrix} \widetilde{S}, \begin{pmatrix} 0 & \lambda V \\ \lambda V^{\dagger} & 0 \end{pmatrix} \end{bmatrix} + \mathcal{O}(\lambda^{3})$$

$$= \begin{pmatrix} H_{\text{CS}}^{\text{eff}} & 0 \\ 0 & H_{\text{HL}}^{\text{eff}} \end{pmatrix} + \mathcal{O}(\lambda^{3}), \tag{5.59}$$

where

$$H_{\rm CS}^{\rm eff} = H_{\rm CS} - \frac{1}{2} \left(S S^{\dagger} H_{\rm CS} + H_{\rm CS} S S^{\dagger} \right) + S H_{\rm HL} S^{\dagger} + i \lambda \left(S V^{\dagger} - S^{\dagger} V \right), \tag{5.60a}$$

$$H_{\rm HL}^{\rm eff} = H_{\rm HL} - \frac{1}{2} \left(S^{\dagger} S H_{\rm HL} + H_{\rm HL} S^{\dagger} S \right) + S^{\dagger} H_{\rm CS} S + i\lambda \left(S^{\dagger} V - V^{\dagger} S \right). \tag{5.60b}$$

Since we have to construct the matrices V, S (which grow quadratically with the number of considered states per SQUID) and $H_{\rm HL}$ (which grows with a power of four), we implement the Schrieffer-Wolff transformation with a variable number of states to be taken into account and increase this number gradually until the computed effective Hamiltonian saturates. We find that considering the 8 lowest states per (qubit-)SQUID is sufficient for this purpose.

We use the Linear Algebra PACKage (LAPACK) to solve Eq. (5.58) numerically and compute $H_{\rm CS}^{\rm eff}$ for a few test cases. We show two examples in Figs. 5.31 and 5.32. Panel (a) shows the terms of the projected Hamiltonian (dashed lines) and the corresponding ones of the effective Hamiltonian (solid lines). To make the differences more clear, we plot in panel (b) the differences of the terms occurring in the effective Hamiltonian (terms which are not shown are, up to numerical imprecision, equal to zero). In panel (c), we plot the probabilities of the computational states in the instantaneous ground state. Large deviations between the probabilities of the instantaneous ground states, corresponding to the projected and the effective Hamiltonians, during the annealing process may also indicate a deviation in the success probabilities for fast annealing if the minimal energy gap is not large enough. Panel (d) shows the instantaneous energy spectrum during the annealing process. Based on the results (not all data is shown), we make the following observations.

- Some of the correction terms are independent of the signs of J and h_i ; for instance the corrections proportional to σ_i^x , if present, are positive.
- The magnitudes and the particular dependence on s of the correction terms depend on the values of the parameters J and h_i .

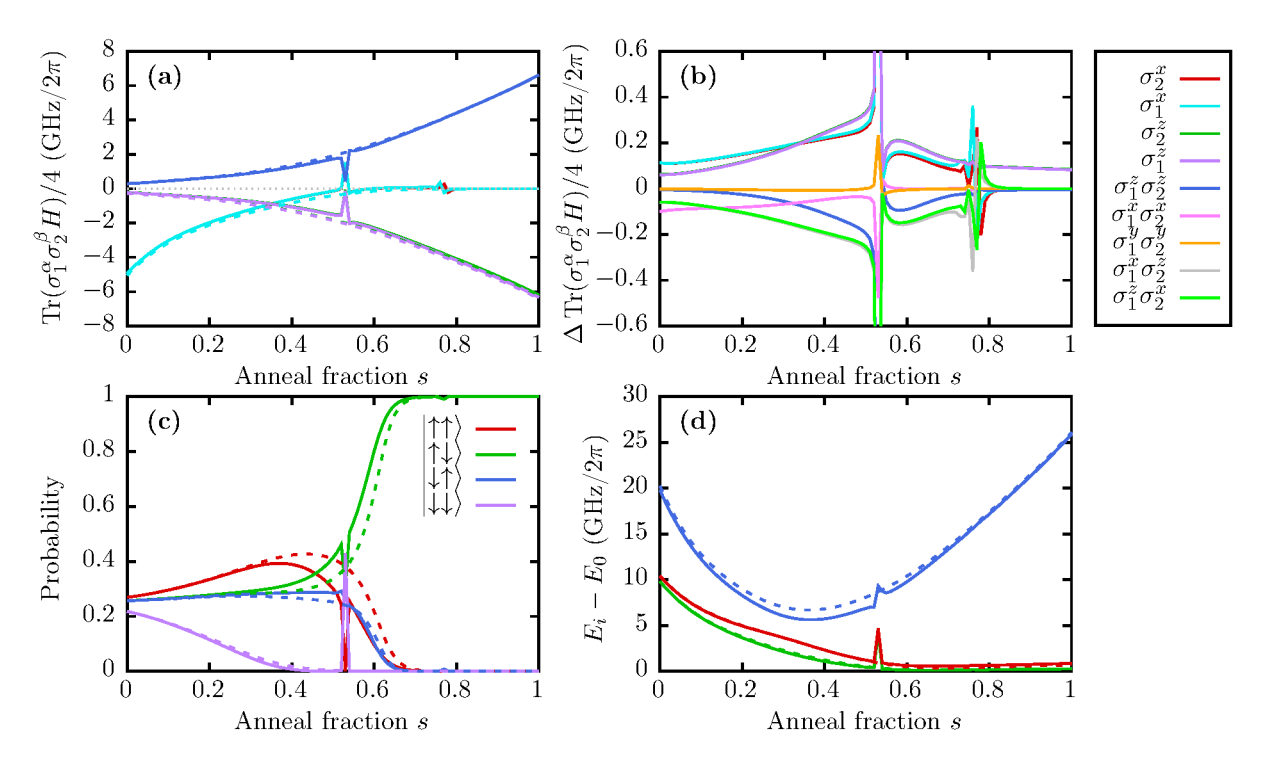


Figure 5.31: Comparison between the projected, i.e., ideal qubit Hamiltonian (dashed lines) and the effective Hamiltonian $H_{\text{CS}}^{\text{eff}}$ (solid lines). The parameters of the problem instance are J=-1, $h_1=0.96$ and $h_2=0.94$. (a) The terms (see legend on the right) of the Hamiltonian during the annealing process. At two points, we see spikes in the data. (b) Differences in the terms (see legend) of the ideal Hamiltonian and the effective Hamiltonian. (c) The probabilities for the computational states of the instantaneous ground state. (d) The instantaneous energy spectrum. In panels (a) and (b), the purple and dark-green (σ_1^z and σ_2^z) and the cyan and red (σ_1^x and σ_2^x) curves are almost on top of each other. Additionally, in panel (b), the bright-green and gray ($\sigma_1^z\sigma_2^x$ and $\sigma_1^x\sigma_2^z$) curves are almost on top of each other.

- The effective Hamiltonian also has contributions in $\sigma_1^x \sigma_2^x$, $\sigma_1^y \sigma_2^y$, $\sigma_1^x \sigma_2^z$, and $\sigma_1^z \sigma_2^x$ which vanish for $s \to 1$.
- For $s \gtrsim 0.8$, all correction terms except the ones proportional to σ_i^z vanish.
- Problem instances with a large gap may show considerable differences between $H_{\text{CS}}^{\text{eff}}$ and H_{CS} , but these differences have little influence on the actual final ground state of the system (due to the large gap).
- In cases where one or more of the higher energy levels exhibit an (avoided) level crossing with one or more of the computational states, the Schrieffer-Wolff transformation breaks down and we observe (divergent) spikes in the plot shown in Fig. 5.31 at positions where the third excited energy crosses the non-computational energy levels (see blue dashed line in Fig. 5.30(b)). Curves before and after such a divergence are often separated by an offset. This might be an indication that up to second order in λ , the transformation is not accurate enough in regions around the (avoided) crossings or that the Schrieffer-Wolff transformation is not applica-

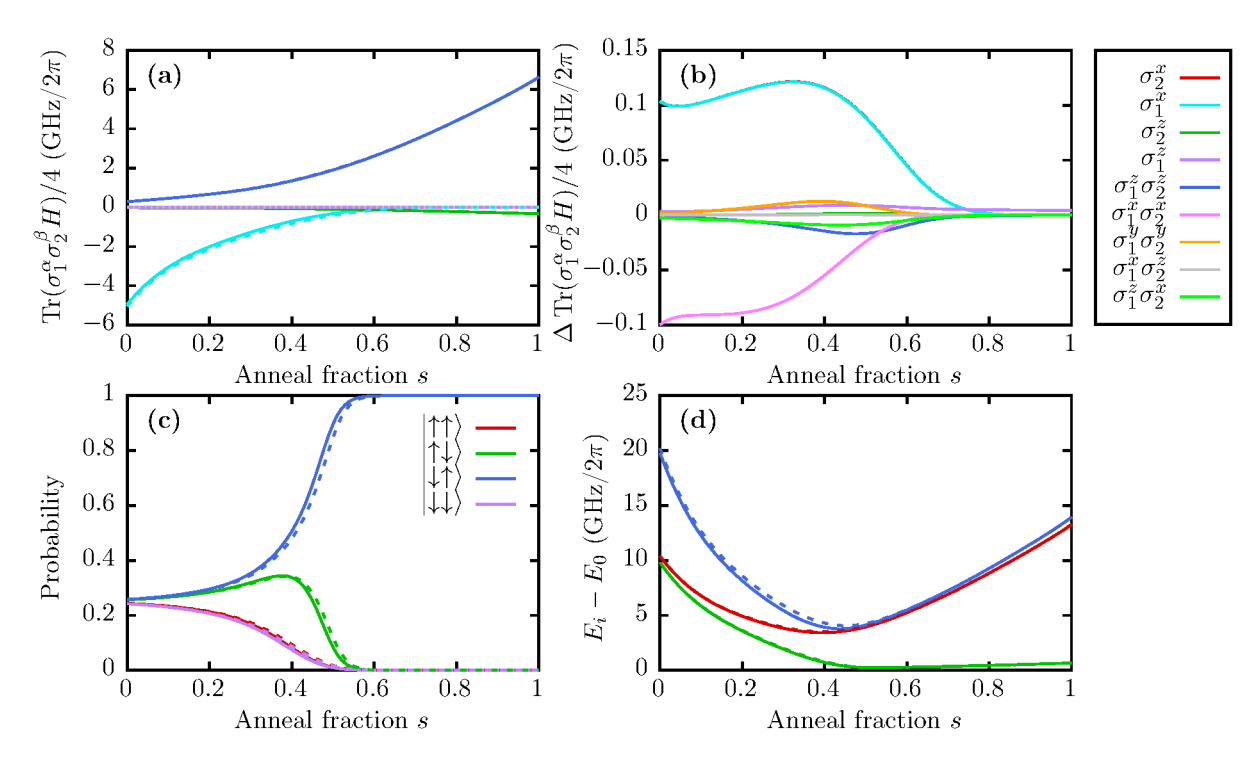


Figure 5.32: Same as Fig. 5.31 but for the problem instance with parameters J=-1, $h_1=0$ and $h_2=0.05$. In panels (a) and (b), the cyan and red (σ_1^x and σ_2^x) curves are on top of each other and in panel (b), in addition, the dark-green and gray (σ_2^z and $\sigma_1^x\sigma_2^z$) curves are almost on top of each other.

ble in larger regions around the (avoided) crossings although a unique solution of Eq. (5.58) exists.

All these observations are consistent with the previous results. However, we found an explanation why this particular class of problem instances shows considerable deviations in the success probability compared to the ideal qubit model. We found by applying a Schrieffer-Wolff transformation that the higher energy levels introduce stronger correction terms in σ_i^z than in $\sigma_i^z\sigma_i^z$ during the annealing process and only corrections in σ_i^z terms close to and at the end of the annealing process, effectively lowering the magnitudes of the h_i for this particular class of problem instances. In the three-fold degenerate case $J=h_1=1, h_2=-1$, we find that the state $|\uparrow\downarrow\rangle$ is no longer contained in the ground state space due to the non-vanishing correction terms in σ_i^z . This still holds if we consider the cross-talk terms (last line in Eq. (4.32)) which effectively increase the magnitudes of the h_i . For the close-to-degenerate cases where the ground state is still given by the correct state, the imbalance between the corrections in the σ_i^z - and $\sigma_1^z\sigma_2^z$ -terms changes the effective spectrum during the annealing process, i.e., the position and size of the minimal energy gap which then leads to enhanced or reduced success probabilities for fast annealing.

Up to now, we have only considered the case of direct coupling without the coupler. Now we ask, if we can generalize these results and use them to explain at least qualitatively the asymmetry in the case including the coupler. We find that this is indeed the case. We already obtained an effective Hamiltonian where the coupler is decoupled from the other two SQUIDS (see Eq. (4.21)). This Hamiltonian is almost equal to the Hamiltonian of

the two directly coupled SQUIDs. We only have to replace E_L by \widetilde{E}_L (see Eq. (4.22)) and use Eq. (4.27) to replace $\beta_{\text{eff}}/(1+\beta_{\text{eff}})$ by J.

For cases with $J \approx -1$ and $h_1 \approx h_2 \approx 1$, we find that the combination of both effects leads to a much smaller deviation than when both effects are treated separately. For instance, A(s) appeared to be enlarged when including the coupler, but it is effectively reduced when including the higher energy levels. And although the magnitude of the σ_i^z and $\sigma_1^z \sigma_2^z$ -terms is in both cases reduced, the relative difference appears to be conserved in the combined case. Thus, in these cases, the probabilities of the ground state for the effective Hamiltonian $H_{\text{CS}}^{\text{eff}}$ including the replacement $E_L \to \widetilde{E}_L$ are very close to the probabilities of the ground state for the projected Hamiltonian Eq. (4.32) where E_L is not replaced by E_L . This can be seen in Fig. 5.33(a)-(b) where the dash-dotted lines indicate the projected Hamiltonian with E_L , the dotted lines indicate the effective Hamiltonian with E_L , the dashed lines indicate the projected Hamiltonian with E_L and the solid lines indicate the effective Hamiltonian with E_L . We see that for the probabilities, the solid lines are much closer to the dash-dotted lines (which also correspond to the qubit Hamiltonian) than the dotted lines. This suggests that for this case (and similar cases) the effects of the coupler and the higher energy levels cancel each other (at least partially). We do not find perfect agreement but this is not surprising since we used the approximate Hamiltonian Eq. (4.21) and the Schrieffer-Wolff transformation only up to second order. However, the qualitative agreement is apparent. Figures 5.33(c) and (f) show the instantaneous energy spectrum with the spikes at the positions of the (avoided) level crossings with energy levels outside the computational space for the two plotted example cases, respectively.

In those cases where $J \approx 1$ and $h_1 \approx -h_2 \approx \pm 1$, we observe the opposite phenomenon: A(s) (the negative of the prefactor of the σ_i^x terms) is effectively even lower than expected from the replacement $E_L \to \widetilde{E}_L$, see Fig. 5.33(d). Furthermore, the probabilities corresponding to the projected Hamiltonian with E_L (dash-dotted lines in Fig. 5.33(e)) differ strongest from the probabilities corresponding to the effective Hamiltonian with \widetilde{E}_L (solid lines). These observations also explain why the simulation results and the calculated annealing function A(s) including \widetilde{E}_L (dashed lines in Figs. 5.21) do not match perfectly well. The results obtained from the simulation include the correction terms induced by the higher energy levels of the (qubit-)SQUIDs which effectively lower A(s) during the annealing process in both cases. For cases with $h_1 = h_2 = 0$, the correction terms proportional to $\sigma_1^z \sigma_2^z$ are small compared to the corrections in σ_i^x and there are no corrections in σ_i^z .

This unsymmetric feature is evidence that the higher energy levels in combination with the shift of the inductive energy caused by the coupler are the reason for the unsymmetric deviations in the success probabilities seen previously. These results also suggest that the corrections due to the coupler and due to the higher energy levels are of a similar type but, depending on the problem instance, with the same or opposite sign. This would imply that both effectively change the inductive energy of the SQUID. In the case of the coupler, this change of the inductive energy depends on the sign of J. In the case of the higher energy levels, the change of the inductive energy would always be a reduction (at least for this class of problem instances; for $J = h_1 = h_2 = 1$, we actually see an increase which suggests that the sign and magnitude of the change depends on a combination of J, h_1 and h_2).

Can we explain some of the reasons for these observations? The eigenvalues of $E_L\varphi_i$,

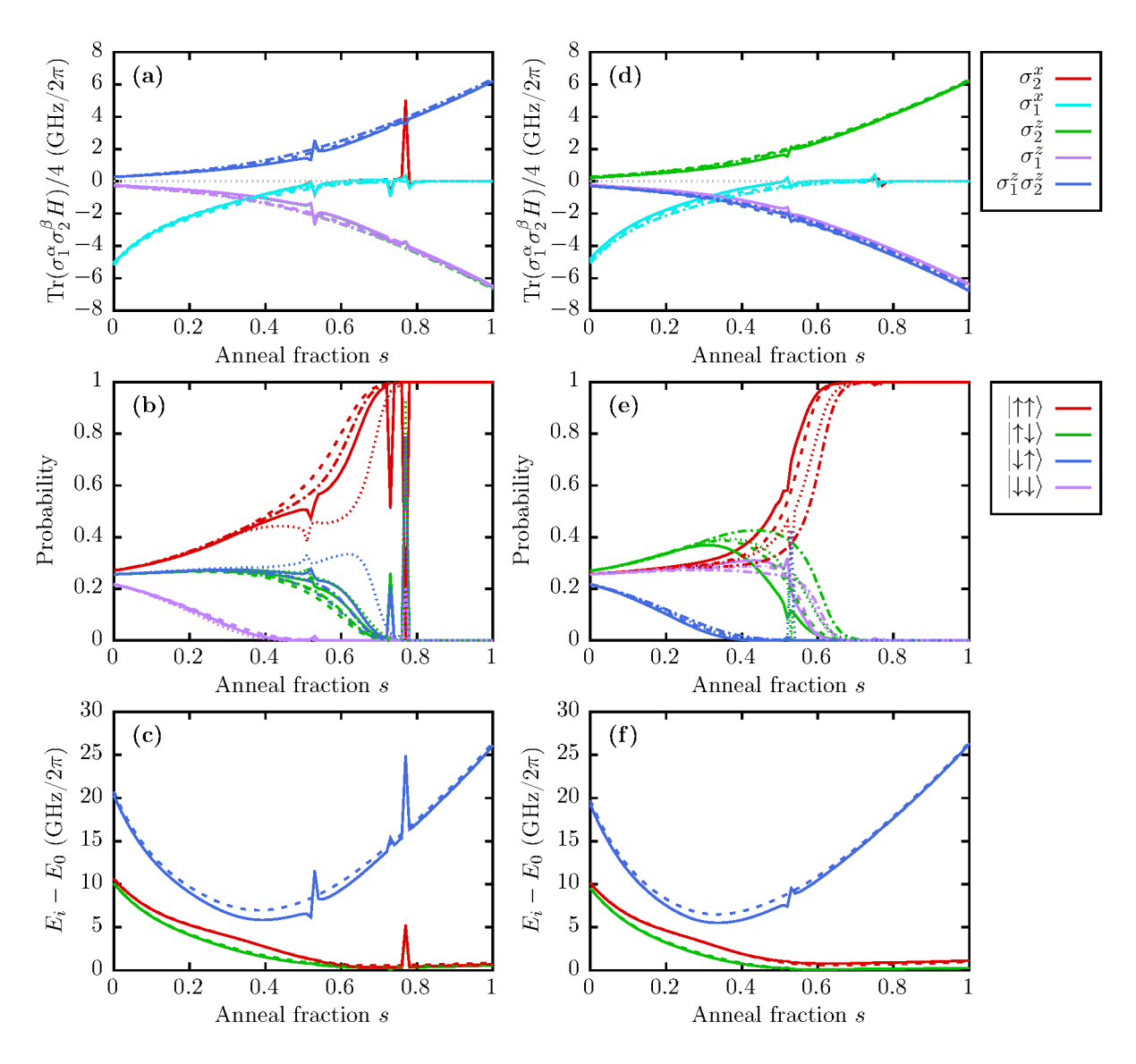


Figure 5.33: Comparison between the projected (dashed and dash-dotted lines) and effective (dotted and solid lines) Hamiltonian with inductive energy E_L (dash-dotted and dotted lines) and \widetilde{E}_L (dashed and solid lines). Panels (a)-(c) show data for the case J=0.96, $h_1=0.99$ and $h_2=1$ and panels (d)-(f) show the case J=1, $h_1=0.96$ and $h_2=-0.94$. Panels (a) and (d) show the coefficients of the terms listed in the legend on the right. The cyan and red (σ_1^x and σ_2^x) curves are, except at the spikes, on top of each other. In panel (a), additionally the purple and green (σ_1^z and σ_2^z) curves are (almost) on top of each other. Panels (b) and (e) show the probabilities to find the computational states if the system is in the instantaneous ground state. Panels (c) and (f) show the instantaneous energy spectrum.

which we labeled $\pm I_p/(2e)$, depend on the inductive energy. Thus, we should actually label it $I_p^{(J)}$ to make this clear. The external fields φ_i^x are linear in I_p (see Eq. (4.29)), i.e., they would in principle depend on the effective inductive energy of the SQUID. Since providing each qubit with its own time-dependent signal is not practicable in a large-scale experiment but φ^x of multiple qubits is controlled through the same control signal (individual tuning is only needed for the time-independent parameter h_i) [Har+10b], we used the values for $I_p^{(0)}$ computed from a single SQUID, i.e., with J=0. In the Hamiltonian Eq. (4.28) (including the dependence on s)

$$H_{\text{eff,sub}} \approx -\frac{\Delta(s)}{2} (\sigma_1^x + \sigma_2^x) - \frac{I_p^{(J)}(s)}{2e} (\varphi_1^x(s)\sigma_1^z + \varphi_2^x(s)\sigma_2^z) - \frac{J\gamma M^2 I_p^{(J)}(s)^2}{L_{\text{eff}}} \sigma_1^z \sigma_2^z + \frac{\widetilde{E}_L}{E_L} \frac{J\gamma I_p^{(J)}(s)M^2}{2e(L + L_{\text{CJJ}}/4)L_{\text{eff}}} (\varphi_1^x(s)\sigma_2^z + \varphi_2^x(s)\sigma_1^z),$$
(5.61)

we then have two different values for $I_p^{(J)}(s)$. Since all $I_p^{(J)}(s)$ entering the annealing function B(s), except the one in $\varphi_i^x(s)$, are obtained from the actual inductive energy, only $I_p^{(0)}(s)$ in

$$\varphi_i^x(s) = h_i \frac{2eI_p^{(0)}(s)M^2\gamma}{L_{\text{eff}}} = h_i \frac{2e(I_p^{(J)}(s) + \epsilon_J(s))M^2\gamma}{L_{\text{eff}}}$$
(5.62)

is actually slightly different from the others with some J-dependent correction ϵ_J . This correction then only occurs in terms proportional to σ_i^z

$$H_{\text{eff,sub}} \approx -\frac{\Delta(s)}{2} (\sigma_1^x + \sigma_2^x) - \left(B(s) + \frac{I_p^{(J)}(s)\epsilon_J(s)M^2\gamma}{L_{\text{eff}}} \right) (h_1\sigma_1^z + h_2^x\sigma_2^z) - JB(s)\sigma_1^z\sigma_2^z + JB(s)\frac{\widetilde{E}_L}{E_L} \frac{\left(1 + \epsilon_J(s)I_p^{(J)}(s)^{-1} \right)M^2\gamma}{(L + L_{\text{CJJ}}/4)L_{\text{eff}}} (h_1\sigma_2^z + h_2\sigma_1^z).$$
(5.63)

What would change if we had taken into account the change in $I_p^{(J)}$ induced by the coupler? The probabilities would follow more closely the dotted lines shown in Fig. 5.33(b) and (e). That is, the deviations would be more symmetric like in the case without the coupler (see also cyan squares in Fig. 5.27). The SQUIDs used by D-Wave Systems Inc. have an integrated L-tuner which is an additional CJJ loop in the main loop and which is used to undo effective changes in the inductance caused by the coupling [Har+10a]. Thus, results from the real device may be closer to the results from the simulation without the coupler.

5.3.6 Brief summary of the results

Summarizing the results, we found that in most cases the two-level approximation works very well with regard to the success probability and also the evolution during the annealing process. We only found a few problem instances which showed larger deviations when comparing the simulation results with the ideal qubit model. These instances were all found to belong to a particular class and they all have in common that their ground state is almost three-fold degenerate. Further investigation revealed that for these instances,

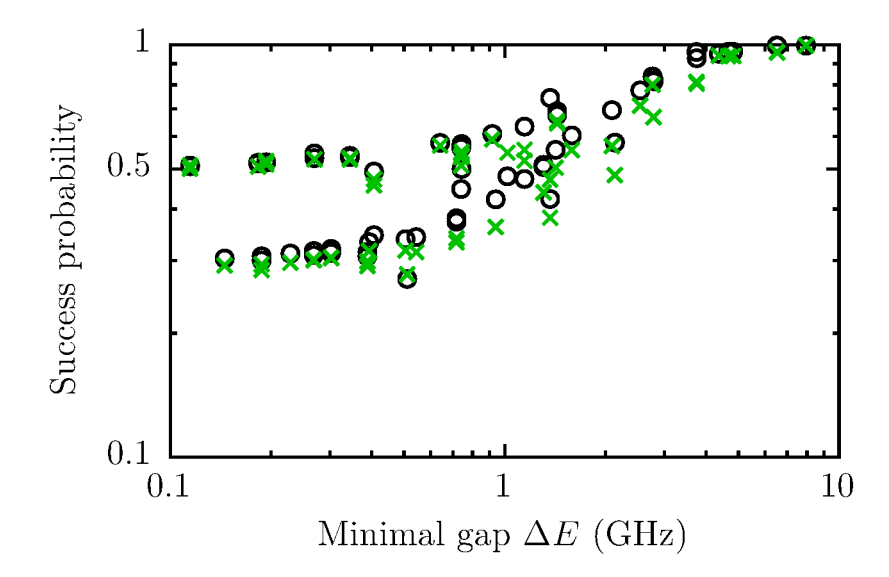


Figure 5.34: Success probabilities at the end of the annealing process with annealing time $t_a = 5$ ns as a function of the minimal energy gap ΔE obtained from the simulation of the flux model Eq. (4.10) (black circles), and from the D-Wave 2000Q quantum annealer with annealing time $t_a = 20 \,\mu\text{s}$ (green crosses).

the difference between the ideal qubit Hamiltonian and an effective Hamiltonian obtained from a Schrieffer-Wolff transformation, eliminating effectively the coupling between the qubit subspace and the higher energy states, is large enough to have visible effects on the success probability.

5.3.7 Comparison with the experiment on the D-Wave 2000Q quantum annealer

Another interesting point is the comparison of the simulation results to results obtained from the real device. The shortest annealing time that can be set on the D-Wave 2000Q quantum annealer is 1μ s which is much longer than the 5 ns of the flux model simulation. Using the qubit model Eq. (2.8) to compute the success probabilities after the annealing process with annealing time $1\,\mu s$ for the investigated cases, we find that the success probabilities are very close to one. Thus, we would expect the D-Wave machine to find the ground state with probability almost one for the cases under investigation. However, running these cases on the D-Wave machine with annealing time $20 \,\mu s$, we do not find the ground state with probability close to one, but rather, the frequencies of measuring the ground state match the success probabilities from the simulation with 5 ns annealing time quite well. The results are shown in Fig. 5.34. At this point, the nice agreement seems likely to be a coincidence. Nevertheless, the fact that the results for the success probability from the real machine differ so much from one suggests that there are still different effects which are not captured by the full, but isolated flux model (at zero temperature). The reason which seems most obvious for the deviation from the expected results is the coupling of the system to the environment. Therefore, in the following chapter, we discuss in more detail the effects due to coupling to the environment for the ideal qubit model in the context of quantum annealing.

Chapter 6

Quantum annealing in the presence of an environment

Although adiabatic quantum computation is considered to be more robust against noise and decoherence than the gate model of quantum computation since the computation takes place in the energy eigenbasis, the robustness turns out to be rather limited; it only holds in certain cases such as weak coupling of the system to the environment or a Markovian (i.e., almost "memoryless") environment [CFP01; SL05; AJN06; ATA09; AAN09; Joh+09; Har+10b; AL15. Moreover, there seems to be an optimal annealing time which maximizes the success probability in the case of open-system adiabatic quantum computation [AJN06; AL15]. In the closed-system case, the annealing time cannot be too long with respect to the success probability as the success probability approaches one for infinite annealing times. However, infinite annealing times would not be useful in practice. In the open-system case and for weak coupling between the qubit system and the environment, the success probability is expected to reach, in the limit of long annealing times, the probability in thermal equilibrium at finite temperature [AL15] which may be large enough (in contrast to the strong-coupling case where the success probability approaches $1/2^N$ – the probability in thermal equilibrium at infinite temperature [AL15] – and there is no advantage over random sampling). However, in the case where basically thermal relaxation determines the success probability, there is no expected speedup (i.e., different scaling and not only a potentially smaller prefactor) over classical algorithms [ALT08].

The debate about noise and decoherence also led to many studies tackling the question if open-system adiabatic quantum computation or quantum annealing at finite temperature only performs classical thermalization (or if it can be described by some other classical model) or if it actually exhibits quantum features [Joh+11; Boi+13; SS13; Boi+14; Shi+14; Alb+15a; Alb+15b; Boi+16].

Additionally, the case of thermally assisted quantum annealing has been studied [ALT08; Dic+13; Arc+17]. In certain cases, such as in the case of a super-Ohmic environment, thermal mixing at the avoided crossing may lead to an improved success probability [ALT08], or fast annealing in the presence of transverse coupling to the environment may also lead to an improvement in the success probability [Arc+17]. An experiment showing thermally assisted quantum annealing has also been reported [Dic+13], quantum annealing at finite temperature yielding higher success probabilities than expected from quantum annealing at zero temperature.

For long annealing times, when the quantum annealer operates in the quasistatic

Table 6.1: Percentage of successful outcomes (ground state) obtained from D-Wave's DW_2000Q_2 chip (1000 reads) for three different problem instances and four different annealing times. The minimal and final gap (in GHz) are denoted by ΔE_{\min} and Δ_p , respectively. The probabilities to find the ideal qubit system in the ground state for $t_a \geq 1 \,\mu$ s is very close to 1 for all three cases.

Case	J	h_1	h_2	ΔE_{\min}	Δ_p	Success rates in %			
						$1\mu\mathrm{s}$	$20\mu\mathrm{s}$	$100\mu\mathrm{s}$	$1\mathrm{ms}$
(a)	-1	0.96	0.94	0.627	1.407	51.4	52.9	53.6	55.6
(b)	0.1	0.3	-0.3	5.481	14.07	92.5	96.2	97.6	98.5
(c)	-1	0	0.05	1.206	3.519	63.0	65.6	67.1	69.7

regime [Ami15], the final probabilities may be determined by the Boltzmann distribution at an earlier time during the annealing process if there is a well-defined freeze-out point late in the annealing process [Ami15; MRH17]. This is not always the case [MRH17] but it was shown that for the class of problems studied in Ref. [Mar+19], inserting a pause at an "optimal pause point", which appeared to be quite generic for most instances shortly after the minimum gap, led to an improved success probability. This could be explained by thermal relaxation as the output distributions also often followed classical Boltzmann distributions, which however relate to a different temperature than the operating temperature [Mar+19].

In this chapter, we study quantum annealing in the presence of an environment by solving the TDSE. We investigate two simple models and study the effects on the quantum annealing process and the success probability. We also compare to what extent we can reproduce the data obtained from the D-Wave 2000Q quantum annealer presented in Fig. 5.34 in Section 5.3.7.

6.1 Motivation: Studying the D-Wave data

In this chapter, we focus on three different problem instances from the set studied in Section 5.3.3. The problem instances and the success rates obtained from the DW_2000Q_2 chip for four different annealing times are listed in Table 6.1 along with the minimal energy gap Δ_{\min} and the energy gap Δ_p at s=1 for the D-Wave annealing scheme (see Fig. 5.10(a), solid lines). We assume that these instances are representative cases of three classes with different energy spectra. The energy spectra of the three cases are presented in Fig. 6.1.

For the operating temperature of the D-Wave 2000Q quantum annealer of $T \approx 13 \,\mathrm{mK}$, which corresponds to an angular frequency of about 1.7 GHz (we use $k_B = 1$, see Appendix B.3 for the conversion between units), the energy differences between the ground state and the first excited state show different features for the three cases. For case (a), the energy gap between the two lowest states of the final Hamiltonian (s = 1) is still smaller than the temperature (in GHz), for case (b), the (minimal) energy gap is much larger than the temperature, and in case (c), the minimal energy gap is smaller than the temperature but the energy gap at s = 1 is larger, see Fig. 6.2.

In equilibrium at inverse temperature β , the probabilities to measure the qubit system

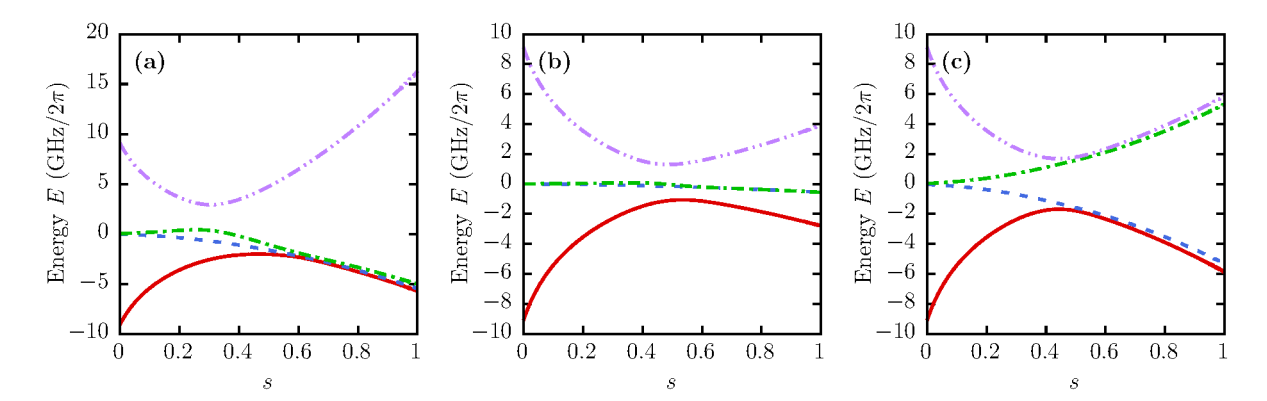


Figure 6.1: Energy spectra of the three cases under investigation. Case (a): For $s \gtrsim 0.6$, the energies of the first and second excited states approach the ground state energy. The parameters of the two-qubit Hamiltonian are J=-1, $h_1=0.96$, and $h_2=0.94$. Case (b): The energy difference between the ground state and the (degenerate) first excited state stays quite large during the annealing process. The parameters are J=0.1, $h_1=0.3$, and $h_2=-0.3$. Case (c): The energy of the first excited state approaches the ground state energy. The parameters are J=-1, $h_1=0$, and $h_2=0.05$.

in the j-th excited state (0 corresponding to the ground state) are given by the Boltzmann distribution

$$p_j^{\text{eq}}(\beta) = \frac{e^{-\beta E_j}}{\sum_{i=0}^3 e^{-\beta E_i}} = \frac{1}{1 + \sum_{i \neq j} e^{-\beta (E_i - E_j)}},$$
(6.1)

where E_i is the energy of the *i*-th excited state of the Hamiltonian at s = 1.

For long annealing times, an open-system quantum annealer shows quasistatic behavior and the probabilities of the eigenstates follow the instantaneous Boltzmann distribution [Ami15]. If a well-defined freeze-out point exists, the relaxation is slowed down when the relaxation rate becomes too small compared to t_a^{-1} and the probabilities start to deviate from the instantaneous Boltzmann distribution but stay close to the Boltzmann distribution at the time of the freeze-out [Ami15]. This need not always be the case as also found in Ref. [MRH17]. In case that a well-defined freeze-out point exists, it has a weak dependence on the annealing time, and the success probability determined by the freeze-out point can be approximated by [Ami15]

$$p_0(t_a) \sim (\kappa/\alpha) \ln(\gamma_0 t_a),$$
 (6.2)

where κ is a constant and α and γ_0 are instance dependent parameters. This function is fitted to the data from the D-Wave 2000Q quantum annealer listed in Table 6.1 for the three cases as a function of the annealing time t_a and shown in Fig. 6.3. The solid lines are from a fit including all four data points and the dashed line originates from a fit excluding the point at $t_a = 1 \,\mu\text{s}$. The fitted curves match the data from the D-Wave 2000Q quantum annealer reasonably well, suggesting that the D-Wave quantum annealer operates in the quasistatic regime for the given annealing times. However, in case (b) (blue squares), the dashed line seems to fit better, hinting at the possibility that in this case, at $t_a = 1 \,\mu\text{s}$, the D-Wave 2000Q quantum annealer may not operate in the quasistatic regime yet.

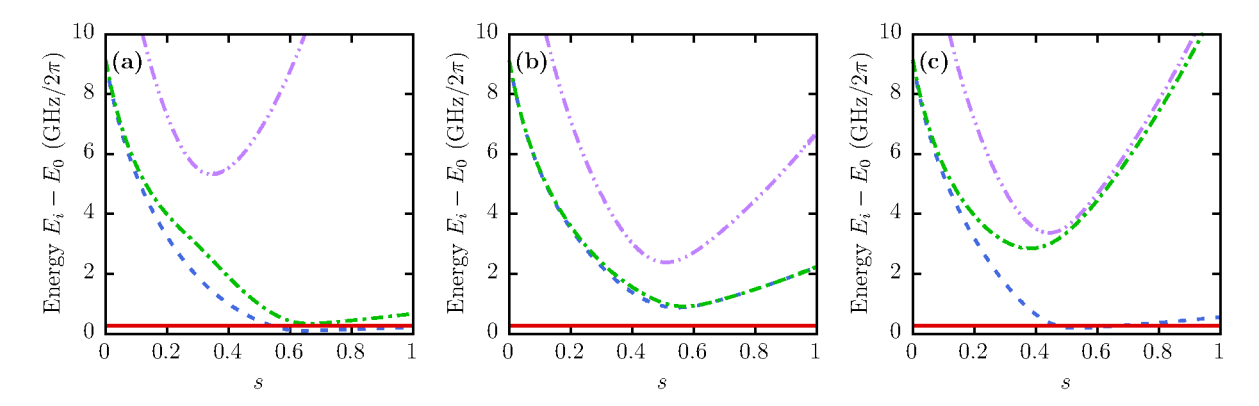


Figure 6.2: Energy differences $E_1 - E_0$ (blue, dashed line), $E_2 - E_0$ (green, dash-dotted line) and $E_3 - E_0$ (purple, dot-dot-dashed line) of the three cases under investigation, see Table 6.1. The solid red line indicates the temperature of the D-Wave device. In case (a), the minimal and the final energy gap are smaller than the temperature. In case (b), the minimal energy gap is larger than the temperature and in case (c), the energy gap is smaller than the temperature and the final energy gap is larger than the temperature.

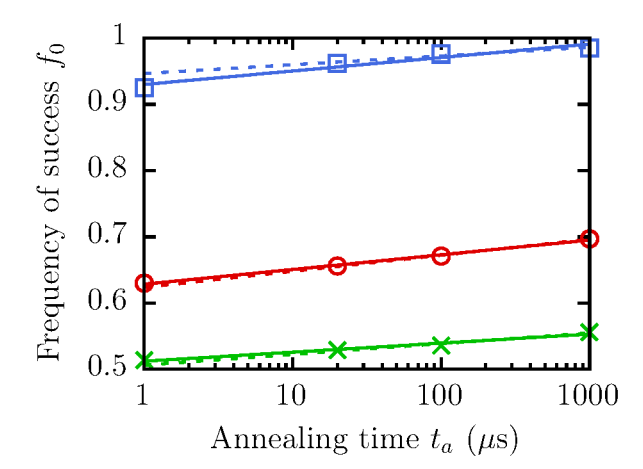


Figure 6.3: Frequency f_0 of successful outcomes from the D-Wave 2000Q quantum annealer as a function of annealing time for the three cases listed in Table 6.1. Data points are obtained from the D-Wave DW_2000Q_2 chip. Solid lines are fits of the function $p_0(t_a) = a \ln(b t_a)$ with a and b fitting parameters, see Eq. (6.2), to all data; dashed lines are fitted to the data excluding the point at $t_a = 1 \,\mu\text{s}$. Green crosses correspond to case (a), blue squares to case (b) and red circles to case (c).

In Fig. 6.4, we plot the probability $p_0^{\rm eq}$ (Eq. (6.1)) of the ground state obtained from the Boltzmann distribution (for temperatures $T \approx 13\,\mathrm{mK}$ (blue) and $T \approx 18.19\,\mathrm{mK}$ (red)) as a function of the annealing fraction s together with the frequencies of success obtained from the D-Wave 2000Q quantum annealer (black straight lines independent of s).

Looking again at the annealing schedule, we recall that A(s) becomes very small for $s \geq 0.6$. Therefore, we may assume that for s > 0.6, the computational basis is a good approximation of the instantaneous eigenbasis. If we are in the quasistatic regime and a well-defined freeze-out point exists where this approximation holds, we would expect to find rates of success which are larger than the minimal probability of the instantaneous ground state given by the Boltzmann distribution for the operating temperature of about $T = 13 \,\mathrm{mK}$. We find that for the (expected) operating temperature of the D-Wave 2000Q quantum annealer, for cases (b) and (c) the final frequencies of success are lower than the minimal probabilities given by the Boltzmann distribution. Since the minimum is reached for values of s < 0.6, it may well be that at these points the computational basis is not a sufficient approximation and for the shorter annealing times, freeze-out happens

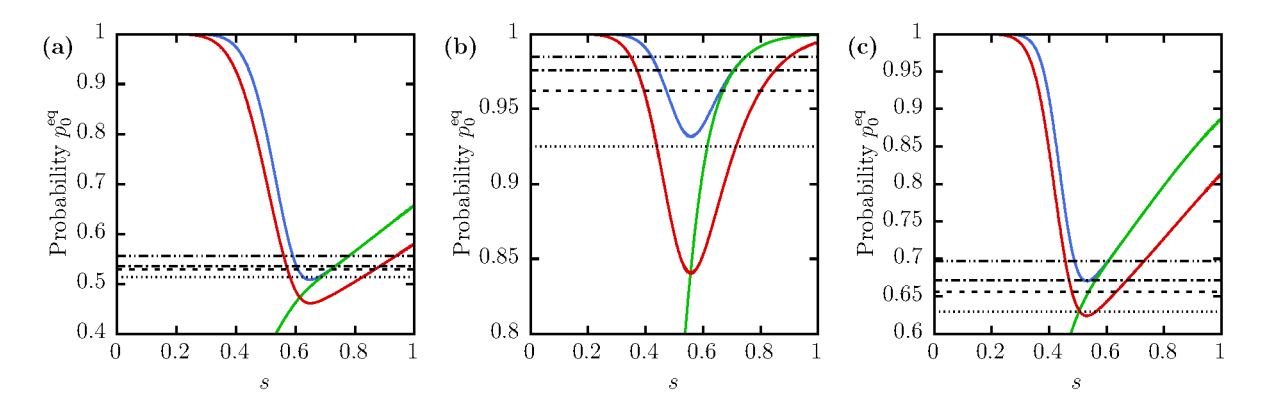


Figure 6.4: Probability $p_0^{\rm eq}$ of the ground state according to the Boltzmann distribution as a function of the annealing fraction s for two different temperatures (blue: $T \approx 13\,\mathrm{mK}$, red: $T \approx 18.19\,\mathrm{mK}$). The green line shows the probability to measure the ground state (of the Hamiltonian $H_Q(s=1)$) if the instantaneous state is in thermal equilibrium at $T \approx 13\,\mathrm{mK}$. The black lines indicate the frequencies of success obtained from the D-Wave 2000Q quantum annealer for annealing times $t_a=1,\,20,\,100,\,1000\,\mu\mathrm{s}$ (from bottom to top). Panels (a), (b) and (c) show the three different cases given in Table 6.1.

for $s \lesssim 0.6$, see the green lines in Fig. 6.4. In this case, though, the final probabilities would not correspond to a "classical" (i.e., in the computational basis) Boltzmann distribution [MRH17]. However, it may also be that the temperature of the device is a bit higher than expected (see the red curves in Fig. 6.4 for $T \approx 18.19\,\mathrm{mK}$) in which case the measured frequencies of success would be larger than the minimal equilibrium probabilities. Both explanations that the D-Wave data could be obtained from the quasistatic regime where the state, and thus the probabilities, "freeze" at a time s < 1 seem reasonable. However, it is also possible that in these cases there is no well defined freeze-out point. For most of the instances studied in Ref. [MRH17], no well-defined freeze-out point was observed in the region with $A(s) \ll B(s)$.

Freeze-out occurring close to the minimal energy gap may also be an explanation for the nice agreement between the frequencies of success observed in the D-Wave data for long annealing times $t_a \approx 20 \,\mu s$ and the success probabilities obtained from the environmentfree simulations with short annealing times $t_a = 5 \,\mathrm{ns}$ (see Fig. 5.34 and Fig. 6.5). For fast annealing of the qubit system without environment, non-adiabatic (Landau-Zener) transitions happen in the vicinity of the minimal energy gap. The final state is then influenced by the (ground) state at the time s^* when the non-adiabatic transition occurs. In other words, the overlap of the ground state of the problem Hamiltonian and the state at s^* strongly influences the success probability (see also the discussion in Section 5.3.4). If the freeze-out point \tilde{s} in the quasistatic regime is close to the minimal energy gap, at \tilde{s} the system is in thermal equilibrium corresponding to the instantaneous energy spectrum at \tilde{s} . The success probability is then related to the probability of the ground state of the problem Hamiltonian at the time \tilde{s} . Since the thermal state and the probability for a non-adiabatic transition to occur depend on the spectrum at $s = \tilde{s} \approx s^*$, it seems reasonable that the success probabilities in these two different cases (thermal or Landau-Zener transitions) can show a strong correlation.

Although the freeze-out point \tilde{s} depends on the particular problem instance, we assume

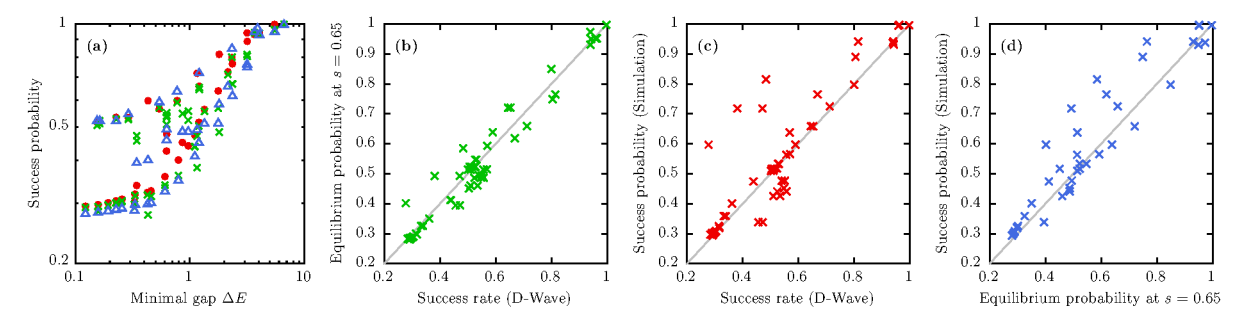


Figure 6.5: (a) Success probabilities plotted as a function of the minimal energy gap $\Delta E_{\rm min}$. Red bullets: data from the ideal qubit simulation (without environment) using the D-Wave annealing scheme and annealing time $t_a=5\,\rm ns$, green crosses: frequency of successful outcomes obtained from D-Wave's DW_2000Q_2 and DW_2000Q_2_1 chips with annealing time $t_a=20\,\mu\rm s$, blue triangles: projected equilibrium probability of the ground state at s=0.65. (b) Scatter plot showing the correlation between the D-Wave data and the projected equilibrium probability at s=0.65 from panel (a). (c) Scatter plot showing the correlation between the success probability obtained from the qubit simulation with annealing time $t_a=5\,\rm ns$ (without environment) and the D-Wave data obtained with annealing time $t_a=20\,\mu\rm s$. (d) Scatter plot showing the correlation between the success probability obtained from the qubit simulation with annealing time $t_a=5\,\rm ns$ (without environment) and the projected equilibrium probability at s=0.65.

that if it exists it may be close to the point where A(s) becomes very small. We take the approximate point s = 0.65 and plot the probability of the ground state at s = 0.65 if the state is in thermal equilibrium (blue triangles in Fig. 6.5(a)). Additionally, we show the scatter plots of the correlations between the D-Wave data, the success probabilities obtained from the isolated qubit model and the probabilities of the ground states at s = 0.65 for the state in thermal equilibrium. Since we find correlations between the success probabilities from the isolated model and the probabilities in thermal equilibrium (Fig. 6.5(d)), it is less surprising that we found the good agreement between the D-Wave data with annealing time $t_a = 20 \,\mu s$ and the flux model simulation with annealing time $t_a = 5 \,\mathrm{ns}$ (Fig. 6.5(a), red bullets and green crosses). Previous studies considering a single qubit [Joh+09] or the two lowest energy levels [AAN09] revealed that under certain conditions, Landau-Zener transitions in the presence of an environment can show results which are very similar to the decoherence-free case. We also find that the D-Wave data shows more correlation with the probabilities obtained from the thermal equilibrium state at s = 0.65 than with the probabilities obtained from the isolated qubit model, although both correlations are quite strong.

To obtain a better understanding of the influence of the environment on the annealing process itself, we study quantum annealing in the presence of an environment for two distinct environment models. In the following section, we introduce these two models.

6.2 Modeling the environment

The noise sources responsible for dephasing and decoherence of superconducting qubits have been studied for many years [Yos+06; KDC07; FI08; Sen+08; Lan+09; Ben+09;

YNT10; Col+10; Pal+14; Gra+18]. Although superconducting circuits and resonators turned out to be a useful tool to study noise and defect states in superconducting and amorphous materials [Sim+04; Sha+10; Lis+15; MCL19] and many models have been proposed that are capable of describing the noise and the resulting decoherence of the qubits reasonably well, the question what exactly the sources, their microscopic origins and their locations are could not yet be answered satisfactorily [Pal+14].

Various models based on spurious two-level systems which couple to the qubits have been investigated with the aim to describe the qubits' decoherence due to noise and coupling to an environment [Shn+05; Gal+07; MSM09; Bur+14; Mül+15]. In particular, these models reproduce the 1/f noise spectrum which is often observed in experiments with superconducting qubits and circuits. Moreover, spectroscopy experiments showed that two-level systems couple to superconducting qubits [Sim+04; Lup+09; Lis+15].

Models comprising two-level systems have already been used for many decades to describe low-temperature properties such as the linear scaling of the specific heat with temperature in glasses and amorphous materials [Phi72; AHV72] where the model is inspired by the idea that atoms in an amorphous material are thermally excited or can tunnel between two (almost) degenerate energy levels. For superconducting circuits, these models may apply to the amorphous insulating barrier in the Josephson junctions, but also electrons, surface spins and other possible origins [Pal+14; MCL19] have been studied as potential sources of flux, charge and critical current noise in superconducting qubits [McD09; BGA09].

In this chapter, we will use two simple models (I and II) based on two-level systems which couple to the qubits to model the environment.

For the system-environment simulations discussed here, we adopt the qubit model for the system. The motivation for this is that the simulation results for the full flux model and the qubit model agree very well for the three instances listed in Table 6.1. Therefore, we describe the system by the two-qubit Hamiltonian

$$H_Q(s) = -A(s) \left(\sigma_1^x + \sigma_2^x\right) - B(s) \left(h_1 \sigma_1^z + h_2 \sigma_2^z + J \sigma_1^z \sigma_2^z\right), \tag{6.3}$$

where A(s) and B(s) are the annealing functions (in GHz) and h_1 , h_2 and J are dimensionless real numbers in the interval [-1,1] and characterize the problem instance.

For the environment, we consider two different models. The first model (I) is a "generic spin bath" and the second model (II) can be thought of as a collection of non-interacting two-level defects which only couple to the qubit system. The Hamiltonian of the complete system, qubits (Q) and environment (E), for the two models $\iota \in \{I, II\}$ reads

$$H_T(s) = H_Q(s) + H_{E,\iota} + \lambda H_{QE,\iota},$$
 (6.4)

where λ is a free parameter determining the overall coupling strength between the qubits and the environment, $H_{E,\iota}$ denotes the environment Hamiltonian and $H_{QE,\iota}$ is the interaction Hamiltonian of the qubits and the environment for model ι .

The state of the complete system $|\psi(t)\rangle$ evolves unitarily in time according to the TDSE. This implies that the computational cost for solving the TDSE numerically for the complete system is proportional to $2^{N_{\rm env}+2}$. However, if we need a statistical ensemble as the initial state for the environment, for instance the canonical ensemble modeled by the density matrix $\rho_E^0 = \exp(-\beta H_{E,\iota})/Z$ where $Z = \text{Tr}_E \exp(-\beta H_{E,\iota})$ denotes the

partition function and β is the inverse temperature, the computational cost to solve the von Neumann equation

$$\frac{\partial}{\partial t}\rho(t) = -i[H(t), \rho(t)],\tag{6.5}$$

where $\rho(t)$ denotes the density matrix of the whole system at time t, is proportional to $2^{N_{\rm env}+2} \times 2^{N_{\rm env}+2}$, which is prohibitive in practice. Fortunately, we can apply the random state technology [Jin+20], also known as quantum dynamical typicality [BG09], to compute expectation values of Hermitian operators at time t for "typical" pure states instead of using the density matrix. We briefly outline the basic concept of the random state technology: For a Hermitian operator \mathcal{A} , it has been shown that [HD00]

$$\operatorname{Tr} \mathcal{A} = D\langle \Phi | \mathcal{A} | \Phi \rangle + \mathcal{O}\left(\frac{1}{\sqrt{D}}\right),$$
 (6.6)

where D denotes the dimension of the Hilbert space (i.e., $D=2^N$) and $|\Phi\rangle$ is a random state (uniformly distributed on the D^2 -dimensional hypersphere). Using this relation, one can show, that it is sufficient to prepare the environment in the pure state [Zha+16; DeR+17]

$$|\Psi(\beta)\rangle = \frac{e^{-\beta H_{E,\iota}/2}|\Psi\rangle}{\sqrt{\langle\Psi|e^{-\beta H_{E,\iota}}|\Psi\rangle}},\tag{6.7}$$

where $|\Psi\rangle$ is a randomly generated state of the environment, and solve the TDSE only once. The result will, up to (small) statistical fluctuations, give the same expectation values as the system evolved from the canonical ensemble. The statistical fluctuations vanish with $1/\sqrt{2^{N_{\rm env}}}$ which means that, for an environment that is large enough, these fluctuations are negligible.

The expectation value of the Hermitian operator A at time t can be computed as

$$\langle \mathcal{A}(t) \rangle = \text{Tr}\left(\rho(t)\mathcal{A}\right) = \text{Tr}\left(U\rho(0)U^{\dagger}\mathcal{A}\right) = \text{Tr}\left(\rho(0)U^{\dagger}\mathcal{A}U\right),$$
 (6.8)

where U is the unitary time evolution operator corresponding to the TDSE with the Hamiltonian given in Eq. (6.4) and we used that the trace is invariant under cyclic permutation of the operators. Since $\rho(0) = |++\rangle\langle++|\otimes\rho_E^0 = |++\rangle\langle++|\otimes\exp(-\beta H_{E,\iota})/Z$ is a product state, we find

$$\langle \mathcal{A}(t) \rangle = \frac{1}{Z} \operatorname{Tr}_{E} \left(e^{-\beta H_{E,\iota}} \operatorname{Tr}_{S} \left(|++\rangle \langle ++|U^{\dagger} \mathcal{A} U \right) \right)$$

$$= \frac{1}{Z} \operatorname{Tr}_{E} \left(e^{-\beta H_{E,\iota}/2} e^{-\beta H_{E,\iota}/2} \langle ++|U^{\dagger} \mathcal{A} U|++\rangle \right)$$

$$= \frac{1}{Z} \operatorname{Tr}_{E} \left(e^{-\beta H_{E,\iota}/2} \langle ++|U^{\dagger} \mathcal{A} U|++\rangle e^{-\beta H_{E,\iota}/2} \right). \tag{6.9}$$

Using Eq. (6.6), to compute Tr_E we have

$$Z = \text{Tr}_E e^{-\beta H_{E,\iota}} \approx D_E \langle \Psi | e^{-\beta H_{E,\iota}} | \Psi \rangle, \tag{6.10}$$

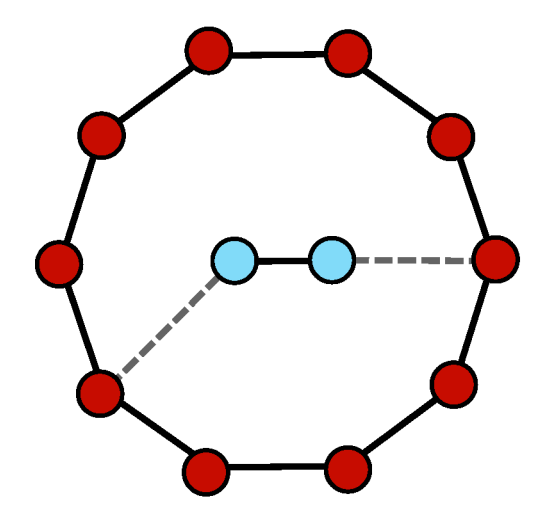


Figure 6.6: Sketch of the model used for the environment in case I. The red circles depict the environment spins with nearest-neighbor interaction on a ring. The blue circles represent the two qubits. The qubits interact with each other and each couples to a random bath spin.

and

$$\langle \mathcal{A}(t) \rangle \approx \frac{1}{\langle \Psi | e^{-\beta H_{E,\iota}} | \Psi \rangle} (\langle ++| \otimes \langle \Psi | e^{-\beta H_{E,\iota}/2}) U^{\dagger} \mathcal{A} U (|++\rangle \otimes e^{-\beta H_{E,\iota}/2} | \Psi \rangle). \tag{6.11}$$

With the state $|\Psi(\beta)\rangle$ defined by Eq. (6.7), we find

$$\langle \mathcal{A}(t) \rangle \approx \langle ++| \otimes \langle \Psi(\beta)| U^{\dagger} \mathcal{A} U| ++ \rangle \otimes |\Psi(\beta)\rangle.$$
 (6.12)

Thus, it is sufficient to solve the TDSE for the state $|++\rangle \otimes |\Psi(\beta)\rangle$ to obtain approximate expectation values with statistical fluctuations of the order of $1/\sqrt{2^{N_{\rm env}}}$.

Primarily, we are interested in the case where \mathcal{A} is one of the projectors $\mathcal{P}_x = |x\rangle\langle x|\otimes \mathbb{I}_E$ onto the two-qubit states $|x\rangle \in \{|\uparrow\uparrow\rangle, |\uparrow\downarrow\rangle, |\downarrow\downarrow\rangle\}$, yielding the probabilities to find the system in the corresponding state.

In the following, we introduce the two different model Hamiltonians for the environment. We denote the Pauli-matrices of the environment spins by μ_i^{α} , $1 \leq i \leq N_{\text{env}}$, $\alpha \in \{x, y, z\}$.

6.2.1 Model I: Generic spin bath

In this case, we model the environment as a ring of two-level systems with nearest-neighbor interaction. The Hamiltonian reads

$$H_{E,I} = -K \sum_{i=1}^{N_{\text{env}}} \left(r_i^x \mu_i^x \mu_{i+1}^x + r_i^y \mu_i^y \mu_{i+1}^y + r_i^z \mu_i^z \mu_{i+1}^z \right), \tag{6.13}$$

where r_i^x , r_i^y and r_i^z are uniformly distributed random numbers in the range [-1,1], K determines the maximal coupling strength and is regarded as a free parameter, and $\mu_{N_{\text{env}}+1}^{\alpha} = \mu_1^{\alpha}$.

The Hamiltonian describing the coupling of the qubits to the environment is given by

$$H_{QE,I} = -r_{1,v}^x \mu_v^x \sigma_1^x - r_{1,v}^y \mu_v^y \sigma_1^y - r_{1,v}^z \mu_v^z \sigma_1^z - r_{2,w}^x \mu_w^x \sigma_2^x - r_{2,w}^y \mu_w^y \sigma_2^y - r_{2,w}^z \mu_w^z \sigma_2^z,$$
 (6.14)

where $r_{1,v}^{\alpha}$, $r_{2,w}^{\alpha}$ ($\alpha \in \{x,y,z\}$) are uniformly distributed random numbers in the range [-1,1] and v, w are randomly chosen integers between 1 and N_{env} . A sketch visualizing the intra-bath and qubit-bath couplings is shown in Fig. 6.6.

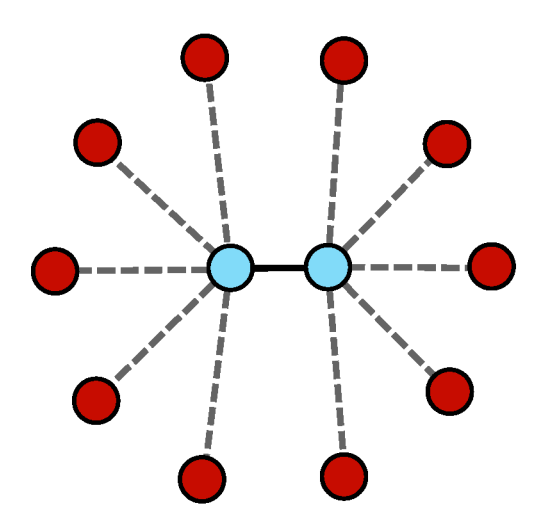


Figure 6.7: Sketch of the model used for the environment in case II. The red circles depict the environment which is modeled as a collection of non-interacting two-level systems. The blue circles represent the two qubits. The qubits interact with each other and each qubit is coupled to one half of the two-level systems.

This model with random intra-bath couplings and random qubit-bath couplings can be regarded as a generic spin bath [Jin+13; Zha+16], which may model, including the initialization of the environment (Eq. (6.7)), a quantum mechanical environment in thermal equilibrium as observed in Ref. [Har+08].

6.2.2 Model II: Non-interacting two-level defects

The second environment model under investigation are non-interacting two-level systems and is related to the model presented in Ref. [Shn+05]. The first (second) half of the two-level systems in the environment couple to qubit one (two), see Fig. 6.7 for a sketch of the model. The Hamiltonian of the environment spins reads

$$H_{E,II} = -\Omega \sum_{i=1}^{N_{\text{env}}} r_i^x \mu_i^x + r_i^y \mu_i^y + r_i^z \mu_i^z,$$
 (6.15)

where again, r_i^x , r_i^y and r_i^z are uniformly distributed random numbers in the range [-1, 1], and Ω is a free parameter setting the energy scale of the level splittings. The Hamiltonian modeling the interaction between the qubit system and the environment is given by

$$H_{QE,II} = \sum_{\alpha \in \{x,y,z\}} \begin{pmatrix} \lceil N_{\text{env}}/2 \rceil & N_{\text{env}}/2 \rceil \\ \sigma_1^{\alpha} \sum_{i=1}^{\alpha} r_{1,i}^{\alpha} \mu_i^{\alpha} + \sigma_2^{\alpha} \sum_{i=\lceil N_{\text{env}}/2 \rceil + 1}^{N_{\text{env}}} r_{2,i}^{\alpha} \mu_i^{\alpha} \end{pmatrix}, \tag{6.16}$$

with $r_{1,i}^{\alpha}$ and $r_{2,i}^{\alpha}$ being uniformly distributed random numbers in the range [-1,1].

This model may describe two-level defects in the dielectrics of the circuits [Sim+04; McD09] or in the material near the qubit wiring which are local to the qubits [Lan+09; YNT10], and far away from each other [MSM09].

6.3 Simulation results

We use the spin-dynamics simulator (in house software) which is based on the product-formula algorithm discussed in Chapter 3 and uses the same parallelization scheme as the massively-parallel quantum computer simulator (JUQCS) [DeR+07; DeR+19].

Earlier studies of model I in the context of equilibration showed that the number of environment spins primarily determines the magnitude of the statistical fluctuations due to the approximation Eq. (6.6) [Zha+16]. Since a simulation run with an annealing time $t_a = 1 \,\mu s$ for a large environment of $N_{\rm env} = 28$ spins takes about a week on 64 compute nodes on the supercomputer JUWELS [Jül19], we decided to use (for most of the runs) a smaller environment of $N_{\rm env} = 16$ spins and average over a few runs with different random numbers in the environment and interaction Hamiltonians, and the random state. In this way, we can also avoid picking accidentally an unfortunate constellation of the random environment and interaction parameters which are not representative. Moreover, on the D-Wave quantum annealer, we also distribute 992 (976) copies of the two-qubit instances over the 2000 qubit chip DW_2000Q_2 (DW_2000Q_2_1), so we expect that each of the 992 (976) copies solved simultaneously on the chip is affected by a different environment.

The determination of model parameters for the environment ($\{K,\lambda\}$ for model I and $\{\Omega,\lambda\}$ for model II) which reproduce the D-Wave data is not straightforward. Since the runtime of a single simulation with $t_a=1\,\mu\mathrm{s}$ including $N_{\mathrm{env}}=16$ environment spins is still quite long (approximately 4 hours on JUWELS) and we need to average over a few runs with different initializations of the random parameters, it is not practical to perform a fit to the D-Wave data. Thus, we scan a "reasonable" range of the parameters and investigate the behavior of the final probabilities of the qubit system depending on the parameter choices. For some fixed sets of parameters, we study the properties of the qubit-environment systems for all three cases listed in Table 6.1. Finally, we relate the simulation results to the data obtained from the D-Wave quantum annealer.

Parts of the results presented in this section have been published in [Wil+20].

6.3.1 Results for the spin bath (model I)

We try several values for the intra-bath coupling strength K in the range [0.05, 15] GHz for three different values of the qubit-bath coupling strength $\lambda \in \{0.1, 0.8, 1.5\}$ GHz. The results for the success probability are shown in Fig. 6.8 for all three cases and for the inverse temperature $\beta = 0.6$ ns (corresponding to the temperature $T \approx 12.7$ mK, see also Appendix B.3). We find that the dependence on the parameters K and λ is not very systematic and sometimes shows strong variations. However, in all three cases we find values for which the success probability coincides with or is close to the equilibrium probability, whereas apart from a few settings only, in the tested ranges, the simulation data do not match the data from the D-Wave quantum annealer very well. Specifically, none of the tested settings yields results that match in all three cases.

Looking at the probabilities for the four computational states during the annealing process for the different parameter settings $\{\lambda, K\}$ (see example plots for a particular initialization of the random numbers in Figs. 6.9, 6.10 and 6.11 for cases (a), (b) and (c), respectively), we can classify the results into four different regions.

It is not easy to name definite ranges for λ and K, as "small" and "large" can have quite a different meaning from case to case. For instance, in case (b), $K = 0.5 \,\text{GHz}$ and $\lambda = 0.8 \,\text{GHz}$ are still small (almost no difference to the isolated case, see Fig. 6.10) but in case (a), for this parameter setting large deviations from the ideal case can be observed (see Fig. 6.9). Thus, we can only put the parameters into approximate ranges which can be different for different cases.

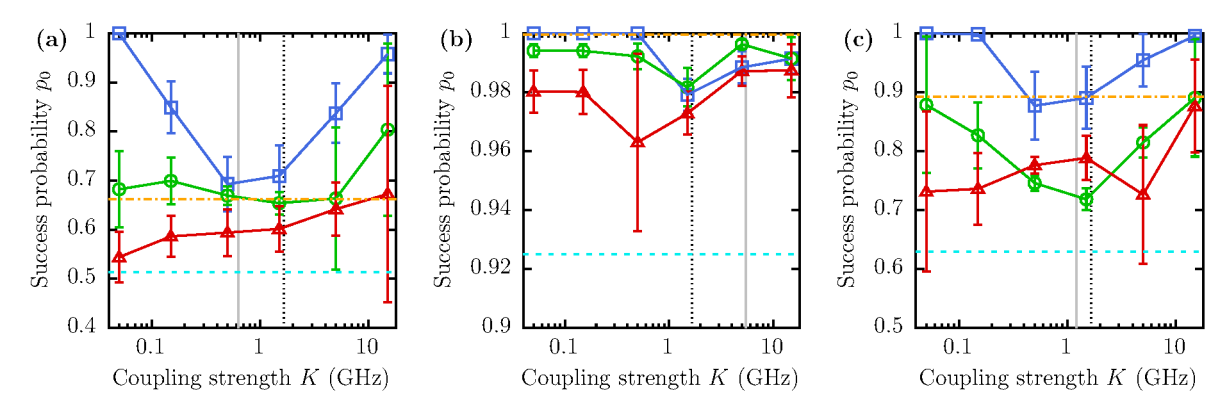


Figure 6.8: Success probabilities as a function of the intra-bath coupling strength K for three different values of the qubit-bath coupling strength λ (blue squares: $\lambda = 0.1\,\mathrm{GHz}$, green circles: $\lambda = 0.8\,\mathrm{GHz}$, red triangles: $\lambda = 1.5\,\mathrm{GHz}$). The data points are obtained from the simulation with annealing time $t_a = 1\,\mu\mathrm{s}$, inverse temperature $\beta = 0.6\,\mathrm{ns}$ and $N_{\rm env} = 16$. Error bars indicate the standard deviation obtained from five runs with different initializations of the random numbers. The dash-dotted orange line indicates the equilibrium probability, the dashed cyan line represents the D-Wave data and the vertical solid gray and dotted black lines show the minimal energy gap and the temperature, respectively. Panels (a), (b) and (c) show the three different cases given in Table 6.1.

The first region of small λ and K shows (almost) no difference from the case of the isolated qubit system.

In the second region (mostly small λ but K can be larger), the probabilities start to "freeze" at some point during the annealing process and stay constant for the rest of the process (see e.g. $\lambda = 0.1\,\mathrm{GHz}, K = 0.5\,\mathrm{GHz}$ in case (a) and (c)). These cases show a freeze-out which resembles Landau-Zener transitions in the case of fast annealing rather than the freeze-out in the quasistatic regime as discussed in Ref. [Ami15]: Here, the probabilities follow the probabilities of the isolated case until transitions in the vicinity of the minimal gap occur and the probabilities stay constant when the gap widens again. These cases are the ones that show the most resemblance with the Landau-Zener transitions for fast annealing discussed in Chapter 5. A possible explanation for this phenomenon could be that under certain conditions, Landau-Zener transitions can also be observed in open quantum systems where the energy gap (or the annealing time) are then effectively rescaled [Joh+09]. Depending on the choice of parameters for $\{\lambda, K\}$, this feature can be stronger or weaker and can be quite smooth or show oscillations in the vicinity of the minimum gap.

In the latter case, K is rather large and we put these cases in the third category. The fluctuations indicate that in this region, the qubit system is entangled with the environment and tunnels between different states while passing through an avoided crossing. Due to the random initializations, the size and form of the gap at such an avoided crossing can be very different and since the transition probability depends exponentially on the gap, the success probabilities appear random with large deviations (as can also be seen in Fig. 6.8).

The fourth region for intermediate K and larger λ shows probabilities that start to deviate from the ideal case and then increase (or decrease, depending on the state) ap-

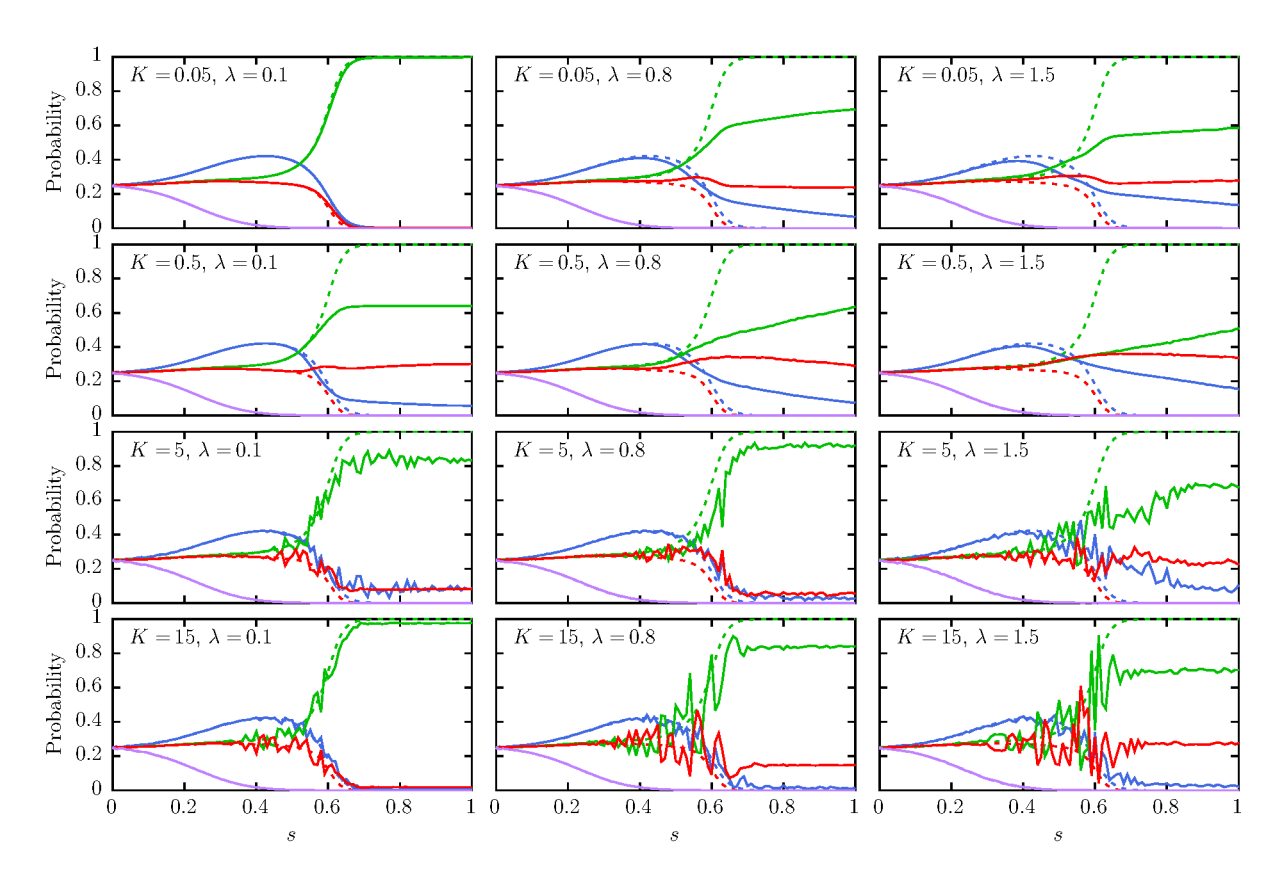


Figure 6.9: Probabilities to measure the qubit system in the state $|\uparrow\uparrow\rangle$ (blue), the state $|\uparrow\downarrow\rangle$ (green), the state $|\downarrow\uparrow\rangle$ (red) or the state $|\downarrow\downarrow\rangle$ (purple) as a function of the annealing fraction s for various values of the parameters $\{K, \lambda\}$ for case (a). The solid lines are obtained from the simulation with annealing time $t_a = 1 \,\mu\text{s}$ and $N_{\text{env}} = 16$. Dashed lines are the probabilities for the isolated qubit system for $t_a \to \infty$.

proximately linearly. In these cases, the probabilities sometimes follow approximately the instantaneous Boltzmann distributions at the operating temperature. This is shown more explicitly in Fig. 6.12(a) where the probabilities for the computational states approximately follow the probabilities (dotted lines) obtained from projecting the Boltzmann distribution, i.e., the probabilities computed by

$$p_x(s) = \text{Tr}(\rho_Q(s)|x\rangle\langle x|) = \langle x|\rho_Q(s)|x\rangle,$$
 (6.17)

where
$$\rho_Q(s) = \frac{e^{-\beta H_Q(s)}}{Z(s)}, \quad Z(s) = \text{Tr}(e^{-\beta H_Q(s)}),$$
 (6.18)

and $x \in \{\uparrow\uparrow, \uparrow\downarrow, \downarrow\uparrow, \downarrow\downarrow\}$. Cases where the probabilities do not follow this distribution but rather show a plateau with slightly linear increase (or decrease), may be explained by the magnetic Föhn effect [SM01].

Rarely, we find cases where the probabilities indicate that a freeze-out as discussed in Ref. [Ami15] happens. One such example is shown in Fig. 6.12(b) where the probabilities follow the projected Boltzmann distribution but then freeze and stay constant during the rest of the annealing process. We also observe transition zones between the four regions.

Figure 6.13 shows the probabilities to measure the qubit system in the four different eigenstates of the problem Hamiltonian as a function of the inverse temperature β . We

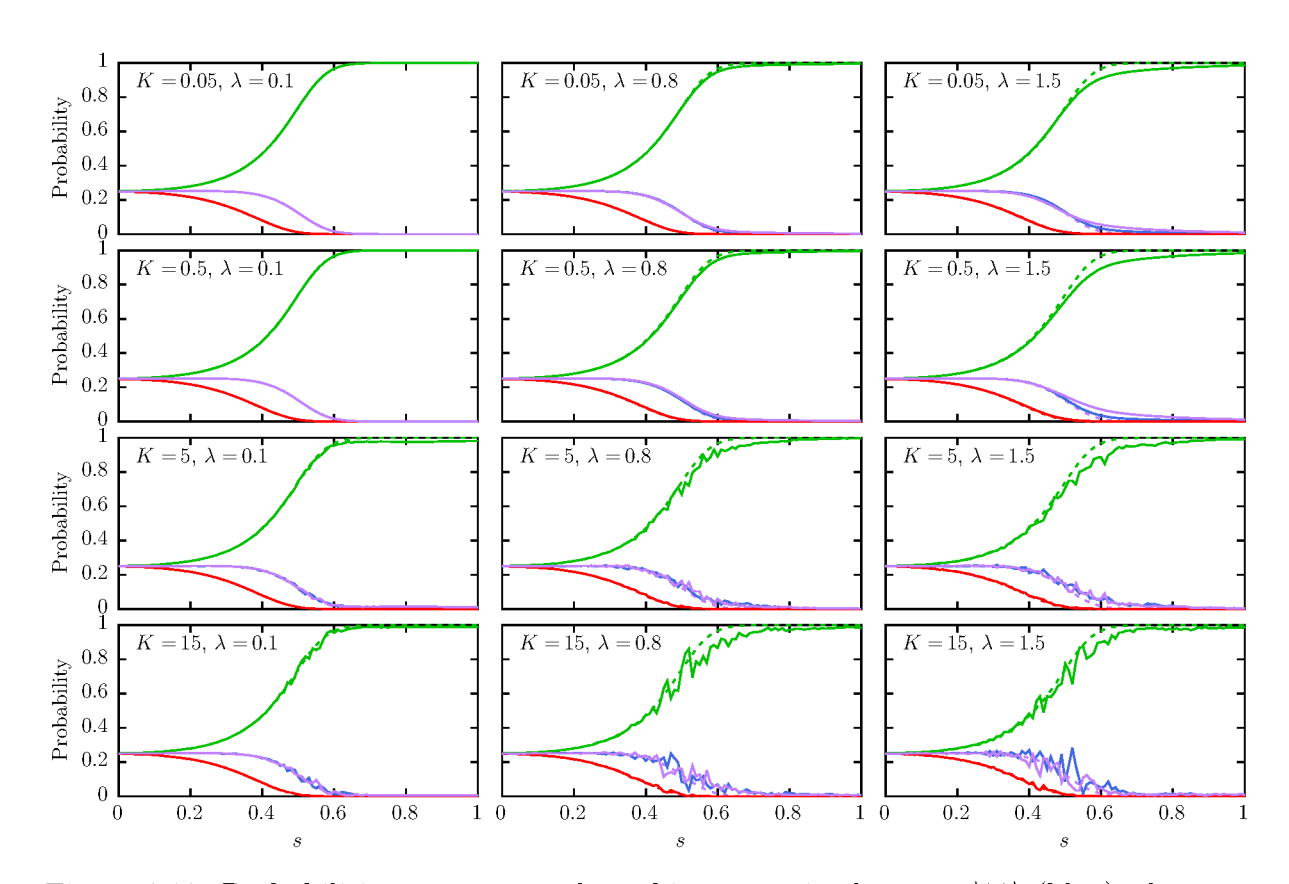


Figure 6.10: Probabilities to measure the qubit system in the state $|\uparrow\uparrow\rangle$ (blue), the state $|\uparrow\downarrow\rangle$ (green), the state $|\downarrow\uparrow\rangle$ (red) or the state $|\downarrow\downarrow\rangle$ (purple) as a function of the annealing fraction s for various values of the parameters $\{K, \lambda\}$ for case (b). The solid lines are obtained from the simulation with annealing time $t_a = 1 \,\mu\text{s}$ and $N_{\text{env}} = 16$. Dashed lines are the probabilities for the isolated qubit system for $t_a \to \infty$.

find that the data points obtained from the simulation match the equilibrium probabilities Eq. (6.1) quite well for $\beta > 0$. For case (a), we also show results for simulations with $N_{\rm env} = 28$ (asterisks). We find that the average values for the smaller environment match the values obtained from the larger environment very well, supporting earlier results that the smaller environment basically shows larger fluctuations than the larger environment. For case (c), the probabilities to find the ground state are (for $\beta > 0$) systematically smaller than the equilibrium probabilities. This appears to agree with the freeze-out theory [Ami15] showing the Boltzmann distribution for an effective higher temperature (smaller β). However, as we observed above, the freeze-out that occurs during the evolution does not match with the assumption of quasistatic behavior. Thus, although we find success probabilities that agree nicely with the equilibrium probabilities, the system is most often not equilibrated. The success probabilities in case (a) which are higher than the equilibrium probabilities also indicate that the system is not in thermal equilibrium when (or if) the freeze-out happens.

Figure 6.14 shows the success probability as a function of annealing time for case (c) with $\beta = 0.6$ ns, for five different initializations of the random numbers and their average (red asterisks). Since we do not observe the logarithmic increase in success probability as expected in the quasistatic region (see Fig. 3 in Ref. [Ami15]), and we only observed for a

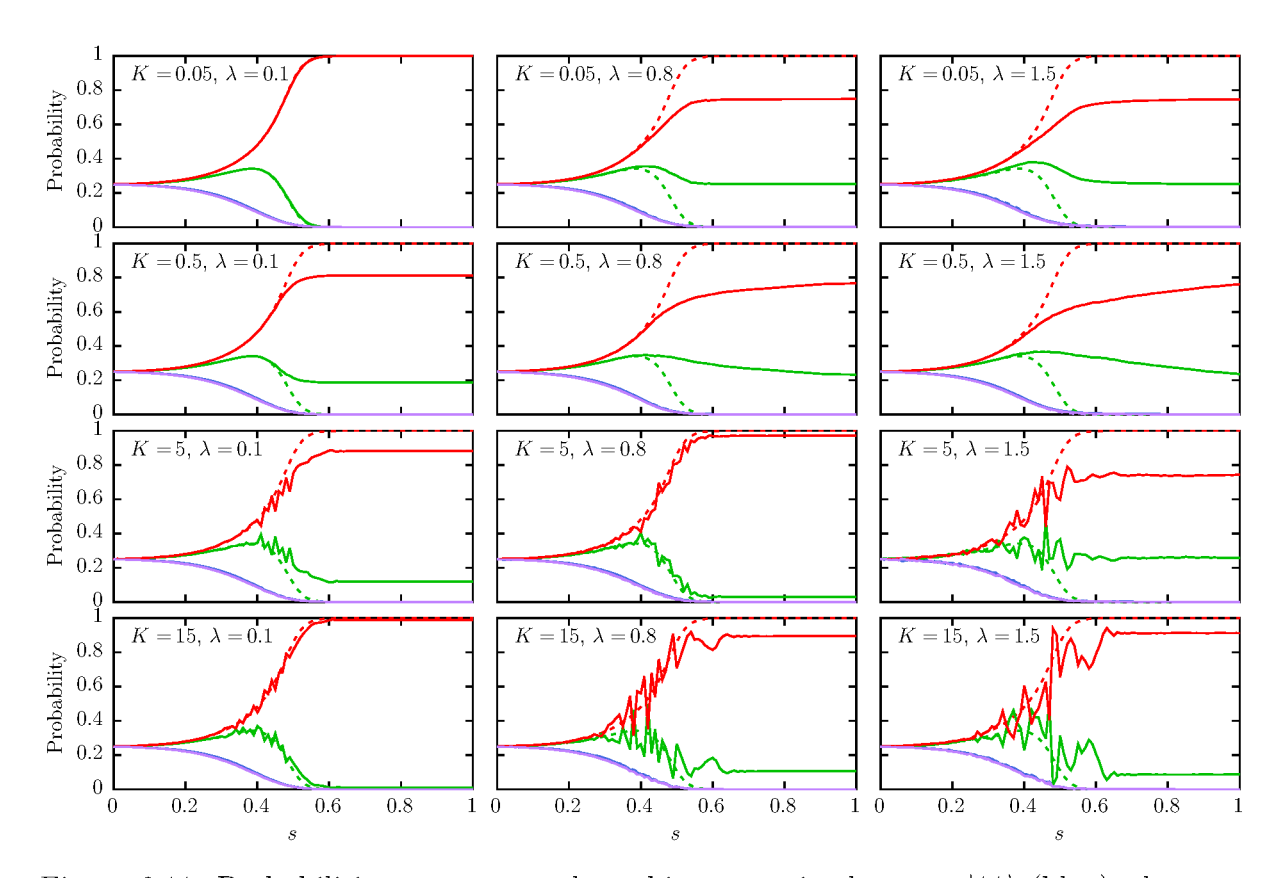


Figure 6.11: Probabilities to measure the qubit system in the state $|\uparrow\uparrow\rangle$ (blue), the state $|\uparrow\downarrow\rangle$ (green), the state $|\downarrow\uparrow\rangle$ (red) or the state $|\downarrow\downarrow\rangle$ (purple) as a function of the annealing fraction s for various values of the parameters $\{K, \lambda\}$ for case (c). The solid lines are obtained from the simulation with annealing time $t_a = 1 \,\mu\text{s}$ and $N_{\text{env}} = 16$. Dashed lines are the probabilities for the isolated qubit system for $t_a \to \infty$.

few parameter settings the agreement with the instantaneous Boltzmann distribution, we are tempted to conclude that for an annealing time of $1\,\mu s$, we are most often not in the quasistatic region but rather in the coherent (for small K and λ) or the non-equilibrium region.

Figure 6.15 shows the success probability as a function of annealing time t_a for different inverse temperatures β and model parameters $K = 5\,\text{GHz}$ and $\lambda = 1\,\text{GHz}$. The probabilities in thermal equilibrium at the different temperatures are indicated by the dashed lines in the corresponding color.

For $\beta \geq 0.2\,\mathrm{ns}$, we find that the success probability approaches the probability in thermal equilibrium for large enough annealing times t_a . For $\beta = 0.1\,\mathrm{ns}$, we find that the success probability oscillates around the equilibrium probability and for $\beta = 0$, the success probability starts oscillating without reaching the equilibrium probability. This may be an indication that for the hotter cases with $\beta \lesssim 0.1\,\mathrm{ns}$ (corresponding to $T \gtrsim 76.4\,\mathrm{mK}$), the bath is unable to equilibrate the qubit system. In general, for the colder temperatures, we find that this kind of environment can equilibrate the qubit system in case (b) very well as is also indicated by the results shown in Fig. 6.13.

We conclude that model I for the environment may be suited to drive the qubit system to its equilibrium distribution for a range of parameters $\{K, \lambda\}$ and temperatures (cor-

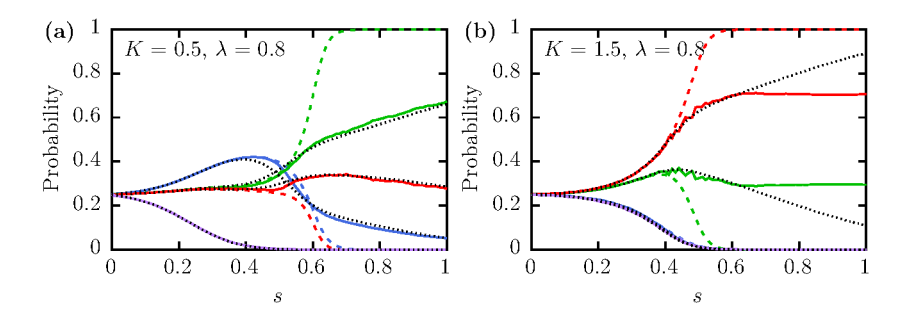


Figure 6.12: Probabilities to measure the qubit system in the state $|\uparrow\uparrow\rangle$ (blue), the state $|\uparrow\downarrow\rangle$ (green), the state $|\downarrow\uparrow\rangle$ (red) or the state $|\downarrow\downarrow\rangle$ (purple) as a function of the annealing fraction s. The solid lines are obtained from the simulation with annealing time $t_a=1\,\mu s$ and $N_{\rm env}=16$. Dashed lines are the probabilities for the isolated qubit system. Shown are two examples where the probabilities approximately follow the Boltzmann distribution (black dotted lines) (a) during the complete annealing process, (b) until a freeze-out point after which the probabilities stay constant.

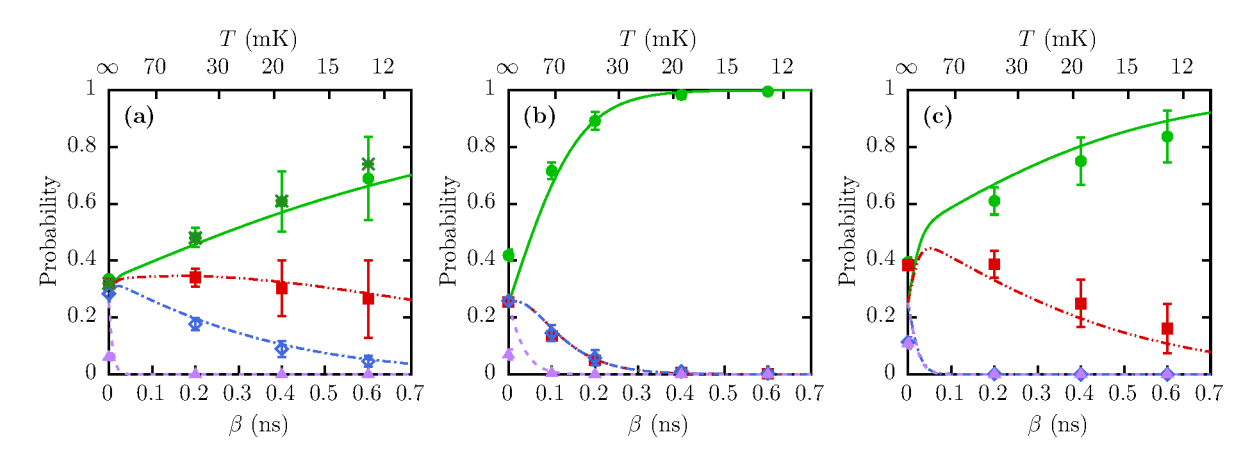
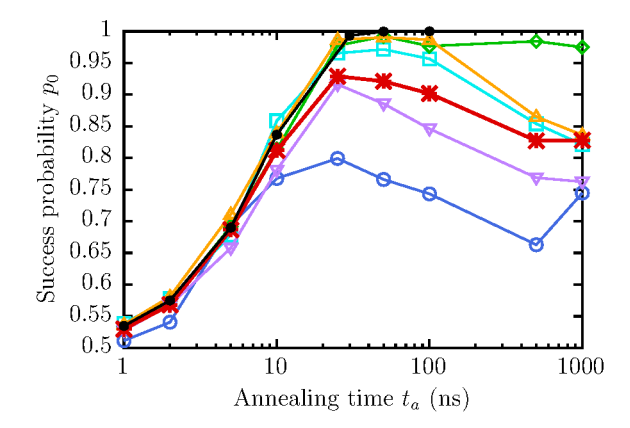


Figure 6.13: Probabilities to measure the qubit system in the ground state (green bullets), the first excited state (red squares), the second excited state (blue diamonds) or the third excited state (purple triangles) as a function of the inverse temperature β . The data points are obtained from the simulation with environment model I specified in Eqs. (6.13) and (6.14) with annealing time $t_a = 1 \,\mu\text{s}$ and bath parameters $K = 5 \,\text{GHz}$, $\lambda = 0.8 \,\text{GHz}$. Ten runs with different initializations of the random parameters r_i^{α} , $r_{1,v}^{\alpha}$, $r_{2,w}^{\alpha}$ ($\alpha \in \{x,y,z\}$) are averaged for bath size $N_{\text{env}} = 16$. Panels (a), (b) and (c) show the three different cases given in Table 6.1. For case (a), we additionally present results from the simulation with $N_{\text{env}} = 28 \,\text{two-level}$ systems (green asterisks). Lines are the equilibrium probabilities as a function of β , see Eq. (6.1).



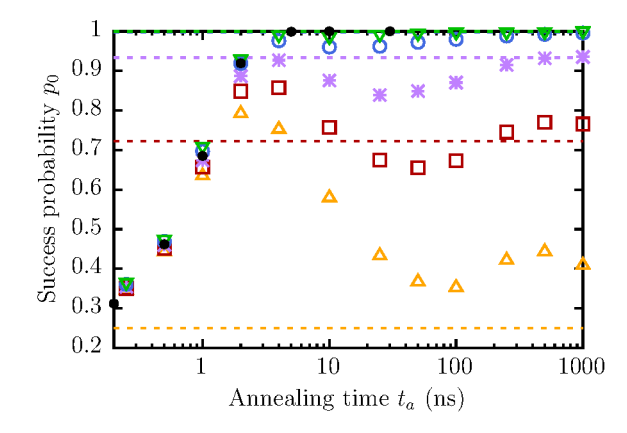


Figure 6.14: Success probability as a function of annealing time t_a for case (c). Data points with open symbols (circles, triangles, squares and diamonds) are obtained from simulation runs with different initializations of the random numbers, red asterisks are the averages and black bullets are from the isolated qubit model. The parameters are $\lambda = 0.6 \,\text{GHz}$ and $K = 5 \,\text{GHz}$.

Figure 6.15: Success probability as a function of annealing time t_a for case (b) and for different inverse temperatures β . Green down-triangles: $\beta = 0.6 \, \text{ns}$, blue circles: $\beta = 0.4 \, \text{ns}$, purple asterisks: $\beta = 0.2 \, \text{ns}$, red squares: $\beta = 0.1 \, \text{ns}$, orange up-triangles: $\beta = 0$. The model parameters are $\lambda = 1 \, \text{GHz}$, and $K = 5 \, \text{GHz}$.

responding to $\beta > 0$), but potentially requiring different annealing times t_a . However, model I does not appear to be very suited for reproducing the data obtained from the D-Wave quantum annealer. Therefore, we carry out a similar analysis for model II in the following section. Note that this conclusion only applies to the tested range of parameters since we cannot rule out that there may be parameters outside of the investigated range which describe the D-Wave data much better.

6.3.2 Results for the non-interacting defects (model II)

As for model I, we test several values for the energy Ω of the environmental two-level systems in the range [0.01, 10] GHz for three different values of the qubit-bath coupling strength $\lambda \in \{0.5, 1.0, 1.5\}$ GHz. For all three cases, we show the results for the success probability in Fig. 6.16.

Compared to model I, we find that for model II, the dependence on the parameters Ω and λ is much more systematic. For energies $\Omega \leq 0.25\,\mathrm{GHz}$, the success probability saturates in all three cases. This seems reasonable, as for energy splittings much smaller than the temperature, the two-level systems of the environment are, to a good approximation, equally likely in the ground state or the excited state.

For Ω much larger than the temperature, the two-level systems of the environment will initially be in the ground state. Then the qubit-environment system undergoes an adiabatic evolution with the qubit system ending in the ground state of the coupled qubit-environment system. If the coupling between the qubits and the environment spins is "strong" (compared to the energy difference between the two lowest energy states of the qubit system at s=1), the ground state projected onto the qubit system is not necessarily the ground state of the problem Hamiltonian. As a result, we find, especially in case (a),

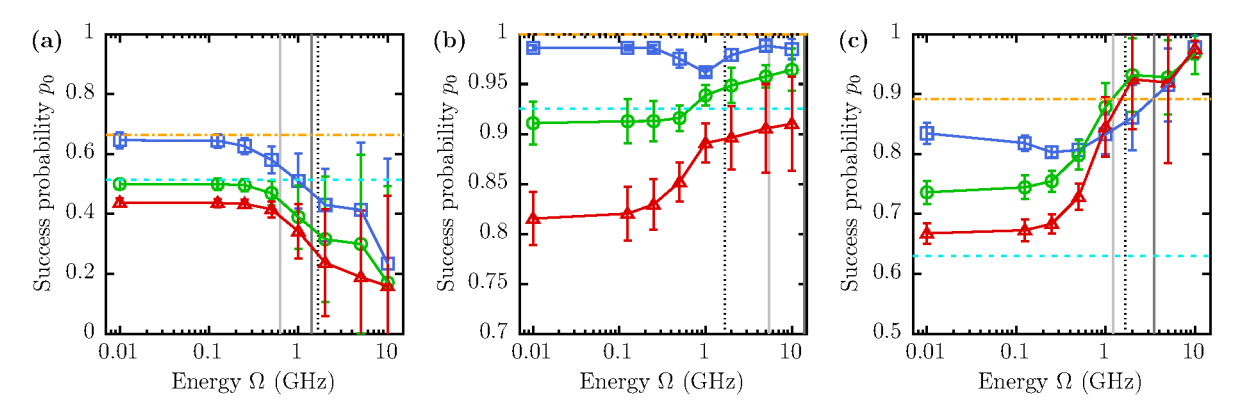


Figure 6.16: Probabilities to measure the qubit system in the ground state as a function of the energy Ω of the environment spins for three different coupling strengths $\lambda=0.5\,\mathrm{GHz}$ (blue squares), $\lambda=1\,\mathrm{GHz}$ (green circles) and $\lambda=1.5\,\mathrm{GHz}$ (red triangles). The data points are obtained from the simulation with $N_{\mathrm{env}}=16$ and annealing time $t_a=1\,\mu\mathrm{s}$. Five runs with different initializations of the random parameters r_i^{α} , $r_{1,i}^{\alpha}$, $r_{2,i}^{\alpha}$ ($\alpha\in\{x,y,z\}$) are averaged. The dash-dotted orange line indicates the equilibrium probability, the dashed cyan line represents the D-Wave data. The vertical solid light-gray, dark-gray and dotted black lines show the minimal energy gap, the final energy gap at s=1 and the temperature, respectively. Panels (a), (b) and (c) show the three different cases given in Table 6.1.

large deviations due to the different random numbers in the environment and interaction Hamiltonians. If the ground state of the system is no longer (even approximately) given by a product state, the probability distribution of the qubit states obtained from the reduced density matrix is no longer describable by a classical Boltzmann distribution [Den+13].

For cases (a) and (b), we find remarkable agreement with the D-Wave data for the parameters $\lambda=1\,\mathrm{GHz}$ and $\Omega\leq0.25\,\mathrm{GHz}$ (see green circles and cyan dashed lines in Fig. 6.16). For case (c), the agreement is better for the parameters $\lambda=1.5\,\mathrm{GHz}$ and $\Omega\leq0.25\,\mathrm{GHz}$ but not as good as for the other two cases. In all three cases we find ranges of values for which the success probability is (closely) below the equilibrium probability. Again, we do not find any setting within our tested range which yields results that match the D-Wave data in all three cases.

Studying the probabilities for the computational states during the evolution, we find that there are two different parameter regions. Figures 6.17, 6.18 and 6.19 show examples of the probabilities during the annealing process for the cases (a), (b) and (c), respectively.

The first region is for small Ω where in many cases the probability distributions are close to a classical Boltzmann distribution at some effective temperature. Figure 6.20 shows examples for $\Omega = 0.125\,\mathrm{GHz}$ where the probabilities either nicely follow the instantaneous Boltzmann distribution (indicated by the black dotted lines) during the whole annealing process or only until a certain point where it starts to deviate similarly to a freeze-out. The effective temperature seems to depend on the coupling strength λ . The second parameter region is the one of large Ω where we observe fluctuations in the probabilities. For large Ω , the two-level systems are initially in their ground states and no additional energy (except the one introduced by the couplings which is comparably small in this region) enters the system. As a consequence, the complete system essentially stays in its ground

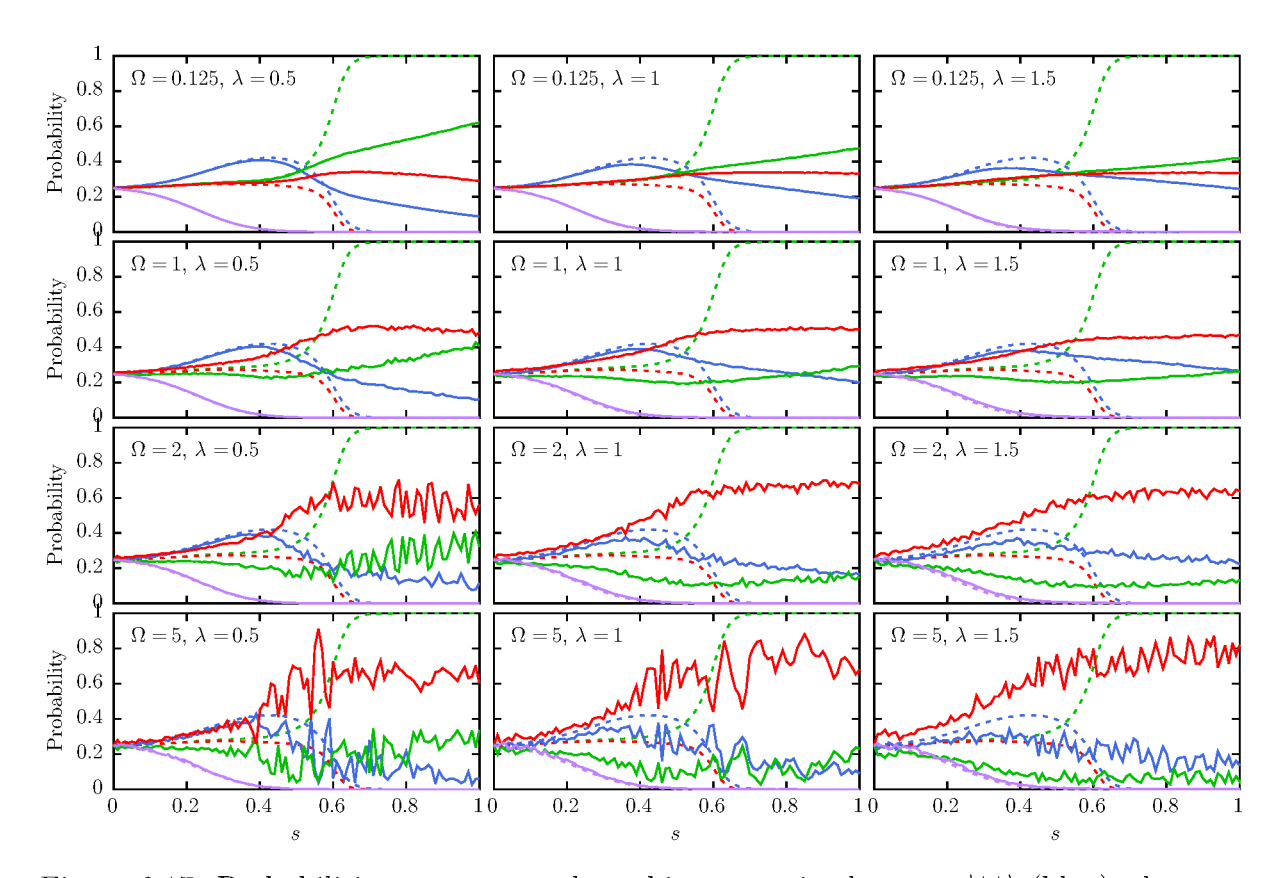


Figure 6.17: Probabilities to measure the qubit system in the state $|\uparrow\uparrow\rangle$ (blue), the state $|\uparrow\downarrow\rangle$ (green), the state $|\downarrow\uparrow\rangle$ (red) or the state $|\downarrow\downarrow\rangle$ (purple) as a function of the annealing fraction s for various values of the parameters (Ω, λ) for case (a). The solid lines are obtained from the simulation with annealing time $t_a = 1 \,\mu\text{s}$ and $N_{\text{env}} = 16$. Dashed lines are the probabilities for the isolated qubit system for $t_a \to \infty$.

or a low-energy excited state during the annealing process. We find that even for small annealing fractions s, the probabilities can deviate strongly from the probabilities in the isolated case. In case (a), we find that often the state with the highest probability is no longer the ground state of the problem Hamiltonian.

For small Ω , the coupling strength λ has a strong influence on the probability distribution since in this region, all two-level systems of the environment are saturated independent of Ω . Thus, in this parameter region, the energy contribution due to the coupling terms between qubits and environment is significant, and the environment cannot be assumed to be in (or close to) thermal equilibrium. For the qubit system, at s=0, the excited states have a high energy. Hence, the coupling terms only introduce a small perturbation and the qubit system can still be regarded as being in thermal equilibrium in the ground state of $H_Q(s=0)$. For the environment, the coupling energy is significant and thus, the equilibrium state of $H_{E,II}$ is not a good approximation of the state in thermal equilibrium. Thus, we would regard the environment as being in a non-equilibrium state and the energy contribution due to the coupling terms scales with the coupling strength λ . During the annealing process, the qubit system seems to relax to thermal equilibrium at some effective temperature determined by λ , see Fig. 6.20. We find that the probabilities follow the instantaneous (projected) Boltzmann distribution

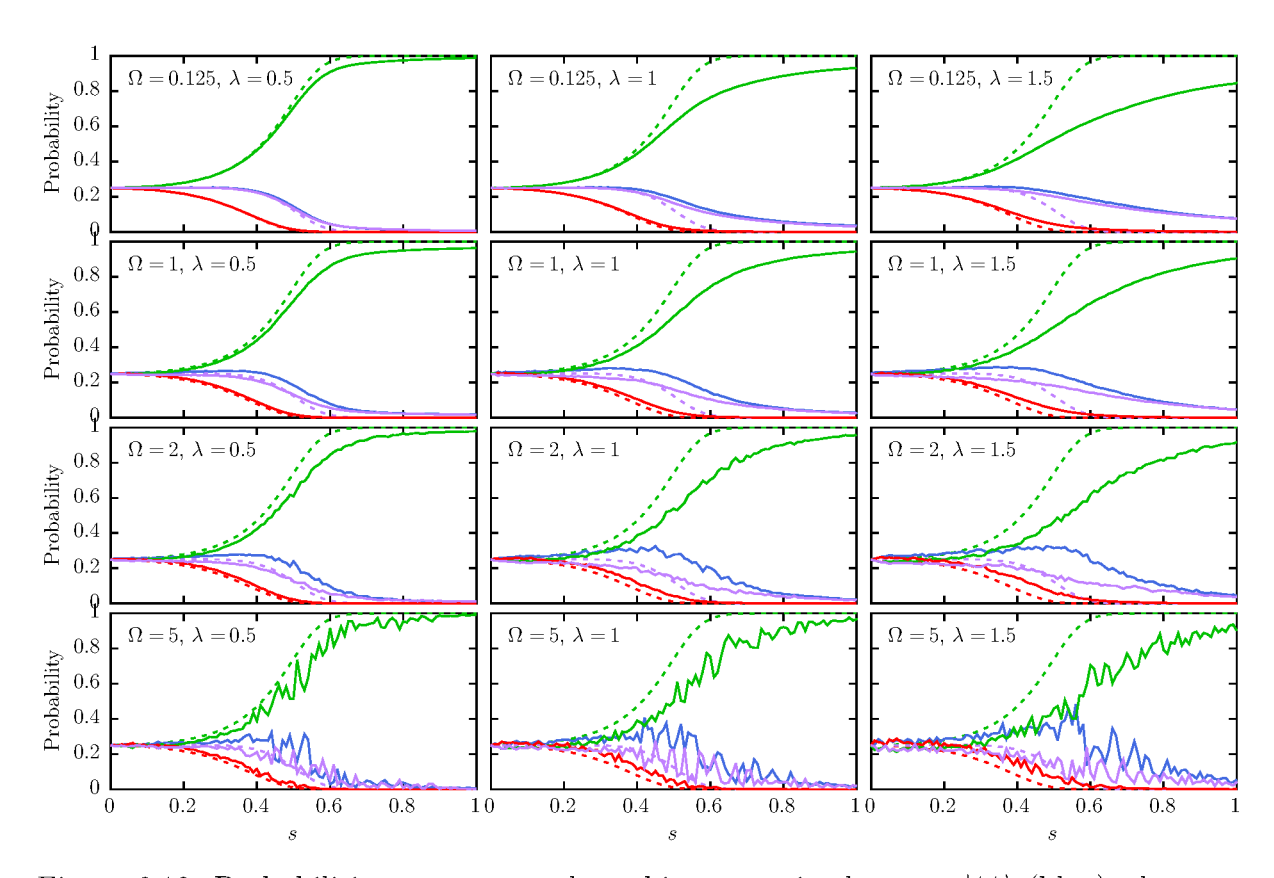


Figure 6.18: Probabilities to measure the qubit system in the state $|\uparrow\uparrow\rangle$ (blue), the state $|\uparrow\downarrow\rangle$ (green), the state $|\downarrow\uparrow\rangle$ (red) or the state $|\downarrow\downarrow\rangle$ (purple) as a function of the annealing fraction s for various values of the parameters (Ω, λ) for case (b). The solid lines are obtained from the simulation with annealing time $t_a = 1 \,\mu\text{s}$ and $N_{\text{env}} = 16$. Dashed lines are the probabilities for the isolated qubit system for $t_a \to \infty$.

at some λ -dependent temperature. The initial non-equilibrium state of the environment explains the difference between the effective temperature obtained by comparison with the Boltzmann distribution and the temperature used to initialize the environment.

Since the D-Wave data matches the simulation results in this region, it could be that there is a weakly coupled quantum-mechanical environment in thermal equilibrium at the operating temperature which may not have a strong effect on the performance of the qubit system, but a few defects which are not in thermal equilibrium at the operating temperature can have serious effects on the qubit system, driving it to a state, which suggests that the system is in thermal equilibrium at a much higher effective temperature. It is difficult to say only on the basis of the final probabilities if an observed Boltzmann distribution at a higher temperature is due to freeze-out (as for model I) or due to non-equilibrium effects (as for model II). Remarkably, though, both models can provide an explanation for an effectively higher temperature.

Next, we study the dependence of the success probability on the annealing time t_a . The success probability for different annealing times is plotted in Fig. 6.21.

We find that all three cases behave differently. For case (a), the success probability appears to saturate; for case (b), after reaching a maximum at about $t_a \approx 20 \,\text{ns}$, it starts to slightly decrease again; and in case (c), the success probability is still increasing for

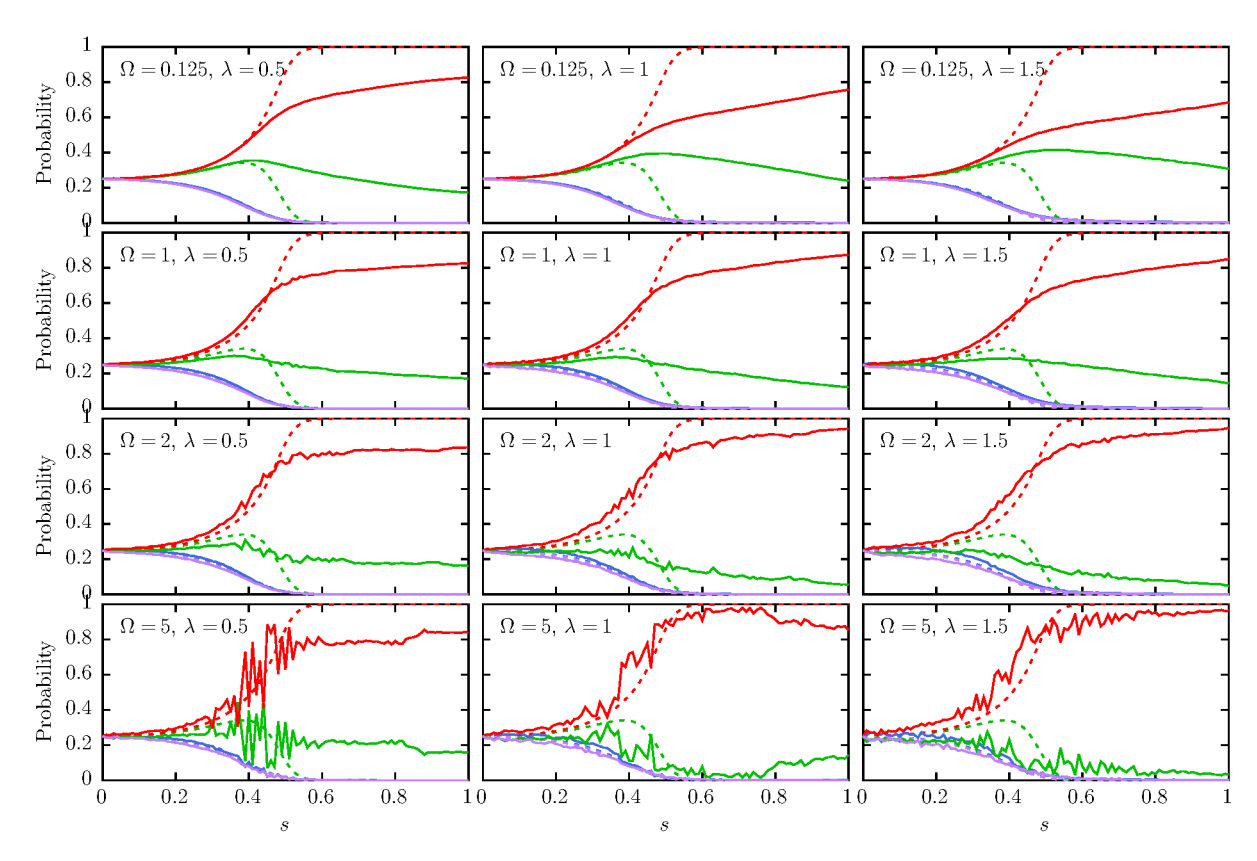


Figure 6.19: Probabilities to measure the qubit system in the state $|\uparrow\uparrow\rangle$ (blue), the state $|\uparrow\downarrow\rangle$ (green), the state $|\downarrow\uparrow\rangle$ (red) or the state $|\downarrow\downarrow\rangle$ (purple) as a function of the annealing fraction s for various values of the parameters (Ω, λ) for case (c). The solid lines are obtained from the simulation with annealing time $t_a = 1 \,\mu\text{s}$ and $N_{\text{env}} = 16$. Dashed lines are the probabilities for the isolated qubit system for $t_a \to \infty$.

 $t_a \approx 1 \,\mu\text{s}$. Comparing with Fig. 3 in Ref. [Ami15], we would assume that all cases are in different parts of the non-equilibrium phase.

For model I, we know that the number of environment spins primarily determines the magnitude of the statistical deviations [Zha+16]. However, we do not know if this also holds in the case of model II. Thus, we study the success probability as a function of the number of environment spins. The results for the three cases are shown in Fig. 6.22.

In case (a) and (c), we find indeed that with increasing number of environment spins, the statistical fluctuations decrease. However, in case (a), the success probability decreases, too. In case (c), the success probability does not change significantly for $N_{\rm env} \gtrsim 6$. In case (b), apart from the outlier at $N_{\rm env} = 4$, the fluctuations increase and the success probability decreases with increasing number of environment spins. It seems that only on the basis of our three example cases, we are not able to make a clear statement about the dependence of the success probability on the number of environment spins.

For model I to act as a generic bath, a certain minimal number of environment spins is required. In contrast, for model II, the number of environment spins can be regarded as a free parameter. Since coherent two-level systems are rather rare in superconducting qubits [Lup+09; Sha+10], a small number of non-interacting environment spins may already describe a realistic scenario. Indeed, this is also supported by the results shown

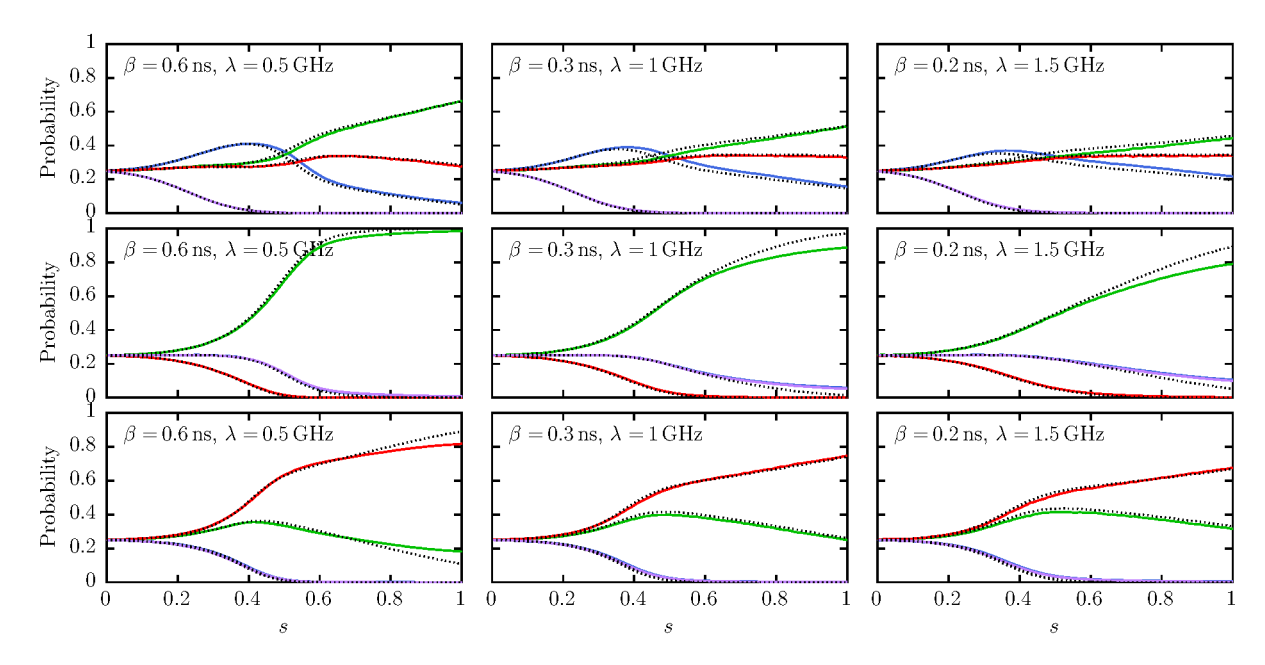


Figure 6.20: Probabilities to find the qubit system in the state $|\uparrow\uparrow\rangle$ (blue), the state $|\uparrow\downarrow\rangle$ (green), the state $|\downarrow\uparrow\rangle$ (red) or the state $|\downarrow\downarrow\rangle$ (purple) as a function of the annealing fraction s for case (a) (top row), case (b) (middle row), and case (c) (bottom row). Solid lines are obtained from the simulation with annealing time $t_a = 1 \,\mu\text{s}$ and $N_{\text{env}} = 16$. Black dotted lines are the probabilities in thermal equilibrium for the indicated value of β .

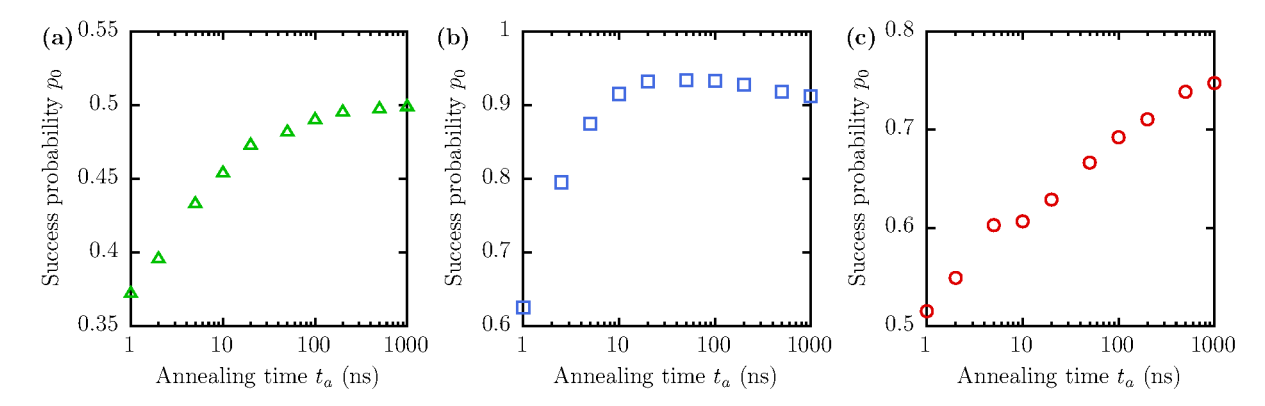


Figure 6.21: Probabilities to observe the qubit system in the ground state as a function of annealing time t_a . The data points are obtained from the simulation with $N_{\rm env} = 16$, coupling strength $\lambda = 1 \,\text{GHz}$ and $\Omega = 0.125 \,\text{GHz}$. Panels (a), (b) and (c) show the three different cases given in Table 6.1.

in Fig. 6.22(a) and (b), where an environment of $N_{\rm env} \approx 10$ spins already produces results close to the data obtained from the D-Wave 2000Q quantum annealer.

6.3.3 Comparison

With model I, we can find parameters which equilibrate the qubit system. But not all tested parameters could drive the qubit system to equilibrium within $1 \mu s$. Nevertheless, model I seems suited to drive the qubit system to equilibrium. The freeze-out during the

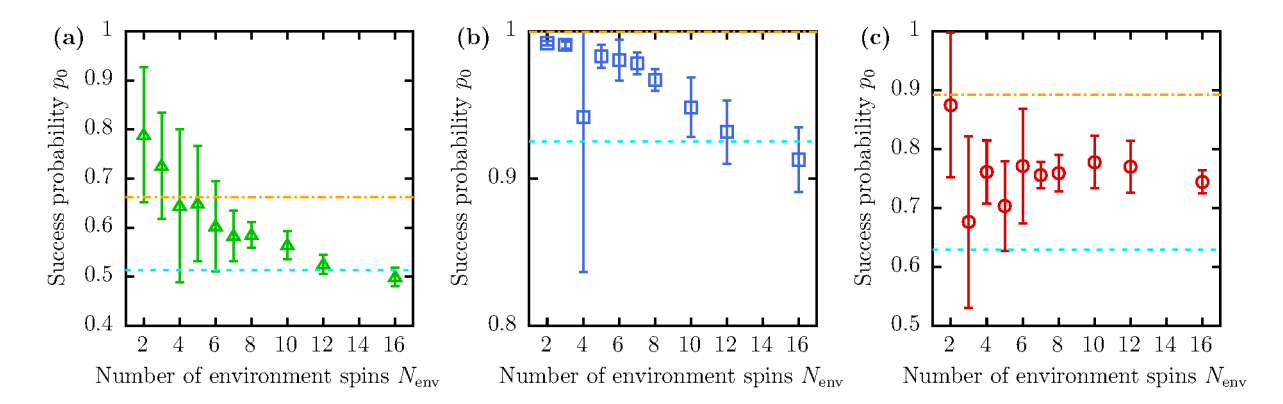


Figure 6.22: Probabilities to observe the qubit system in the ground state as a function of the number of environment spins $N_{\rm env}$. The data points are obtained from the simulation with annealing time $t_a = 1 \,\mu s$, coupling strength $\lambda = 1 \,{\rm GHz}$ and $\Omega = 0.125 \,{\rm GHz}$. Five runs with different initializations of the random parameters r_i^{α} , $r_{1,i}^{\alpha}$, $r_{2,i}^{\alpha}$ ($\alpha \in \{x,y,z\}$) are averaged. The dash-dotted orange line indicates the equilibrium probability, and the dashed cyan line represents the D-Wave data. Panels (a), (b) and (c) show the three different cases given in Table 6.1.

evolution as well as the instantaneous Boltzmann distribution of the probabilities during the evolution which we observed in some cases match with the quasistatic behavior of quantum annealers [Ami15]. However, these cases are rather rare. More often, we observed a freeze-out which does not match the quasistatic behavior but the probabilities showed similar behavior to the Landau-Zener transitions for fast annealing. We could not find a parameter setting which reproduces the D-Wave result in all cases simultaneously.

Model II basically shows two distinct regions for small and large energies Ω . For small Ω we found that the qubit system often seems to equilibrate to an effective temperature determined by the coupling strength λ . In this region we found excellent agreement with the D-Wave data for cases (a) and (b), see Figs. 6.16 and 6.22(a) and (b). For case (c) we found very good agreement with the D-Wave data for a different coupling strength λ . For large Ω , we did not find a good agreement.

From our results we would conclude that model II, modeling non-interacting two-level systems coupling to the qubits, describes the D-Wave data better than model I which models a generic spin bath. Thus, to check our conjecture, we choose three additional test cases and compare the D-Wave data to the simulation outcomes for model I with the parameter settings ($K = 0.05\,\mathrm{GHz}$, $\lambda = 1.5\,\mathrm{GHz}$), and for model II with the parameter settings ($\Omega = 0.01\,\mathrm{GHz}$, $\lambda = 1\,\mathrm{GHz}$) and ($\Omega = 0.01\,\mathrm{GHz}$, $\lambda = 1.5\,\mathrm{GHz}$). The results are shown in Fig. 6.23 for the success probabilities only and in Fig. 6.24 for all four computational basis states. For the new cases (e) and (f) we find perfect agreement with the simulation data obtained for model II with $\lambda = 1.5\,\mathrm{GHz}$. Case (d) shows very good agreement for model II with both parameter choices.

This suggests that the good agreement in case (a) and (b) with model II for $\lambda = 1 \,\text{GHz}$ might be caused by some other effect not taken into account. For instance, both have the ground state $|\uparrow\downarrow\rangle$. So there might be some bias for this state leading to the slightly higher success probabilities which would also comply with case (d). In case (a), it is also possible that the higher energy levels have some effect as the strong asymmetry observed

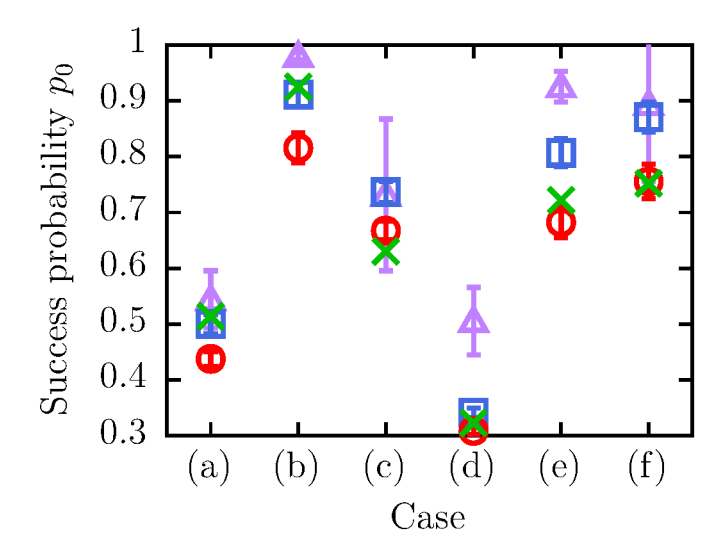


Figure 6.23: Success probability for the cases (a), (b) and (c) and in addition for (d) J = -0.01, $h_1 = 0.01$, $h_2 = -0.01$ (e) J = 0, $h_1 = 0.1$, $h_2 = 0.1$ and (f) J = 1, $h_1 = 0.9$, $h_2 = -0.8$ averaged over 5 simulation runs with different random numbers. The parameters are $\beta = 0.6 \,\mathrm{ns}$, $N_{\rm env} = 16$ and $t_a = 1 \,\mu\mathrm{s}$. Purple triangles: $K = 0.05 \,\mathrm{GHz}$, $\lambda = 1.5 \,\mathrm{GHz}$, blue squares: $\Omega = 0.01 \,\mathrm{GHz}$, $\lambda = 1 \,\mathrm{GHz}$, red circles: $\Omega = 0.01 \,\mathrm{GHz}$, $\lambda = 1.5 \,\mathrm{GHz}$, green crosses: DW_2000Q_2 data.

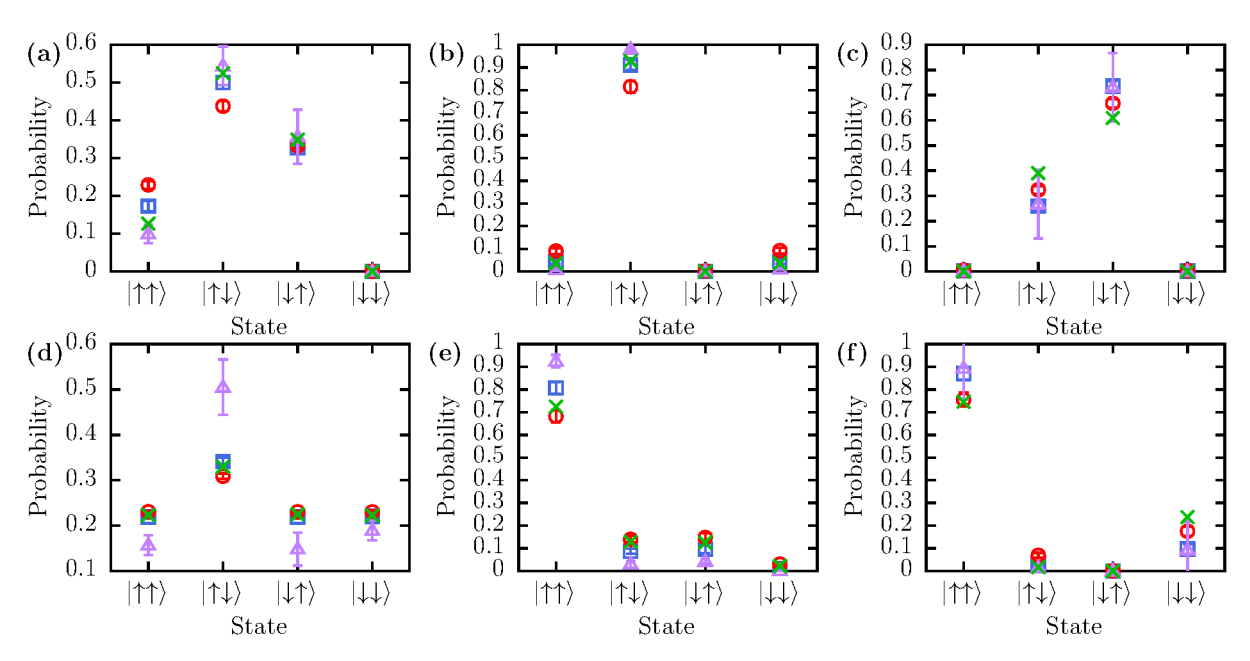


Figure 6.24: Probabilities to observe the qubit system in the computational states for the cases (a), (b), (c), (d) J = -0.01, $h_1 = 0.01$, $h_2 = -0.01$, (e) J = 0, $h_1 = 0.1$, $h_2 = 0.1$, and (f) J = 1, $h_1 = 0.9$, $h_2 = -0.8$ shown in the corresponding panel. The data points are obtained from the simulation with annealing time $t_a = 1 \,\mu\text{s}$, $N_{\text{env}} = 16$, coupling strength $\lambda = 1\,\text{GHz}$ and $\Omega = 0.01\,\text{GHz}$ (blue squares), $\lambda = 1.5\,\text{GHz}$ and $\Omega = 0.01\,\text{GHz}$ (red circles), $\lambda = 1.5\,\text{GHz}$ and $K = 0.05\,\text{GHz}$ (purple triangles). Five runs with different initializations of the random parameters r_i^{α} , $r_{1,i}^{\alpha}$, $r_{2,i}^{\alpha}$ ($\alpha \in \{x,y,z\}$) are averaged. Green crosses show data from the DW_2000Q_2_1 chip.

in Section 5.3.5 for a particular class of instances, as for example J = -1, $h_1 = 0.96$, $h_2 = 0.94$ and J = 1, $h_1 = 0.96$, $h_2 = -0.94$, might be less strong on the real device, potentially leading to some offset for case (a). While model I still produced reasonably good results for cases (a), (b), (c) and (f) (at least when considering the error bars), the results for cases (d) and (e) are far off. These results suggest that our conjecture that

model II is more suited to reproduce the D-Wave data than model I is appropriate.

Since we observed very different behavior of the probability distributions describing the qubit system during the annealing process it would be interesting to get such data for the D-Wave quantum annealer to compare which model also captures more of the evolution during the annealing process and not only the final probability distribution.

On the basis of the probabilities at the end of the annealing process only, it is impossible to determine if the system equilibrated at some effective temperature $1/\beta^*$ or if it was in thermal equilibrium at the temperature $1/\beta$ before a freeze-out happened at a time s^* (the freeze-out point). If freeze-out occurs, the final probabilities are then given by the Boltzmann distribution at the time s^* . This distribution is equivalent to the one where no freeze-out happens but the effective temperature is higher (β^* is lower) since $\beta B(s^*)H_{\text{fin}} =$ $\beta^* B(1) H_{\text{fin}}$ for $\beta^* = \beta B(s^*) / B(1)$ with $B(s^*) < B(1)$. A similar argument in the context of the optimal pause point is also given in Ref. [Mar+19]. Thus, to understand what happens during the annealing process, only knowing the final distribution is not sufficient. The "quenches" which are a relatively new feature of the D-Wave machine [DWa19] are not applicable in our case as we already use the shortest possible annealing time of $t_a = 1 \,\mu s$. Furthermore, it might be interesting to examine hybrid models comprising of a mixture of model I and II, or to use a time-dependent coupling between the qubit and the environment or a time-dependent energy of the environment which scale for instance with B(s), i.e., which change during the annealing process. Another option is to initialize the complete qubit-environment system in thermal equilibrium and study the evolution or to explicitly initialize the environment in a non-equilibrium state. We leave an analysis in this direction for future research.

Chapter 7

Summary and conclusion

In this thesis, we studied in detail the behavior of SQUID-based flux qubits during a quantum annealing process by simulating, on conventional digital computers and supercomputers, the time evolution of the quantum system according to the time-dependent Schrödinger equation. We focused on two aspects: the two-level approximation of the flux variables describing the dynamics of the magnetic fluxes of the superconducting circuit, and the influence of an environment coupling to the qubit system. For the investigation regarding the first aspect, we simulated the dynamics of the flux variables and compared the results obtained from projecting onto the qubit subspace to the results expected from the ideal qubit model. Regarding the second aspect, we considered two different models based on two-level systems for the environment. We studied their influence on the qubit system and to what extent these models can be used to describe the data obtained from the D-Wave 2000Q quantum annealer.

In Chapter 2, we outlined the basic aspects of the idea of quantum annealing [Fin+94; Bro+99] and adiabatic quantum computation [Far+00; Far+01].

For our simulations, we used the Suzuki-Trotter product-formula algorithm [Suz76; DeR87] which we reviewed in Chapter 3. After the description of the implementation of the algorithm, we additionally derived an error bound for the evaluation of observables, which is found to be tight.

In Chapter 4, we first reviewed the Josephson effect and the circuit quantization rules [Dev97; Bis10]. Then, we introduced the SQUID Hamiltonian and the Hamiltonian of three coupled SQUIDs where the middle SQUID serves as a tunable coupler [Har+09a] between the other two SQUIDs functioning as the qubits. We also scrutinized the two-level approximation of the flux model [Har+09b; Har+10a] to arrive at the qubit Hamiltonian and found that the external fluxes which determine the parameters of the final Hamiltonian have to be specific functions of the annealing fraction or the desired coupling strength J of the final Hamiltonian.

After we discussed the discretization of the flux model Hamiltonian and some technical aspects at the beginning of Chapter 5, we presented our results of the flux model simulation. We showed that the coupling strength J, extracted from the simulation, matches the value used as input for the simulation very well when we use the function for the external flux of the coupler obtained from the mapping to the qubit model. We computed the effective qubit Hamiltonian during the annealing process for equidistant values of the annealing fraction s, to obtain values of the effective annealing functions A(s) and B(s). We compared these to the annealing functions computed from the single SQUID model

and found that they differ slightly. The deviations depend on the coupling strength J, which is consistent with experimental observations that the coupling slightly changes the effective inductance [Har+09a].

Our main conclusion regarding the comparison of the flux model and the qubit model is that the two-level approximation works very well for most cases. Although leakage to higher energy levels can be observed during the annealing process, the effects on the final probabilities are small. However, we found a certain class of problem instances for which the final probabilities of the two models deviate. The problem instances in this class are close to having a frustrated Hamiltonian with a three-fold degenerate ground state. We compared these results also to the ones obtained from the model of two directly coupled SQUIDs to determine whether these effects are solely due to the presence of the coupler. We found that the presence of the coupler introduces an asymmetry by enhancing the effect if J is positive and reducing it if J is negative (and if the magnitudes of J, h_1 and h_2 are not too small). The deviations between the final probabilities obtained from the flux model and the qubit model were found to be a consequence of the higher energy levels which lead to an effective Hamiltonian that differs slightly from the projected Hamiltonian during the annealing process. This effective Hamiltonian then has a slightly different energy spectrum and thus a minimal energy gap at a slightly different position and/or of a slightly different size. This can lead to different transition probabilities (the probability for a Landau-Zener transition [Lan32; Zen32] depends exponentially on the gap size). But also at the end of the annealing process, the effective Hamiltonian has correction terms proportional to σ_i^z only, which then leads to an undesired imbalance between the σ_i^z and $\sigma_1^z \sigma_2^z$ terms. As a consequence, degeneracies can be lifted in the final effective Hamiltonian.

We also compared the simulation results with data obtained from the D-Wave 2000Q quantum annealer. Although for the flux model we only simulated the annealing process for 5 ns while the minimum annealing time on the D-Wave 2000Q quantum annealer is $1\,\mu\text{s}$, we found good agreement between the experimental data for $t_a=20\,\mu\text{s}$ and the simulation results for 5 ns. For annealing times of $1\,\mu\text{s}$ or longer, we would expect a success probability, i.e, probability to measure the correct ground state at the end of the annealing process, of about 100%. This disagreement with the expectation for $20\,\mu\text{s}$ cannot be explained by the presence of the higher energy levels. Since neither the flux model nor the qubit model contain an explicit environment, we studied in Chapter 6 which influence the presence of an environment composed of two-level systems has on the annealing procedure and whether this is sufficient to explain the agreement of the D-Wave data (for an annealing time $t_a=20\,\mu\text{s}$) with the flux model simulation for annealing time $t_a=5\,\text{ns}$.

We studied two models for the environment. The first one, model I, is a ring of two-level systems with nearest-neighbor interaction and each of the two system qubits couples to a random two-level system of the environment. This model with random interaction strengths describes a generic spin bath [Jin+13; Zha+16]. The second model, model II, consists of non-interacting two-level systems which couple to one of the two qubits each. We found that for a suitable choice of model parameters, model II can produce data which describes the observed frequencies of measured states obtained from the D-Wave 2000Q quantum annealer at the end of the annealing process. In the tested range of parameters for model I, we did not find a set of model parameters which could reproduce

the D-Wave data as nicely as model II. However, we found evidence that model I might be well suited to thermalize the qubit system during a quantum annealing process to the operating temperature. Moreover, we observed that the qubit system behaves differently during the annealing process for the two different models I and II. While in the case of model I, we observed occasionally that freeze-out [Joh+11; Ami15] (i.e., the quantum state stops changing before the end of the annealing process) occurs, in the case of model II, the probabilities of the computational states often appeared to follow probability distributions of a system in thermal equilibrium of the instantaneous Hamiltonian but at an effectively higher temperature than the operating temperature.

Although both models predict different time evolutions during the annealing process, both models can produce similar final probability distributions. Thus, by only studying the final probability distribution, we cannot infer which process is better suited to describe the dynamics of the real device during the annealing process. This would be an interesting point for future studies when future versions of quantum annealers provide the option to measure the state during the annealing process and not only at the end.

Appendix A

Circuit quantization of the studied systems

A.1 Double SQUID

We use the circuit quantization rules [Dev97] discussed in Section 4.1.2 to derive the Hamiltonian of the (symmetric) double SQUID Eq. (4.8). Figure A.1 shows the circuit of a SQUID with CJJ loop. The circuit has four nodes including ground with corresponding node fluxes Φ_a , Φ_b , Φ_c and $\Phi_{\text{ground}} = 0$ and five branch fluxes which we label ϕ_1 , ϕ_2 , ϕ_3 , ϕ_4 and ϕ_5 as indicated in the figure. The external fluxes are denoted ϕ'^x and ϕ^x_{CJJ} . We choose the branches connecting the nodes a, b and c to ground as tree branches. Thus, the branch fluxes ϕ_1 , ϕ_2 and ϕ_5 correspond to tree branches and can be expressed by the node fluxes as follows:

$$\phi_1 = \Phi_a - \Phi_{\text{ground}} = \Phi_a, \tag{A.1}$$

$$\phi_2 = \Phi_b - \Phi_{\text{ground}} = \Phi_b, \tag{A.2}$$

$$\phi_5 = \Phi_c - \Phi_{\text{ground}} = \Phi_c. \tag{A.3}$$

Since the circuit has two closed loops, we have two closure branches which means that the two corresponding fluxes ϕ_3 and ϕ_4 can be written in terms of the node fluxes as follows:

$$\phi_3 = \Phi_c - \Phi_a + \phi'^x + \phi_{\text{CJJ}}^x, \tag{A.4}$$

$$\phi_4 = \Phi_c - \Phi_b + \phi'^x \tag{A.5}$$

or in terms of the tree branch fluxes:

$$\phi_3 = \phi_5 - \phi_1 + \phi'^x + \phi_{\text{CLI}}^x \tag{A.6}$$

$$\phi_4 = \phi_5 - \phi_2 + \phi'^x. \tag{A.7}$$

For the Lagrangian, we obtain by using the quantization rules

$$\mathcal{L} = \frac{C_1}{2}\dot{\phi}_1^2 + \frac{C_2}{2}\dot{\phi}_2^2 + E_J\cos(2e\phi_1) + E_J\cos(2e\phi_2) - \frac{1}{L}\frac{\phi_5^2}{2} - \frac{1}{L_{\text{CJJ}}/2}\frac{\phi_3^2}{2} - \frac{1}{L_{\text{CJJ}}/2}\frac{\phi_4^2}{2}$$

$$= \frac{C_1}{2}\dot{\phi}_1^2 + \frac{C_2}{2}\dot{\phi}_2^2 + E_J\cos(2e\phi_1) + E_J\cos(2e\phi_2) - \frac{1}{L}\frac{\phi_5^2}{2} - \frac{1}{L_{\text{CJJ}}/2}\frac{(\phi_3 + \phi_4)^2 + (\phi_4 - \phi_3)^2}{4}.$$
(A.8)

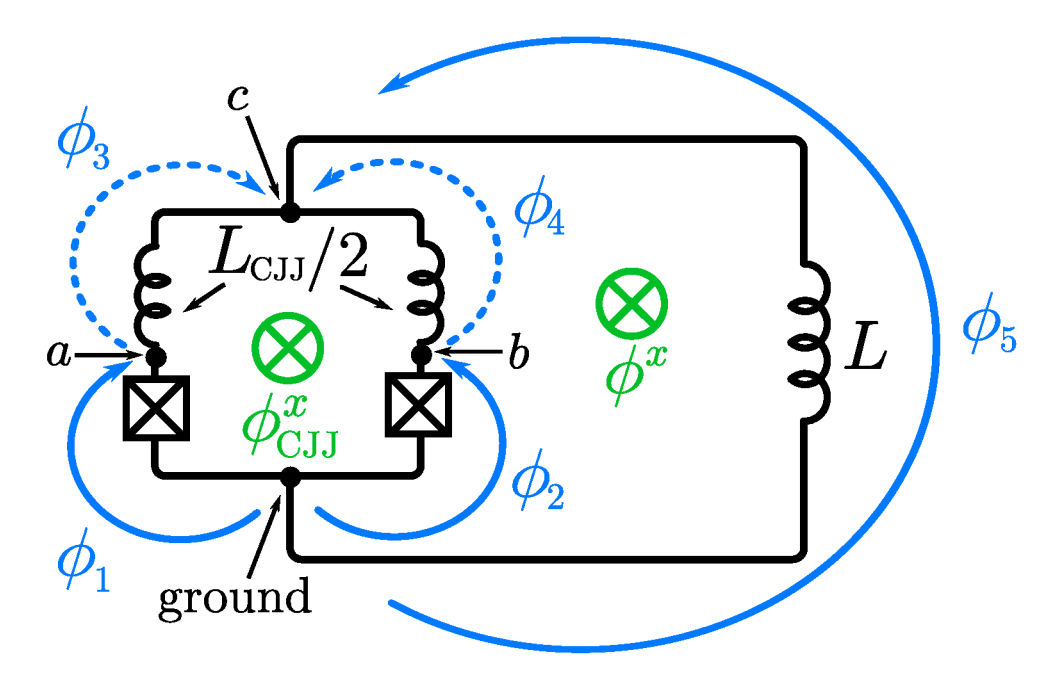


Figure A.1: Circuit of a SQUID with CJJ loop.

Substituting Eqs. (A.6) and (A.7) into Eq. (A.8) yields

$$\mathcal{L} = \frac{C_1}{2}\dot{\phi}_1^2 + \frac{C_2}{2}\dot{\phi}_2^2 + E_J\cos(2e\phi_1) + E_J\cos(2e\phi_2) - \frac{1}{L}\frac{\phi_5^2}{2} - \frac{1}{L_{\text{CJJ}}/2}\frac{(2\phi_5 + 2\phi'^x - \phi_1 - \phi_2 + \phi_{\text{CJJ}}^x)^2 + (\phi_1 - \phi_2 - \phi_{\text{CJJ}}^x)^2}{4}.$$
 (A.9)

Since $\dot{\phi}_5$ does not occur in the Lagrangian, we can use the Euler-Lagrange equation to solve for ϕ_5 :

$$0 = \frac{d}{dt} \frac{\partial \mathcal{L}}{\partial \dot{\phi}_5} = \frac{\partial \mathcal{L}}{\partial \phi_5} = -\frac{\phi_5}{L} - \frac{\phi_5 + \phi'^x - (\phi_1 + \phi_2 - \phi_{\text{CJJ}}^x)/2}{L_{\text{CJJ}}/4}$$
(A.10)

$$\Rightarrow \phi_5 = \frac{L}{L + L_{\text{CJI}}/4} \frac{\phi_1 + \phi_2 - 2\phi'^x - \phi_{\text{CJJ}}^x}{2}.$$
 (A.11)

Inserting Eq. (A.11) into Eq. (A.9) gives

$$\mathcal{L} = \frac{C_1}{2}\dot{\phi}_1^2 + \frac{C_2}{2}\dot{\phi}_2^2 + E_J\cos(2e\phi_1) + E_J\cos(2e\phi_2) - \frac{1}{L_{\text{CJJ}}}\frac{(\phi_1 - \phi_2 - \phi_{\text{CJJ}}^x)^2}{2} - \frac{L_{\text{CJJ}}/4}{(L + L_{\text{CJJ}}/4)^2}\frac{(2\phi'^x - \phi_1 - \phi_2 + \phi_{\text{CJJ}}^x)^2}{8} - \frac{L}{(L + L_{\text{CJJ}}/4)^2}\frac{(\phi_1 + \phi_2 - 2\phi'^x - \phi_{\text{CJJ}}^x)^2}{8}.$$
(A.12)

The variable transformation

$$\phi = \frac{\phi_1 + \phi_2}{2},$$
 $\phi_{\text{CJJ}} = \phi_1 - \phi_2,$
(A.13)

$$\phi_1 = \phi + \frac{\phi_{\text{CJJ}}}{2}, \qquad \phi_2 = \phi - \frac{\phi_{\text{CJJ}}}{2} \tag{A.14}$$

leads to the Lagrangian

$$\mathcal{L} = \frac{C_1}{2} \left(\dot{\phi} + \frac{\dot{\phi}_{\text{CJJ}}}{2} \right)^2 + \frac{C_2}{2} \left(\dot{\phi} - \frac{\dot{\phi}_{\text{CJJ}}}{2} \right)^2 + E_J \cos \left(2e\phi + \frac{2e\phi_{\text{CJJ}}}{2} \right) \\
+ E_J \cos \left(2e\phi - \frac{2e\phi_{\text{CJJ}}}{2} \right) - \frac{1}{L_{\text{CJJ}}} \frac{(\phi_{\text{CJJ}} - \phi_{\text{CJJ}}^x)^2}{2} - \frac{1}{L + L_{\text{CJJ}}/4} \frac{(2\phi - 2\phi'^x - \phi_{\text{CJJ}}^x)^2}{8} \\
= \frac{C_1 + C_2}{2} \dot{\phi}^2 + \frac{C_1 + C_2}{8} \dot{\phi}_{\text{CJJ}}^2 + \frac{C_1 - C_2}{2} \dot{\phi} \dot{\phi}_{\text{CJJ}} + 2E_J \cos(2e\phi) \cos \left(\frac{2e\phi_{\text{CJJ}}}{2} \right) \\
- \frac{1}{L_{\text{CJJ}}} \frac{(\phi_{\text{CJJ}} - \phi_{\text{CJJ}}^x)^2}{2} - \frac{1}{L + L_{\text{CJJ}}/4} \frac{(\phi - \phi'^x - \phi_{\text{CJJ}}^x/2)^2}{2}. \tag{A.15}$$

For convenience, we define

$$\phi^x = \phi'^x + \frac{\phi_{\text{CJJ}}^x}{2}.\tag{A.16}$$

Depending on the actual implementation of the CJJ-SQUID, this step may not be necessary (the circuit quantization rules apply to two-dimensional circuits, if the design is three-dimensional, the mapping is not unambiguous).

Assuming $C_1 \approx C_2 = C$ and performing the Legendre transformation

$$Q = \frac{\partial \mathcal{L}}{\partial \dot{\phi}} = 2C\dot{\phi} \quad \Rightarrow \dot{\phi} = \frac{Q}{2C},\tag{A.17}$$

$$Q_{\text{CJJ}} = \frac{\partial \mathcal{L}}{\partial \dot{\phi}_{\text{CJJ}}} = \frac{C}{2} \dot{\phi}_{\text{CJJ}} \implies \dot{\phi}_{\text{CJJ}} = \frac{2}{C} Q_{\text{CJJ}}, \tag{A.18}$$

we obtain the Hamiltonian of the system

$$H = \frac{\partial \mathcal{L}}{\partial \dot{\phi}} \dot{\phi} + \frac{\partial \mathcal{L}}{\partial \dot{\phi}_{\text{CJJ}}} \dot{\phi}_{\text{CJJ}} - \mathcal{L}$$
(A.19)

$$= \frac{1}{4C}Q^{2} + \frac{1}{C}Q_{\text{CJJ}}^{2} - 2E_{J}\cos(2e\phi)\cos\left(\frac{2e\phi_{\text{CJJ}}}{2}\right) + \frac{1}{L_{\text{CJJ}}}\frac{(\phi_{\text{CJJ}} - \phi_{\text{CJJ}}^{x})^{2}}{2} + \frac{1}{L + L_{\text{CJJ}}/4}\frac{(\phi - \phi^{x})^{2}}{2}.$$
(A.20)

At this point, we can perform the quantization step with the operators ϕ and Q (and ϕ_{CJJ} and Q_{CJJ} , accordingly) which fulfill $[\phi, Q] = i$. Using dimensionless variables

$$\phi = \frac{\phi_0}{2\pi}\varphi = \frac{1}{2e}\varphi,\tag{A.21}$$

$$\phi_{\text{CJJ}} = \frac{1}{2e} \varphi_{\text{CJJ}},\tag{A.22}$$

$$Q = 2en, (A.23)$$

$$Q_{\rm CJJ} = 2en_{\rm CJJ},\tag{A.24}$$

and writing the Hamiltonian in φ -space, we finally get

$$H = -\frac{2e^{2}}{2C}\partial_{\varphi}^{2} - \frac{2e^{2}}{C/2}\partial_{\varphi_{\text{CJJ}}}^{2} - 2E_{J}\cos(\varphi)\cos\left(\frac{\varphi_{\text{CJJ}}}{2}\right) + \frac{1}{4e^{2}L_{\text{CJJ}}}\frac{(\varphi_{\text{CJJ}} - \varphi_{\text{CJJ}}^{x})^{2}}{2} + \frac{1}{4e^{2}(L + L_{\text{CJJ}}/4)}\frac{(\varphi - \varphi^{x})^{2}}{2}.$$
 (A.25)

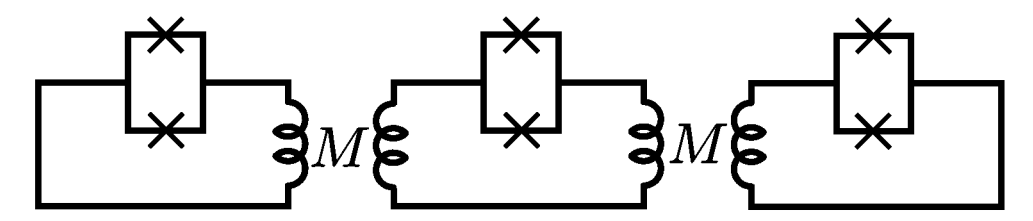


Figure A.2: Sketch of the circuit of three coupled double SQUIDs with mutual inductances M. The circuits of the individual SQUIDs are the same as depicted in Fig. A.1.

A.2 Coupled SQUIDs

For three coupled SQUIDs labeled by A, B (corresponding to the qubits) and C (corresponding to the coupler) with mutual inductances M as shown in Fig. A.2, we can use the same procedure as in Section A.1 to obtain the branch fluxes $\phi_{1,X}$, $\phi_{2,X}$, $\phi_{3,X}$, $\phi_{4,X}$ and $\phi_{5,X}$ with $X \in \{A, B, C\}$. However, instead of the relations $\phi_{5,X} = L_X I_{5,X}$, the set of linear equations

$$\phi_{5,A} = LI_{5,A} - MI_{5,C},\tag{A.26}$$

$$\phi_{5,C} = L_C I_{5,C} - M I_{5,A} - M I_{5,B}, \tag{A.27}$$

$$\phi_{5,B} = LI_{5,B} - MI_{5,C} \tag{A.28}$$

holds because we have to take into account the influence of the currents in the neighboring loops inducing a magnetic flux. We can write Eqs. (A.26) - (A.28) as a matrix equation

$$\begin{pmatrix} \phi_{5,A} \\ \phi_{5,C} \\ \phi_{5,B} \end{pmatrix} = \mathbb{L} \begin{pmatrix} I_{5,A} \\ I_{5,C} \\ I_{5,B} \end{pmatrix}, \tag{A.29}$$

with the inductance matrix

$$\mathbb{L} = \begin{pmatrix} L & -M & 0 \\ -M & L_C & -M \\ 0 & -M & L \end{pmatrix},$$
(A.30)

and its inverse

$$\mathbb{L}^{-1} = \begin{pmatrix} \frac{1}{L} \left(1 + \frac{M^2}{LL'} \right) & \frac{M}{LL'} & \frac{M^2}{L^2L'} \\ \frac{M}{LL'} & \frac{1}{L'} & \frac{M}{LL'} \\ \frac{M^2}{L^2L'} & \frac{M}{LL'} & \frac{1}{L} \left(1 + \frac{M^2}{LL'} \right) \end{pmatrix}, \tag{A.31}$$

where $L' = L_C - 2M^2/L$, L_C denotes the inductance of the coupling SQUID and L denotes the inductances of the SQUIDs A and B corresponding to qubits. Using that for two mutually coupled inductances L and L_C the potential energy is given by (see e.g. Chapter 5 in [Jac99])

$$E_{AC} = \frac{1}{2}LI_A^2 + \frac{1}{2}L_CI_C^2 \pm MI_AI_C, \tag{A.32}$$

where we have to use the minus sign as the current flow in opposite directions at the "contact" assuming that the direction of the current is the same for each circuit. Thus, instead of simply subtracting the terms for the potential energy $\phi_{5,X}^2/(2L_X)$ due to the inductances L_X to the Lagrangian (as done to arrive at Eq. (A.8)), we have to subtract the terms for the potential energy given by

$$E_{ABC} = \frac{1}{2}LI_{5,A}^2 + \frac{1}{2}LI_{5,B}^2 + \frac{1}{2}L_CI_{5,C}^2 - MI_{5,A}I_{5,C} - MI_{5,B}I_{5,C}$$
 (A.33)

$$= \frac{1}{2} \begin{pmatrix} I_{5,A} & I_{5,C} & I_{5,B} \end{pmatrix} \mathbb{L} \begin{pmatrix} I_{5,A} \\ I_{5,C} \\ I_{5,B} \end{pmatrix}$$
(A.34)

$$= \frac{1}{2} \begin{pmatrix} \phi_{5,A} & \phi_{5,C} & \phi_{5,B} \end{pmatrix} \mathbb{L}^{-1} \begin{pmatrix} \phi_{5,A} \\ \phi_{5,C} \\ \phi_{5,B} \end{pmatrix}. \tag{A.35}$$

So we obtain for the Lagrangian

$$\mathcal{L} = \sum_{X \in \{A,B,C\}} \left(\frac{C_{1,X}}{2} \dot{\phi}_{1,X}^2 + \frac{C_{2,X}}{2} \dot{\phi}_{2,X}^2 + E_J \left(\cos(2e\phi_{1,X}) + \cos(2e\phi_{2,X}) \right) - \frac{1}{L_{CJJ,X}/2} \left(\frac{\phi_{3,X}^2}{2} + \frac{\phi_{4,X}^2}{2} \right) \right) - \frac{1}{2} \left(\phi_{5,A} \ \phi_{5,C} \ \phi_{5,B} \right) \mathbb{L}^{-1} \begin{pmatrix} \phi_{5,A} \\ \phi_{5,C} \\ \phi_{5,B} \end{pmatrix}$$

$$= \sum_{X \in \{A,B,C\}} \left(\frac{C_{1,X}}{2} \dot{\phi}_{1,X}^2 + \frac{C_{2,X}}{2} \dot{\phi}_{2,X}^2 + E_J \left(\cos(2e\phi_{1,X}) + \cos(2e\phi_{2,X}) \right) - \frac{1}{L_{CJJ,X}/2} \left(\frac{\phi_{3,X}^2}{2} + \frac{\phi_{4,X}^2}{2} \right) \right) - \frac{M^2}{L^2 L'} \phi_{5,A} \phi_{5,B} - \frac{M}{LL'} \left(\phi_{5,A} + \phi_{5,B} \right) \phi_{5,C} - \frac{1}{L} \left(1 + \frac{M^2}{LL'} \right) \frac{\phi_{5,A}^2}{2} - \frac{1}{L} \left(1 + \frac{M^2}{LL'} \right) \frac{\phi_{5,B}^2}{2} - \frac{1}{L'} \frac{\phi_{5,C}^2}{2}. \tag{A.37}$$

Using Eqs. (A.6) and (A.7), which still hold for all SQUIDs, we get

$$\mathcal{L} = \sum_{X \in \{A,B,C\}} \left(\frac{C_{1,X}}{2} \dot{\phi}_{1,X}^2 + \frac{C_{2,X}}{2} \dot{\phi}_{2,X}^2 + E_J \left(\cos(2e\phi_{1,X}) + \cos(2e\phi_{2,X}) \right) - \frac{1}{L_{\text{CJJ},X}/2} \frac{\left(2\phi_{5,X} + 2\phi_X'^x - \phi_{1,X} - \phi_{2,X} + \phi_{\text{CJJ},X}^x \right)^2 + \left(\phi_{1,X} - \phi_{2,X} - \phi_{\text{CJJ},X}^x \right)^2}{4} \right) - \frac{1}{L} \left(1 + \frac{M^2}{LL'} \right) \frac{\phi_{5,A}^2}{2} - \frac{1}{L} \left(1 + \frac{M^2}{LL'} \right) \frac{\phi_{5,B}^2}{2} - \frac{1}{L'} \frac{\phi_{5,C}^2}{2} - \frac{M^2}{L^2L'} \phi_{5,A} \phi_{5,B} - \frac{M}{LL'} \left(\phi_{5,A} + \phi_{5,B} \right) \phi_{5,C}. \tag{A.38}$$

Again, we find that the Lagrangian does not depend on $\dot{\phi}_{5,X}$, so from the Euler-Lagrange equation we still find that

$$\frac{\partial \mathcal{L}}{\partial \phi_{5,X}} = 0. \tag{A.39}$$

However, instead of a single equation we have a system of equations ($L_{\text{CJJ},A} = L_{\text{CJJ},B} = L_{\text{CJJ}}$, $L_{\text{CJJ},C} = L_{\text{co}}$):

$$\frac{\partial \mathcal{L}}{\partial \phi_{5,A}} = -\frac{1}{L_{\text{CJJ}}/4} \frac{2\phi_{5,A} + 2\phi_{A}'^{x} - \phi_{1,A} - \phi_{2,A} + \phi_{\text{CJJ},A}^{x}}{2}$$

$$-\frac{1}{L} \left(1 + \frac{M^{2}}{LL'} \right) \phi_{5,A} - \frac{M^{2}}{L^{2}L'} \phi_{5,B} - \frac{M}{LL'} \phi_{5,C} = 0 \qquad (A.40)$$

$$\frac{\partial \mathcal{L}}{\partial \phi_{5,C}} = -\frac{1}{L_{\text{co}}/4} \frac{2\phi_{5,C} + 2\phi_{C}'^{x} - \phi_{1,C} - \phi_{2,C} + \phi_{\text{CJJ},C}^{x}}{2} - \frac{1}{L'} \phi_{5,C} - \frac{M}{LL'} (\phi_{5,A} + \phi_{5,B}) = 0$$

$$\frac{\partial \mathcal{L}}{\partial \phi_{5,B}} = -\frac{1}{L_{\text{CJJ}}/4} \frac{2\phi_{5,B} + 2\phi_{B}'^{x} - \phi_{1,B} - \phi_{2,B} + \phi_{\text{CJJ},B}^{x}}{2}$$

$$-\frac{1}{L} \left(1 + \frac{M^{2}}{LL'} \right) \phi_{5,B} - \frac{M^{2}}{L^{2}L'} \phi_{5,A} - \frac{M}{LL'} \phi_{5,C} = 0 \qquad (A.42)$$

Solving this system of equations using Mathematica, we arrive at

$$\phi_{5,A} = \frac{2L^{2}(4L' + L_{co})}{L(4L + L_{CJJ})(4L' + L_{co}) + 8L_{CJJ}M^{2}} (\phi_{1,A} + \phi_{2,A} - 2\phi_{A}'^{x} - \phi_{CJJ,A}^{x})$$

$$- \frac{2LL_{CJJ}M}{L(4L + L_{CJJ})(4L' + L_{co}) + 8L_{CJJ}M^{2}} (\phi_{1,C} + \phi_{2,C} - \phi_{CJJ,C}^{x} - 2\phi_{C}'^{x})$$

$$+ \frac{8LL_{CJJ}M^{2}(\phi_{1,A} + \phi_{2,A} - 2\phi_{A}'^{x} - \phi_{CJJ,A}^{x} - \phi_{1,B} - \phi_{2,B} + 2\phi_{B}'^{x} + \phi_{CJJ,B}^{x})}{(4L + L_{CJJ})(L(4L + L_{CJJ})(4L' + L_{co}) + 8L_{CJJ}M^{2})} (A.43)$$

$$\phi_{5,C} = \frac{8L'L^{2} + 4L_{CJJ}M^{2} + 2LL'L_{CJJ}}{L(4L + L_{CJJ})(4L' + L_{co}) + 8L_{CJJ}M^{2}} (\phi_{1,C} + \phi_{2,C} - \phi_{CJJ,C}^{x} - 2\phi_{C}'^{x})$$

$$- \frac{2LL_{co}M(\phi_{1,A} + \phi_{1,B} + \phi_{2,A} + \phi_{2,B} - 2\phi_{A}'^{x} - 2\phi_{B}'^{x} - \phi_{CJJ,A}^{x} - \phi_{CJJ,B}^{x})}{L(4L + L_{CJJ})(4L' + L_{co}) + 8L_{CJJ}M^{2}} (\phi_{1,B} + \phi_{2,B} - 2\phi_{B}'^{x} - \phi_{CJJ,B}^{x})$$

$$- \frac{2L^{2}(4L' + L_{co})}{L(4L + L_{CJJ})(4L' + L_{co}) + 8L_{CJJ}M^{2}} (\phi_{1,C} + \phi_{2,C} - \phi_{CJJ,C}^{x} - 2\phi_{C}'^{x})$$

$$+ \frac{8LL_{CJJ}M^{2}(\phi_{1,B} + \phi_{2,B} - 2\phi_{B}'^{x} - \phi_{CJJ,B}^{x} - \phi_{CJJ,A}^{x} - \phi_{CJJ,A}^{x})}{(4L + L_{CJJ})(L(4L + L_{CJJ})(4L' + L_{co}) + 8L_{CJJ}M^{2})} (A.45)$$

Substituting Eqs. (A.43) - (A.45) into Eq. (A.38) we obtain (using MATHEMATICA):

$$\mathcal{L} = \sum_{X \in \{A,B,C\}} \left(\frac{C_{1,X}}{2} \dot{\phi}_{1,X}^2 + \frac{C_{2,X}}{2} \dot{\phi}_{2,X}^2 + E_J \left(\cos(2e\phi_{1,X}) + \cos(2e\phi_{2,X}) \right) \right.$$

$$\left. - \frac{1}{L_{\text{CJJ},X}} \frac{\left(\phi_{1,X} - \phi_{2,X} - \phi_{\text{CJJ},X}^x \right)^2}{2} \right)$$

$$\left. - \frac{1}{8 \left(L + L_{\text{CJJ}} / 4 \right)} \left(\left(\phi_{1,A} + \phi_{2,A} - 2\phi_A'^x - \phi_{\text{CJJ},A}^x \right)^2 + \left(\phi_{1,B} + \phi_{2,B} - 2\phi_B'^x - \phi_{\text{CJJ},B}^x \right)^2 \right)$$

$$\left. - \frac{2LM^2 \left(\phi_{1,A} + \phi_{2,A} - 2\phi_A'^x - \phi_{\text{CJJ},A}^x + \phi_{1,B} + \phi_{2,B} - 2\phi_B'^x - \phi_{\text{CJJ},B}^x \right)^2}{\left(L + L_{\text{CJJ}} / 4 \right) \left(L \left(4L + L_{\text{CJJ}} \right) \left(4L' + L_{\text{co}} \right) + 8L_{\text{CJJ}} M^2 \right)} \right.$$

$$\frac{LM\left(\phi_{1,A} + \phi_{2,A} - 2\phi_{A}^{\prime x} - \phi_{\text{CJJ},A}^{x} + \phi_{1,B} + \phi_{2,B} - 2\phi_{B}^{\prime x} - \phi_{\text{CJJ},B}^{x}\right)\left(\phi_{1,C} + \phi_{2,C} - 2\phi_{C}^{\prime x} - \phi_{\text{CJJ},C}^{x}\right)}{L(L + L_{\text{CJJ}}/4)(4L' + L_{\text{co}}) + 2L_{\text{CJJ}}M^{2}} - \frac{L(4L + L_{\text{CJJ}})\left(\phi_{1,C} + \phi_{2,C} - 2\phi_{C}^{\prime x} - \phi_{\text{CJJ},C}^{x}\right)^{2}}{2\left(L(4L + L_{\text{CJJ}})(4L' + L_{\text{co}}) + 8L_{\text{CJJ}}M^{2}\right)}.$$
(A.46)

As in the case of a single SQUID, we can perform the variable transformation

$$\phi_X = \frac{\phi_{1,X} + \phi_{2,X}}{2},$$
 $\phi_{\text{CJJ},X} = \phi_{1,X} - \phi_{2,X},$
(A.47)

$$\phi_{1,X} = \phi_X + \frac{\phi_{\text{CJJ},X}}{2},$$
 $\phi_{2,X} = \phi_X - \frac{\phi_{\text{CJJ},X}}{2},$ (A.48)

which yields

$$\mathcal{L} = \sum_{X \in \{A,B,C\}} \left(\frac{C_{1,X} + C_{2,X}}{2} \dot{\phi}_X^2 + \frac{C_{1,X} + C_{2,X}}{8} \dot{\phi}_{\text{CJJ},X}^2 + \frac{C_{1,X} - C_{2,X}}{2} \dot{\phi}_X \dot{\phi}_{\text{CJJ},X} \right) + 2E_{J,X} \cos(2e\phi_X) \cos\left(\frac{2e\phi_{\text{CJJ},X}}{2}\right) - \frac{1}{L_{\text{CJJ},X}} \frac{(\phi_{\text{CJJ},X} - \phi_{\text{CJJ},X}^*)^2}{2} \right) - \frac{1}{L_{\text{CJJ},X}} \frac{(\phi_{\text{CJJ},X} - \phi_{\text{CJJ},X}^*)^2}{2} - \frac{1}{L_{\text{CJJ}}/4} \left(\frac{(\phi_A - \phi_A^{\prime X} - \phi_{\text{CJJ},A}^{\prime X}/2)^2}{2} + \frac{(\phi_B - \phi_B^{\prime X} - \phi_{\text{CJJ},B}^{\prime X}/2)^2}{2} \right) - \frac{M^2 (\phi_A - \phi_A^{\prime X} - \phi_{\text{CJJ},A}^{\prime X}/2 + \phi_B - \phi_B^{\prime X} - \phi_{\text{CJJ},B}^{\prime X}/2)^2}{2(L + L_{\text{CJJ}}/4)((L + L_{\text{CJJ}}/4)(L_C + L_{\text{co}}/4) - 2M^2)} - \frac{M (\phi_A - \phi_A^{\prime X} - \phi_{\text{CJJ},A}^{\prime X}/2 + \phi_B - \phi_B^{\prime X} - \phi_{\text{CJJ},B}^{\prime X}/2) (\phi_C - \phi_C^{\prime X} - \phi_{\text{CJJ},C}^{\prime X}/2)}{(L + L_{\text{CJJ}}/4)(L_C + L_{\text{co}}/4) - 2M^2} - \frac{1}{L_C + L_{\text{co}}/4 - 2M^2/(L + L_{\text{CJJ}}/4)} \frac{(\phi_C - \phi_C^{\prime X} - \phi_{\text{CJJ},C}^{\prime X})^2}{2}$$

$$= \sum_{X \in \{A,B,C\}} \left(\frac{C_{1,X} + C_{2,X}}{2} \dot{\phi}_X^2 + \frac{C_{1,X} + C_{2,X}}{8} \dot{\phi}_{\text{CJJ},X}^2 + \frac{C_{1,X} - C_{2,X}}{2} \dot{\phi}_X \dot{\phi}_{\text{CJJ},X}} \right) - \frac{1}{L_{\text{CJJ}}/X} \left(\frac{\phi_{\text{CJJ},X}}{2} - \phi_{\text{CJJ},X}^2}\right)^2 - \frac{1}{L_{\text{CJJ}}/X} \left(\frac{\phi_{\text{CJJ},X}}{2} - \phi_{\text{CJJ},X}^2}\right)^2 - \frac{1}{L_{\text{CJJ}}/4} \left(1 + \frac{M^2}{(L + L_{\text{CJJ}}/4)L_{\text{eff}}}\right) \left(\frac{(\phi_A - \phi_A^{\prime X} - \phi_{\text{CJJ},A}^2/2)^2}{2} + \frac{(\phi_B - \phi_B^{\prime X} - \phi_{\text{CJJ},B}^2/2)^2}{2}\right) - \frac{M}{(L + L_{\text{CJJ}}/4)L_{\text{eff}}} \left(\phi_A - \phi_A^{\prime X} - \frac{\phi_{\text{CJJ},A}}{2} + \phi_B - \phi_B^{\prime X} - \frac{\phi_{\text{CJJ},A}}{2}\right) \left(\phi_C - \phi_C^{\prime X} - \frac{\phi_{\text{CJJ},C}}{2}\right),$$

$$(A.50)$$

where we used $L' = L_C - 2M^2/L$ and defined $L_{\text{eff}} = L_C + L_{\text{co}}/4 - 2M^2/(L + L_{\text{CJJ}}/4)$.

Since the variables ϕ_X and $\phi_{\text{CJJ},X}$ for different X do not couple in Eq. (A.50), we can use the same Legendre transformation as for a single SQUID, i.e., Eqs. (A.17) and (A.18) if we

assume that $C_{1,X} \approx C_{2,X} = C_X$, and we arrive at the Hamiltonian (with $\phi_X^{\prime x} + \phi_{\text{CJJ},X}^x/2 = \phi_X^x$)

$$H = \sum_{X \in \{A,B,C\}} \left(\frac{1}{4C_X} Q_X^2 + \frac{1}{C_X} Q_{\text{CJJ},X}^2 - 2E_{J,X} \cos(2e\phi_X) \cos\left(\frac{2e\phi_{\text{CJJ},X}}{2}\right) + \frac{\left(\phi_{\text{CJJ},X} - \phi_{\text{CJJ},X}^x\right)^2}{2L_{\text{CJJ},X}} \right)$$

$$+ \frac{1}{L + L_{\text{CJJ}}/4} \left(1 + \frac{M^2}{(L + L_{\text{CJJ}}/4)L_{\text{eff}}} \right) \left(\frac{\left(\phi_A - \phi_A^x\right)^2}{2} + \frac{\left(\phi_B - \phi_B^x\right)^2}{2} \right)$$

$$+ \frac{1}{L_{\text{eff}}} \frac{\left(\phi_C - \phi_C^x\right)^2}{2} + \frac{M^2}{(L + L_{\text{CJJ}}/4)^2L_{\text{eff}}} \left(\phi_A - \phi_A^x\right) \left(\phi_B - \phi_B^x\right)$$

$$+ \frac{M}{(L + L_{\text{CJJ}}/4)L_{\text{eff}}} \left(\phi_A - \phi_A^x + \phi_B - \phi_B^x\right) \left(\phi_C - \phi_C^x\right). \tag{A.51}$$

Writing the Hamiltonian with dimensionless variables in φ -space yields

$$H = \sum_{X \in \{A,B,C\}} \left(-\frac{2e^{2}}{2C_{X}} \partial_{\varphi_{X}}^{2} - \frac{2e^{2}}{C_{X}/2} \partial_{\varphi_{\text{CJJ},X}}^{2} - 2E_{J,X} \cos(\varphi_{X}) \cos\left(\frac{\varphi_{\text{CJJ},X}}{2}\right) \right)$$

$$+ \frac{1}{4e^{2}L_{\text{CJJ}}} \left(\frac{\left(\varphi_{\text{CJJ},A} - \varphi_{\text{CJJ},A}^{x}\right)^{2}}{2} + \frac{\left(\varphi_{\text{CJJ},B} - \varphi_{\text{CJJ},B}^{x}\right)^{2}}{2} \right) + \frac{1}{4e^{2}L_{\text{co}}} \frac{\left(\varphi_{\text{CJJ},C} - \varphi_{\text{CJJ},C}^{x}\right)^{2}}{2}$$

$$+ \frac{1}{4e^{2}(L + L_{\text{CJJ}}/4)} \left(1 + \frac{M^{2}}{(L + L_{\text{CJJ}}/4)L_{\text{eff}}} \right) \left(\frac{\left(\varphi_{A} - \varphi_{A}^{x}\right)^{2}}{2} + \frac{\left(\varphi_{B} - \varphi_{B}^{x}\right)^{2}}{2} \right)$$

$$+ \frac{1}{4e^{2}L_{\text{eff}}} \frac{\left(\varphi_{C} - \varphi_{C}^{x}\right)^{2}}{2} + \frac{M^{2}}{4e^{2}(L + L_{\text{CJJ}}/4)^{2}L_{\text{eff}}} \left(\varphi_{A} - \varphi_{A}^{x}\right) \left(\varphi_{B} - \varphi_{B}^{x}\right)$$

$$+ \frac{M}{4e^{2}(L + L_{\text{CJJ}}/4)L_{\text{eff}}} \left(\varphi_{A} - \varphi_{A}^{x} + \varphi_{B} - \varphi_{B}^{x}\right) \left(\varphi_{C} - \varphi_{C}^{x}\right). \tag{A.52}$$

Appendix B

Additional calculations and proofs

This chapter contains calculations and proofs which are outsourced from Section 4.2 and Chapter 5.

B.1 Basis transformation

Here, we present the calculation of the basis transformation applied in Section 4.2.2. The total Hamiltonian where $\varphi_{\text{CJJ},0}$ is replaced by its expectation value $\langle \varphi_{\text{CJJ},0} \rangle$ is given by

$$H_{\text{total}}^{\langle \varphi_{\text{CJJ},0} \rangle} = \sum_{i=1}^{2} \left(-E_{C} \partial_{\varphi_{i}}^{2} - E_{C_{\text{CJJ}}} \partial_{\varphi_{\text{CJJ},i}}^{2} - E_{J} \cos\left(\varphi_{i}\right) \cos\left(\frac{\varphi_{\text{CJJ},i}}{2}\right) + E_{L_{\text{CJJ}}} \frac{\left(\varphi_{\text{CJJ},i} - \varphi_{\text{CJJ}}^{x}\right)^{2}}{2} \right)$$

$$-E_{C_{0}} \partial_{\varphi_{0}}^{2} - E_{J_{0}} \cos\left(\varphi_{0}\right) \cos\left(\frac{\langle \varphi_{\text{CJJ},0} \rangle}{2}\right) + E_{L_{\text{eff}}} \frac{\varphi_{0}^{2}}{2}$$

$$+E_{L} \left(1 + \frac{M^{2}}{(L + L_{\text{CJJ}}/4)L_{\text{eff}}}\right) \left(\frac{\left(\varphi_{1} - \varphi_{1}^{x}\right)^{2}}{2} + \frac{\left(\varphi_{2} - \varphi_{2}^{x}\right)^{2}}{2}\right)$$

$$+\frac{M^{2}E_{L}}{(L + L_{\text{CJJ}}/4)L_{\text{eff}}} \left(\varphi_{1} - \varphi_{1}^{x}\right) \left(\varphi_{2} - \varphi_{2}^{x}\right) + \frac{ME_{L}}{L_{\text{eff}}} \left(\varphi_{1} - \varphi_{1}^{x} + \varphi_{2} - \varphi_{2}^{x}\right) \varphi_{0}, \tag{B.1}$$

and the change-of-basis matrix T is given by

$$T = i\alpha(\varphi_1 - \varphi_1^x + \varphi_2 - \varphi_2^x)\partial_{\varphi_0}, \tag{B.2}$$

yielding the following commutators:

$$[iT, H_{\text{total}}^{\langle \varphi_{\text{CJJ},0} \rangle}] = \alpha E_C \partial_{\varphi_0} [\varphi_1 + \varphi_2, \partial_{\varphi_1}^2 + \partial_{\varphi_2}^2]$$

$$+ \alpha E_{J_0} \cos \left(\frac{\langle \varphi_{\text{CJJ},0} \rangle}{2} \right) (\varphi_1 - \varphi_1^x + \varphi_2 - \varphi_2^x) [\partial_{\varphi_0}, \cos(\varphi_0)]$$

$$- \alpha (\varphi_1 - \varphi_1^x + \varphi_2 - \varphi_2^x) [\partial_{\varphi_0}, \frac{E_{L_{\text{eff}}}}{2} \varphi_0^2 + \frac{ME_L}{L_{\text{eff}}} (\varphi_1 - \varphi_1^x + \varphi_2 - \varphi_2^x) \varphi_0]$$

$$= -2\alpha E_C \partial_{\varphi_0} (\partial_{\varphi_1} + \partial_{\varphi_2}) - \alpha E_{J_0} \cos \left(\frac{\langle \varphi_{\text{CJJ},0} \rangle}{2} \right) (\varphi_1 - \varphi_1^x + \varphi_2 - \varphi_2^x) \sin(\varphi_0)$$

$$- \alpha (\varphi_1 - \varphi_1^x + \varphi_2 - \varphi_2^x) \left(E_{L_{\text{eff}}} \varphi_0 + \frac{ME_L}{L_{\text{eff}}} (\varphi_1 - \varphi_1^x + \varphi_2 - \varphi_2^x) \right)$$
(B.3)

$$[iT, [iT, H_{\text{total}}^{\langle \varphi_{\text{CJJ},0} \rangle}]] = 2\alpha^{2} E_{C} \partial_{\varphi_{0}}^{2} [\varphi_{1} + \varphi_{2}, \partial_{\varphi_{1}} + \partial_{\varphi_{2}}]$$

$$+ \alpha^{2} E_{J_{0}} \cos \left(\frac{\langle \varphi_{\text{CJJ},0} \rangle}{2}\right) (\varphi_{1} - \varphi_{1}^{x} + \varphi_{2} - \varphi_{2}^{x})^{2} [\partial_{\varphi_{0}}, \sin(\varphi_{0})]$$

$$+ \alpha^{2} E_{L_{\text{eff}}} (\varphi_{1} - \varphi_{1}^{x} + \varphi_{2} - \varphi_{2}^{x})^{2} [\partial_{\varphi_{0}}, \varphi_{0}]$$

$$= -4\alpha^{2} E_{C} \partial_{\varphi_{0}}^{2} + \alpha^{2} E_{J_{0}} \cos \left(\frac{\langle \varphi_{\text{CJJ},0} \rangle}{2}\right) (\varphi_{1} - \varphi_{1}^{x} + \varphi_{2} - \varphi_{2}^{x})^{2} \cos(\varphi_{0})$$

$$+ \alpha^{2} E_{L_{\text{eff}}} (\varphi_{1} - \varphi_{1}^{x} + \varphi_{2} - \varphi_{2}^{x})^{2}$$
(B.4)

$$[iT, [iT, [iT, H_{\text{total}}^{\langle \varphi_{\text{CJJ},0} \rangle}]]] = -\alpha^3 E_{J_0} \cos \left(\frac{\langle \varphi_{\text{CJJ},0} \rangle}{2}\right) (\varphi_1 - \varphi_1^x + \varphi_2 - \varphi_2^x)^3 [\partial_{\varphi_0}, \cos(\varphi_0)]$$
$$= \alpha^3 E_{J_0} \cos \left(\frac{\langle \varphi_{\text{CJJ},0} \rangle}{2}\right) (\varphi_1 - \varphi_1^x + \varphi_2 - \varphi_2^x)^3 \sin(\varphi_0) \tag{B.5}$$

For the missing commutators, we show by using

$$[iT, H]^n = \underbrace{[iT, [iT, \dots [iT, H]]]}_{n \text{ times}},$$
(B.6)

that is, for instance $[iT, H]^2 = [iT, [iT, H]]$, that for $n \in \mathbb{N}, n \ge 1$

$$[iT, -\cos(\varphi_0)]^{2n-1} = (-1)^n \alpha^{2n-1} (\varphi_1 - \varphi_1^x + \varphi_2 - \varphi_2^x)^{2n-1} \sin(\varphi_0)$$
 (B.7)

$$[iT, -\cos(\varphi_0)]^{2n} = (-1)^{n+1}\alpha^{2n} (\varphi_1 - \varphi_1^x + \varphi_2 - \varphi_2^x)^{2n} \cos(\varphi_0).$$
 (B.8)

First, we show the base case with n = 1:

$$[iT, -\cos(\varphi_0)]^1 = (-1)^1 \alpha^1 (\varphi_1 - \varphi_1^x + \varphi_2 - \varphi_2^x)^1 \sin(\varphi_0)$$
(B.9)

$$[iT, -\cos(\varphi_0)]^2 = (-1)^2 \alpha^2 (\varphi_1 - \varphi_1^x + \varphi_2 - \varphi_2^x)^2 \cos(\varphi_0)$$
 (B.10)

We now show that if Eqs. (B.7) and (B.8) hold for $n \in \mathbb{N}, n \ge 1$, Eqs. (B.7) and (B.8) also hold for n + 1:

$$[iT, -\cos(\varphi_0)]^{2(n+1)-1} = [iT, -\cos(\varphi_0)]^{2n+1} = [iT, [iT, -\cos(\varphi_0)]^{2n}]$$

$$\stackrel{\text{Eq. } (B.8)}{=} (-1)^{n+1} \alpha^{2n} (\varphi_1 - \varphi_1^x + \varphi_2 - \varphi_2^x)^{2n} [iT, \cos(\varphi_0)]$$

$$= (-1)^{n+2} \alpha^{2n+1} (\varphi_1 - \varphi_1^x + \varphi_2 - \varphi_2^x)^{2n+1} [\partial_{\varphi_0}, \cos(\varphi_0)]$$

$$= (-1)^{n+1} \alpha^{2(n+1)-1} (\varphi_1 - \varphi_1^x + \varphi_2 - \varphi_2^x)^{2(n+1)-1} \sin(\varphi_0) \quad (B.11)$$

$$[iT, -\cos(\varphi_0)]^{2(n+1)} = [iT, -\cos(\varphi_0)]^{2n+2} = [iT, [iT, -\cos(\varphi_0)]^{2(n+1)-1}]$$

$$\stackrel{\text{Eqs. } (B.7), (B.11)}{=} (-1)^{n+1} \alpha^{2n+1} (\varphi_1 - \varphi_1^x + \varphi_2 - \varphi_2^x)^{2n1} [iT, \sin(\varphi_0)]$$

$$= (-1)^{n+2} \alpha^{2n+2} (\varphi_1 - \varphi_1^x + \varphi_2 - \varphi_2^x)^{2n+2} [\partial_{\varphi_0}, \sin(\varphi_0)]$$

$$= (-1)^{n+2} \alpha^{2(n+1)} (\varphi_1 - \varphi_1^x + \varphi_2 - \varphi_2^x)^{2(n+1)} \cos(\varphi_0) \quad (B.12)$$

This proves Eqs. (B.7) and (B.8) by induction.

Using Eqs. (B.7) and (B.8), we can evaluate the sum

$$\sum_{n=1}^{\infty} \frac{1}{n!} [iT, -\cos(\varphi_0)]^n = \sum_{n=1}^{\infty} \frac{1}{(2n-1)!} [iT, -\cos(\varphi_0)]^{(2n-1)} + \frac{1}{(2n)!} [iT, -\cos(\varphi_0)]^{(2n)}$$

$$= \sum_{n=0}^{\infty} \frac{1}{(2n+1)!} (-1)^{n+1} \alpha^{2n+1} (\varphi_1 - \varphi_1^x + \varphi_2 - \varphi_2^x)^{2n+1} \sin(\varphi_0)$$

$$+ \sum_{n=1}^{\infty} \frac{1}{(2n)!} (-1)^{n+1} \alpha^{2n} (\varphi_1 - \varphi_1^x + \varphi_2 - \varphi_2^x)^{2n} \cos(\varphi_0)$$

$$= -\sin (\alpha(\varphi_1 - \varphi_1^x + \varphi_2 - \varphi_2^x)) \sin(\varphi_0)$$

$$-\cos (\alpha(\varphi_1 - \varphi_1^x + \varphi_2 - \varphi_2^x)) \cos(\varphi_0) + \cos(\varphi_0)$$

$$= -\cos (\alpha(\varphi_1 - \varphi_1^x + \varphi_2 - \varphi_2^x) - \varphi_0) + \cos(\varphi_0).$$
 (B.13)

Finally, we obtain

$$e^{iT}H_{\text{total}}^{(\varphi_{\text{CJJ},0})}e^{-iT} = H_{\text{total}}^{(\varphi_{\text{CJJ},0})} + \sum_{n=1}^{\infty} \frac{1}{n!} [-iT, H_{\text{total}}^{(\varphi_{\text{CJJ},0})}]^n$$

$$= \sum_{i=1}^{2} \left(-E_C \partial_{\varphi_i}^2 - E_{C_{\text{CJJ}}} \partial_{\varphi_{\text{CJJ},i}}^2 - E_J \cos(\varphi_i) \cos\left(\frac{\varphi_{\text{CJJ,i}}}{2}\right) + E_{L_{\text{CJJ}}} \frac{(\varphi_{\text{CJJ,i}} - \varphi_{\text{CJJ}}^2)^2}{2} \right)$$

$$-E_{C_0} \partial_{\varphi_0}^2 - E_{J_0} \cos(\varphi_0) \cos\left(\frac{(\varphi_{\text{CJJ,0}})}{2}\right) - 2\alpha E_C \partial_{\varphi_0} (\partial_{\varphi_1} + \partial_{\varphi_2})$$

$$+E_L \left(1 + \frac{M^2}{(L + L_{\text{CJJ}}/4)L_{\text{eff}}}\right) \left(\frac{(\varphi_1 - \varphi_1^x)^2}{2} + \frac{(\varphi_2 - \varphi_2^x)^2}{2}\right) + E_{L_{\text{eff}}} \frac{\varphi_0^2}{2}$$

$$+ \frac{M^2 E_L}{(L + L_{\text{CJJ}}/4)L_{\text{eff}}} (\varphi_1 - \varphi_1^x) (\varphi_2 - \varphi_2^x) + \frac{ME_L}{L_{\text{eff}}} (\varphi_1 - \varphi_1^x + \varphi_2 - \varphi_2^x) \varphi_0$$

$$-\alpha (\varphi_1 - \varphi_1^x + \varphi_2 - \varphi_2^x) \left(E_{L_{\text{eff}}} \varphi_0 + \frac{ME_L}{L_{\text{eff}}} (\varphi_1 - \varphi_1^x + \varphi_2 - \varphi_2^x)\right)$$

$$-2\alpha^2 E_C \partial_{\varphi_0}^2 + \frac{\alpha^2 E_{L_{\text{eff}}}}{2} (\varphi_1 - \varphi_1^x + \varphi_2 - \varphi_2^x)^2 + E_{J_0} \cos\left(\frac{(\varphi_{\text{CJJ,0}})}{2}\right) \cos(\varphi_0)$$

$$-E_{J_0} \cos\left(\frac{(\varphi_{\text{CJJ,0}})}{2}\right) \cos(\alpha (\varphi_1 - \varphi_1^x + \varphi_2 - \varphi_2^x) - \varphi_0)$$

$$= \sum_{i=1}^2 \left(-E_C \partial_{\varphi_i}^2 - E_{C_{\text{CJJ}}} \partial_{\varphi_{\text{CJJ,i}}}^2 - E_J \cos(\varphi_i) \cos\left(\frac{\varphi_{\text{CJJ,i}}}{2}\right) + E_{L_{\text{CJJ}}} \frac{(\varphi_{\text{CJJ,i}} - \varphi_{\text{CJJ}}^x)^2}{2}\right)$$

$$-(E_{C_0} + 2\alpha^2 E_C) \partial_{\varphi_0}^2 + \left(\frac{ME_L}{L_{\text{eff}}} - \alpha E_{L_{\text{eff}}}\right) (\varphi_1 - \varphi_1^x + \varphi_2 - \varphi_2^x) \varphi_0$$

$$+E_L \left(1 + \frac{M^2}{(L + L_{\text{CJJ}}/4)L_{\text{eff}}} + \alpha^2 \frac{L + L_{\text{CJJ}}/4}{L_{\text{eff}}} - 2\alpha \frac{M}{L_{\text{eff}}}\right) \left(\frac{(\varphi_1 - \varphi_1^x)^2}{2} + \frac{(\varphi_2 - \varphi_2^x)^2}{2}\right)$$

$$-2\alpha E_C \partial_{\varphi_0} (\partial_{\varphi_1} + \partial_{\varphi_2})$$

$$-2\alpha E_C \partial_{\varphi_0} (\partial_{\varphi_1} + \partial_{\varphi_2})$$

$$-E_{J_0} \cos\left(\frac{(\varphi_{\text{CJJ,0}})}{2}\right) \cos(\alpha (\varphi_1 - \varphi_1^x + \varphi_2 - \varphi_2^x) - \varphi_0),$$
(B.14)

which we use in the basis transformation.

B.2 Monotonicity

In this appendix, we prove the following statement which we used in Section 4.2.3.

(S1) The function

$$\gamma(\varphi_{\mathrm{CJJ},0}^{x}) = \frac{E_L^2}{\widetilde{E}_L^2(\varphi_{\mathrm{CJJ},0}^{x})} \frac{\beta_{\mathrm{eff}}(\varphi_{\mathrm{CJJ},0}^{x})}{1 + \beta_{\mathrm{eff}}(\varphi_{\mathrm{CJJ},0}^{x})}$$

is strictly monotonically decreasing in $\varphi_{\text{CJJ},0}^x$ for $0 \leq \varphi_{\text{CJJ},0}^x \leq 3\pi/2$.

Proof: To prove (S1), we show that $\partial_{\varphi_{\text{CJJ},0}^x} \gamma(\varphi_{\text{CJJ},0}^x) < 0$ for $0 < \varphi_{\text{CJJ},0}^x < 3\pi/2$. First we apply the chain rule to look at the derivative in two parts:

$$\frac{\partial \gamma}{\partial \varphi_{\text{CJJ},0}^x} = \frac{\partial \gamma}{\partial \beta_{\text{eff}}} \frac{\partial \beta_{\text{eff}}}{\partial \varphi_{\text{CJJ},0}^x}.$$
(B.15)

For the first part we have with $\beta = E_{J_0}/E_{L_{\text{eff}}} > 0$

$$\frac{\partial \beta_{\text{eff}}}{\partial \varphi_{\text{CJJ,0}}^{x}} = \frac{\partial}{\partial \varphi_{\text{CJJ,0}}^{x}} \left(\beta \cos \left(\frac{\varphi_{\text{CJJ,0}}^{x}}{2} - \frac{E_{J_0} \sin \left(\varphi_{\text{CJJ,0}}^{x}/2 \right)}{4E_{L_{\text{CJJ,0}}} + E_{J_0} \cos \left(\varphi_{\text{CJJ,0}}^{x}/2 \right)} \right) \right)
= -\beta \sin \left(\frac{\varphi_{\text{CJJ,0}}^{x}}{2} - \frac{E_{J_0} \sin \left(\varphi_{\text{CJJ,0}}^{x}/2 \right)}{4E_{L_{\text{CJJ,0}}} + E_{J_0} \cos \left(\varphi_{\text{CJJ,0}}^{x}/2 \right)} \right)
\times \frac{16E_{L_{\text{CJJ,0}}}^{2} + 4E_{L_{\text{CJJ,0}}}E_{J_0} \cos \left(\varphi_{\text{CJJ,0}}^{x}/2 \right) - E_{J_0}^{2} \sin^{2} \left(\varphi_{\text{CJJ,0}}^{x}/2 \right)}{2\left(4E_{L_{\text{CJJ,0}}} + E_{J_0} \cos \left(\varphi_{\text{CJJ,0}}^{x}/2 \right) \right)^{2}}.$$
(B.16)

Since the denominator is positive and $\beta > 0$ as well as

$$16E_{L_{\text{CJJ},0}}^{2} + 4E_{L_{\text{CJJ},0}}E_{J_{0}}\cos\left(\varphi_{\text{CJJ},0}^{x}/2\right) - E_{J_{0}}^{2}\sin^{2}\left(\varphi_{\text{CJJ},0}^{x}/2\right)$$

$$\geq 16E_{L_{\text{CJJ},0}}^{2} - E_{J_{0}}(4E_{L_{\text{CJJ},0}} + E_{J_{0}}) \geq 16E_{L_{\text{CJJ},0}}^{2} - 5E_{L_{\text{CJJ},0}}E_{J_{0}} \geq 11E_{L_{\text{CJJ},0}}^{2} > 0, \quad (B.17)$$

because $E_{L_{\text{CJJ},0}} > E_{J_0}$, we only have to look at the sign of the sine. For $0 < \varphi_{\text{CJJ},0}^x < 2\pi$, the sine is positive (because $E_{L_{\text{CJJ},0}} > E_{J_0}$ and therefore the denominator is positive and larger than E_{J_0}). Thus, we have

$$\frac{\partial \beta_{\text{eff}}}{\partial \varphi_{\text{CJJ},0}^x} < 0 \quad \text{for } 0 < \varphi_{\text{CJJ},0}^x < 2\pi.$$
 (B.18)

The next step is to look at

$$\frac{\partial}{\partial \varphi_{\text{CJJ},0}^{x}} \left(\frac{\beta_{\text{eff}}}{1 + \beta_{\text{eff}}} \right) = \frac{\partial}{\partial \beta_{\text{eff}}} \left(\frac{\beta_{\text{eff}}}{1 + \beta_{\text{eff}}} \right) \frac{\partial \beta_{\text{eff}}}{\partial \varphi_{\text{CJJ},0}^{x}} = \frac{1}{(1 + \beta_{\text{eff}})^{2}} \frac{\partial \beta_{\text{eff}}}{\partial \varphi_{\text{CJJ},0}^{x}}$$
(B.19)

which is negative for $0 < \varphi_{\text{CJJ},0}^x < 3\pi/2$ and if $\beta < 2$ (which is true for our set of parameters; and the offset in the cosine actually is in our favor) as the derivative diverges for $\beta_{\text{eff}} \to -1$. Since $\beta_{\text{eff}}/(1+\beta_{\text{eff}})$ is strictly monotonically decreasing, we can infer that its maximum is at $\varphi_{\text{CJJ},0}^x = 0$ yielding $\beta/(1+\beta) \leq 1$.

The final step is to compute the derivative

$$\frac{\partial \gamma}{\partial \beta_{\text{eff}}} = \frac{\partial}{\partial \beta_{\text{eff}}} \left(\frac{1}{\left(1 + \frac{M^2}{LL_{\text{eff}}} \frac{\beta_{\text{eff}}}{1 + \beta_{\text{eff}}} \right)^2} \frac{\beta_{\text{eff}}}{1 + \beta_{\text{eff}}} \right) = \frac{\partial}{\partial \beta_{\text{eff}}} \left(\frac{\beta_{\text{eff}} + \beta_{\text{eff}}^2}{\left(1 + \beta_{\text{eff}} + \frac{M^2}{LL_{\text{eff}}} \beta_{\text{eff}} \right)^2} \right)
= \frac{1 + \beta_{\text{eff}} - \frac{M^2}{LL_{\text{eff}}} \beta_{\text{eff}}}{\left(1 + \beta_{\text{eff}} + \frac{M^2}{LL_{\text{eff}}} \beta_{\text{eff}} \right)^3} = \frac{1 + \beta_{\text{eff}} \left(1 - \frac{M^2}{LL_{\text{eff}}} \right)}{\left(1 + \beta_{\text{eff}} \left(1 + \frac{M^2}{LL_{\text{eff}}} \right) \right)^3}.$$
(B.20)

For $\beta_{\text{eff}} > -1/(1 + M^2/(LL_{\text{eff}}))$, the denominator is positive and for the numerator we have

$$1 + \beta_{\text{eff}} \left(1 - \frac{M^2}{LL_{\text{eff}}} \right) \ge 1 - \frac{1 - \frac{M^2}{LL_{\text{eff}}}}{1 + \frac{M^2}{LL_{\text{eff}}}} = \frac{2M^2}{LL_{\text{eff}}} > 0.$$
 (B.21)

This only puts a slightly tighter condition on $\beta < 2/(1 + M^2/(LL_{\text{eff}}))$.

Thus, under the conditions $E_{L_{\text{CJJ},0}} > E_{J_0}$ and $\beta < 2/(1 + M^2/(LL_{\text{eff}}))$ (which are satisfied for our set of parameters), $\gamma(\varphi_{\text{CJJ},0}^x)$ is strictly monotonically decreasing.

B.3 Computing energies from device parameters

For the energies, we list the conversion from SI units to GHz:

$$E_{L} = \frac{1}{4e^{2}L} = \frac{C}{4eL[nH] \times 10^{-9}eVs \times s} = \frac{6.58211928 \times 10^{-16} \times 10^{9}}{4 \times 1.6021766208 \times 10^{-19}L[nH]s} = \frac{1027.058939}{L[nH]} GHz$$

$$(B.22)$$

$$E_{C} = \frac{2e^{2}}{C} = \frac{2e \times eV}{C[fF] C \times 10^{-15}} = \frac{2 \times 1.6021766208 \times 10^{-19}}{6.58211928 \times 10^{-16} \times C[fF] \times 10^{-15}s} = \frac{486.826979}{C[fF]} GHz$$

$$(B.23)$$

$$E_{J} = \frac{I_{c}}{2e} = \frac{I_{c}[\mu A] \times 10^{-6} C}{2e \times s} = \frac{I_{c}[\mu A] \times 10^{-6}}{2 \times 1.6021766208 \times 10^{-19} s} = 3120.75456 \times I_{c}[\mu A] GHz$$

$$(B.24)$$

$$E_{th} = \frac{k_{B}T}{\hbar} = \frac{1.380649 \times 10^{-23} J/K \times T[mK] \times 10^{-3} K}{1.054571817 \times 10^{-34} Js} = 0.130920339 \times T[mK] GHz$$

$$(B.25)$$

B.4 Time evolution of the coupler

In this section we show that

$$e^{-i\tau\left(\omega a^{\dagger}a\pm 2g\left(a^{\dagger}+a\right)\right)}|0\rangle = e^{i\tau\frac{4g^{2}}{\omega}}|\mp\frac{2g}{\omega}\left(1-e^{-i\omega\tau}\right)\rangle,\tag{B.26}$$

which we used in Section 5.3.1.

Proof: Since $a|0\rangle = 0$, we have

$$\left(a \pm \frac{2g}{\omega}\right)|0\rangle = \pm \frac{2g}{\omega}|0\rangle. \tag{B.27}$$

This implies that $|0\rangle$ is an eigenstate of the shifted annihilation operator $(a \pm 2g/\omega)$. An eigenstate of the annihilation operator is called a coherent state and its eigenvalue is the displacement of the coherent state. Thus, $|0\rangle$ is a coherent state with displacement $\pm 2g/\omega$ w.r.t. the operator $(a \pm 2g/\omega)$. The time evolution of a coherent state $|\alpha\rangle$ with eigenvalue α of the annihilation operator a is given by

$$e^{-i\tau\omega a^{\dagger}a}|\alpha\rangle = |\alpha e^{-i\omega\tau}\rangle,$$
 (B.28)

that is, the eigenvalue of $|\alpha e^{-i\omega\tau}\rangle$ w.r.t. a is given by $\alpha e^{-i\omega\tau}$. We are interested in the time evolution of $|0\rangle$:

$$e^{-i\tau\left(\omega a^{\dagger}a\pm 2g\left(a^{\dagger}+a\right)\right)}|0\rangle = e^{i\tau\frac{4g^{2}}{\omega}}e^{-i\tau\omega\left(a^{\dagger}\pm\frac{2g}{\omega}\right)\left(a\pm\frac{2g}{\omega}\right)}|0\rangle. \tag{B.29}$$

We know that the eigenvalue of the evolved state has to be $\pm e^{-i\omega\tau} 2g/\omega$, and therefore

$$\left(a \pm \frac{2g}{\omega}\right) e^{-i\tau\omega \left(a^{\dagger} \pm \frac{2g}{\omega}\right) \left(a \pm \frac{2g}{\omega}\right)} |0\rangle = \pm \frac{2g}{\omega} e^{-i\omega\tau} e^{-i\tau\omega \left(a^{\dagger} \pm \frac{2g}{\omega}\right) \left(a \pm \frac{2g}{\omega}\right)} |0\rangle. \tag{B.30}$$

We use Eq. (B.30) to infer the displacement of $\exp(-i\tau\omega(a^{\dagger}\pm 2g/\omega)(a\pm 2g/\omega))|0\rangle$ w.r.t. the annihilation operator a:

$$ae^{-i\tau\omega\left(a^{\dagger}\pm\frac{2g}{\omega}\right)\left(a\pm\frac{2g}{\omega}\right)}|0\rangle = \pm\frac{2g}{\omega}(e^{-i\omega\tau}-1)e^{-i\tau\omega\left(a^{\dagger}\pm\frac{2g}{\omega}\right)\left(a\pm\frac{2g}{\omega}\right)}|0\rangle.$$
(B.31)

Thus, the displacement is given by $\mp 2g \left(1 - e^{-i\omega\tau}\right)/\omega$ and we write

$$e^{-i\tau\omega\left(a^{\dagger}\pm\frac{2g}{\omega}\right)\left(a\pm\frac{2g}{\omega}\right)}|0\rangle = |\mp\frac{2g}{\omega}\left(1-e^{-i\omega\tau}\right)\rangle,\tag{B.32}$$

which is equivalent to

$$e^{-i\tau\left(\omega a^{\dagger}a\pm 2g\left(a^{\dagger}+a\right)\right)}|0\rangle = e^{i\tau\frac{4g^{2}}{\omega}}|\mp\frac{2g}{\omega}\left(1-e^{-i\omega\tau}\right)\rangle,\tag{B.33}$$

what we wanted to show.

B.5 Perturbation theory during the annealing process

In this section, we present the calculation of the perturbation theory up to third order used to generate the plot shown in Fig. (5.29) in Section 5.3.4 for the case J=0.94, $h_1=0.99=J+0.05=J+\varepsilon_1$, $h_2=-1=-J-0.06=-(J+\varepsilon_2)$.

First region $(A(s) > JB(s) > \varepsilon_i B(s))$: The unperturbed Hamiltonian is $-A(s)H_{\text{init}}$, and the perturbation is given by $H_J = -JB(s)(\sigma_1^z - \sigma_2^z + \sigma_1^z \sigma_2^z)$. The eigenstates and eigenenergies of the unperturbed Hamiltonian are given by

$$|v_0\rangle = \frac{1}{2} (|\uparrow\uparrow\rangle + |\uparrow\downarrow\rangle + |\downarrow\downarrow\rangle + |\downarrow\downarrow\rangle), \qquad E_0^{(0)} = -\Delta(s)$$
 (B.34)

$$|v_1\rangle = \frac{1}{\sqrt{2}} (|\uparrow\uparrow\rangle - |\downarrow\downarrow\rangle), \qquad E_1^{(0)} = 0$$
 (B.35)

$$|v_2\rangle = \frac{1}{\sqrt{2}} (|\uparrow\downarrow\rangle - |\downarrow\uparrow\rangle), \qquad E_2^{(0)} = 0$$
 (B.36)

$$|v_3\rangle = \frac{1}{2} \left(-|\uparrow\uparrow\rangle + |\uparrow\downarrow\rangle + |\downarrow\uparrow\rangle - |\downarrow\downarrow\rangle \right), \qquad E_3^{(0)} = \Delta(s).$$
 (B.37)

Since the eigenenergy 0 is degenerate, the perturbation Hamiltonian H_J needs to be diagonalized in the subspace spanned by $|v_1\rangle$ and $|v_2\rangle$. We find that this is already the case and the first order corrections for these states are $\pm JB(s)$. The first order $(\langle v_i|H_J|v_i\rangle)$ energy corrections for the other two states are zero. The second order correction terms to the energy are computed by

$$E_i^{(2)} = \sum_{j: E_i^{(0)} \neq E_i^{(0)}} \frac{|\langle v_j | H_J | v_i \rangle|^2}{E_i^{(0)} - E_j^{(0)}},$$
(B.38)

and the third order energy corrections are computed by

$$E_{i}^{(3)} = \sum_{j: E_{j}^{(0)} \neq E_{i}^{(0)}} \sum_{k: E_{k}^{(0)} \neq E_{i}^{(0)}} \frac{\langle v_{i} | H_{J} | v_{k} \rangle \langle v_{k} | H_{J} | v_{j} \rangle \langle v_{j} | H_{J} | v_{i} \rangle}{\left(E_{i}^{(0)} - E_{j}^{(0)}\right) \left(E_{i}^{(0)} - E_{k}^{(0)}\right)} - \langle v_{i} | H_{J} | v_{i} \rangle \sum_{j: E_{j}^{(0)} \neq E_{i}^{(0)}} \frac{|\langle v_{j} | H_{J} | v_{i} \rangle|^{2}}{\left(E_{i}^{(0)} - E_{j}^{(0)}\right)^{2}}.$$
(B.39)

The matrix of the Hamiltonian H_J in the basis of the $|v_i\rangle$ is given by

$$H_{J} = \begin{pmatrix} 0 & 0 & JB(s) & -\sqrt{2}JB(s) \\ 0 & -JB(s) & 0 & 0 \\ JB(s) & 0 & JB(s) & -\sqrt{2}JB(s) \\ -\sqrt{2}JB(s) & 0 & -\sqrt{2}JB(s) & 0 \end{pmatrix}.$$
 (B.40)

We obtain for the corrected energies in the beginning of the annealing process

$$E_0 = -\Delta(s) - \frac{5(JB(s))^2}{2\Delta(s)} + \frac{4(JB(s))^3}{\Delta(s)^2},$$
(B.41)

$$E_1 = -JB(s), (B.42)$$

$$E_2 = JB(s) - \frac{8(JB(s))^3}{\Delta(s)^2},$$
(B.43)

$$E_3 = \Delta(s) + \frac{5(JB(s))^2}{2\Delta(s)} + \frac{4(JB(s))^3}{\Delta(s)^2}.$$
 (B.44)

Second region $(JB(s) > A(s) > \varepsilon_i B(s))$: The unperturbed Hamiltonian is H_J , and the perturbations are $-A(s)H_{\text{init}}$ and $H_{\varepsilon} = -B(s)(\varepsilon_1 \sigma_1^z - \varepsilon_2 \sigma_2^z)$, where $A(s) > \varepsilon_i B(s)$. The eigenstates and eigenenergies of the unperturbed Hamiltonian are given by

$$|v_0\rangle = \frac{1}{2} \left(|\uparrow\uparrow\rangle + \sqrt{2}|\uparrow\downarrow\rangle + |\downarrow\downarrow\rangle \right), \qquad E_0^{(0)} = -JB(s)$$
 (B.45)

$$|v_1\rangle = \frac{1}{\sqrt{2}}(|\uparrow\uparrow\rangle - |\downarrow\downarrow\rangle), \qquad \qquad E_1^{(0)} = -JB(s)$$
 (B.46)

$$|v_2\rangle = \frac{1}{2} \left(-|\uparrow\uparrow\rangle + \sqrt{2}|\uparrow\downarrow\rangle - |\downarrow\downarrow\rangle \right), \qquad E_2^{(0)} = -JB(s)$$
 (B.47)

$$|v_3\rangle = |\downarrow\uparrow\rangle,$$
 $E_3^{(0)} = 3JB(s).$ (B.48)

For the three-fold degenerate eigenspace, we used the eigenstates already computed in Section 5.3.4 to obtain the states in which the perturbation Hamiltonian $-A(s)H_{\text{init}}$ is diagonal in this subspace. The matrix of the Hamiltonian $-A(s)H_{\text{init}}$ in the basis of the $|v_i\rangle$ is given by

$$-A(s)H_{\text{init}} = \begin{pmatrix} -\Delta(s)/\sqrt{2} & 0 & 0 & -\Delta(s)/2\\ 0 & 0 & 0 & 0\\ 0 & 0 & \Delta(s)/\sqrt{2} & \Delta(s)/2\\ -\Delta(s)/2 & 0 & \Delta(s)/2 & 0 \end{pmatrix},$$
(B.49)

and the matrix of the Hamiltonian H_{ε} in the basis of the $|v_i\rangle$ is given by

$$H_{\varepsilon} = B(s) \begin{pmatrix} -(\varepsilon_1 + \varepsilon_2)/2 & -(\varepsilon_1 - \varepsilon_2)/\sqrt{2} & -(\varepsilon_1 + \varepsilon_2)/2 & 0\\ -(\varepsilon_1 - \varepsilon_2)/\sqrt{2} & 0 & (\varepsilon_1 - \varepsilon_2)/\sqrt{2} & 0\\ -(\varepsilon_1 + \varepsilon_2)/2 & (\varepsilon_1 - \varepsilon_2)/\sqrt{2} & -(\varepsilon_1 + \varepsilon_2)/2 & 0\\ 0 & 0 & 0 & (\varepsilon_1 + \varepsilon_2) \end{pmatrix}.$$
(B.50)

Using Eqs. (B.38) and (B.39) where we replace H_J by $-A(s)H_{\text{init}}$ or H_{ε} and use the matrix elements from Eq. (B.49) and Eq. (B.50), we obtain for the corrected energies in this region

$$E_0 = -JB(s) - \frac{\Delta(s)}{\sqrt{2}} - \frac{\Delta(s)^2}{16JB(s)} + \frac{\Delta(s)^3}{64\sqrt{2}(JB(s))^2} - \frac{B(s)(\varepsilon_1 + \varepsilon_2)}{2},$$
 (B.51)

$$E_1 = -JB(s), (B.52)$$

$$E_2 = -JB(s) + \frac{\Delta(s)}{\sqrt{2}} - \frac{\Delta(s)^2}{16JB(s)} - \frac{\Delta(s)^3}{64\sqrt{2}(JB(s))^2} - \frac{B(s)(\varepsilon_1 + \varepsilon_2)}{2},$$
 (B.53)

$$E_3 = 3JB(s) + \frac{\Delta(s)^2}{8JB(s)} + B(s)\left(\varepsilon_1 + \varepsilon_2\right). \tag{B.54}$$

Third region $(JB(s) > \varepsilon_i B(s) > A(s))$: The Hamiltonian is given by $-B(s)H_P = H_J + H_{\varepsilon}$, and the perturbation is $A(s)H_{\text{init}}$. The eigenstates and eigenenergies of the unperturbed Hamiltonian are given by

$$|v_0\rangle = |\uparrow\downarrow\rangle,$$
 $E_0^{(0)} = -(J + \varepsilon_1 + \varepsilon_2)B(s)$ (B.55)

$$|v_1\rangle = |\downarrow\downarrow\rangle,$$
 $E_1^{(0)} = -(J - \varepsilon_1 + \varepsilon_2)B(s)$ (B.56)

$$|v_2\rangle = |\uparrow\uparrow\rangle,$$
 $E_2^{(0)} = -(J + \varepsilon_1 - \varepsilon_2)B(s)$ (B.57)

$$|v_3\rangle = |\downarrow\uparrow\rangle,$$
 $E_3^{(0)} = (3J + \varepsilon_1 + \varepsilon_2)B(s).$ (B.58)

The matrix of the Hamiltonian $-A(s)H_{\text{init}}$ in the basis of the $|v_i\rangle$ is given by

$$-A(s)H_{\text{init}} = -\frac{\Delta}{2} \begin{pmatrix} 0 & 1 & 1 & 0 \\ 1 & 0 & 0 & 1 \\ 1 & 0 & 0 & 1 \\ 0 & 1 & 1 & 0 \end{pmatrix}, \tag{B.59}$$

and we obtain for the corrected energies

$$E_0 = -(J + \varepsilon_1 + \varepsilon_2)B(s) - \frac{\Delta(s)^2}{8\varepsilon_1 B(s)} - \frac{\Delta(s)^2}{8\varepsilon_2 B(s)},$$
(B.60)

$$E_1 = -(J - \varepsilon_1 + \varepsilon_2)B(s) + \frac{\Delta(s)^2}{8\varepsilon_1 B(s)} - \frac{\Delta(s)^2}{8(2J + \varepsilon_2)B(s)},$$
(B.61)

$$E_2 = -(J + \varepsilon_1 - \varepsilon_2)B(s) + \frac{\Delta(s)^2}{8\varepsilon_2 B(s)} - \frac{\Delta(s)^2}{8(2J + \varepsilon_1)B(s)},$$
(B.62)

$$E_3 = (3J + \varepsilon_1 + \varepsilon_2)B(s) + \frac{\Delta(s)^2}{8(2J + \varepsilon_2)B(s)} + \frac{\Delta(s)^2}{8(2J + \varepsilon_1)B(s)}.$$
 (B.63)

Acknowledgments

First of all, I would like to thank my supervisor Kristel Michielsen for giving me the opportunity to work on this thesis and supporting me during this and other projects. Thank you, too, for proofreading my thesis although you have been so busy.

Special thanks go to Hans De Raedt for numerous, sometimes endless discussions on the topic of my thesis as well as many others. QS4ever, you know:). Thank you for updating the spin-dynamics simulator to my needs and helping me with the large runs; and of course, for proofreading basically (oh yeah, I know you love that word:D) everything that I wrote.

Next, I thank Dennis Willsch for being such a loving and considerate husband. I am happy that we got the opportunity to work in the same group as it makes things so much easier. Thank you, too, for critically reading my thesis, for finding nasty typos that no one else spotted and for all your comments that have improved the clarity. I also thank you and Fengping Jin for discussions on programming, maths and physics as well as helpful comments on the analysis of my results.

I appreciate all helpful discussions related to this thesis and about other projects with Seiji Miyashita, David DiVincenzo, Ioan Pop, Martin Spiecker and Daria Gusenkova.

I would also like to thank all current and former members of the QIP group at JSC. I am lucky that I can work in such a nice and funny group; especially Fengping's lunch stories were often a highlight. Also, I really enjoyed our joint projects of which we will probably have even more in the future now that the thesis is finished.

Next, I'd like to thank Bernhard Klemt and Marco Hufnagel: Thanks a million to the two best best men we could've ever had! I appreciate that we managed to organize our *el pacto* meetings although you have moved so far away, and I hope that we can manage to keep that up in the future, too.

Then, I would like to thank my family and in-laws for supporting me all these years during my studies and during the work on this thesis, as well as supporting Dennis and me during our wedding preparations.

I also thank my friends for (sometimes really necessary) distractions from work. Joint trips, games, sport or just sitting together and relaxing have been enjoyable diversions.

I would like to thank Mauricio Reis from D-Wave Systems Inc. for providing technical information on the D-Wave 2000Q quantum processor, and D-Wave Systems Inc. for providing access to and computing time on the D-Wave machine located at the headquarters of D-Wave Systems Inc. in Burnaby (Canada).

Finally, I gratefully acknowledge the Gauss Centre for Supercomputing e.V. for funding this project by providing computing time on the GCS Supercomputer JUWELS at Jülich Supercomputing Centre (JSC) and also the computing time granted through JARA on the supercomputer JURECA at Forschungszentrum Jülich.

Bibliography

- [AAN09] M. H. S. Amin, D. V. Averin, and J. A. Nesteroff, *Decoherence in adiabatic quantum computation*, Phys. Rev. A **79**, 022107 (2009) [cit. on pp. 18, 97, 102].
- [AB09] S. Arora and B. Barak, Computational Complexity: A Modern Approach, Cambridge University Press, 2009 [cit. on p. 13].
- [ACF89] B. APOLLONI, C. CARVALHO, AND D. DE FALCO, Quantum stochastic optimization, Stoch. Process. Their Appl. 33, 233 (1989) [cit. on p. 9].
- [Aha+07] D. Aharonov et al., Adiabatic Quantum Computation is Equivalent to Standard Quantum Computation, SIAM J. Comput. 37, 166 (2007) [cit. on pp. 2, 10].
- [AHV72] P. W. Anderson, B. I. Halperin, and C. M. Varma, Anomalous low-temperature thermal properties of glasses and spin glasses, Phil. Mag. 25, 1 (1972) [cit. on p. 103].
- [AJN06] S. ASHHAB, J. R. JOHANSSON, AND F. NORI, Decoherence in a scalable adiabatic quantum computer, Phys. Rev. A 74, 052330 (2006) [cit. on pp. 7, 97].
- [AL15] T. Albash and D. A. Lidar, Decoherence in adiabatic quantum computation, Phys. Rev. A **91**, 062320 (2015) [cit. on p. 97].
- [AL18] T. Albash and D. A. Lidar, *Adiabatic quantum computation*, Rev. Mod. Phys. **90**, 015002 (2018) [cit. on pp. 2, 10, 11, 13, 15].
- [Alb+15a] T. Albash, T. Rønnow, M. Troyer, and D. Lidar, Reexamining classical and quantum models for the D-Wave One processor, Eur. Phys. J. Spec. Top. **224**, 111 (2015) [cit. on p. 97].
- [Alb+15b] T. Albash, W. Vinci, A. Mishra, P. A. Warburton, and D. A. Lidar, Consistency tests of classical and quantum models for a quantum annealer, Phys. Rev. A **91**, 042314 (2015) [cit. on pp. 49, 97].
- [ALT08] M. H. S. AMIN, P. J. LOVE, AND C. J. S. TRUNCIK, *Thermally Assisted Adiabatic Quantum Computation*, Phys. Rev. Lett. **100**, 060503 (2008) [cit. on pp. 11, 97].
- [Ami09] M. H. S. Amin, Consistency of the Adiabatic Theorem, Phys. Rev. Lett. 102, 220401 (2009) [cit. on p. 10].
- [Ami15] M. H. AMIN, Searching for quantum speedup in quasistatic quantum annealers, Phys. Rev. A **92**, 052323 (2015) [cit. on pp. 98, 99, 108–110, 117, 119, 125].

- [Arc+17] L. Arceci, S. Barbarino, R. Fazio, and G. E. Santoro, *Dissipative Landau-Zener problem and thermally assisted Quantum Annealing*, Phys. Rev. B **96**, 054301 (2017) [cit. on pp. 7, 11, 97].
- [Aru+19] F. Arute et al., Quantum supremacy using a programmable superconducting processor, Nature, (2019) [cit. on p. 2].
- [ATA09] M. H. S. Amin, C. J. S. Truncik, and D. V. Averin, Role of single-qubit decoherence time in adiabatic quantum computation, Phys. Rev. A 80, 022303 (2009) [cit. on pp. 7, 97].
- [Bar+13] R. BARENDS ET AL., Coherent Josephson Qubit Suitable for Scalable Quantum Integrated Circuits, Phys. Rev. Lett. 111, 080502 (2013) [cit. on p. 6].
- [Bar+95] A. BARENCO ET AL., Elementary gates for quantum computation, Phys. Rev. A 52, 3457 (1995) [cit. on pp. 1, 5].
- [BBY05] A. M. VAN DEN BRINK, A. J. BERKLEY, AND M. YALOWSKY, Mediated tunable coupling of flux qubits, New J. Phys. 7, 230 (2005) [cit. on pp. 6, 43, 44].
- [BCS57] J. BARDEEN, L. N. COOPER, AND J. R. SCHRIEFFER, *Theory of Super-conductivity*, Phys. Rev. **108**, 1175 (1957) [cit. on p. 37].
- [Ben+09] D. A. BENNETT ET AL., Decoherence in rf SQUID qubits, Quantum Inf. Process. 8, 217 (2009) [cit. on pp. 6, 102].
- [BF28] M. BORN AND V. FOCK, Beweis des Adiabatensatzes, Z. Phys. **51**, 165 (1928) [cit. on pp. 9, 10].
- [BG09] C. Bartsch and J. Gemmer, Dynamical Typicality of Quantum Expectation Values, Phys. Rev. Lett. 102, 110403 (2009) [cit. on p. 104].
- [BGA09] J. BERGLI, Y. M. GALPERIN, AND B. L. ALTSHULER, Decoherence in qubits due to low-frequency noise, New J. Phys. 11, 025002 (2009) [cit. on p. 103].
- [Bis10] L. S. BISHOP, Circuit Quantum Electrodynamics, PhD thesis, Yale University, 2010 [cit. on pp. 38, 123].
- [BKD04] G. Burkard, R. H. Koch, and D. P. Divincenzo, *Multilevel quantum description of decoherence in superconducting qubits*, Phys. Rev. B **69**, 064503 (2004) [cit. on p. 37].
- [Boi+13] S. BOIXO, T. ALBASH, F. M. SPEDALIERI, N. CHANCELLOR, AND D. A. LIDAR, Experimental signature of programmable quantum annealing, Nat. Commun. 4, 2067 (2013) [cit. on pp. 7, 12, 97].
- [Boi+14] S. BOIXO ET AL., Evidence for quantum annealing with more than one hundred qubits, Nat. Phys. 10, 218 (2014) [cit. on pp. 9, 15, 97].
- [Boi+16] S. BOIXO ET AL., Computational multiqubit tunnelling in programmable quantum annealers, Nat. Commun. 7, 10327 (2016) [cit. on pp. 47, 52, 97].
- [Boi+18] S. BOIXO ET AL., Characterizing quantum supremacy in near-term devices, Nat. Phys. 14, 595 (2018) [cit. on p. 2].

- [Bou+98] V. BOUCHIAT, D. VION, P. JOYEZ, D. ESTEVE, AND M. H. DEVORET, Quantum Coherence with a Single Cooper Pair, Phys. Scr. **T76**, 165 (1998) [cit. on p. 6].
- [Bra+08] S. Bravyi, D. P. Divincenzo, R. Oliveira, and B. M. Terhal, *The complexity of stoquastic local Hamiltonian problems*, Quantum Inf. Comput. 8, 0361 (2008) [cit. on p. 13].
- [Bra+16] J. Braumüller et al., Concentric transmon qubit featuring fast tunability and an anisotropic magnetic dipole moment, Appl. Phys. Lett. **108**, 032601 (2016) [cit. on p. 6].
- [Bro+99] J. BROOKE, D. BITKO, T. F., ROSENBAUM, AND G. AEPPLI, Quantum Annealing of a Disordered Magnet, Science 284, 779 (1999) [cit. on pp. 1, 9, 12, 123].
- [Bun+14] P. I. Bunyk et al., Architectural Considerations in the Design of a Superconducting Quantum Annealing Processor, IEEE Trans. Appl. Superconduct. 24, 1 (2014) [cit. on pp. 12, 15].
- [Bur+14] J. Burnett et al., Evidence for interacting two-level systems from the 1/f noise of a superconducting resonator, Nat. Commun. 5, 4119 (2014) [cit. on p. 103].
- [Bur+19] J. J. Burnett et al., Decoherence benchmarking of superconducting qubits, npj Quantum Inf. 5, 54 (2019) [cit. on p. 6].
- [Cal+18] S. A. CALDWELL ET AL., Parametrically Activated Entangling Gates Using Transmon Qubits, Phys. Rev. Applied 10, 034050 (2018) [cit. on p. 6].
- [Can+11] T. CANEVA, T. CALARCO, R. FAZIO, G. E. SANTORO, AND S. MON-TANGERO, Speeding up critical system dynamics through optimized evolution, Phys. Rev. A 84, 012312 (2011) [cit. on p. 11].
- [CFP01] A. M. CHILDS, E. FARHI, AND J. PRESKILL, Robustness of adiabatic quantum computation, Phys. Rev. A 65, 012322 (2001) [cit. on pp. 1, 7, 9, 11, 97].
- [Che+14] Y. CHEN ET AL., Qubit Architecture with High Coherence and Fast Tunable Coupling, Phys. Rev. Lett. 113, 220502 (2014) [cit. on p. 6].
- [Che+16] Z. Chen et al., Measuring and Suppressing Quantum State Leakage in a Superconducting Qubit, Phys. Rev. Lett. **116**, 020501 (2016) [cit. on p. 6].
- [Chi+02] A. M. CHILDS, E. FARHI, J. GOLDSTONE, AND S. GUTMANN, Finding cliques by quantum adiabatic evolution, Quantum Inf. Comput. 2, 181 (2002) [cit. on pp. 11, 15].
- [Chi00] F. Chiarello, Quantum computing with superconducting quantum interference devices: a possible strategy, Phys. Lett. A **277**, 189 (2000) [cit. on p. 6].
- [Cho+10] J. M. CHOW ET AL., Optimized driving of superconducting artificial atoms for improved single-qubit gates, Phys. Rev. A 82, 040305(R) (2010) [cit. on p. 6].

- [Cho+11] J. M. CHOW ET AL., Simple All-Microwave Entangling Gate for Fixed-Frequency Superconducting Qubits, Phys. Rev. Lett. **107**, 080502 (2011) [cit. on p. 6].
- [Cho10] V. Choi, Adiabatic Quantum Algorithms for the NP-Complete Maximum-Weight Independent Set, Exact Cover and 3SAT Problems, arXiv:1004.2226 (2010) [cit. on p. 15].
- [Col+10] J. H. Cole et al., Quantitative evaluation of defect-models in superconducting phase qubits, Appl. Phys. Lett. 97, 252501 (2010) [cit. on p. 103].
- [Cro+14] E. CROSSON, E. FARHI, C. Y.-Y. LIN, H.-H. LIN, AND P. SHOR, Different Strategies for Optimization Using the Quantum Adiabatic Algorithm, arXiv:1401.7320 (2014) [cit. on pp. 11, 13].
- [CT15] E. COHEN AND B. TAMIR, Quantum annealing foundations and frontiers, Eur. Phys. J. Spec. Top. **224**, 89 (2015) [cit. on p. 9].
- [DA11] N. G. DICKSON AND M. H. S. AMIN, *Does Adiabatic Quantum Optimization Fail for NP-Complete Problems?*, Phys. Rev. Lett. **106**, 050502 (2011) [cit. on p. 15].
- [DBK06] D. P. DIVINCENZO, F. BRITO, AND R. H. KOCH, Decoherence rates in complex Josephson qubit circuits, Phys. Rev. B **74**, 014514 (2006) [cit. on p. 44].
- [DD83] H. DE RAEDT AND B. DE RAEDT, Applications of the generalized Trotter formula, Phys. Rev. A 28, 3575 (1983) [cit. on p. 20].
- [Den+13] Q. DENG, D. V. AVERIN, M. H. AMIN, AND P. SMITH, Decoherence induced deformation of the ground state in adiabatic quantum computation, Sci. Rep. 3, 1479 (2013) [cit. on p. 114].
- [DeR+07] K. DE RAEDT ET AL., Massively parallel quantum computer simulator, Comput. Phys. Commun. 176, 121 (2007) [cit. on p. 106].
- [DeR+17] H. DE RAEDT, F. JIN, M. KATSNELSON, AND K. MICHIELSEN, Relaxation, thermalization, and Markovian dynamics of two spins coupled to a spin bath, Phys. Rev. E **96**, 053306 (2017) [cit. on p. 104].
- [DeR+19] H. DE RAEDT ET AL., Massively parallel quantum computer simulator, eleven years later, Comput. Phys. Commun. 237, 47 (2019) [cit. on p. 106].
- [DeR+97] H. DE RAEDT, S. MIYASHITA, K. SAITO, D. GARCÍA-PABLOS, AND N. GARCÍA, Theory of quantum tunneling of the magnetization in magnetic particles, Phys. Rev. B **56**, 11761 (1997) [cit. on p. 18].
- [DeR87] H. DE RAEDT, Product formula algorithms for solving the time dependent Schrödinger equation, Comp. Phys. Rep. 7, 1 (1987) [cit. on pp. 19–21, 30, 123].
- [Dev97] M. Devoret, Quantum Fluctuations in Electrical Circuits, Fluctuations Quantiques/Quantum Fluctuations: Les Houches Session LXIII, pp. 351, ed. by S. Reynaud, E. Giacobino, and J. Zinn-Justin (1997) [cit. on pp. 37, 38, 123, 127].

- [DiC+09] L. DICARLO ET AL., Demonstration of two-qubit algorithms with a superconducting quantum processor, Nature **460**, 240 (2009) [cit. on p. 6].
- [Dic+13] N. G. DICKSON ET AL., Thermally assisted quantum annealing of a 16-qubit problem, Nat. Commun. 4, 1903 (2013) [cit. on pp. 7, 9, 11, 97].
- [DiV00] D. P. DIVINCENZO, The Physical Implementation of Quantum Computation, Fortschr. Phys. 48, 771 (2000) [cit. on pp. 1, 6].
- [DM06] H. DE RAEDT AND K. MICHIELSEN, "Computational Methods for Simulating Quantum Computers", *Handbook of Theoretical and Computational Nanotechnology*, ed. by M. Rieth and W. Schommers, Los Angeles: American Scientific Publishers, 2006, 2 [cit. on p. 21].
- [DS15] A. DAS AND S. SUZUKI, *Quo Vadis quantum annealing?*, Eur. Phys. J. Spec. Top. **224**, 5 (2015) [cit. on p. 9].
- [DWa] D-WAVE SYSTEMS INC., FAQ: What is the standard annealing schedule: A(s) and B(s)? https://support.dwavesys.com/hc/en-us/articles/360003710353-What-is-the-Standard-Annealing-Schedule-A-s-and-B-s-, as in July 2020 [cit. on p. 12].
- [DWa19] D-WAVE SYSTEMS INC., Technical Description of the D-Wave Quantum Processing Unit, 2019 [cit. on pp. 49, 62, 121].
- [Far+00] E. FARHI, J. GOLDSTONE, S. GUTMANN, AND M. SIPSER, Quantum Computation by Adiabatic Evolution, arXiv:quant-ph/0001106 (2000) [cit. on pp. 1, 9, 11, 12, 123].
- [Far+01] E. FARHI ET AL., A Quantum Adiabatic Evolution Algorithm Applied to Random Instances of an NP-Complete Problem, Science 292, 472 (2001) [cit. on pp. 9, 11, 12, 15, 123].
- [Far+08] E. FARHI, J. GOLDSTONE, S. GUTMANN, AND D. NAGAJ, *How to make the quantum adiabatic algorithm fail*, Int. J. Quantum Inf. **06**, 503 (2008) [cit. on p. 11].
- [Far+12] E. Farhi et al., Performance of the quantum adiabatic algorithm on random instances of two optimization problems on regular hypergraphs, Phys. Rev. A 86, 052334 (2012) [cit. on p. 15].
- [Fey82] R. P. FEYNMAN, Simulating physics with computers, Int. J. Theor. Phys. 21, 467 (1982) [cit. on p. 1].
- [Fey86] R. P. FEYNMAN, Quantum mechanical computers, Found. Phys. 16, 507 (1986) [cit. on p. 1].
- [FGG02] E. FARHI, J. GOLDSTONE, AND S. GUTMANN, Quantum Adiabatic Evolution Algorithms with Different Paths, quant-ph/0208135 (2002) [cit. on p. 11].
- [FGG14] E. FARHI, J. GOLDSTONE, AND S. GUTMANN, A Quantum Approximate Optimization Algorithm, arXiv:1411.4028 (2014) [cit. on p. 1].
- [FI08] L. FAORO AND L. B. IOFFE, Microscopic Origin of Low-Frequency Flux Noise in Josephson Circuits, Phys. Rev. Lett. **100**, 227005 (2008) [cit. on p. 102].

- [Fin+94] A. FINNILA, M. GOMEZ, C. SEBENIK, C. STENSON, AND J. DOLL, Quantum annealing: A new method for minimizing multidimensional functions, Chem. Phys. Lett. **219**, 343 (1994) [cit. on pp. 1, 9, 123].
- [Fri+00] J. R. FRIEDMAN, V. PATEL, W. CHEN, S. K. TOLPYGO, AND J. E. LUKENS, Quantum superposition of distinct macroscopic states, Nature 406, 43 (2000) [cit. on pp. 42, 43].
- [Gal+07] Y. M. GALPERIN, B. L. ALTSHULER, J. BERGLI, D. SHANTSEV, AND V. VINOKUR, Non-Gaussian dephasing in flux qubits due to 1/f noise, Phys. Rev. B **76**, 064531 (2007) [cit. on p. 103].
- [Gam+11] J. M. GAMBETTA, F. MOTZOI, S. T. MERKEL, AND F. K. WILHELM, Analytic control methods for high-fidelity unitary operations in a weakly nonlinear oscillator, Phys. Rev. A 83, 012308 (2011) [cit. on p. 6].
- [Gam13] J. M. GAMBETTA, Control of Superconducting Qubits, Quantum Information Processing: Lecture Notes of the 44th IFF Spring School 2013, pp. B4.1, ed. by D. DiVincenzo (2013) [cit. on p. 88].
- [GLB76] K. GRAMM, L. LUNDGREN, AND O. BECKMAN, SQUID Magnetometer for Mangetization Measurements, Phys. Scr. 13, 93 (1976) [cit. on p. 41].
- [Gon+19] M. GONG ET AL., Genuine 12-Qubit Entanglement on a Superconducting Quantum Processor, Phys. Rev. Lett. 122, 110501 (2019) [cit. on p. 6].
- [Gra+04] M. GRAJCAR ET AL., Low-frequency measurement of the tunneling amplitude in a flux qubit, Phys. Rev. B **69**, 060501(R) (2004) [cit. on p. 6].
- [Gra+18] S. E. DE GRAAF ET AL., Suppression of low-frequency charge noise in superconducting resonators by surface spin desorption, Nat. Commun. 9, 1143 (2018) [cit. on p. 103].
- [Har+07] R. HARRIS ET AL., Sign- and Magnitude-Tunable Coupler for Superconducting Flux Qubits, Phys. Rev. Lett. **98**, 177001 (2007) [cit. on pp. 6, 43].
- [Har+08] R. HARRIS ET AL., Probing Noise in Flux Qubits via Macroscopic Resonant Tunneling, Phys. Rev. Lett. 101, 117003 (2008) [cit. on pp. 42, 106].
- [Har+09a] R. Harris et al., Compound Josephson-junction coupler for flux qubits with minimal crosstalk, Phys. Rev. B **80**, 052506 (2009) [cit. on pp. 6, 42–44, 76, 123, 124].
- [Har+09b] R. HARRIS ET AL., Synchronization of multiple coupled rf-SQUID flux qubits, New J. Phys. 11, 123022 (2009) [cit. on pp. 6, 41, 47, 123].
- [Har+10a] R. HARRIS ET AL., Experimental demonstration of a robust and scalable flux qubit, Phys. Rev. B **81**, 134510 (2010) [cit. on pp. 2, 6, 42, 43, 47, 76, 94, 123].
- [Har+10b] R. HARRIS ET AL., Experimental investigation of an eight-qubit unit cell in a superconducting optimization processor, Phys. Rev. B 82, 024511 (2010) [cit. on pp. 11, 12, 43, 94, 97].
- [Har+18] R. HARRIS ET AL., Phase transitions in a programmable quantum spin glass simulator, Science **361**, 162 (2018) [cit. on p. 15].

- [HD00] A. HAMS AND H. DE RAEDT, Fast algorithm for finding the eigenvalue distribution of very large matrices, Phys. Rev. E **62**, 4365 (2000) [cit. on p. 104].
- [HD90] J. HUYGHEBAERT AND H. DE RAEDT, Product formula methods for time-dependent Schrödinger problems, J. Phys. A: Math. Gen. 23, 5777 (1990) [cit. on p. 30].
- [Hen+15] I. Hen et al., Probing for quantum speedup in spin-glass problems with planted solutions, Phys. Rev. A 92, 042325 (2015) [cit. on p. 15].
- [HLL89] S. HAN, J. LAPOINTE, AND J. E. LUKENS, *Thermal activation in a two-dimensional potential*, Phys. Rev. Lett. **63**, 1712 (1989) [cit. on p. 42].
- [Hob15] L. Hobl, Simulating on the D-Wave Two and Emulating its Behavior on an Ordinary Computer, MA thesis, RWTH Aachen University, 2015 [cit. on p. 18].
- [Hog03] T. Hogg, Adiabatic quantum computing for random satisfiability problems, Phys. Rev. A 67, 022314 (2003) [cit. on p. 15].
- [Hor+17] L. HORMOZI, E. W. BROWN, G. CARLEO, AND M. TROYER, *Nonstoquastic Hamiltonians and quantum annealing of an Ising spin glass*, Phys. Rev. B **95**, 184416 (2017) [cit. on pp. 11, 13].
- [HS14] M. HOFMANN AND G. SCHALLER, Probing nonlinear adiabatic paths with a universal integrator, Phys. Rev. A 89, 032308 (2014) [cit. on p. 11].
- [HY11] I. HEN AND A. P. YOUNG, Exponential complexity of the quantum adiabatic algorithm for certain satisfiability problems, Phys. Rev. E 84, 061152 (2011) [cit. on pp. 12, 15].
- [Jac99] J. D. JACKSON, Classical Electrodynamics (3rd ed.) New York: John Wiley & Sons, 1999 [cit. on p. 130].
- [Jin+13] F. Jin et al., Quantum decoherence scaling with bath size: Importance of dynamics, connectivity, and randomness, Phys. Rev. A 87, 022117 (2013) [cit. on pp. 106, 124].
- [Jin+20] F. JIN ET AL., Random state technology, (2020) [cit. on p. 104].
- [Joh+09] J. JOHANSSON ET AL., Landau-Zener transitions in a superconducting flux qubit, Phys. Rev. B 80, 012507 (2009) [cit. on pp. 97, 102, 108].
- [Joh+11] M. W. JOHNSON ET AL., Quantum annealing with manufactured spins, Nature 473, 194 (2011) [cit. on pp. 11, 97, 125].
- [Jos62] B. D. Josephson, Possible new effects in superconductive tunnelling, Phys. Lett. 1, 251 (1962) [cit. on pp. 37, 38].
- [Jos64] B. D. JOSEPHSON, *Coupled Superconductors*, Rev. Mod. Phys. **36**, 216 (1964) [cit. on pp. 37, 38].
- [Jül18] JÜLICH SUPERCOMPUTING CENTRE, JURECA: Modular supercomputer at Jülich Supercomputing Centre, Journal of large-scale research facilities 4, (2018) [cit. on p. 77].

- [Jül19] JÜLICH SUPERCOMPUTING CENTRE, JUWELS: Modular Tier-0/1 Super-computer at the Jülich Supercomputing Centre, Journal of large-scale research facilities 5, (2019) [cit. on p. 107].
- [Kar+10] K. Karimi et al., Investigating the Performance of an Adiabatic Quantum Optimization Processor, arXiv:1006.4147 (2010) [cit. on p. 15].
- [Kat50] T. Kato, On the Adiabatic Theorem of Quantum Mechanics, J. Phys. Soc. Jpn. 5, 435 (1950) [cit. on p. 10].
- [KDC07] R. H. KOCH, D. P. DIVINCENZO, AND J. CLARKE, Model for 1/f Flux Noise in SQUIDs and Qubits, Phys. Rev. Lett. 98, 267003 (2007) [cit. on p. 102].
- [Kel+14] J. Kelly et al., Optimal Quantum Control Using Randomized Benchmarking, Phys. Rev. Lett. 112, 240504 (2014) [cit. on p. 6].
- [KGV83] S. KIRKPATRICK, C. D. GELATT, AND M. P. VECCHI, Optimization by Simulated Annealing, Science 220, 671 (1983) [cit. on p. 9].
- [Kin+18] A. D. King et al., Observation of topological phenomena in a programmable lattice of 1,800 qubits, Nature 560, 456 (2018) [cit. on pp. 2, 15].
- [Kli+18] P. V. Klimov et al., Fluctuations of Energy-Relaxation Times in Superconducting Qubits, Phys. Rev. Lett. 121, 090502 (2018) [cit. on p. 6].
- [KM14] A. D. KING AND C. C. McGeoch, Algorithm engineering for a quantum annealing platform, arXiv:1410.2628 (2014) [cit. on p. 9].
- [KN98] T. KADOWAKI AND H. NISHIMORI, Quantum annealing in the transverse Ising model, Phys. Rev. E 58, 5355 (1998) [cit. on pp. 9, 11, 12].
- [Koc+07] J. Koch et al., Charge-insensitive qubit design derived from the Cooper pair box, Phys. Rev. A 76, 042319 (2007) [cit. on pp. 6, 41].
- [Koc+14] G. Kochenberger et al., The unconstrained binary quadratic programming problem: a survey, J. Comb. Optim. 28, 58 (2014) [cit. on pp. 13–15].
- [Kra+19] P. Krantz et al., A quantum engineer's guide to superconducting qubits, Appl. Phys. Rev. 6, 021318 (2019) [cit. on p. 7].
- [Lan+09] T. LANTING ET AL., Geometrical dependence of the low-frequency noise in superconducting flux qubits, Phys. Rev. B **79**, 060509 (2009) [cit. on pp. 102, 106].
- [Lan+14] T. Lanting et al., Entanglement in a Quantum Annealing Processor, Phys. Rev. X 4, 021041 (2014) [cit. on p. 11].
- [Lan32] L. LANDAU, Zur Theorie der Energieübertragung. II, Phys. Z. Sowjetunion 2, 46 (1932) [cit. on pp. 16, 124].
- [Lar+15] T. W. LARSEN ET AL., Semiconductor-Nanowire-Based Superconducting Qubit, Phys. Rev. Lett. 115, 127001 (2015) [cit. on p. 6].
- [Lee+09] P. J. LEEK ET AL., Using sideband transitions for two-qubit operations in superconducting circuits, Phys. Rev. B **79**, 180511(R) (2009) [cit. on p. 6].

- [LHL90] J. LAPOINTE, S. HAN, AND J. LUKENS, Observation of final state effects on macroscopic quantum transitions, Physica B **165-166**, 951 (1990) [cit. on p. 42].
- [Lis+15] J. LISENFELD ET AL., Observation of directly interacting coherent two-level systems in an amorphous material, Nat. Commun. 6, 6182 (2015) [cit. on p. 103].
- [Luc+10] E. LUCERO ET AL., Reduced phase error through optimized control of a superconducting qubit, Phys. Rev. A 82, 042339 (2010) [cit. on p. 6].
- [Luc14] A. Lucas, *Ising formulations of many NP problems*, Front. Phys. **2**, 5 (2014) [cit. on pp. 14, 15].
- [Lup+09] A. Lupaşcu, P. Bertet, E. F. C. Driessen, C. J. P. M. Harmans, and J. E. Mooij, *One- and two-photon spectroscopy of a flux qubit coupled to a microscopic defect*, Phys. Rev. B **80**, 172506 (2009) [cit. on pp. 103, 117].
- [Maj+07] J. MAJER ET AL., Coupling superconducting qubits via a cavity bus, Nature 449, 443 (2007) [cit. on p. 6].
- [Man+09] V. E. MANUCHARYAN, J. KOCH, L. I. GLAZMAN, AND M. H. DEVORET, Fluxonium: Single Cooper-Pair Circuit Free of Charge Offsets, Science 326, 113 (2009) [cit. on p. 6].
- [Mar+02] J. M. MARTINIS, S. NAM, J. AUMENTADO, AND C. URBINA, *Rabi Oscillations in a Large Josephson-Junction Qubit*, Phys. Rev. Lett. **89**, 117901 (2002) [cit. on pp. 6, 41].
- [Mar+19] J. MARSHALL, D. VENTURELLI, I. HEN, AND E. G. RIEFFEL, Power of Pausing: Advancing Understanding of Thermalization in Experimental Quantum Annealers, Phys. Rev. Applied 11, 044083 (2019) [cit. on pp. 11, 98, 121].
- [McC+16] J. R. McClean, J. Romero, R. Babbush, and A. Aspuru-Guzik, *The theory of variational hybrid quantum-classical algorithms*, New J. Phys. **18**, 023023 (2016) [cit. on p. 1].
- [McD09] R. McDermott, Materials Origins of Decoherence in Superconducting Qubits, IEEE Trans. Appl. Superconduct. 19, 2 (2009) [cit. on pp. 103, 106].
- [McK+17] D. C. McKay, C. J. Wood, S. Sheldon, J. M. Chow, and J. M. Gambetta, *Efficient Z gates for quantum computing*, Phys. Rev. A **96**, 022330 (2017) [cit. on p. 6].
- [McK+19] D. C. McKay, S. Sheldon, J. A. Smolin, J. M. Chow, and J. M. Gambetta, *Three-Qubit Randomized Benchmarking*, Phys. Rev. Lett. **122**, 200502 (2019) [cit. on p. 6].
- [MCL19] C. MÜLLER, J. H. COLE, AND J. LISENFELD, Towards understanding two-level-systems in amorphous solids: insights from quantum circuits, Rep. Prog. Phys. 82, 124501 (2019) [cit. on p. 103].
- [Mes61] A. Messiah, Quantum mechanics 1, North Holland, 1961 [cit. on p. 45].
- [MN08] S. MORITA AND H. NISHIMORI, Mathematical foundation of quantum annealing, J. Math. Phys. 49, 125210 (2008) [cit. on pp. 9, 11].

- [MNK09] Y. Matsuda, H. Nishimori, and H. G. Katzgraber, Quantum annealing for problems with ground-state degeneracy, J. Phys.: Conf. Ser. 143, 012003 (2009) [cit. on p. 83].
- [Moo+99] J. E. MOOIJ ET AL., Josephson Persistent-Current Qubit, Science 285, 1036 (1999) [cit. on p. 6].
- [Mot+09] F. MOTZOI, J. M. GAMBETTA, P. REBENTROST, AND F. K. WILHELM, Simple Pulses for Elimination of Leakage in Weakly Nonlinear Qubits, Phys. Rev. Lett. 103, 110501 (2009) [cit. on p. 6].
- [MRH17] J. MARSHALL, E. G. RIEFFEL, AND I. HEN, Thermalization, Freeze-out, and Noise: Deciphering Experimental Quantum Annealers, Phys. Rev. Applied 8, 064025 (2017) [cit. on pp. 98, 99, 101].
- [MSM09] C. MÜLLER, A. SHNIRMAN, AND Y. MAKHLIN, Relaxation of Josephson qubits due to strong coupling to two-level systems, Phys. Rev. B 80, 134517 (2009) [cit. on pp. 103, 106].
- [MSS00] Y. MAKHLIN, G. SCHÖN, AND A. SHNIRMAN, Nano-Electronic Realizations of Quantum Bits, J. Low Temp. Phys. 118, 751 (2000) [cit. on p. 42].
- [MSS01] Y. MAKHLIN, G. SCHÖN, AND A. SHNIRMAN, Quantum-state engineering with Josephson-junction devices, Rev. Mod. Phys. **73**, 357 (2001) [cit. on p. 6].
- [Mül+15] C. MÜLLER, J. LISENFELD, A. SHNIRMAN, AND S. POLETTO, Interacting two-level defects as sources of fluctuating high-frequency noise in superconducting circuits, Phys. Rev. B **92**, 035442 (2015) [cit. on p. 103].
- [Nak+02] Y. NAKAMURA, Y. A. PASHKIN, T. YAMAMOTO, AND J. S. TSAI, *Charge Echo in a Cooper-Pair Box*, Phys. Rev. Lett. **88**, 047901 (2002) [cit. on p. 6].
- [NC10] M. A. NIELSEN AND I. L. CHUANG, Quantum Computation and Quantum Information, Cambridge University Press, 2010 [cit. on p. 2].
- [Nei+18] C. NEILL ET AL., A blueprint for demonstrating quantum supremacy with superconducting qubits, Science **360**, 195 (2018) [cit. on p. 2].
- [Ngu+19] L. B. NGUYEN ET AL., *High-Coherence Fluxonium Qubit*, Phys. Rev. X **9**, 041041 (2019) [cit. on p. 6].
- [NPT99] Y. NAKAMURA, Y. A. PASHKIN, AND J. S. TSAI, Coherent control of macroscopic quantum states in a single-Cooper-pair box, Nature 398, 786 (1999) [cit. on p. 6].
- [Orl+99] T. P. Orlando et al., Superconducting persistent-current qubit, Phys. Rev. B **60**, 15398 (1999) [cit. on p. 6].
- [Ozf+20] I. OZFIDAN ET AL., Demonstration of a Nonstoquastic Hamiltonian in Coupled Superconducting Flux Qubits, Phys. Rev. Applied 13, 034037 (2020) [cit. on p. 13].
- [Pai+16] H. Paik et al., Experimental Demonstration of a Resonator-Induced Phase Gate in a Multiqubit Circuit-QED System, Phys. Rev. Lett. 117, 250502 (2016) [cit. on p. 6].

- [Pai72] C. C. PAIGE, Computational Variants of the Lanczos Method for the Eigenproblem, IMA J. Appl. Math. 10, 373 (1972) [cit. on pp. 19, 76].
- [Pal+14] E. PALADINO, Y. M. GALPERIN, G. FALCI, AND B. L. ALTSHULER, 1/f noise: Implications for solid-state quantum information, Rev. Mod. Phys. 86, 361 (2014) [cit. on p. 103].
- [Per+14] A. PERUZZO ET AL., A variational eigenvalue solver on a photonic quantum processor, Nat. Commun. 5, 4213 (2014) [cit. on p. 1].
- [Phi72] W. A. PHILLIPS, Tunneling states in amorphous solids, J. Low Temp. Phys. 7, 351 (1972) [cit. on p. 103].
- [PJ92] P. M. PARDALOS AND S. JHA, Complexity of uniqueness and local search in quadratic 0–1 programming, Oper. Res. Lett. 11, 119 (1992) [cit. on pp. 13, 14].
- [Plo+04] B. L. T. PLOURDE ET AL., Entangling flux qubits with a bipolar dynamic inductance, Phys. Rev. B **70**, 140501(R) (2004) [cit. on pp. 6, 42].
- [Pop+14] I. M. POP ET AL., Coherent suppression of electromagnetic dissipation due to superconducting quasiparticles, Nature **508**, 369 (2014) [cit. on p. 6].
- [Pra+81] R. J. Prance et al., Macroscopic quantum electrodynamic effects in a superconducting ring containing a Josephson weak link, Nature 289, 543 (1981) [cit. on p. 41].
- [Pre] J. PRESKILL, Lecture Notes for Ph219/CS219: Quantum Information http://theory.caltech.edu/~preskill/ph229/, as in October 2019 [cit. on p. 2].
- [Pre18] J. PRESKILL, Quantum Computing in the NISQ era and beyond, Quantum 2, 79 (2018) [cit. on pp. 1, 10].
- [PT13] A. PAPAGEORGIOU AND J. F. TRAUB, Measures of quantum computing speedup, Phys. Rev. A 88, 022316 (2013) [cit. on p. 13].
- [RC02] J. ROLAND AND N. J. CERF, Quantum search by local adiabatic evolution, Phys. Rev. A 65, 042308 (2002) [cit. on pp. 11, 15].
- [RHL95] R. ROUSE, S. HAN, AND J. E. LUKENS, Observation of Resonant Tunneling between Macroscopically Distinct Quantum Levels, Phys. Rev. Lett. **75**, 1614 (1995) [cit. on p. 42].
- [Ric18] S. RICHER, Design of an inductively shunted transmon qubit with tunable transverse and longitudinal coupling, PhD thesis, RWTH Aachen University, 2018 [cit. on p. 39].
- [Rol+19] M. A. ROL ET AL., Fast, High-Fidelity Conditional-Phase Gate Exploiting Leakage Interference in Weakly Anharmonic Superconducting Qubits, Phys. Rev. Lett. 123, 120502 (2019) [cit. on p. 6].
- [Røn+14] T. F. RØNNOW ET AL., Defining and detecting quantum speedup, Science **345**, 420 (2014) [cit. on pp. 13, 15].
- [RSA78] R. L. RIVEST, A. SHAMIR, AND L. ADLEMAN, A Method for Obtaining Digital Signatures and Public-Key Cryptosystems, Commun. ACM 21, 120 (1978) [cit. on p. 1].

- [San+02] G. E. SANTORO, R. MARTOŇÁK, E. TOSATTI, AND R. CAR, Theory of Quantum Annealing of an Ising Spin Glass, Science **295**, 2427 (2002) [cit. on pp. 11, 12].
- [Sch+08] J. A. Schreier et al., Suppressing charge noise decoherence in superconducting charge qubits, Phys. Rev. B 77, 180502(R) (2008) [cit. on p. 6].
- [Sen+08] S. SENDELBACH ET AL., Magnetism in SQUIDs at Millikelvin Temperatures, Phys. Rev. Lett. **100**, 227006 (2008) [cit. on p. 102].
- [Sha+10] Y. SHALIBO ET AL., Lifetime and Coherence of Two-Level Defects in a Josephson Junction, Phys. Rev. Lett. **105**, 177001 (2010) [cit. on pp. 103, 117].
- [Shi+14] S. W. Shin, G. Smith, J. A. Smolin, and U. Vazirani, *How "Quantum"* is the *D-Wave Machine?*, arXiv:1401.7087 (2014) [cit. on p. 97].
- [Shn+05] A. Shnirman, G. Schön, I. Martin, and Y. Makhlin, Low- and High-Frequency Noise from Coherent Two-Level Systems, Phys. Rev. Lett. **94**, 127002 (2005) [cit. on pp. 103, 106].
- [Sho94] P. W. Shor, Algorithms for quantum computation: discrete logarithms and factoring, Proceedings 35th Annual Symposium on Foundations of Computer Science, pp. 124 (1994) [cit. on p. 1].
- [Sho97] P. W. Shor, Polynomial-Time Algorithms for Prime Factorization and Discrete Logarithms on a Quantum Computer, SIAM J. Comput. 26, 1484 (1997) [cit. on p. 1].
- [Sim+04] R. W. SIMMONDS ET AL., Decoherence in Josephson Phase Qubits from Junction Resonators, Phys. Rev. Lett. **93**, 077003 (2004) [cit. on pp. 103, 106].
- [SL05] M. S. SARANDY AND D. A. LIDAR, Adiabatic Quantum Computation in Open Systems, Phys. Rev. Lett. 95, 250503 (2005) [cit. on pp. 7, 97].
- [SM01] K. Saito and S. Miyashita, Magnetic Foehn Effect in Adiabatic Transition, J. Phys. Soc. Jpn. **70**, 3385 (2001) [cit. on p. 109].
- [SNK12] R. D. SOMMA, D. NAGAJ, AND M. KIEFEROVÁ, Quantum Speedup by Quantum Annealing, Phys. Rev. Lett. 109, 050501 (2012) [cit. on pp. 11, 15].
- [SS13] J. A. SMOLIN AND G. SMITH, Classical signature of quantum annealing, arXiv:1305.4904 (2013) [cit. on p. 97].
- [SSH97] A. Shnirman, G. Schön, and Z. Hermon, Quantum Manipulations of Small Josephson Junctions, Phys. Rev. Lett. **79**, 2371 (1997) [cit. on pp. 6, 41].
- [ST06] G. E. SANTORO AND E. TOSATTI, Optimization using quantum mechanics: quantum annealing through adiabatic evolution, J. Phys. A: Math. Gen. 39, R393 (2006) [cit. on p. 9].
- [Ste+06] M. STEFFEN ET AL., State Tomography of Capacitively Shunted Phase Qubits with High Fidelity, Phys. Rev. Lett. 97, 050502 (2006) [cit. on p. 6].

- [Ste+10] M. STEFFEN ET AL., *High-Coherence Hybrid Superconducting Qubit*, Phys. Rev. Lett. **105**, 100502 (2010) [cit. on p. 6].
- [STT01] V. N. SMELYANSKIY, U. V. TOUSSAINT, AND D. A. TIMUCIN, Simulations of the adiabatic quantum optimization for the Set Partition Problem, arXiv:quant-ph/0112143 (2001) [cit. on p. 15].
- [Suz76] M. Suzuki, Generalized Trotter's formula and systematic approximants of exponential operators and inner derivations with applications to many-body problems, Commun. Math. Phys. **51**, 83 (1976) [cit. on pp. 20, 123].
- [Suz85] M. Suzuki, Decomposition formulas of exponential operators and Lie exponentials with some applications to quantum mechanics and statistical physics, J. Math. Phys. **26**, 601 (1985) [cit. on p. 20].
- [Suz91] M. Suzuki, General theory of fractal path integrals with applications to many-body theories and statistical physics, J. Math. Phys. **32**, 400 (1991) [cit. on p. 21].
- [SW66] J. R. Schrieffer and P. A. Wolff, Relation between the Anderson and Kondo Hamiltonians, Phys. Rev. 149, 491 (1966) [cit. on pp. 45, 88].
- [SZ67] A. H. SILVER AND J. E. ZIMMERMAN, Quantum States and Transitions in Weakly Connected Superconducting Rings, Phys. Rev. **157**, 317 (1967) [cit. on p. 41].
- [TK84] H. TAL-EZER AND R. KOSLOFF, An accurate and efficient scheme for propagating the time dependent Schrödinger equation, J. Chem. Phys. 81, 3967 (1984) [cit. on p. 19].
- [Tro59] H. F. TROTTER, On the product of semi-groups of operators, Proc. Amer. Math. Soc. 10, 545 (1959) [cit. on p. 20].
- [VAL16] W. VINCI, T. ALBASH, AND D. A. LIDAR, Nested quantum annealing correction, npj Quantum Inf. 2, 16017 (2016) [cit. on p. 10].
- [Wal+00] C. H. VAN DER WAL ET AL., Quantum Superposition of Macroscopic Persistent-Current States, Science 290, 773 (2000) [cit. on p. 6].
- [WBE16] J. J. WALLMAN, M. BARNHILL, AND J. EMERSON, Robust characterization of leakage errors, New J. Phys. 18, 043021 (2016) [cit. on p. 6].
- [Wen17] G. Wendin, Quantum information processing with superconducting circuits: a review, Rep. Prog. Phys. 80, 106001 (2017) [cit. on pp. 6, 41].
- [WG18] C. J. WOOD AND J. M. GAMBETTA, Quantification and characterization of leakage errors, Phys. Rev. A 97, 032306 (2018) [cit. on p. 6].
- [Wil+17] D. WILLSCH, M. NOCON, F. JIN, H. DE RAEDT, AND K. MICHIELSEN, Gate-error analysis in simulations of quantum computers with transmon qubits, Phys. Rev. A **96**, 062302 (2017) [cit. on p. 6].
- [Wil+20] M. WILLSCH, D. WILLSCH, F. JIN, H. DE RAEDT, AND K. MICHIELSEN, Real-time simulation of flux qubits used for quantum annealing, Phys. Rev. A 101, 012327 (2020) [cit. on pp. 7, 42, 47, 49, 70, 107].

- [Wil20] D. Willsch, Supercomputer simulations of transmon quantum computers, PhD thesis, RWTH Aachen University, 2020 [cit. on p. 34].
- [WL02] L.-A. WU AND D. A. LIDAR, *Qubits as parafermions*, J. Math. Phys. **43**, 4506 (2002) [cit. on p. 37].
- [WS07] G. WENDIN AND V. S. SHUMEIKO, Quantum bits with Josephson junctions (Review Article), Low Temp. Phys. 33, 724 (2007) [cit. on p. 41].
- [Yan+16] F. YAN ET AL., The flux qubit revisited to enhance coherence and reproducibility, Nat. Commun. 7, 12964 (2016) [cit. on p. 6].
- [YNT10] F. YOSHIHARA, Y. NAKAMURA, AND J. S. TSAI, Correlated flux noise and decoherence in two inductively coupled flux qubits, Phys. Rev. B 81, 132502 (2010) [cit. on pp. 103, 106].
- [Yos+06] F. YOSHIHARA, K. HARRABI, A. O. NISKANEN, Y. NAKAMURA, AND J. S. TSAI, *Decoherence of Flux Qubits due to 1/f Flux Noise*, Phys. Rev. Lett. **97**, 167001 (2006) [cit. on p. 102].
- [Yos+14] F. Yoshihara et al., Flux qubit noise spectroscopy using Rabi oscillations under strong driving conditions, Phys. Rev. B **89**, 020503(R) (2014) [cit. on p. 7].
- [You+07] J. Q. You, X. Hu, S. Ashhab, and F. Nori, *Low-decoherence flux qubit*, Phys. Rev. B **75**, 140515(R) (2007) [cit. on p. 6].
- [YSK19] X. YOU, J. A. SAULS, AND J. KOCH, Circuit quantization in the presence of time-dependent external flux, Phys. Rev. B **99**, 174512 (2019) [cit. on p. 39].
- [Zen32] C. Zener, *Non-adiabatic crossing of energy levels*, Proc. R. Soc. London, Ser A **137**, 696 (1932) [cit. on pp. 16, 124].
- [Zha+16] P. Zhao, H. De Raedt, S. Miyashita, F. Jin, and K. Michielsen, Dynamics of open quantum spin systems: An assessment of the quantum master equation approach, Phys. Rev. E **94**, 022126 (2016) [cit. on pp. 104, 106, 107, 117, 124].
- [ZTH70] J. E. ZIMMERMAN, P. THIENE, AND J. T. HARDING, Design and Operation of Stable rf-Biased Superconducting Point-Contact Quantum Devices, and a Note on the Properties of Perfectly Clean Metal Contacts, J. Appl. Phys. 41, 1572 (1970) [cit. on p. 41].
- [ZZS16] L. ZENG, J. ZHANG, AND M. SAROVAR, Schedule path optimization for adiabatic quantum computing and optimization, J. Phys. A: Math. Theor. 49, 165305 (2016) [cit. on p. 11].

List of Publications

- [1] M. Willsch, D. Willsch, F. Jin, H. De Raedt, and K. Michielsen, Real-time simulation of flux qubits used for quantum annealing, Phys. Rev. A **101**, 012327 (2020)
- [2] M. Willsch, D. Willsch, F. Jin, H. De Raedt, and K. Michielsen, Benchmarking the Quantum Approximate Optimization Algorithm, Quantum Inf. Process. 19, 197 (2020)
- [3] M. Willsch, D. Willsch, K. Michielsen, F. Jin, T. Denkmayr, S. Sponar, Y. Hasegawa, and H. De Raedt, Long-time correlations in single-neutron interferometry data, J. Phys. Soc. Jpn. 89, 064005 (2020)
- [4] D. Willsch, M. Willsch, H. De Raedt, and K. Michielsen, Support vector machines on the D-Wave quantum annealer, Comput. Phys. Commun. **248**, 107006 (2020)
- [5] D. Willsch, H. Lagemann, M. Willsch, F. Jin, H. De Raedt, K. Michielsen, Benchmarking Supercomputers with the Jülich Universal Quantum Computer Simulator, NIC Symposium 2020, Publication Series of the John von Neumann Institute for Computing (NIC) NIC Series 50, 255 (2020)
- [6] H. De Raedt, F. Jin, D. Willsch, M. Willsch, N. Yoshioka, N. Ito, S. Yuan, and K. Michielsen, Massively parallel quantum computer simulator, eleven years later, Comput. Phys. Commun. 237, 47 (2019)
- [7] D. Willsch, M. Willsch, F. Jin, H. De Raedt, and K. Michielsen, Testing quantum fault tolerance on small systems, Phys. Rev. A 98, 052348 (2018)
- [8] D. Willsch, M. Nocon, F. Jin, H. De Raedt, and K. Michielsen, Gate-error analysis in simulations of quantum computers with transmon qubits, Phys. Rev. A 96, 062302 (2017)
- [9] K. Michielsen, M. Nocon, D. Willsch, F. Jin, Th. Lippert, and H. De Raedt, Benchmarking gate-based quantum computers, Comput. Phys. Commun. 220, 44 (2017)

Eidesstattliche Erklärung

Ich, Madita Franziska Willsch, erkläre hiermit, dass diese Dissertation und die darin dargelegten Inhalte die eigenen sind und selbstständig, als Ergebnis der eigenen originären Forschung, generiert wurden.

Hiermit erkläre ich an Eides statt

- a) Diese Arbeit wurde vollständig oder größtenteils in der Phase als Doktorand dieser Fakultät und Universität angefertigt;
- b) Sofern irgendein Bestandteil dieser Dissertation zuvor für einen akademischen Abschluss oder eine andere Qualifikation an dieser oder einer anderen Institution verwendet wurde, wurde dies klar angezeigt;
- c) Wenn immer andere eigene- oder Veröffentlichungen Dritter herangezogen wurden, wurden diese klar benannt;
- d) Wenn aus anderen eigenen- oder Veröffentlichungen Dritter zitiert wurde, wurde stets die Quelle hierfür angegeben. Diese Dissertation ist vollständig meine eigene Arbeit, mit der Ausnahme solcher Zitate;
- e) Alle wesentlichen Quellen von Unterstützung wurden benannt;
- f) Wenn immer ein Teil dieser Dissertation auf der Zusammenarbeit mit anderen basiert, wurde von mir klar gekennzeichnet, was von anderen und was von mir selbst erarbeitet wurde;
- g) Teile dieser Arbeit wurden zuvor veröffentlicht und zwar in:
 - M. Willsch, D. Willsch, F. Jin, H. De Raedt, and K. Michielsen, Real-time simulation of flux qubits used for quantum annealing, Phys. Rev. A **101**, 012327 (2020)

Datum und Unterschrift		